

A rheological assessment of polyacrylamide-based solutions and hydrogels filled with silica nanoparticles

by

Olawunmi Odunola

Department of Chemical Engineering

McGill University

Montreal, Quebec, Canada

March, 2022

A thesis submitted to McGill University in partial fulfillment of the requirements
for the degree of

Doctor of Philosophy

© Olawunmi Odunola, 2022

Abstract

Nanoparticle (NP)-cross-linked polymer solutions and hydrogels are gaining attention in many engineering and biomedical fields due to their unique response to environmental stimuli, high surface area, particle dispersibility, and tuneable properties. Silica NPs embedded in polymer matrix increased mechanical properties through polymer-NPs attractive interactions or structural changes in the polymer network surrounding the NPs. This thesis consists of two parts: the first part explores the fundamental interaction between silica NPs and polyacrylamide solutions. NPs (bare and PA-coated) served as physical cross-linkers in polyacrylamide solutions and chemically (bis-) cross-linked hydrogels, and the resulting nanocomposites were characterized using rheology. The second part investigated the impact of large deformation on the microstructural changes and mechanical response of bis- and dual-cross-linked hydrogels by using large amplitude oscillatory shear (LAOS) and mean strain superposition test protocols.

To establish an understanding of the PA/NP interactions, several experimental methods were used. Polymer coating was found to reduce mobility and increase both the ζ -potential and the hydrodynamic diameter of the NPs at varying pH levels when measured using electrokinetic-sonic amplitude. The adsorbed amounts were calculated from data obtained by thermogravimetric analysis at various polymer concentrations. The role of bare and PA-coated silica NPs as a physical cross-linker on the morphology of polymer solutions and bis-cross-linked hydrogels was studied over a broad range of viscoelastic properties to ascertain their effects on the nanocomposites' viscoelasticity. Rheological studies in the linear regime of the nanocomposites showed enhanced dynamic moduli compared to the neat polymer solution or hydrogels. Time-concentration superposition (TCS) for the NP-cross-linked polymer solution furnished a master plot with horizontal and vertical shift factors, which provides a relationship between monomer concentration and relaxation time and crossover moduli, respectively. TCS for the dual cross-linked hydrogels yielded relaxation exponents that were

lower than bis-cross-linked hydrogels due to additional physical entanglements with longer relaxation times. Time-temperature superposition was adopted to extend dynamic spectra and furnish the activation energy. For NP-cross-linked polymer solutions, negative apparent activation energy at higher temperatures is interpreted as polymer detachment from the NPs followed by chains swelling and blob network formation.

LAOS was used to study the effects of silica NP cross-linking on the flow-induced microstructure of polyacrylamide hydrogels. Nonlinearity is identified by the dependence of storage and loss moduli on strain amplitude. The onset and degree of nonlinearity were quantified, revealing that silica NPs have no significant effects until strain amplitudes are greater than 3. The gels exhibited strain stiffening and a weak strain overshoot for the “stiff” gels at large strain amplitudes. Stress-strain curves distinguished between the viscoelastic response of the “soft” and “stiff” hydrogels. These insights into the interactions of silica NPs and polyacrylamide, and the linear and nonlinear viscoelasticity of NP-cross-linked polymer solutions and hydrogels are vital for making predictions of engineering performance in many applications.

Abrégé

Les solutions de polymères réticulés par nanoparticules (NP) et les hydrogels attirent l'attention dans de nombreux domaines de l'ingénierie et de la biomédicaux en raison de leur réponse unique aux stimuli environnementaux, de leur surface élevée, de leur dispersibilité des particules et de leurs propriétés accordables. Les NP de silice incorporés dans la matrice polymère augmentent les propriétés mécaniques par des interactions attirantes entre les NP et les polymères ou par des changements structurels dans le réseau polymère entourant les NP. Cette thèse se compose de deux parties: la première partie explore l'interaction fondamentale entre les NP de silice et les solutions de polyacrylamide. Les NP (nus et revêtus de PA) ont servi de réticulants physiques dans des solutions de polyacrylamide et des hydrogels réticulés chimiquement (bis-), et les nanocomposites résultants ont été caractérisés par rhéologie. Dans la deuxième partie, nous avons étudié l'impact d'une déformation importante sur les changements microstructuraux et la réponse mécanique des hydrogels réticulés en deux ou en deux étapes en utilisant des protocoles d'essai de cisaillement oscillatoire à grande amplitude (LAOS) et de superposition de déformation moyenne.

Pour établir une compréhension des interactions PA/NP, plusieurs méthodes expérimentales ont été utilisées. Il a été constaté que le revêtement polymère réduisait la mobilité et augmentait à la fois le potentiel ζ et le diamètre hydrodynamique des NP à différents niveaux de pH lorsqu'ils étaient mesurés à l'aide de l'amplitude électro-cinétique-sonique. Les quantités adsorbées ont été calculées à partir des données obtenues par analyse thermogravimétrique à différentes concentrations de polymère. Le rôle des NP de silice nues et revêtues de PA en tant qu'agent de réticulation physique sur la morphologie des solutions de polymères et des hydrogels bis-réticulés a été étudié sur une large gamme de propriétés viscoélastiques pour déterminer leurs effets sur la viscoélasticité des nanocomposites. Des études rhéologiques dans le régime linéaire des nanocomposites ont montré des modules dynamiques améliorés par rapport à la solution de polymère pure ou aux hydrogels. La superposition temps-

concentration (TCS) pour la solution de polymère réticulé NP a fourni un tracé principal avec des facteurs de décalage horizontaux et verticaux, qui fournit une relation entre la concentration de monomère et le temps de relaxation et les modules de croisement, respectivement. Le TCS pour les hydrogels à double réticulation a donné des exposants de relaxation inférieurs à ceux des hydrogels bis-réticulés en raison d'enchevêtrements physiques supplémentaires avec des temps de relaxation plus longs. La superposition temps-température a été adoptée pour étendre les spectres dynamiques et fournir l'énergie d'activation. Pour les solutions de polymères réticulés par le NP, l'énergie d'activation apparente négative à des températures plus élevées est interprétée comme un détachement du polymère des NP suivi d'un gonflement des chaînes et formation d'un réseau de blobs.

LAOS a été utilisé pour étudier les effets de la réticulation du NP de silice sur la microstructure induite par l'écoulement des hydrogels de polyacrylamide. La non-linéarité est identifiée par la dépendance des modules de stockage et de perte sur l'amplitude de la déformation. Le début et le degré de non-linéarité ont été quantifiés, révélant que les NP de silice n'ont aucun effet significatif jusqu'à ce que les amplitudes de déformation soient supérieures à 3. Les gels présentaient un raidissement de la déformation et un faible dépassement de la déformation pour les gels "rigides" à de grandes amplitudes de déformation. Les courbes contrainte-déformation distinguent la réponse viscoélastique des hydrogels "doux" et "rigides". Ces connaissances sur les interactions des NP de silice et du polyacrylamide, ainsi que sur la viscoélasticité linéaire et non linéaire des solutions de polymères réticulés au NP et des hydrogels, sont essentielles pour faire des prédictions de performance technique dans de nombreuses applications.

Acknowledgements

I gratefully acknowledge my supervisor and co-author, Prof. Reghan J. Hill, who gave me the opportunity to study at McGill University. His constant support, advice, and mentorship helped me throughout the time of research and writing this thesis. Accomplishing this thesis would not have been possible without his patience, motivation, invaluable knowledge and ideas, careful editing, and excellent feedback.

I am grateful to all of those with whom I have had the pleasure to work with during this research project. Past and present members of Prof. Hill's research group have all directly or indirectly provided me with research guidance and taught me a great deal about both scientific research and life in general. I would especially like to thank Dr. G. Afuwape, who provided training to perform electrokinetic-sonic-amplitude (ESA) and rheology measurements, and supported and guided my stay in Montréal. Dr. C. Du provided guidance on rheology measurements. Dr. Al-Amodi provided confocal microscopy training, and was always a joy to have around in the laboratory and office.

Outside the group, I am sincerely grateful to Mr F. Caporuscio, who was always very resourceful and willing to help. Mr. A. Golsztajn provided a great deal of support, recommended a thermogravimetric analysis expert in Chemistry department, and provided training on size-exclusion chromatography. Mr. Ranjan Roy answered my questions on instrumentation, and Ms. Louise Miller-Aspin provided valued administrative assistance.

This work would not have been possible without the financial support of the past President of Nigeria (Dr. Goodluck Jonathan: 2006–2015) for the merit-based scholarship via the National University Commission (NUC) and Petroleum Technology Development Fund (PTDF). I am especially indebted to Prof. Reghan J. Hill and McGill University for additional funding through McGill Engineering Doctoral and Graduate Excellence Awards, as well as the NSERC Discovery and Research Tools and Instruments grants that supported

this research.

Special thanks to my parents, Mr. and Mrs. Odunola, and my siblings for their support, appreciation, encouragement, and a keen interest in my academic achievements. Finally, on a personal note, my gratitude goes to my favourite people: my loving and supportive husband, Olanrewaju Ogunmola, and my beloved son, Timileyin Ogunmola, who showered me with love and unending inspiration.

Contents

Abstract	i
Abrégé	iii
Acknowledgements	v
List of figures	xiii
List of tables	xxvi
Abbreviations	xxx
Symbols	xxxi
1 Introduction	1
1.1 Motivation	1
1.2 Thesis objectives	2
1.3 Thesis organization	3
1.4 Contributions of authors	4
2 Literature review	5

2.1	Colloids	5
2.1.1	Stability of colloidal dispersions	6
2.1.2	Surface properties of silica nanoparticles	11
2.2	Hydrogels	13
2.2.1	Nanoparticle-cross-linked polyacrylamide hydrogels	17
2.3	Rheology	18
2.3.1	Shear flow	19
2.3.2	Viscoelasticity	22
2.3.3	Nonlinear rheology	23
2.4	Polymer adsorption and electrophoresis	29
3	Adsorption of polyacrylamide onto silica nanoparticles: Role of particle-polymer interactions	32
3.1	Preface	32
3.2	Introduction	33
3.3	Materials and methods	37
3.3.1	Materials	37
3.3.2	TGA	37
3.3.3	Electroacoustic measurements	39
3.3.4	Rheology	40
3.4	Results and discussion	41
3.4.1	Properties of colloidal silica	41

3.4.2	Properties of polyacrylamide	43
3.4.3	Adsorption isotherms of PA on colloidal silica using TGA	43
3.4.4	Effect of pH on the particle/polymer suspension	47
3.4.5	Rheology	57
3.5	Conclusions	65
Appendices		67
3.A	TGA	67
3.B	Polyacrylamide properties	68
4	Silica nanoparticle cross-linking of polyacrylamide: Linear viscoelasticity	69
4.1	Preface	69
4.2	Introduction	70
4.3	Materials and methods	74
4.3.1	Rheology	75
4.4	Results and discussion	76
4.4.1	Polymerization time series	76
4.4.2	Complex viscosity spectra	78
4.4.3	Dynamic moduli spectra	83
4.4.4	Time-concentration superposition	85
4.4.5	Time-temperature superposition	89
4.4.6	Apparent activation energy and effective cross-link density	92
4.4.7	Relaxation times	98

4.5	Hysteresis	100
4.6	Conclusions	102
Appendices		106
4.A	Loss tangent	106
5	Linear viscoelasticity of weakly cross-linked hydrogel nanocomposites	108
5.1	Preface	108
5.2	Introduction	109
5.3	Materials and methods	113
5.3.1	Rheology	115
5.4	Results and discussion	115
5.4.1	Dual cross-linking: chemical and NP	115
5.4.2	Synergistic NP enhancements	116
5.4.3	Dynamic moduli spectra and TCS	118
5.4.4	Time-temperature superposition	120
5.4.5	Apparent activation energy and effective cross-link density	123
5.5	Conclusions	129
Appendices		131
5.A	Steady state storage and loss moduli	131
5.B	Oscillatory sweep response	132
6	Nonlinear rheology of silica-doped polyacrylamide hydrogels under large	

amplitude oscillatory shear (LAOS)	134
6.1 Preface	134
6.2 Introduction	135
6.3 LAOS and FT-rheology theory	138
6.4 Materials and methods	144
6.4.1 Materials	144
6.4.2 Methods	145
6.5 Results and discussion	147
6.5.1 Linear viscoelastic response	147
6.5.2 LAOS test and FT-rheology	150
6.5.3 Hysteresis	163
6.6 Conclusions	164
7 Analysis of linearized rheological response	167
7.1 Preface	167
7.2 Introduction	168
7.3 Theory	169
7.3.1 Linearized dynamic response	169
7.3.2 Nonlinear extension	171
7.4 Materials and methods	173
7.4.1 Materials	173
7.4.2 Methods	173

7.5	Results and discussion	175
7.6	Conclusions	185
8	Conclusions and future work	187
8.1	Summary	187
8.2	Contributions to knowledge	189
8.3	Suggestions for future work	190
	References	192

List of Figures

2.1	Schematic representation of the electrical charge and potential distribution in the electric double layer. The potential distribution is based on Debye-Hückel approximation for Poisson-Boltzmann equation.	7
2.2	Polymer-colloidal particle interactions.	11
2.3	ARES-G2 rheometer with a measured stress transducer, an applied strain motor, and an advanced Peltier system for temperature control. The schematic shows the parallel-plate geometry mostly used in this study with an evaporation blocker on the right.	18
2.4	Simple shear of a fluid along the x -direction with applied force F and a velocity gradient along the y -direction.	20
2.5	Shear stress versus shear rate plots for various flow behaviour (a). Typical shear flow curve for shear thinning (pseudoplastic) fluids in the absence of apparent yield stress (η increases as $\dot{\gamma} \rightarrow 0$, (b). Where, n is the power-law exponent, η_0 and η_∞ are the zero shear and infinite shear viscosity. Yield stress is the stress required for the fluid to flow.	21
2.6	Pipkin diagram for different flow regimes of viscoelastic fluids.	25
2.7	Oscillatory strain sweep at fixed ω . This can be used to determine the linear (SAOS) and the nonlinear (LAOS) viscoelastic regime.	26
2.8	Oscillatory stress response for the sweep test in Figure 2.7. In the SAOS regime the stress response is sinusoidal, whereas in the LAOS regime the stress waveforms are distorted and the shapes change with strain amplitude.	26

2.9	Schematic of an adsorbed polymer chain.	30
3.1	Structural mechanism of PA-modified colloidal silica. Adapted from Gu et al. (2014)	36
3.2	(a) ζ -potential of colloidal silica dispersions (from the ESA) versus the silica volume fraction ϕ adjusted by dilution in RO water at $T \approx 21^\circ\text{C}$ and $\text{pH} \approx 9$. (b) ζ -potential versus the double layer thickness κ^{-1} (from Eqns. (3.11) and (3.12)) with $\phi = 5, 10, 15,$ and 20 v% (κ^{-1} decreases with increasing ϕ). Line is $\zeta = A\kappa^{-1} + B$ with empirical fitting parameters $A \approx -6.5$ mV nm $^{-1}$ and $B \approx -77$ mV. (c) Electrostatic interaction energy according to Eqn. (3.13) with $a = 28$ nm for the four particle volume fractions in (a). Error bars are the standard error σ/\sqrt{n} from $n = 3$ samples.	42
3.3	Adsorbed amount Γ versus PA concentration c for molecular weights 150 kDa (red) and 40 kDa (blue). The data obtained directly from TGA (circles) are compared with counterparts (squares) obtained by subtracting the amount of polymer in interstitial voids of the silica pellets. Error bars are the standard error σ/\sqrt{n} from $n = 3$ samples. Lines are modified Langmuir isotherms with optimal fitting parameters in Table 3.1. Data at 75 mg ml $^{-1}$ for the 150 kDa polymer were not included in the fitting, since doing so furnished negative values of the equilibrium constant K , prompting use of the BET isotherm (3.5). 44	44
3.4	(a) Theoretical maximum adsorbed amount Γ_{max} , (b) equilibrium constant K , and (c) R^2 versus the isotherm exponent n from non-linear fitting of Eqn. (3.3) to data (identified by the symbols and colors in Figure 3.3).	45
3.5	The same as Figure 3.3, but lines are BET isotherms Eqn. (3.5) with fitting parameters Γ_{max} , K_S and K_L in Table 3.2.	48
3.6	(a) ζ -potential (b) hydrodynamic diameter of bare (blue) and PA-coated silica NPs (red) versus pH (3, 6 and 9): silica volume fraction 5 v%, $T \approx 21^\circ\text{C}$. Error bars are the standard error σ/\sqrt{n} from $n = 3$ samples. δ_h is the hydrodynamic polymer layer thickness.	49

3.7	Variation of double layer thickness [κ^{-1} , red, Eqn. (3.11)], hydrodynamic coating thickness (δ_h , blue) and electrophoretic layer thickness [δ_e , yellow, Eqn. (3.14) and green, Eqn. (3.15)] versus pH: silica volume fraction 5 v%, $T \approx 21^\circ\text{C}$. Error bars are the standard errors propagated from the standard error σ/\sqrt{n} of 3 sample measurements of ζ , d , and K_∞	50
3.8	Dynamic mobility magnitude (left) and argument spectra (right) for silica NPs in RO water (blue) and in PA solution (red) at pH = 3 (\diamond), 6 (\square) and 9 (\circ): silica volume fraction $\phi = 5$ v%, $T \approx 21^\circ\text{C}$. K_∞ and κ^{-1} are provided in Table 3.3.	53
3.9	Dynamic mobility magnitude (left) and argument (right) spectra for (a) NPs in reverse-osmosis water with $\zeta = -113.8 \pm 0.20$ mV, and (b) NPs in PA solution with $\zeta = -98.2 \pm 0.65$ mV (from the ESA software) at pH = 9. Circles are experimental data, and lines are Eqn. (3.7) for various particle diameters d . Other prescribed parameters: solvent viscosity $\eta = 9 \times 10^{-4}$ Pa s, temperature $T = 294.15$ K, solvent density $\rho = 998$ kg m $^{-3}$, particle density $\rho_p = 2200$ kg m $^{-3}$	55
3.10	Dynamic mobility magnitude (left) and argument (right) spectra for NPs in reverse-osmosis water (blue), and (b) NPs in PA solution (red) at pH = 9. Circles are experimental data, and solid lines are O'Brien's theory (Eqns. (3.7)–(3.9)). The shear viscosity for the PA-coated NPs is replaced with the theory of Wang and Hill (2009) (Eqn. (3.16)). Fitting parameters (4 for the PA/silica and 2 for the bare silica) are provided in Table 3.5 with prescribed parameters: solvent viscosity 0.9 mPa s, $T = 294.15$ K, solvent density $\rho = 998$ kg m $^{-3}$, particle density $\rho_p = 2200$ kg m $^{-3}$	56
3.11	(a) Steady-shear viscosity η versus shear rate $\dot{\gamma}$ for various 150 kDa PA concentrations in RO water. (b) Specific viscosity versus 150 kDa PA concentration in RO water ($T \approx 21^\circ\text{C}$). Lines are power-law fits with exponents ≈ 1.10 (when $c < c^*$) and ≈ 2.85 (when $c > c^*$) for the dilute and semi-dilute unentangled regions, respectively, with intersection identifying an overlap concentration $c^* \approx 1.94$ w%.	58

3.12 (a) Reduced viscosity η_{sp}/c versus PA concentration c and (b) specific viscosity η_{sp} versus c ($T = 21^\circ\text{C}$). Dashed lines in (a) and (b) are linear and quadratic fits, respectively, to the data (averaged η over all shear rates) with standard errors ($\text{SE}_{\eta_{sp}/c} = 1/c \text{SE}_{\eta_{sp}}$). When the fits are compared to the Huggins Eqns. (3.20) and (3.21), they furnish the intrinsic viscosity and Huggins coefficients presented in Table 3.6.	59
3.13 (a) Steady-shear stress versus shear rate for 150 kDa PA concentration $c = 1.25$ w% with various colloidal silica concentrations 2, 5, 10, 15 and 20 v% (increasing blue to red) ($T = 21^\circ\text{C}$). (b) Relative viscosity η_r versus colloidal silica volume fraction ϕ (blue circles). Solid lines are the fit to the data [blue, Eqn. (3.25)], Einstein [black, Eqn. (3.23)] and Krieger-Dogherty [red, Eqn. (3.24)] models, Afuwape and Hill (2021) [green, Eqn. (3.26)], rheological virial expansions Eqns. (3.27) (purple) and Eqns. (3.28) (yellow) for, respectively, low and high Péclet numbers.	62
3.14 (a) Loss modulus and dynamic viscosity (b) spectra for $c = 1.25$ w% 150 kDa PA solutions with varying colloidal silica concentrations 2, 5, 10, and 20 v% (same as Figure 3.13) ($T = 21^\circ\text{C}$). The dashed line shows the viscosity of water at 21°C	64
3.A.1 Raw TGA data for a mixture of 5 wt% PA and 10 v% colloidal silica.	67
3.A.2 TGA curves of bare and PA-coated colloidal silica with increasing PA concentration in the range $c = 0\text{--}75$ mg ml ⁻¹ and silica concentration 10 v%.	67
4.2.1 Schematic representation of (a) polymer network, (b) particle network and (c) polymer-particle network. Adapted from Isono and Aoyama (2013)	71
4.2.2 Maxwell (single-relaxation time) viscoelastic model furnishing dynamic storage G' and loss G'' moduli spectra with power-law regimes $G' \sim \omega^2$ and $G'' \sim \omega^1$ in the terminal region.	72

4.4.1 Storage (left) and loss (right) moduli time series during polymerization at $\omega \approx 10 \text{ rad s}^{-1}$ and $\gamma \approx 0.2$ for samples A_x (blue), A_xN_5 (green) and A_xC_5 (red) at $T \approx 21^\circ\text{C}$. Subscripts x identify the monomer concentrations in w/v% ≈ 5 (0.7 mol l^{-1}), 8 (1.1 mol l^{-1}) and 10 (1.4 mol l^{-1}), as indicated in each panel.	77
4.4.2 Samples A_{10} , $A_{10}N_5$ and $A_{10}C_5$ after degassing and polymerization, stored in airtight glass tubes at 21°C	78
4.4.3 Storage (circles) and loss (squares) moduli versus strain amplitude at $\omega \approx 10 \text{ rad s}^{-1}$ for samples A_x (blue), A_xN_5 (green) and A_xC_5 (red) at $T \approx 21^\circ\text{C}$. Subscripts x identify the monomer concentrations in w/v% ≈ 5 (0.7 mol l^{-1}), 8 (1.1 mol l^{-1}) and 10 (1.4 mol l^{-1}), as indicated in each panel. The strain amplitude $\gamma \approx 0.2$ is used to define a linear viscoelastic regime for experiments reported here.	79
4.4.4 Complex viscosity $ \eta^* $ spectra at $T = 21$ and 51°C for PAAm sample A_{10} (blue), and silica NP loaded PAAm samples $A_{10}N_5$ (green) and $A_{10}C_5$ (red). $\gamma \approx 0.2$ in the linear viscoelastic regime.	80
4.4.5 Cole-Cole plots accompanying Figure 4.4.4.	82
4.4.6 Storage (open) and loss (filled) moduli spectra accompanying Figure 4.4.4.	83
4.4.7 Han plots accompanying Figure 4.4.4.	85
4.4.8 Left: Storage (circles) and loss (square) moduli spectra of samples A_x , A_xN_5 and A_xC_5 with $c_a = 3, 5, 8, 10$ w/v% (blue, yellow, green, red) at $T = 21^\circ\text{C}$. Right: TCS spectra referenced to the sample with $c_a = 10$ w/v% (red).	86
4.4.9 Horizontal a (blue) and vertical b (red) shift factors versus monomer concentration c_a (wt%) from dynamic moduli spectra in Figure 4.4.8. Lines are fits $a = c_1e^{c_2x}$ and $b = c_3x + c_4$ with $x = c_a$, where the fitting parameters c_1 – c_4 are in table 4.4.3.	87

4.4.10(a)	Horizontal and vertical shift factors versus monomer concentration for PA samples A_x from TCS in Figure 4.4.8. Solid lines are power-law fits [Eqns. (4.3)] and dashed lines are the scaling for ideal solutions (Baumgärtel and Willenbacher, 1996). (b) Zero-shear viscosity versus monomer concentration for samples A_x at $T = 21^\circ\text{C}$. Data from averaging $ \eta^*(\omega) $ as $\omega \rightarrow 0$. Line is $\eta_0 = 2 \times 10^{-6} c_a^{7.45}$, $R^2 = 0.9873$. Error bars are the standard error of the mean.	89
4.4.11	Left: Storage (circles) and loss (square) moduli spectra for samples A_{10} , $A_{10}N_2$ and $A_{10}N_{10}$ ($c_a = 10$ w/v%) at temperatures in the range $T = 21\text{--}56^\circ\text{C}$ (increasing blue to red). Right: TTS spectra referenced to $T = 21^\circ\text{C}$	90
4.4.12	Left: Storage (circles) and loss (square) moduli spectra for samples $A_{10}N_5$ and $A_{10}C_5$ ($c_a = 10$ w/v%) at temperatures in the range $T = 21\text{--}56^\circ\text{C}$ (increasing blue to red). Right: TTS spectra referenced to $T = 21^\circ\text{C}$	91
4.4.13	Temperature dependence for samples A_{10} (blue), $A_{10}N_2$ (yellow), $A_{10}N_{10}$ (purple), $A_{10}N_5$ (green) and $A_{10}C_5$ (red). (a) Logarithm to base 10 of the horizontal shift factor a_T . Line is a fit of Eqn. (4.4). (b) Apparent activation energy E_a from local Arrhenius fits to data triplets in (a). (c) Vertical shift factor b_T . Error bars are the standard error σ/\sqrt{n} from $n = 3$ samples.	94
4.4.14	van Gorp-Palmen plots in the low-temperature range $T = 21\text{--}33.5^\circ\text{C}$ (increasing blue to red) for samples (a) A_{10} , (b) $A_{10}N_2$, (c) $A_{10}N_{10}$, (d) $A_{10}N_5$ and (e) $A_{10}C_5$	96
4.4.15	The same as Figure 4.4.14, but in the high-temperature range $T = 21\text{--}56^\circ\text{C}$ (increasing blue to red).	97
4.4.16(a)	Relaxation time $\tau = \omega_c^{-1}$ versus temperature T at temperatures for which there exists a cross-over angular frequency ω_c in the experimental range. Lines are fits of Eqn. (4.6) with C_1 , C_2 and T_0 from Table 4.4.4, and τ_0 in Table 4.4.5. (b) $\tau = \tau_0 a_T$ versus temperature T . Samples A_{10} (blue), $A_{10}N_2$ (yellow), $A_{10}N_{10}$ (purple), $A_{10}N_5$ (green) and $A_{10}C_5$ (red). Error bars are the standard error σ/\sqrt{n} from $n = 3$ samples.	98

4.4.17	Temperature dependence of (a) storage modulus G' , (b) loss modulus G'' , (c) loss tangent at $\omega \approx 10 \text{ rad s}^{-1}$ and (d) Shear viscosity $ \eta^* $ with $\gamma \approx 0.2$ in the linear viscoelastic regime ($\omega \approx 10 \text{ rad s}^{-1}$). Samples A_{10} (blue), $A_{10}N_2$ (yellow), $A_{10}N_{10}$ (purple), $A_{10}N_5$ (green) and $A_{10}C_5$ (red). Error bars are the standard error σ/\sqrt{n} from $n = 3$ samples.	101
4.5.1	Left: Heating and cooling temperature dependence of the storage modulus G' at $\omega = 10 \text{ rad s}^{-1}$. Right: Storage and loss moduli spectra at $T = 21^\circ\text{C}$ prior the heating cycle (subscript H) and after the subsequent cooling cycle (subscript C). Error bars are the standard error σ/\sqrt{n} from $n = 3$ samples. . . .	103
4.5.2	Heating (blue) and cooling (black) temperature dependence of the storage modulus G' for polymer solution A_{10} over the maximum temperature range $21\text{--}56^\circ\text{C}$. Error bars are the standard error σ/\sqrt{n} from $n = 3$ samples.	104
4.5.3	(a) Heating (blue) and cooling (black) temperature dependence of storage modulus G' for nanocomposite sample $A_{10}N_5$ within a reduced temperature range $21\text{--}36^\circ\text{C}$ not exceeding the critical temperature for this sample ($\approx 38^\circ\text{C}$, Figure 4.4.16). (b) Temperature dependence of the storage modulus G' at $\omega = 1, 10, \text{ and } 100 \text{ rad s}^{-1}$. Error bars are the standard error σ/\sqrt{n} from $n = 3$ samples.	104
4.A.1	Loss tangent versus strain amplitude at $\omega \approx 10 \text{ rad s}^{-1}$ and $T \approx 21^\circ\text{C}$ for samples A_x (blue), A_xN_5 (green) and A_xC_5 (red). Subscript x represents the monomer concentration in w/v% ≈ 5 (0.7 mol l^{-1}), 8 (1.1 mol l^{-1}) and 10 (1.4 mol l^{-1}) as indicated in each panel.	107
5.4.1	Storage (top) and loss moduli (bottom) time series ($\omega \approx 10 \text{ rad s}^{-1}$, $\gamma \approx 0.02$, $T \approx 21^\circ\text{C}$) for samples with acrylamide concentration $c_a \approx 1.4 \text{ mol l}^{-1}$, bis-to-acrylamide concentration ratios $x = 0\text{--}0.6$ (colors identified in the top right panel), bare silica volume fractions 5 and $10 \text{ v}\%$, and a PA-coated silica concentration $\phi = 5 \text{ v}\%$	116

5.4.2	Scaled (a) storage and (b) loss moduli versus silica NP volume fraction for samples B_xN_0 , B_xN_5 , and B_xN_{10} . (c) Scaled moduli versus chemical cross-linker ratio for samples B_xN_5 (circles), B_xC_5 (squares), and B_xN_{10} (diamonds). $\gamma \approx 0.02$, $\omega \approx 10 \text{ rad s}^{-1}$, $T \approx 21^\circ\text{C}$. $G'_{0\infty}$ and $G''_{0\infty}$ are the steady state storage and loss moduli in the absence of NPs. Dashed line is the enhancement for passive NPs according to Eqn. (5.1). Solid lines are to guide the eye. The steady-state moduli G'_∞ and G''_∞ versus chemical cross-linker ratio at $\omega \approx 10 \text{ rad s}^{-1}$ is shown in Figure 5.A.1.	117
5.4.3	Storage (circles) and loss moduli (squares) spectra for dual-cross-linked gels with bis-to-acrylamide ratio $x = 0$ (blue), $x = 0.1$ (yellow), 0.2 (purple), 0.4 (green) and $0.6 \text{ mmol mol}^{-1}$ (red) at $T \approx 21^\circ\text{C}$. Time-concentration superpositions (TCS) are on the right, referenced to the sample with $x = 0.6 \text{ mmol mol}^{-1}$ (red). Shift factors a (blue) and b (red) for scaling the frequency and moduli are provided in the insets, plotted versus the bis-to-acrylamide concentration ratio c_{bis}/c_a with power-law fits and their exponents.	119
5.4.4	Low frequency power-law exponents versus bis-to-acrylamide concentration ratio from loss (a) and storage (b) moduli for gels with NP volume fractions $\phi = 0\%$ (blue), 5% (bare silica, yellow), 5% (PA-coated silica, black) and 10% (bare silica, red). Exponents were obtained from power-law fits to spectra in the left panel of Figure 5.4.3 at angular frequencies in the range $\omega \approx 0.1\text{--}0.7 \text{ rad s}^{-1}$ at various c_{bis}/c_a	121
5.4.5	Storage modulus G' at $\omega = 0.1 \text{ rad s}^{-1}$ and $T = 21^\circ\text{C}$ versus bis-to-acrylamide concentration ratio for gels with NP volume fractions $\phi = 0$ (blue), 5 (bare silica, yellow), 5 (PA-coated silica, black) and $10 \text{ v}\%$ (bare silica, red). Solid lines are linear fits to the data. Dashed line identifies the apparent percolation threshold where $G'_{0,1} = 0$ for the bis-only cross-linked gel, $c_{\text{bis}}/c_a \approx 0.12 \text{ mmol mol}^{-1}$. Increasing the silica NP loading decreases the bis-cross-linking percolation limit, vanishing when $\phi \approx 10 \text{ v}\%$	121
5.4.6	Loss tangent spectra for dual cross-linked gels with varying NP concentration, as indicated at $T = 21^\circ\text{C}$ and $\gamma = 2\%$. The bis-to-acrylamide concentration varies from 0.1 (yellow), 0.2 (purple), 0.4 (green) and $0.6 \text{ mmol mol}^{-1}$ (red).	122

5.4.7 Storage (circles) and loss moduli (squares) spectra for dual-cross-linked gels following time-temperature superposition (TTS) with temperature ranging from $T = 21 - 56^\circ\text{C}$, increasing from blue to red, referenced to $T = 21^\circ\text{C}$. . .	124
5.4.8 Loss tangent spectra for dual-cross-linked gels following time-temperature superposition (TTS) with temperature ranging from $T = 21 - 56^\circ\text{C}$, increasing from blue to red, referenced to $T = 21^\circ\text{C}$	125
5.4.9 Temperature dependence of (a) horizontal shift factor a_T (solid lines are fits of the WLF Eqn. (5.3), (b) apparent activation energy E_a (calculated from local Arrhenius fits to data triplets in (a) (solid lines are Eqn. (5.5)), and (c) vertical shift factor b_T , for samples $\text{B}_{0.4}\text{N}_0$ (blue), $\text{B}_{0.4}\text{N}_5$ (yellow), $\text{B}_{0.4}\text{C}_5$ (black), and $\text{B}_{0.4}\text{N}_{10}$ (red).	127
5.4.10 Temperature dependence of (a) storage G' , (b) loss moduli G'' , and (c) loss tangent $\tan \delta$, for samples $\text{B}_{0.4}\text{N}_0$ (blue), $\text{B}_{0.4}\text{N}_5$ (yellow), $\text{B}_{0.4}\text{C}_5$ (black), and $\text{B}_{0.4}\text{N}_{10}$ (red) at $\omega \approx 10 \text{ rad s}^{-1}$ with $\gamma \approx 2\%$	128
5.A.1 Steady state storage (a) and loss (b) moduli at $\omega = 10 \text{ rad s}^{-1}$ and $T = 21^\circ\text{C}$ versus bis-to-acrylamide concentration ratio for gels with NP volume fractions $\phi = 0$ (blue, $G'_{0\infty}$ and $G''_{0\infty}$), 5 (bare silica, yellow), 5 (PA-coated silica, black) and 10 v% (bare silica, red). $G'_{0\infty}$ and $G''_{0\infty}$ are the steady state storage and loss moduli in the absence of NPs. Solid lines are linear fits to the data.	131
5.B.1 Storage (circles) and loss (squares) moduli versus strain amplitude (at $\omega \approx 10 \text{ rad s}^{-1}$) for bis-to-acrylamide ratios 0 (blue), 0.1 (yellow), 0.2 (purple), 0.4 (green) and 0.6 mmol mol^{-1} (red).	132
5.B.2 Loss tangent accompanying the dynamic moduli in Figure 5.B.1.	133

6.3.1 Stress waveforms (left) and Lissajous-Bowditch plots for the nonlinear viscoelastic response of “soft” PA hydrogel with 3 w% acrylamide and 2.6 w% bis-acrylamide to acrylamide ratio in the pregel solution at $\gamma_0 \approx 6$ and $\omega \approx 10 \text{ rad s}^{-1}$ (top); and “stiff” PA hydrogel with 5 w% acrylamide and 5.3 w% bis-acrylamide to acrylamide ratio in the pregel solution at $\gamma_0 \approx 0.4$ and $\omega \approx 1 \text{ rad s}^{-1}$ (bottom). The first harmonic modulus G'_1 , minimum-strain modulus G'_M and the large-strain modulus G'_L are distinctly defined on each Lissajous-Bowditch curve.	141
6.3.2 Lissajous-Bowditch plot for the nonlinear viscoelastic response of a “stiff” PA nanocomposite hydrogel with 5 w% acrylamide, 5.3 w% bis-acrylamide to acrylamide ratio and 2 v% silica NPs in the pregel solution at $\omega \approx 1 \text{ rad s}^{-1}$ and $\gamma_0 \approx 1$ (blue curve). This is enclosed by a rectangle representing a perfect plastic model response with $\gamma_0 \approx 1.0$ and maximum stress $\sigma_{\text{max}} \approx 653 \text{ Pa}$. The energy dissipation ratio $\phi_E = 0.813$	142
6.5.1 Storage (left) and loss (right) moduli time series during polymerization and cross-linking with $\gamma_0 \approx 0.02$ and $\omega \approx 10 \text{ rad s}^{-1}$ for samples $A_3B_{2.6}$, $A_3B_{2.6}N_5$, and $A_3B_{2.6}C_5$ (a) and $\omega \approx 1 \text{ rad s}^{-1}$ for samples $A_5B_{5.3}$, $A_5B_{5.3}N_2$ (b).	148
6.5.2 Steady-state storage (circles) and loss (squares) moduli spectra, loss tangent spectra accompanying the time series in Figure 6.5.1, in the linear-viscoelastic regime ($\gamma_0 \approx 0.02$).	149
6.5.3 First-harmonic elastic G'_1 (circles) and loss G''_1 (squares) moduli versus strain amplitude γ_0 at $\omega = 10 \text{ rad s}^{-1}$ for “soft” gels (a) and $\omega = 1 \text{ rad s}^{-1}$ for the “stiff” gels (b). Colors are the same as in Figure 6.5.1.	150
6.5.4 Comparison of the first harmonic elastic modulus G'_1 (circles), large-strain modulus G'_L (squares), and minimum-strain modulus G'_M (diamonds).	152
6.5.5 First-harmonic moduli G'_1 , G''_1 (top), large-strain elastic modulus G'_L , and minimum-strain elastic modulus G'_M (bottom) versus strain amplitude γ_0 at $\omega = 1 \text{ rad s}^{-1}$ for sample $A_5B_{5.3}$. Different rheometer plate geometries (indicated) are reported to investigate the existence or not of wall-slip. The cross-over amplitude and modulus for each plate geometry are shown in the inset of (a).	154

6.5.6	Third order elastic Chebyshev coefficient e_3 (circles) and strain-stiffening ratio S (triangles). Colors are the same as in Figure 6.5.1.	155
6.5.7	Third order elastic Chebyshev coefficient e_3 (circles) and strain-stiffening ratio S (triangles) for sample $A_5B_{5.3}$. Different rheometer plate geometries (indicated) are reported to investigate the existence or not of wall-slip.	155
6.5.8	Stress waveforms (left) and Lissajous-Bowditch plots (right) for samples $A_3B_{2.6}$ (blue), $A_3B_{2.6}N_5$ (red), and $A_3B_{2.6}C_5$ (black) at specified strain amplitudes $\gamma_0 \approx 0.05, 0.2, 1$ and 6 with $\omega \approx 10 \text{ rad s}^{-1}$	157
6.5.9	Stress waveforms (left) and Lissajous–Bowditch plots for samples $A_5B_{5.3}$, $A_5B_{5.3}N_2$ at specified strain amplitudes $\gamma_0 \approx 0.05, 0.2, 1$ and 6 with $\omega \approx 1 \text{ rad s}^{-1}$	158
6.5.10	Dissipation ratio as a function of strain amplitude for “stiff” hydrogels $A_5B_{5.3}$ and $A_5B_{5.3}N_2$ at $\omega \approx 1 \text{ rad s}^{-1}$	159
6.5.11	Relative harmonic intensity $I_{n/1}$ as a function of strain amplitude γ_0 measured at $\omega \approx 10 \text{ rad s}^{-1}$ (a, b, and c) and γ_0 measured at $\omega \approx 1 \text{ rad s}^{-1}$ (d and e).	160
6.5.12	The relative third harmonic intensity $I_{3/1}$ as a function of strain amplitude γ_0 measured at $\omega \approx 10 \text{ rad s}^{-1}$ (a) for the soft gels and $\omega \approx 1 \text{ rad s}^{-1}$ (b) for the stiff gels. Lines are fits from Eqn. (6.11) to the experimental data in the strain range specified with fitting parameters in Table 6.5.1. Colors are the same as in Figure 6.5.11.	162
6.5.13	The nonlinear material coefficient Q as a function of strain amplitude γ_0 measured at $\omega \approx 10 \text{ rad s}^{-1}$ (a) for the “soft” gels and $\omega \approx 1 \text{ rad s}^{-1}$ (b) for the “stiff” gels. Lines are fits using Eqn. (6.15) to describe the experimental data in the strain range specified in Table 6.5.2. Fitting parameters are summarized in Table 6.5.2. Colors are the same as in Figure 6.5.11.	163

6.5.1	Nonlinear viscoelastic parameters as a function of strain amplitude at $\omega = 1 \text{ rad s}^{-1}$ for sample $A_5B_{5.3}N_2$. The data represent increasing (forward cycle 1), decreasing (backward cycle) and increasing (forward cycle 2) strain amplitude. The cross-over of the moduli for each cycle are identified by the red dashed circle in the inset.	165
7.5.1	Storage (circles) and loss (squares) moduli spectra, loss tangent spectra with $\gamma_0 \approx 0.02$ (linear viscoelastic regime) and $T \approx 21^\circ\text{C}$ for samples $A_3B_{2.6}$ (blue), $A_3B_{2.6}N_5$ (red), $A_3B_{2.6}C_5$ (black), and $A_5B_{5.3}$ (purple).	176
7.5.2	Stress and strain time series for steady shear $\gamma = \bar{\gamma}$ (left), and mixed shear $\gamma = \bar{\gamma} + \gamma' \sin(\omega t)$ (right). Nanocomposite sample $A_3B_{2.6}N_5$ (top) and hydrogel sample $A_5B_{5.3}$ (bottom) at $T \approx 21^\circ\text{C}$	177
7.5.3	Storage (left) and loss (right) moduli versus strain at $\omega = 10 \text{ rad s}^{-1}$. Solid lines are quadratic fits. Moduli are defined by Eqn. (7.20) (steady shear, green), Eqn. (7.21) (mixed infinitesimal oscillatory shear with $\gamma' = 0.02$ (linear dynamic response) and varying $\bar{\gamma}$, red), Eqn. (7.22) (finite-amplitude oscillatory shear, blue), Eqn. (7.23) (finite-amplitude oscillatory shear, black).	178
7.5.4	Storage (left) and loss (right) moduli versus strain for sample $A_5B_{5.3}$ at $\omega = 1$ (top) and 10 rad s^{-1} (bottom). Solid lines are quadratic fits. Moduli are defined by Eqn. (7.20) (steady shear, green), Eqn. (7.21) (mixed infinitesimal oscillatory shear with $\gamma' = 0.02$ (linear dynamic response) and varying $\bar{\gamma}$, red), Eqn. (7.22) (finite-amplitude oscillatory shear, blue).	179
7.5.5	Normalized storage moduli from Figure (7.5.3) versus strain at $\omega = 10 \text{ rad s}^{-1}$. Solid lines in the left panels are quadratic fits with parameters specified in Table 7.5.3. Solid lines in the right panels are fits of the theoretical Eqn. (7.15) (blue and green) and Eqn. (7.16) (red) to ascertain the values of N (polymer segments between cross-links) provided in Table 7.5.5.	181

7.5.6 Normalized storage moduli from Figure (7.5.4) versus strain at $\omega = 1$ (top) and 10 rad s^{-1} (bottom). Solid lines in the left panels are quadratic fits with parameters specified in Table 7.5.4. Solid lines in the right panels are fits of the theoretical Eqn. (7.15) (blue and green) and Eqn. (7.16) (red) to ascertain the values of N (polymer segments between cross-links) provided in Table 7.5.6.182

List of Tables

3.1	Optimal modified-Langmuir isotherm parameters (maximizing R^2 with respect to n) from Figure 3.4.	46
3.2	BET isotherm parameters accompanying Figure 3.5, with $c_{\text{BET}} = K_S/K_L$ and $c_0 = 1/K_L$	48
3.3	Conductivity at the beginning (K_0) and end (K_∞) of ESA experiments. κ^{-1} are calculated from Eqns. (3.11) and (3.12). K_0 and K_∞ have standard errors σ/\sqrt{n} from $n = 3$ samples, while for κ^{-1} , $\text{SE}_{\kappa^{-1}} = \kappa^{-1}/(2K_\infty) \text{SE}_{K_\infty}$	51
3.4	Total adsorbed layer thickness, as defined by Carasso et al. (1997) , dimensionless thickness, and dimensionless particle radius. Errors are the standard errors propagated from the standard error σ/\sqrt{n} of 3 sample measurements of ζ , d , and K_∞	52
3.5	Model parameters for the O'Brien's theory (Eqns. (3.7)–(3.9)) in Figure 3.10 and measurements from Acoustosizer II instrument software. Shear viscosity is the viscosity of water. It is replaced with Eqn. (3.16) (Wang and Hill, 2009) for the silica NPs in polymer solution in Figure 3.10.	57
3.6	The Huggins coefficient k_H , intrinsic viscosity $[\eta]$, and molecular weight M for nominal 150 kDa PA in RO water at $T = 21^\circ\text{C}$	60
3.B.1	Polyacrylamide properties from (Du and Hill, 2019a) for molecular weights 150 and (40) kDa.	68

4.3.1 ζ -potential, acoustic-attenuation diameter, conductivity and pH of bare and PA-coated silica NPs dispersed in reverse-osmosis water (Type 1, $\sigma \approx 5.6 \mu\text{S m}^{-1}$, $\Omega \approx 18 \text{ MOhm cm}$ at 25°C) at $\approx 21^\circ\text{C}$. These were measured using an AcoustoSizer II instrument (Colloidal Dynamics LLC, USA).	75
4.4.1 Fitting parameters for the power-law model [Eqn. (4.2)] for the neat polymer solutions and nanocomposites shown in Figure 4.4.4 in the specified temperature and angular frequency ω range.	82
4.4.2 Power-law fitting parameters for the neat polymer solutions and nanocomposites in Figure 4.4.6(a) at $T \approx 21^\circ\text{C}$, where G' or $G'' \sim \omega^x$ at low frequency and G' or $G'' \sim \omega^y$ at high frequency.	84
4.4.3 Fitting parameters for the lines in Figure 4.4.9. Shift factors $a = c_1 e^{c_2 x}$ and $b = c_3 x + c_4$ with $x = c_a$	88
4.4.4 Fitting parameters in the WLF Eqn. (4.4) for the samples in Figure 4.4.13(a) for the specified temperature range.	93
4.4.5 Fitting parameter τ_0 in the WLF Eqn. (4.6) for the samples in Figure 4.4.16 over the prescribed temperature range.	99
5.3.1 Compositions of bis- and dual-cross-linked gels, where c_a , x , and y denote acrylamide concentration, bis-acrylamide-to-acrylamide ratio, and NP volume fraction in the pre-gel solution.	114
5.3.2 ζ -potential, acoustic-attenuation diameter, conductivity and pH of bare and PA-coated silica NPs dispersed in reverse-osmosis water (Type 1, $\sigma \approx 5.6 \mu\text{S m}^{-1}$, $\Omega \approx 18 \text{ MOhm cm}$ at 25°C) at $\approx 21^\circ\text{C}$. These were measured using an AcoustoSizer II instrument (Colloidal Dynamics LLC, USA).	114
5.4.1 Fitting parameters for the shift factors in the inset of Figure 5.4.3 of the form $a \approx Ax^y$ and $b \approx Bx^z$. $\Delta = z/y$ is the critical relaxation exponent. Acrylamide concentration for all samples is $c_a \approx 1.4 \text{ mol l}^{-1}$	120
5.4.2 Fitting parameters in WLF Eqn. (5.3) for the pure polymer and nanocomposites shown in Figure 5.4.9(a) in the temperature T range specified.	126

6.4.1 Compositions and steady-state linear viscoelastic properties of PA hydrogels and nanocomposite hydrogels at $\omega \approx 10 \text{ rad s}^{-1}$ (for the soft gels), $\omega \approx 1 \text{ rad s}^{-1}$ (for the stiff gels), with $\gamma_0 \approx 0.02$	145
6.5.1 Parameters A , B and C from fitting Eqn. (6.11) to experimental $I_{3/1}$ data in the strain amplitude range specified at $\omega \approx 10 \text{ rad s}^{-1}$ for the soft gels and 1 rad s^{-1} for the stiff gels.	161
6.5.2 Fitting parameters from fitting Eqn. (6.15) to experimental Q data in the strain amplitude range specified at $\omega \approx 10 \text{ rad s}^{-1}$ for the soft gels and 1 rad s^{-1} for the stiff gels, complex modulus G^* in the linear regime, and NLR [Eqn. (6.16)] of the nanocomposite hydrogels.	164
7.4.1 Compositions and steady-state linear viscoelastic properties of PA hydrogels and nanocomposite hydrogels at $\omega \approx 10 \text{ rad s}^{-1}$ with $\gamma_0 \approx 0.02$	174
7.5.1 Quadratic fitting parameters defined by $y = a + b\gamma + c\gamma^2$, for the curves shown in the left panel of Figure 7.5.3 at $\omega = 10 \text{ rad s}^{-1}$	180
7.5.2 Quadratic fitting parameters defined by $y = a + b\gamma + c\gamma^2$, for the curves shown in the left panel of Figure 7.5.4 at $\omega = 1$ and 10 rad s^{-1}	183
7.5.3 Quadratic fitting parameters defined by $y_0 = 1 + d\gamma + e\gamma^2$, for lines shown in the left panel of Figure 7.5.5 at $\omega = 10 \text{ rad s}^{-1}$. These parameters are consistent with the values from the fitting coefficients in Table (7.5.1).	184
7.5.4 Quadratic fitting parameters defined by $y_0 = 1 + d\gamma + e\gamma^2$, for lines shown in Figure 7.5.6 at $\omega = 1$ and 10 rad s^{-1} . These parameters are consistent with the values from the fitting coefficients in Table (7.5.2) for hydrogel sample A ₅ B _{5.3}	184
7.5.5 Fitting parameter N in Eqns. (7.15) (blue and green lines) and (7.16) (red lines) shown in the right panels of Figure 7.5.5 at $\omega = 10 \text{ rad s}^{-1}$ in the strain range 0–1. $S = (X^T X)^{-1}s^2$, where s^2 is the mean squared error, X is the Jacobian of the fitted values with respect to N , and X^T is the transpose of X . The Student's t is at the 95% confidence level (The MathWorks, 2022).	185

7.5.6 Fitting parameter N in Eqns. (7.15) (blue and green lines) and (7.16) (red lines) shown in the right panels of Figure 7.5.6 at $\omega = 1$ and 10 rad s^{-1} in the strain range 0–1 for hydrogel sample A₅B_{5.3}. $S = (X^T X)^{-1} s^2$, where s^2 is the mean squared error, X is the Jacobian of the fitted values with respect to N , and X^T is the transpose of X . The Student's t is at the 95% confidence level ([The MathWorks, 2022](#)). 186

Abbreviations

A	Acrylamide
APS	Ammonium persulfate
bis	bis-acrylamide
PA	Polyacrylamide
RO	Reverse osmosis
SAOS	Small-amplitude oscillatory shear
TCS	Time-concentration superposition
TEMED	<i>N,N,N',N'</i> -tetramethylethylenediamine
TGA	Thermogravimetric analysis
TTS	Time-temperature superposition
WLF	Williams-Landel-Ferry

Symbols

E_a	Apparent activation energy
G'	Storage modulus
G''	Loss modulus
G_N^0	Plateau modulus
$\tan \delta$	Loss tangent
χ	Flory-Huggins interaction parameter

Introduction

1.1 Motivation

Nanoparticle (NP) -cross-linked polymer solutions and hydrogels have gained widespread attention in recent years, mainly due to the unique properties of NPs. Silica NPs have a large surface area, which promotes strong physical contact and efficient stress transfer between the NPs and the hydrophilic polymer matrix without aggregation or sedimentation. The ability of nanoparticles to remain adsorbed at an interface between two soft materials makes it possible to use them as efficient adhesives. NPs added to enhanced oil recovery displacement fluids can alter the wettability state of the rock, improve the rheological properties, and lower the interfacial tension. The introduction of nanoparticles into tissue-engineering scaffolds offers enormous potential and opportunities for bioactivity enhancement and more customized properties of scaffolds.

Despite the functionalities of NPs, their stability and interactions with the polymer matrix still pose significant challenges in diverse applications. Many fundamental processes that control polymer-NPs or hydrogel-NPs interactions are poorly understood; these include NP surface functionality, time and temperature dependence of viscoelasticity, homogeneity of the polymer/NP networks, reversibility of the rheological properties, and nonlinear rheology resulting from large deformations. Most soft materials tend to have a complex microstructure. The responses of these materials to an applied deformation are often highly nonlinear, even at small deformation. In many cases, nonlinearity is due to changes in the interfacial microstructure.

As a means to tailor polyacrylamide solution and polyacrylamide hydrogel properties, NPs and polymer-coated NPs are added to the pre-gel solution to act as physical cross-linkers. Rheology is used to study how these interactions affect bulk properties at small and

large deformations. The NP surface is chemically modified with polymer to maximize the interactions between the different phases in the polymeric chains of the gel matrix, control their spatial distribution, and, ultimately, enhance the performance of the polymer-NPs or hydrogel-NPs. The adsorbed amount is determined using thermogravimetric analysis, and electroacoustic spectroscopy is used to non-invasively probe the adsorption dynamics.

1.2 Thesis objectives

The principal objective of this thesis is to achieve a fundamental understanding of silica and PA-coated silica NP cross-linking on polyacrylamide solutions and hydrogels, their dynamics, interactions, and effects on mechanical properties. The following specific objectives are pursued in the following chapters:

- Verify the adsorption of PA on colloidal silica and determine the influence of polymer on colloidal stability, structure, and mechanical properties of silica NPs using rheology, electroacoustic spectroscopy, and thermogravimetric analysis.
- Investigate NP-polymer interactions and flow behaviour by measuring the influence of NP cross-linking on the viscoelasticity of polyacrylamide solutions.
- Investigate the structure and dynamics of silica-cross-linked polyacrylamide by measuring the effects of temperature on rheological properties.
- Probe the effect of temperature and varying chemical cross-link density on viscoelasticity, to ascertain the structural changes due to the addition of NPs to weak chemical cross-linked gels.
- Quantify the rheological response of PA hydrogels at large deformation using nonlinear parameters and compare the microstructural changes of the neat PA hydrogels and silica-PA hydrogel nanocomposites under large deformation.
- Differentiate between the nonlinear viscoelasticity of “soft” and “stiff” hydrogels.
- Investigate the strain stiffening response of the hydrogels at large deformation.

1.3 Thesis organization

A review of the literature on colloids, hydrogels, and adsorption is provided in Chapter 2. Background theories for interpreting experimental techniques: rheology, thermogravimetric analysis, and electroacoustic spectroscopy are included.

Colloidal silica is the NP used as a cross-linker in polyacrylamide solutions and hydrogels in this thesis. For effective interactions of polymer-NPs and hydrogel-NPs, the silica surface is modified with PA. Varying literature data on polyacrylamide adsorption to silica NPs prompts the studies reported in Chapter 3. Quantitative analysis of adsorbed amounts was determined using TGA. The effect of the adsorbed polyacrylamide on the colloidal stability, diameter, and mobility of the silica particles was carried out using a non-invasive electrokinetic sonic amplitude (ESA) approach. Rheological characterization of the PA-coated NPs compared to bare NPs and aqueous PA reveals the interactions of PA and silica NPs. The results provide useful benchmarks with which to assess NP and PA-coated NPs of polyacrylamide solutions and hydrogels in the following chapters.

NP cross-linking of polyacrylamide solutions using bare and PA-coated silica NPs is studied in Chapter 4, probing fundamental parameters that influence NP cross-linking. Rheological characterization furnishes dynamic moduli spectra at different temperatures, from which relaxation times are obtained. The temperature-dependent and concentration-dependent relaxation properties are described by time-temperature superposition (TTS) and time-concentration superposition (TCS), respectively. The rheological examination undertaken here reveals that NP-cross-linked gels are viscous fluids on long-time scales at room temperature. This motivated the studies in Chapter 5, where very low chemical cross-linker (bis-acrylamide) ratios are added to the pre-gel solution containing bare or PA-coated silica NPs. Here, the focus is on gelation kinetics, dynamic moduli spectra, and time-dependent concentration and temperature.

The nonlinear viscoelasticity of “soft” and “stiff” polyacrylamide and NP-cross-linked polyacrylamide hydrogels are compared in Chapter 6. Large amplitude oscillatory shear (LAOS) parameters obtained from FT-rheology and Chebyshev stress decomposition are used to compare the microstructural changes, determine the degree of nonlinearity, and the effect of silica NPs on the flow-induced microstructure. Chapter 7 introduces a nonlinear rheology characterization that superimposes a mean strain on a small oscillatory strain. The

resulting stress and input strain are transformed into tangent moduli that are correlated with nonlinear extension models to highlight strain stiffening at large deformation.

Chapter 8 summarizes the thesis and the original contributions to knowledge.

1.4 Contributions of authors

The author (O. Odunola) conducted all the experiments and data analysis with guidance from the author's supervisor (R. J. Hill), who assisted with the experimental designs and interpretations of the results. Initial drafts of Chapters 1–7 were written by the author and edited by R. J. Hill, who also derived the theory for the shear modulus under finite strain presented in Chapter 7. The thesis is submitted in traditional format with Chapters 3–7 the basis of manuscripts to be submitted for publication with O. Odunola (first author) and R. J. Hill as coauthor.

Literature review

2.1 Colloids

In this thesis, the colloidal behaviour and interactions of silica are the central theme. Colloids are a special class of mixtures composed of a continuous medium and one or more dispersed phases. Their properties depend largely on particle size and shape. The particles in a colloidal system are evenly distributed in the solution with sizes generally ranging from 1 nm to 1 μm , small enough that they tend not to settle upon standing but large enough to induce light scattering. Colloids unlike solutions have a solute phase dispersed in a solvent phase. The particle shapes are classified as spheres for example silica sols, gold, and some proteins. Other non-spherical shapes are rods and discs. They are known to have a large surface area to volume ratio. Colloids are found in foods, gels, coatings, natural waters, and biological systems ([Mewis and Wagner, 2011](#)).

Colloidal particles in a dispersion medium are constantly colliding, causing random and rapid motions known as Brownian motion. The nature of the interactions between colloidal particles during such collisions determines the stability and other important characteristics of dispersion. A stable colloidal system is achieved when the particles do not aggregate since there exists a repulsive potential barrier greater than the thermal energy associated with the particle motions. A colloidal system in the dispersed state is mostly stable, however, when its properties change from being in the dispersed to the aggregated state, they tend to become unstable. Therefore, studying the electrostatic interactions in colloidal systems is important to understand colloidal stability and their interactions with other systems like polymers and hydrogels.

2.1.1 Stability of colloidal dispersions

Electromagnetic or van der Waals forces, electrostatic forces, steric forces due to adsorbed molecules at the particle interface, and solvation forces all exist between colloidal particles. These forces control the dynamics of the colloidal system and can cause coagulation of the particles and changes in their spatial distribution, causing the colloid to become unstable. Electrostatic (charge) stabilization or steric stabilization, achieved by the addition of various additives such as polymers, surfactants, or chemical ligands, are two of the most prevalent ways of stabilizing colloidal dispersions. Through Coulombic or steric repulsion between the particles, these stabilizing agents create an energy barrier to particle agglomeration. The stability of a colloidal system is thus achieved when the forces of repulsion balance out the forces of attraction similarly to stable mechanical equilibrium. The repulsive potential barrier hence overcomes the thermal energy associated with the particle motions defined as $k_B T$, where k_B is the Boltzmann constant and T is the absolute temperature.

Electrostatic stabilization of colloids

The surfaces of colloidal particles are mostly charged for several reasons. When charged particles are dispersed in an ionic solution, they attract counterions, which distribute equally throughout the solvent when subjected to thermal motion, generating an electric double layer around each particle. A few opposing charge ions do, however, stay densely packed around the particle surface. This inner layer is known as the *Stern layer*, while the concentration of the rest of the ions known as mobile or solvated ions with the same charge as the initial dispersed material decreases gradually with distance from the particle surface eventually approaching the bulk counterions concentration is known as outer or *diffuse layer*. The electrostatic potential ψ obeys the Poisson-Boltzmann equation (Russel et al., 1989)

$$\nabla^2 \psi = \frac{-1}{\epsilon_0 \epsilon_s} \sum_i n_i^0 z_i e \exp\left(\frac{-z_i e \psi}{k_B T}\right), \quad (2.1)$$

where ϵ_s and ϵ_0 are the solvent and vacuum permittivity, respectively, n_i^0 and z_i are the bulk concentration and valence of ion of type i , and e is the elementary charge unit. Equation 2.1 reduces to $\psi = A \exp(-\kappa x)$, when $|z_i e \psi| < k_B T$ (the Debye-Hückel approximation), where A is a constant and decay constant

$$\kappa^{-1} = (e^2 \sum_i n_i^0 z_i^2 / \epsilon_0 \epsilon_r k_B T)^{-1/2} \quad (2.2)$$

is called the Debye length, and represents the double layer thickness. This length scale is determined by the ionic strength of the solution and the dielectric properties of the suspending medium. For typical colloidal dispersions, κ^{-1} ranges from a fraction of a nanometer to several tens of nanometers.

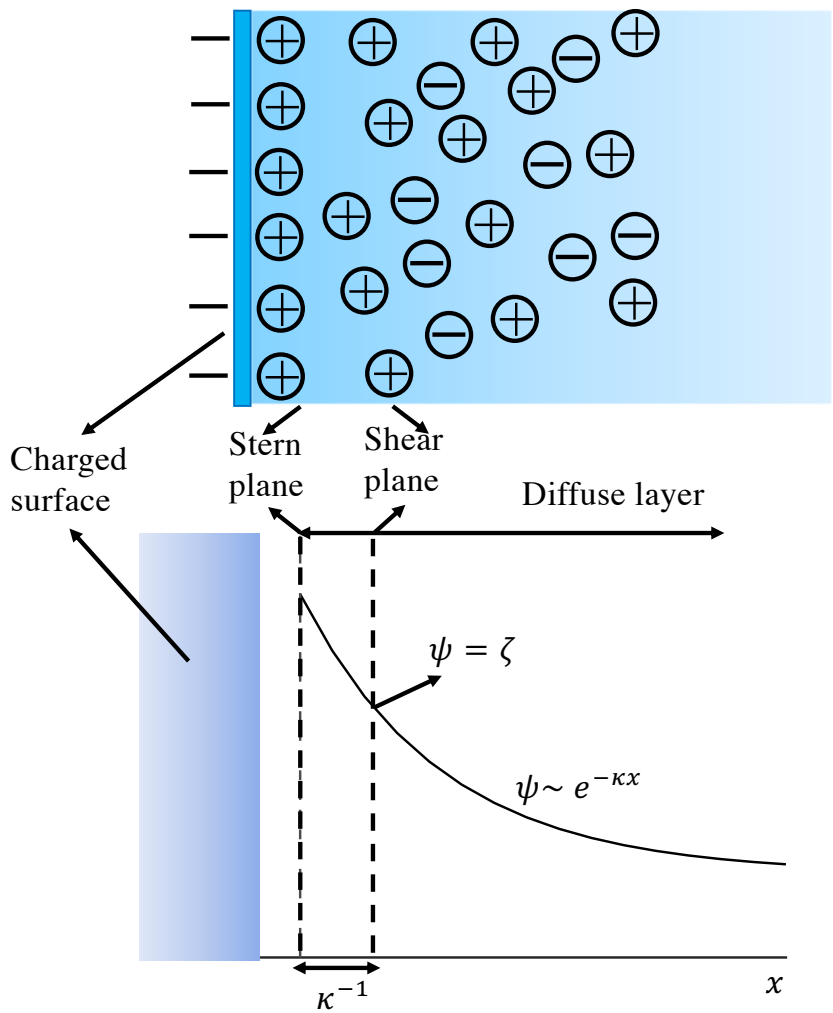


Figure 2.1: Schematic representation of the electrical charge and potential distribution in the electric double layer. The potential distribution is based on Debye-Hückel approximation for Poisson-Boltzmann equation.

The diffuse layer can move under applied stress. The ions in the Stern layer are considered to be immobile and this region acts as a capacitor over which the potential decays linearly. The electric potential at the shear plane where the relative liquid velocity with respect to the particle is zero is termed zeta (ζ)-potential. Although the magnitude of the ζ -potential is very sensitive to a correct determination of the shear plane location, it is often the only

measurable quantity to characterize the double layer properties and is widely used to quantify the magnitude of the surface charge.

When the electric double layers of two particles overlap, the van der Waals attraction force counterbalances the repulsive electrostatic force, resulting in colloidal electrostatic stability (Hiemenz and Rajagopalan, 2016). The Derjaguin–Landau–Verwey–Overbeek (DLVO) theory describes the interaction potential energy between two approaching particles as the sum of the attractive interaction due to van der Waals forces U_V and the electrostatic repulsive forces U_R to explain stability in colloidal systems. The total energy of interactions between particles is

$$U_T = U_V + U_R. \quad (2.3)$$

The DLVO theory is based on the following assumptions: (i) the colloidal dispersion is dilute, (ii) the particle surface has a uniform distribution of electric charge and other properties, and (iii) Brownian motion, electrostatic force, and entropic dispersion dictate the ion distribution. An energy barrier may emerge between the two surfaces depending on the relative strengths of the electrostatic repulsive and van der Waals attraction forces, resulting in particle kinetic stability. When the surface charge of colloidal particles is reduced (for example, by lowering the pH of silica dispersions) or the double-layer shrinks (by adding salt), an attractive interaction occurs, and the colloidal particles coalesce.

The van der Waals attractive forces arise from interactions of the fluctuating dipoles of atoms and molecules. These forces are always present in colloidal interactions, although they are not as strong as hydrogen bonding interactions (Hassan et al., 2012). For attractive pair potential between two atoms, the van der Waals attractive force can be written in its simplest form as:

$$U_V(r) = -\frac{C}{r^6}, \quad (2.4)$$

where C is a proportionality constant that depends on the dipole moment and polarizability of the molecules. Equation (2.3) is based on the assumption that the attractive interaction is additive. For a set of N molecules

$$U_V(r) = \frac{1}{2} \sum_{i=1}^N \sum_{j=1(\neq i)}^N U_{V,ij} r_{ij}, \quad (2.5)$$

where $r_{ij} = |r_i - r_j|$ is the separation distance between molecules. The interaction energy between two spherical bodies of equal radius a and center-to-center distance r is (Hamaker,

1937)

$$U_V(r) = -\frac{A}{6} \left[\frac{2a^2}{r^2 - 4a^2} + \frac{2a^2}{r^2} + \ln \left(\frac{r^2 - 4a^2}{r^2} \right) \right], \quad (2.6)$$

where A is the Hamaker constant.

The electrostatic repulsive forces between two particles arise mainly from charges on the particles' surface, which diminishes to an extent by the double layers. For spherical particles with sufficiently thin double layers ($\kappa a > 10$) and low surface potential, the electrostatic repulsive energy under the condition of constant charge is (Wiese and Healy, 1970)

$$U_R = 2\pi\epsilon_0\epsilon_s a\psi_s^2 \exp(-\kappa h), \quad (2.7)$$

where ψ_s is the surface potential, and h is the separation distance. The repulsive energy depends on the particle surface charge and double layer thickness. When two particles are far apart, there will be no overlap of two double layers, and electrostatic repulsion between two particles is zero.

The interactions between the ions and the colloidal particle are treated as solely electrostatic in the DLVO theory. When ions are close to the particle (surfaces with low intrinsic charge), however, they are more likely to be vulnerable to ion-specific interactions such as solvent-mediated attractive forces. The DLVO theory ignores ion-ion correlations, which are significant at high salt concentrations or for multivalent ions (Horinek, 2014).

Polymeric stabilization of colloids

The addition of polymeric molecules to the dispersion medium influences colloidal stability by preventing colloidal particle aggregation. The polymer solution, like electrostatic stabilization, provides a repulsive force that balances off the attractive van der Waals forces acting on a particle in close proximity to another particle. When compared to electrostatic stabilization, polymeric stabilization promotes colloidal stability for longer periods of time and at larger concentrations (Russel et al., 1989). Polymer molecules influence colloidal stability in the following ways: (i) steric stabilization, (ii) bridging flocculation, and (iii) depletion interaction.

As demonstrated in Figure 2.2(a), steric stabilization is the technique of stabilizing colloidal dispersions using nonionic surfactants or polymer adsorption. It is more successful

than electrostatic stabilization at stabilizing colloidal dispersions in non-aqueous and high-ionic-strength media (Napper, 1977). Entropic repulsion exists between the two sterically stabilized colloidal particles. The repulsive interaction results from the limited interpenetration of polymer segments that are projected away from particle surfaces. For sterically stabilized systems, Eqn. (2.3) can be written as

$$U_T = U_V + U_R + U_S, \quad (2.8)$$

where U_S is the steric interaction component. Steric stabilization provides a more robust method of colloidal stability due to its effectiveness at a wide range of particle volume fractions, effectiveness in aqueous and non-aqueous dispersion media, and its ability to permit reversible flocculation (Liz-Marzán et al., 2001). The interaction between polymer chains will be repulsive if the polymer-solvent interactions are more favourable than polymer-polymer interactions. The solvent in this case is a good solvent. In poor solvents, the polymer chains on one particle have attractive interactions with the chains on the other particles. For effective steric stabilization: (i) the adsorbed polymer should fully coat the surface to avoid polymer bridging (whereby a polymer molecule simultaneously adsorbs on two or more particles) or flocculation caused by van der Waals attraction, (ii) the polymer chain should be highly soluble in the solvent and strongly solvated by its molecules, (iii) the polymer chain should be strongly anchored to the particle surface, and (iv) the adsorbed layer thickness should be greater than 5 nm to prevent weak flocculation (Tadros, 2013).

Flocculation by polymer bridging occurs when high molecular weight polymer chains adsorb simultaneously on more than one particle as shown in Figure 2.2(b), accompanied by the formation and growth of flocs. For bridging flocculation to occur, the polymer chains must be sufficiently long to span the range of the inter-particle repulsion, and insufficient to fully cover the particle surface.

Non-adsorbing polymers induce phase separation by the mechanism of depletion flocculation as shown in Figure 2.2(c). Adding non-adsorbing polymers to colloidal dispersions imparts an osmotic pressure that influences the solvent activity between approaching particles. When the two particles approach each other, the depletion zones overlap causing an increase in the entropy of the dissolved polymer chains due to a larger available volume (Fan and Tuinier, 2010).

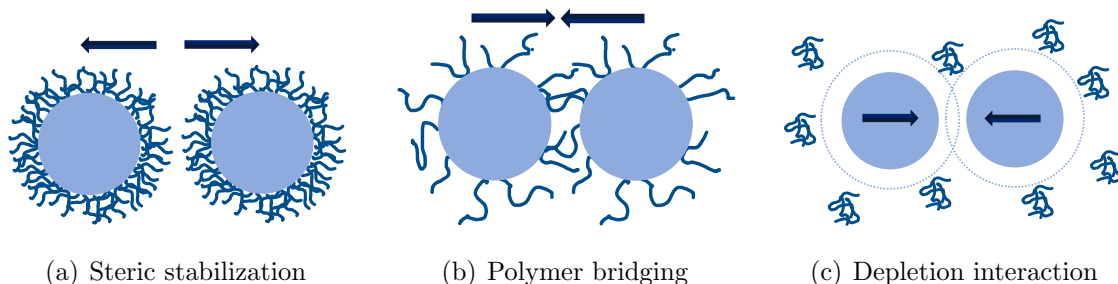


Figure 2.2: Polymer-colloidal particle interactions.

2.1.2 Surface properties of silica nanoparticles

Silicon dioxide (SiO_2) or silica has been used extensively in many industrial applications, including ceramics, glass, electronics, optics, food, pulp, and paper technology, catalysis, and health care, due to its availability, ease of recovery, and precise control of particle size and distribution (Bergna and Roberts, 2006).

Colloidal silica has a variety of intriguing properties that make it ideal for numerous research interests. These properties include (i) a relatively large surface area, (ii) biocompatibility, (iii) low toxicity, (iv) tunability, (v) controllable porosity, (vi) optical transparency, (vii) rich surface chemistry, (viii) high colloidal stability in a variety of solvents under various conditions, and (ix) relative chemical and thermal stability (Lieberman et al., 2014, Bergna and Roberts, 2006, Hyde et al., 2016). Colloidal silica dispersions were found to be stable at the isoelectric point ($\text{pH} \approx 2$) and anomalously stable at high electrolyte concentrations (Atkins et al., 1997). Colloidal silica is used as an additive in the cosmetic, food, and paints industry, as a polishing agent in the electronics industry, as a surface treatment in the pulp and paper industry, and as a supplement in drugs manufacturing. Silicates are necessary for the development and calcification of bone tissue, according to Carlisle (1981).

The presence of silanol groups (SiOH^-), composition, morphology, structure, and surface charge of silica plays significant roles in many biological and bioprocessing activities (Perry, 2009, Niu et al., 2013, Zych et al., 2021). Zych et al. (2021) investigated the effects of dispersing high and low specific surface area silica in a polymer matrix for application in guided bone regeneration (GBR). They reported significant influences of silica on the physicochemical properties such as surface free energy and wetting contact angle of the polymer matrix, and the crystallinity of the nanocomposites. These parameters are useful in cells differentia-

tion, proliferation, and design of nanocomposite 3D scaffolds (Zych et al., 2021). Silica was added to polymer solutions used as injection fluids to lower contact angle, reduce interfacial tension and improve rheological properties for enhanced oil recovery applications (Maghzi et al., 2011, Maurya and Mandal, 2016, Fan et al., 2021, Kumar et al., 2022). Silica NPs have been used to detect a variety of metals in soil with great success. In terms of sensor stability, accuracy, and sensitivity, silica NPs have an advantage over most other known inorganic NPs as a smart delivery system for crops due to their core-shell structure (Sun et al., 2016, Rastogi et al., 2019). The ability to positively influence plant growth for sustainable agriculture are attributes related to the NP surface properties, tunable pore sizes, and concentration (Wanyika et al., 2012, Rastogi et al., 2019). Silica NPs in combination with other NPs such as silver NPs can potentially act as effective sensors for agricultural use (Rastogi et al., 2019). The ability to form strong chemically inert and thermally stable hydrogen and ionic bonds with fibrous and granular materials makes colloidal silica useful as adhesives, catalysts, and coating materials (Atkins et al., 1997, Liu and Han, 2010, Gao et al., 2011, Kim et al., 2017).

Surface modification of colloidal silica by coating, grafting, or adsorption has further expanded their uses. Once modified, the silica particles provide an increased coefficient of friction important in many industrial and architectural coatings. The silica surface can be modified by attaching specific functional groups that create hydrophobic, or fluorophilic surfaces. Polymer grafting on silica has been reported to limit particles aggregation, increase the degree of crystallinity, and improve NPs dispersion, tensile strength, and toughness when loaded in polymer matrix for biomedical applications (Yan et al., 2007, Wu et al., 2013, Shi et al., 2019, Lagarrigue et al., 2020). Surface-treated fumed silica NPs have been added to polymer matrices to improve their thermo-mechanical stability for packaging applications (Fambri et al., 2020, Sepulveda et al., 2020).

The numerous silanol (Si-O-H) and siloxane (Si-O-Si) groups present in the surface and internal structure of colloidal silica determine the chemical characteristics of the material. Organic chemicals or polymers can easily modify the hydroxy ($-\text{OH}$) groups on the surface of silica particles. In general, inorganic materials' surfaces are functionalized with polymer chains either physically (by physisorption) or chemically (by chemisorption) (through covalent bonding). Physisorption is a surface mechanism that uses hydrogen bonding, van der Waals forces, electrostatic forces, and hydrophobic interactions to connect two contacting particles. The non-covalent adsorption makes the process reversible, especially

during processing, and is not a favoured technique. In contrast, covalent bonding is a chemical reaction between the surface and the adsorbate. This technique is preferred because it maximizes stable interfacial compatibility between the two phases, and it involves stronger interactions.

Surface modification of silica nanoparticles with polyacrylamide (PA) has attracted considerable attention in recent years (Bessaies-Bey et al., 2018). Acrylamide-based polymers such as PA are an important class of materials because of their use in many industrial applications such as coatings (Fijałkowska et al., 2021), flocculants (Xiong et al., 2018), paper making (Fijałkowska et al., 2021), enhanced oil recovery (Maurya and Mandal, 2016, Li et al., 2017, Hu et al., 2017), electrophoresis (Stringer, 2005) and biological applications (Yang, 2008). Graft polymerization or adsorption of PA on silica NPs results in a polymer-colloid complex where the polymer chains are covalently bonded to silica, and there is an attraction of the grafted chains with the particle surface through hydrogen bonding. The main parameters influencing the adsorption of PA on silica were reported by Bessaies-Bey et al. (2018) as the state of the silica surface and the physicochemical behaviour of the polymer chains in an aqueous solution.

2.2 Hydrogels

Hydrogels are three-dimensional networks of hydrophilic polymers with the capacity to swell in water and absorb a large amount of water while keeping the structure. The ability to maintain their structure is basically through physical or chemical cross-linking of individual polymer chains. The presence of water in hydrogels aids the transport of active substances into and out of the gel. The unique ability of hydrogels to absorb water arises from hydrophilic functional groups attached to the polymeric backbone, while their resistance to dissolution arises from cross-links between network chains (Gerlach and Arndt, 2010). The following are the different types of water found in hydrogels (Singhal and Gupta, 2016, Parhi, 2017): (i) hydrophilic and hydrophobic bound water, which is an integral part of the hydrogel structure and can be removed under extreme conditions, (ii) free water or bulk water trapped in the network due to the osmotic driving force of the chains, (iii) semi-bound water, which exists between the bound water and the free water, and (iv) interstitial water present in the interstices of the swollen network, physically trapped but not attached to the gel network.

The diversity in the gelation chemistry strategies imparts hydrogels with unique and tailored functionalities for various applications. Hydrogels' unique properties include biocompatibility, biodegradability, low cytotoxicity, the possibility to tailor the hydrogel into an injectable gel, and their similarity to the physiological environment. Because of their three-dimensional structural similarity to the native extracellular matrix (ECM), inherent biocompatibility, and tuneable biophysical and biochemical properties to control cell functions such as cell adhesion, migration, proliferation, and differentiation, hydrogels are frequently used in tissue engineering (Li et al., 2018, Barrett-Catton et al., 2021). Hydrogels' elasticity, flexibility, and self-healing capability make them useful materials as electrodes and electrolytes in flexible devices, bioelectronics, and energy devices, such as batteries and supercapacitors (Guo et al., 2020). The ability to adapt to various stimuli, such as chemical, electrical, humidity, light, pH, solvent, and temperature, makes hydrogels develop from merely static materials to "smart" responsive materials. This uniqueness makes them important materials in electronics, robotics, catalysts, absorbents for carbon capture, chemical detectors (Bahram et al., 2016, Li et al., 2018, Guo et al., 2020), and in biomedical applications such as drug delivery and release (Guo et al., 2020). Tunable porosity and stimuli responsiveness are highly desirable for drug delivery (Lakkadwala et al., 2015). The response of hydrogels to external stimuli is due to the nature of the monomer, chains, charge density, and the degree of cross-linking. The magnitude of response is proportional to the applied external stimulus (Bahram et al., 2016).

Cross-linking in hydrogels contributes immensely to the ability to tune their morphologies, structures, and properties. Cross-linking can be classified into either physical (non-covalent) or chemical (covalent) bonding, and in some cases a combination of both in designing tailored functional materials for specific applications (Guo et al., 2020). Cross-linking methods are selected based on the material's chemistry and expected functionalities. Hydrogels having cross-linkers that can bind specific molecules may exhibit volume changes arising from the presence of specific molecules, so volume changes can be linked to molecular concentration. Most volume responses to external stimuli are reversible, so hydrogels can be considered transducers that convert chemical energy into mechanical energy. These provide tremendous potential for use as sensors, actuators, and artificial muscle (Gerlach and Arndt, 2010).

Physical cross-linking

Physically cross-linked hydrogels have transient junctions that arise mainly from polymer chain entanglements or physical interactions such as hydrogen bonds, hydrophobic interactions, or ionic interactions. Environmental factors such as pH, ionic strength, and temperature can likewise trigger physical cross-linking of polymer chains (Singhal and Gupta, 2016). Physical cross-linking is often reversible and can be reformed by changing pH, temperature, or the solvent concentration (Osada et al., 2004). Physically cross-linked self-healing hydrogels are capable of recovery by reforming their three-dimensional networks via non-covalent interactions such as hydrogen bonds, metal coordination, ionic interactions, and several combined intermolecular interactions (Wei et al., 2014). However, the inability to control the gelation time, chemical functionalization, pore size, and degradation rate limits their performance in several applications (Parhi, 2017). Wang et al. (2010) prepared a physically-cross-linked hydrogel by mixing nanoclay and dendritic molecular binder, showing large mechanical strength, self-healing, and rapid self-recovery ability at room temperature. Singhal and Gupta (2010) synthesized copolymer hydrogel based on acrylamide (AAm), acrylic acid (AAc), and butyl methacrylate (BMA) with a high swelling ratio in an acidic medium. The swelling ratio increased up to ~ 100 times due to the breakage of hydrogen bonds in the acidic medium. Physically cross-linked hydrogels of PVA and xanthan can be achieved by freeze-thawing (Willcox et al., 1999, Giannouli and Morris, 2003). Interactions may occur between charges of a polymer and a small molecule or two polymers of opposite charges to form a hydrogel (Singhal and Gupta, 2016).

Chemical cross-linking

Chemically cross-linked hydrogels have networks with permanent junctions. These hydrogels use covalent bonding that introduces mechanical integrity, stability, and degradation resistance compared to physically cross-linked hydrogels (Bahram et al., 2016). They have improved flexibility and stronger binding energy (Li et al., 2018). However, their use in many biological and tissue engineering applications is limited by the toxicity of the cross-linker (Li et al., 2018). Chemical cross-links are often formed by chemical reactions initiated through pH changes, heat, pressure, or irradiation. Chemically cross-linked gels can be obtained by radical polymerization of low molecular weight monomers in the presence of appropriate cross-linking agents, high energy irradiation, and enzymatic cross-linking reaction. Gelation

starts with polymer clusters that grow simultaneously from multiple points in the system, and eventually come into contact. Most polymer networks formed by free-radical copolymerization are heterogenous on the nanoscale, imparting a distribution of mesh sizes (the distances between adjacent crosslinks), and topological defects, such as dangling chain ends, loops, and cross-linker-cross-linker shortcuts (Di Lorenzo and Seiffert, 2015).

Chemically cross-linked hydrogels are irreversible, and until the covalent connections are disrupted, they cannot be dissolved in solvents. Some covalent bonds, such as acyl hydrazone bonds, boronate ester bonds, disulfide bonds, and imine bonds, allow for the recovery of the gel network in chemically cross-linked hydrogels with self-healing capability (Wei et al., 2014) but are often triggered by an external stimulus such as alternating current, pH, and ultra-violet light. Hydrogels synthesized by radiation-induced cross-linking are often considered safe for most biomedical applications because of the mild processing conditions and absence of toxic chemical cross-linkers (Singhal and Gupta, 2016).

Deformation of cross-linked polymers is generally described using the *affine network model* (Ferry, 1970). It is the simplest network model of microscopic chain deformation. The main assumption of this model is that all crosslinks deform with the macroscopic network *i.e.*, the end of the network strands are fixed in space and are displaced affinely with the whole network. The plateau storage shear modulus predicted under the affine network for a cross-linker functionality $f = 4$ is

$$G_N^0 = \nu k_B T = f n k_B T / 2 = 2 n k_B T, \quad (2.9)$$

where ν is the network strand (polymer segments between two neighbouring crosslinks) number density, n is the crosslink number density, k_B is the Boltzmann constant, T is the absolute temperature, and $k_B T$ is the thermal energy. The *phantom network model* (Ferry, 1970) allows for thermal fluctuations of partial chains about the mean positions of the crosslinks, giving

$$G_N^0 = (1 - 2/f) \nu k_B T = n k_B T. \quad (2.10)$$

Akagi et al. (2013) observed for the first time the transition between the phantom and affine network models occurs at the concentration at which polymer coils begin to overlap (polymer-overlap concentration). Basu et al. (2011) found the degree of PA gel nonaffinity to be independent of the monomer and cross-linker concentrations in the range they studied. Defects in the network causes a portion of cross-linkers to not act as elastically effective cross-links. For PA gels having different monomer concentrations, the maximum cross-

linking efficiency is achieved by seeking optimum cross-linker ratios. Using the affine model to calculate G_N^0 for ideal networks, the maximum cross-linking efficiencies have been reported by [Gerlach and Arndt \(2010\)](#) as 0.01 for 3% w/v, 0.09 for 5% w/v, and 0.2 for 7% w/v gels; [Basu et al. \(2011\)](#) reported cross-linking efficiencies of 0.12 for 7.5% w/v and 0.9 for 15% w/v gels; and [Adibnia and Hill \(2016\)](#) reported 0.012 for 3% w/v gels.

Dual cross-linking

To further improve or expand the applicability and functionality of hydrogels, both covalent and noncovalent cross-linking are been used to design hydrogels. Some other advantages of combining the two cross-linking mechanisms include improved biocompatibility, efficient gelation, and enhanced physical and mechanical properties ([Singhal and Gupta, 2016](#)).

Tensile strength, morphology, and rheological testing are typically used to identify self-healing characteristics. [Wang et al. \(2019\)](#) prepared dual-cross-linked hydrogels combining noncovalent ionic coordination and chemical cross-linking, to design tough and elastic hydrogels (~ 6 MPa tensile strength and 27 MJ m^{-3} toughness) with high extensibility ($\sim 700\%$) and self-recovery capability. Self-healing is achieved by introducing breakable crosslinks. Cross-link breakage and reformation dissipate energy, imparting a form of mechanical reinforcement. NP-cross-linked gels have been proposed as materials with the potential for exhibiting self-healing characteristics ([Qin et al., 2019](#), [Lin and Hsu, 2020](#)).

2.2.1 Nanoparticle-cross-linked polyacrylamide hydrogels

The inclusion of nanofillers in the hydrogel matrix gives rise to nanocomposite hydrogels. Recent attention has been paid to nanoparticles as cross-linker because of their potential benefits. Their incorporation and specific interactions with hydrogel polymer chains reinforce the matrix, contribute to the network elasticity, and increase the mechanical strength of the hydrogel ([Haraguchi et al., 2011b](#), [Lin and Hsu, 2020](#)). Inorganic NPs introduce a variety of functionalities or properties to the hydrogel, such as reversibility, electronic conductivity, and magnetic response ([Kumar et al., 2018](#)). The addition of NPs is strategic not only for enhancing the mechanical properties of the soft matrix but likewise to improve their self-healing properties ([Dai et al., 2018](#), [Qin et al., 2019](#), [Lin and Hsu, 2020](#)).

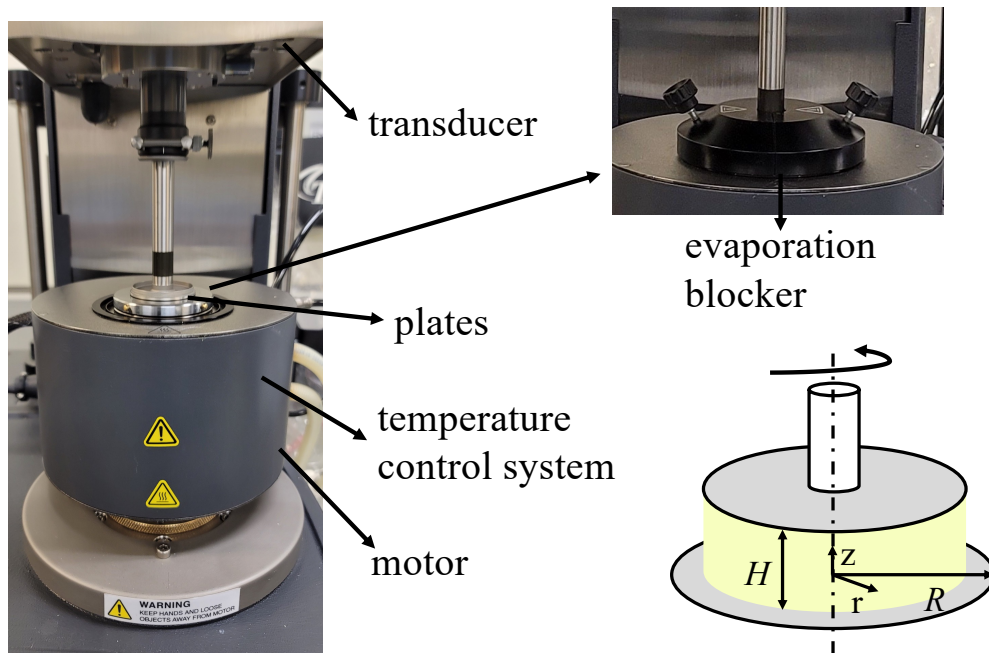


Figure 2.3: ARES-G2 rheometer with a measured stress transducer, an applied strain motor, and an advanced Peltier system for temperature control. The schematic shows the parallel-plate geometry mostly used in this study with an evaporation blocker on the right.

2.3 Rheology

Rheology is the science that studies the flow and deformation of a material in response to an applied force. It is used widely as a tool for characterizing the structure and properties of polymer solutions, melts, suspensions and gels. As deformation and flow are termed strain or strain rate, respectively, rheology is the study of stress-strain relationships in materials. A commercial rheometer, such as the ARES-G2 (TA Instrument), shown in Figure 2.3, contains the material of interest in a geometric configuration (cone, plate, parallel plate, concentric cylinder, *etc.*), controls the environment around it (with a water bath or Peltier element), and applies and measures wide ranges of stress, strain, and strain rate. The rheometer uses a separate motor and transducer to impose deformation and measure torque. The instrument measures both viscosity and viscoelasticity of fluids, semi-solids, and solids.

Rheological characterizations of polymer nanocomposites can be affected by polymer-NP interactions, NP volume fractions, degree of dispersions, imposed stress, particle size, and shape and surface characteristics of the NPs. Flow orientation due to the presence of

dispersed phases, concentration gradient due to nonhomogeneity, and lack of coherence of material properties are some of the other factors known to affect the rheological behaviour of polymer nanocomposites (Puglia and Kenny, 2018).

Rheology has a wide range of applications. The most applied methods are steady-shear, oscillatory shear, and extensional rheology. The first two are the focus of the present work, hence more details will be provided. Steady-state shear is useful for predicting the performance of the materials and provides information about the flow-induced changes in morphology. Dynamic measurements are useful in analyzing the viscoelastic response of materials. These measurements provide a prediction of the interconnecting microstructure of the materials. To obtain dynamic shear moduli, a sinusoidal oscillatory strain γ with a small amplitude (in the linear viscoelastic regime) is applied to the sample at an angular frequency ω . For ideal viscous materials, the resulting stress σ is 90° out of phase with γ . There is no storage of energy, so the work of deformation is dissipated. For ideal elastic materials, σ is perfectly in phase with γ , because these materials store and release elastic energy without dissipation. Under these ideal conditions, σ is independent of ω .

2.3.1 Shear flow

Shear flow can be described as layers of fluid sliding over one another, with each upper layer moving faster than the one beneath it. The bottom layer of the fluid is stationary while the uppermost layer has the maximum velocity as shown in Figure 2.4. The material is sheared between a stationary bottom plate and a rotating top plate at a given stress or strain. The shear stress versus shear rate plot is called a "flow curve". In a Newtonian fluid, the ratio between shear stress and shear rate is viscosity. There is a linear relationship between shear stress and shear rate. Examples of Newtonian fluids are oil and water.

Viscosity is the material's resistance to deformation. It is a function of shear rate $\dot{\gamma}$ and stress, with time, pressure and temperature dependence:

$$\eta = \frac{\sigma}{\dot{\gamma}}, \quad (2.11)$$

where η is the shear viscosity (unit is Pa s), associated with kinetic energy loss in the system and provides a quantitative measure of the internal fluid friction. The shear force (F) acting on the fluid over a unit area (A) is the shear stress σ (unit is Pa). $\dot{\gamma}$ is the rate of change of strain with time ($d\gamma/dt$). In non-Newtonian fluids, viscosity varies as a function of the

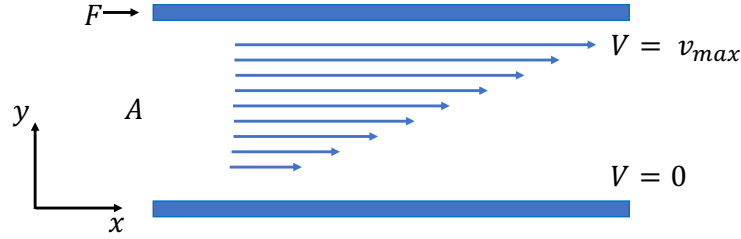


Figure 2.4: Simple shear of a fluid along the x -direction with applied force F and a velocity gradient along the y -direction.

applied shear stress or shear rate. Some commonly observed non-Newtonian behaviours are dilatant (shear thickening), pseudoplastic (shear thinning), and Bingham fluid, with shear stress versus strain rate curves as shown in Figure 2.5(a).

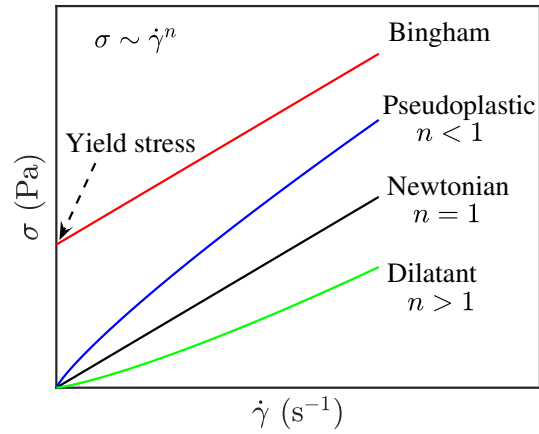
Non-Newtonian shear rheology

Shear-thinning is the decrease in apparent viscosity with shear rate. Very important for nearly all polymers and suspensions. It is the most common type of non-Newtonian behaviour and is of practical importance in polymer solutions and melts, suspensions, and nanocomposites processing. As shown in Figure 2.5(b), the onset of the shear-thinning region is indicated by a significant drop in the viscosity. At low enough shear rate ($\dot{\gamma} \rightarrow 0$), shear-thinning fluid have a viscosity independent of $\dot{\gamma}$, known as the zero shear viscosity η_0 . Another viscosity plateau is observed at very high $\dot{\gamma}$, known as the infinite shear viscosity η_∞ .

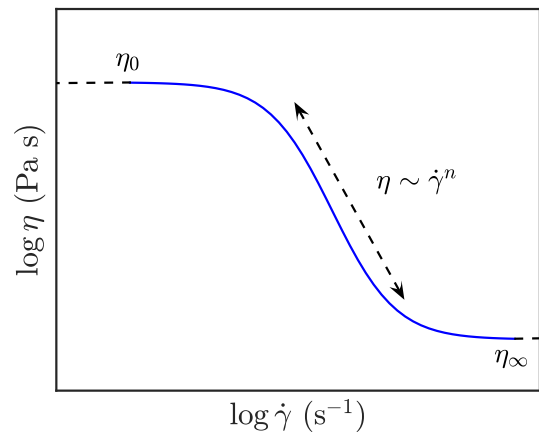
In shear thickening fluids, on the other hand, the viscosity increases with the shear rate. This behaviour typically occurs at higher particle volume fractions and higher shear rates. The relationship between shear stress and shear rate can be described by a power law,

$$\sigma = k\dot{\gamma}^n, \quad (2.12)$$

where constant k is the consistency index, and n the power law index, varies for different materials as shown in Figure 2.5(a).



(a)



(b)

Figure 2.5: Shear stress versus shear rate plots for various flow behaviour (a). Typical shear flow curve for shear thinning (pseudoplastic) fluids in the absence of apparent yield stress (η increases as $\dot{\gamma} \rightarrow 0$, (b). Where, n is the power-law exponent, η_0 and η_∞ are the zero shear and infinite shear viscosity. Yield stress is the stress required for the fluid to flow.

2.3.2 Viscoelasticity

Materials that combine the properties of elastic solids with those of viscous fluids are known as viscoelastic materials. The stress in these materials decay in time after the application of a shear deformation which is then held constant. Elastic materials store energy under strain, but viscous materials dissipate energy. Viscoelastic materials show both types of these behaviours with varying ω . The difference in the mechanical behaviour of elastic, viscous, and viscoelastic materials can best be explained using time-or frequency-dependent measurements.

For a parallel-plate geometry (see Figure 2.3), with the material placed between two plates of same symmetry axis, the viscous and elastic effects can be evaluated separately by applying strain oscillation and measuring the resulting stress response σ :

$$\gamma = \gamma_0 \sin(\omega t), \quad \gamma = \frac{R\theta}{H}, \quad (2.13)$$

$$\sigma = \sigma_0 \sin(\omega t + \delta), \quad \sigma = \frac{M}{2\pi R^3} \left(3 + \frac{d \ln M}{d \ln \dot{r}_R} \right), \quad (2.14)$$

where γ_0 and σ_0 are the maximum amplitude of the strain and stress, δ is the phase angle, R is the parallel plate radius, H is the distance between two infinite parallel plates, θ is the oscillation displacement, M is the generated torque (N m), and \dot{r}_R is the shear rate at the plate rim. When the material is probed in the linear regime (small γ) (Ferry, 1970):

$$\sigma = \gamma_0 [G' \sin(\omega t) + G'' \cos(\omega t)], \quad (2.15)$$

where G' and G'' are storage (elastic) and loss (viscous) moduli, in-phase and 90° out-of-phase with the strain, respectively. Combining Eqns. (2.13)–(2.15) and simplifying gives

$$G' = (\sigma_0/\gamma_0) \cos \delta, \quad G'' = (\sigma_0/\gamma_0) \sin \delta, \quad \text{and} \quad G''/G' = \tan \delta,$$

where, $\tan \delta$ is the loss tangent. If $\tan \delta > 1$, the sample mainly behaves fluid-like and if $\tan \delta < 1$, the sample has a dominant solid-like (elastic) behaviour.

The complex modulus

$$G^* \equiv \sigma^*/\gamma^* = G' + iG'', \quad (2.16)$$

where $\sigma^* = \sigma_0 \exp[i(\omega t + \delta)]$, and $\gamma^* = \gamma_0 \exp(i\omega t)$ are the complex forms of the stress and strain, respectively. The viscosity measured in an oscillatory experiment is a complex viscosity, defined as:

$$\eta^* = G^*/(i\omega) = \eta' - i\eta'', \quad (2.17)$$

where η' and η'' are the ratio of stress to the rate of strain in phase and 90° out of phase with rate of strain, respectively. For viscoelastic liquids, $\eta' \rightarrow \eta_0$ as $\omega \rightarrow 0$, where η_0 is the zero-shear viscosity defined as $\eta(\dot{\gamma} \rightarrow 0)$. Complex viscosity is related to steady shear viscosity according to the Cox-Merz rule (Cox and Merz, 1958),

$$|\eta^*(\omega)| = \eta(\dot{\gamma} = \omega), \quad (2.18)$$

which is applicable to most polymer melts, concentrated and semi-dilute solutions. The absolute value of complex viscosity $|\eta^*(\omega)| = (\eta'^2 + \eta''^2)^{1/2}$ is called the dynamic viscosity. Deviations from the Cox-Merz rule mostly occur at high frequencies. The rule does not apply to certain dilute solutions, cross-linked or gelled, and composite systems.

The dynamic linear viscoelastic behaviour can be described using a generalized Maxwell model. This model approximates a viscoelastic material with a series combination of a spring (with a stiffness analogous to the shear modulus G) and a dashpot (with a frictional resistance analogous to the viscosity η). The resulting relaxation time η/G is a characteristic of the system and can be used to compare their mechanical behaviour. However, in real polymers, the relaxation does not occur at a single time. Maxwell model considers a superposition of a series of N independent relaxation processes, each process having a relaxation time τ_i and stiffness G_i . The force on each element relaxes exponentially, furnishing the overall relaxation modulus (Ferry, 1970)

$$G(t) = \sigma(t)/\gamma = \sum_{i=1}^N G_i \exp(-t/\tau_i). \quad (2.19)$$

Dynamic moduli are thus defined as:

$$G'(\omega) = \sum_i G_i \frac{\omega^2 \tau_i^2}{1 + \omega^2 \tau_i^2}, \quad (2.20)$$

$$G''(\omega) = \sum_i G_i \frac{\omega \tau_i}{1 + \omega^2 \tau_i^2}. \quad (2.21)$$

Many entangled polymer melts, entangled polymer solutions, and physical gels obey the Maxwell model, which predicts $G' \sim \omega^2$ and $G'' \sim \omega^1$ in the terminal regime.

2.3.3 Nonlinear rheology

Linear viscoelasticity is useful for understanding the relationship between the rheological properties and the microstructure of complex fluids. However, when large and rapid deformations occur, it is important to bear in mind that the linear viscoelasticity theory is

no longer valid. Many polymer networks and composite materials of industrial and biological significance exhibit complex nonlinear rheological behaviour. The response to the deformation depends on the rate, size, and kinetics of the deformation.

The nonlinear viscoelastic response is a complex phenomenon that depends on size distribution, stabilization, and concentration. It occurs when the deformations are large and the theory of linear viscoelasticity which uses small strain amplitude (small amplitude oscillatory shear, SAOS), no longer applies. SAOS test is based on the assumption that the material response is in the linear regime within the accuracy of the rheometer and therefore the rheological properties G' and G'' provide a full characterization of the material response. However, at larger strain amplitudes, G' and G'' are not uniquely defined once the material response becomes nonlinear since a nonlinear stress response is not a single-harmonic sinusoid (Ewoldt et al., 2008). Therefore the nonlinear dynamic test in this regime is typically referred to as large amplitude oscillatory shear (LAOS). Complex fluids with similar linear viscoelastic properties may exhibit distinctly different nonlinear viscoelastic properties (Hyun et al., 2011). Nonlinear phenomena become important when the Deborah number is large as shown in Figure 2.6. Deborah number is defined as the product of relaxation time and characteristic strain rate (Macosko and Larson, 1994):

$$De = \tau \dot{\gamma}. \quad (2.22)$$

Low Deborah numbers ($De \ll 1$) correspond to a viscous response of the material, while an elastic response can be observed at $De \gg 1$. At intermediate Deborah numbers $De \approx 1$, viscoelastic behaviour is observed. Other sources of nonlinear viscoelasticity in fluids include non-Newtonian flow, frequency-dependent complex viscosity, shear-rate-dependent normal stresses, shear-thinning, extensional thickening, recoil, and hysteresis loops (Byron Bird and Carreau, 1968, Macosko and Larson, 1994). These are common occurrences in most complex fluids. Therefore, it is important to understand, model, and predict the nonlinear behaviour of complex fluids under large deformation.

Large amplitude oscillatory shear (LAOS)

LAOS provides a quantitative approach to analyzing the progressive transition from linear to nonlinear rheological behaviour as the strain amplitude γ_0 is increased at any given applied frequency ω . Figure 2.7 schematically illustrates a fixed frequency oscillatory strain

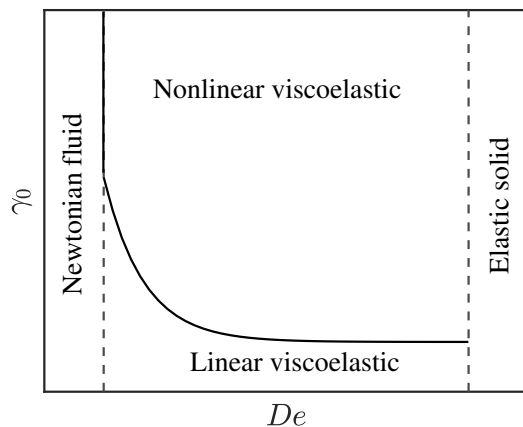


Figure 2.6: Pipkin diagram for different flow regimes of viscoelastic fluids.

sweep test for a hydrogel nanocomposite with varying applied strain amplitude. In the linear regime, identified by sufficiently small γ_0 , both G' and G'' are independent of γ_0 . For most homopolymer melts and solutions, the range of γ_0 in the linear regime is often very small and of the order 0.01–0.1. For more complex systems like block copolymer solutions, nanocomposites, and suspensions, the linear viscoelastic regime is limited to smaller $\gamma_0 < 0.01$. As shown in Figure 2.7, there is a transition from SAOS to LAOS (large γ_0), G' and G'' are dependent on γ_0 . Hyun et al. (2002) defined four typical nonlinear material responses based on the combined experimental and simulation analysis to classify the complex fluids. Type I (strain thinning) is a commonly observed behaviour in polymer melts and solutions, which occurs when both G' and G'' decrease in the nonlinear region as a result of the alignment of network segments with the flow field. For type II (strain-hardening), both G' and G'' increase; for type III (weak strain overshoot), G' decreases, while G'' first increases and then decreases. Finally, for type IV (strong strain overshoot), G' and G'' initially increase, followed by a decrease in both. Figure 2.7 shows a typical type III behaviour.

The oscillatory stress response in the linear regime is sinusoidal, as shown in Figure 2.8. Whereas, in the nonlinear regime, the periodic waveforms are distorted (Figure 2.8) and deviate significantly from a sinusoidal waveform. The shape of the oscillatory stress response in the nonlinear regime varies.

The accuracy of LAOS measurements can be greatly influenced by sample stability and uniformity, wall slip, edge fracture, or swelling between geometries (Klein et al., 2007, Hyun

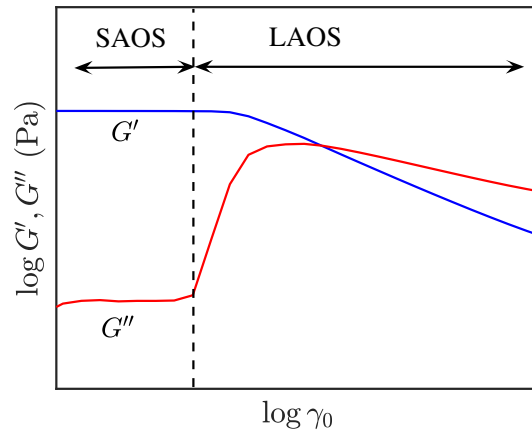


Figure 2.7: Oscillatory strain sweep at fixed ω . This can be used to determine the linear (SAOS) and the nonlinear (LAOS) viscoelastic regime.

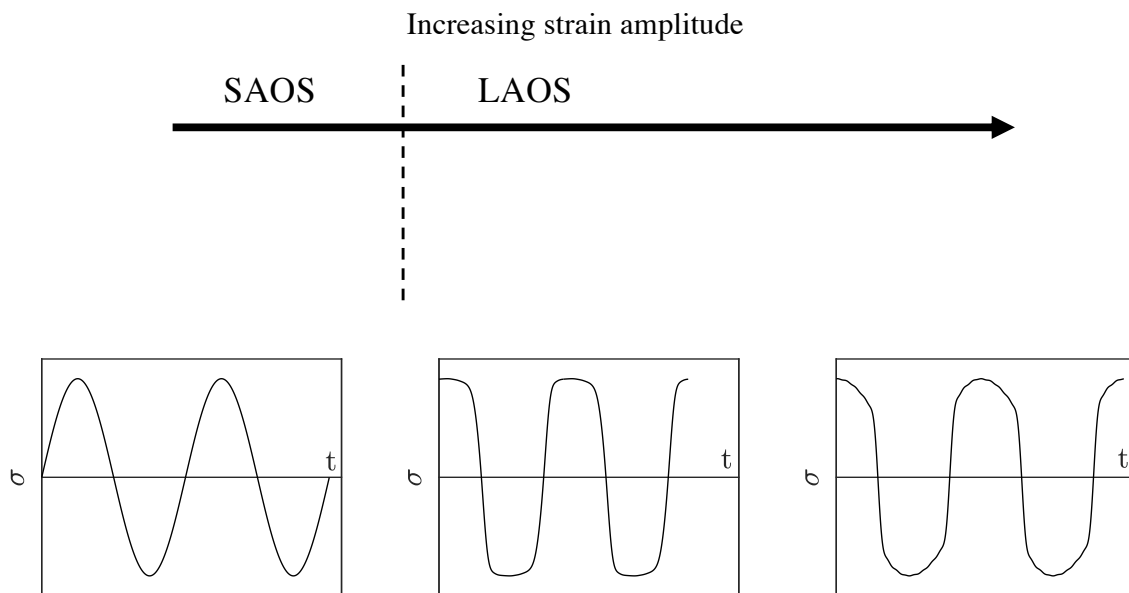


Figure 2.8: Oscillatory stress response for the sweep test in Figure 2.7. In the SAOS regime the stress response is sinusoidal, whereas in the LAOS regime the stress waveforms are distorted and the shapes change with strain amplitude.

et al., 2011, Kamkar et al., 2021). The LAOS technique is widely used due to its versatility and ease of implementation in the most conventional rheometer. It allows strain amplitude and frequency to be controlled independently. Several methods have been proposed to interpret and quantify nonlinear viscoelasticity for various polymer systems.

The most commonly used method is the Fourier transform rheology (FT-Rheology) analysis. This method has been used for various complex fluids and materials, such as polymer melts and solutions with different topologies (Neidhöfer et al., 2001, 2003, Vittorias et al., 2007, Hyun et al., 2007), suspensions (Abbasi M. et al., 2020), polymer nanocomposites (Lim et al., 2013, Kim et al., 2019, Kim and Hyun, 2021), hydrogels, elastomers and rubber (Fan et al., 2019). The resulting stress signal from the applications of deformations, such as shown in Figure 2.8, can be analyzed using FT-Rheology and the nonlinear viscoelasticity of material under LAOS can be quantified. Fourier transformation is used to decompose the stress and produce a spectrum of relative intensity for higher-order odd harmonics, which increase from zero with increasing strain in the non-linear regime. An increase in the even harmonics indicates secondary flows or wall slip (Klein et al., 2007). To avoid the wall slip effect, cone-plate geometries are often used for LAOS tests. When using parallel-plate geometries, sand-paper coated plates or serrated plates (Kamkar et al., 2021) may be required to eliminate wall-slip effects. FT-Rheology, compared to other methods, is simple, much more sensitive, and accurate, from a hardware point of view (Wilhelm, 2002).

Another method is the stress decomposition method (Cho et al., 2005, Ong et al., 2020), which can be used to obtain information about high harmonics. The stress decomposition method is effective in steady oscillation, but only for signals with odd harmonics. However, this method cannot be used in processes with even harmonics, such as normal stress differences (Yu et al., 2009). The stress decomposition method, therefore, suffers from nonorthogonality of the resulting material responses (Ewoldt et al., 2008). Yu et al. (2009) proposed a new general stress decomposition method that accounts for both odd and even harmonics. The method decomposes the signal into a Fourier series with no limitations on whether the signal is in steady-state or not.

Time-temperature and time-concentration superpositions

The ARES-G2 rheometer (Figure 2.3) probe frequencies in the range 10^{-3} to 628 rad s^{-1} . At low frequencies, however, the data collection time becomes too long, and, at high frequencies

(> 10^2 rad s⁻¹), sample-geometry inertia can cause measurement error. Therefore, frequency-sweep tests are often undertaken in the range 10^{-1} – 10^2 rad s⁻¹. However, to examine the viscoelastic properties of materials at distinct regions of physical behaviours, a much wider frequency range is required. This is accomplished using time-temperature superposition (TTS) or time-concentration superposition (TCS).

TTS is extensively used to obtain the rheological spectra at extremely low and high frequencies. The spectra measured at experimentally accessible frequencies and different temperatures are *superposed* to a common reference temperature, furnishing a composite rheological spectrum. The master curve corresponds to the wider frequency range. Each modulus and relaxation time has the same dependence on the temperature (Dealy and Plazek, 2009). Therefore, on a log-log plot, a change in the temperature shifts the relaxation times, *i.e.*, shifts G' and G'' along the frequency axis without changing the shape of the curve. Similarly, the curve is shifted along the modulus axis due to the dependence of each modulus G_i and the chain density on the temperature. The horizontal a_T and vertical b_T shift factors are obtained via

$$b_T G^*(\omega, T) = G^*(\omega a_T, T_0), \quad (2.23)$$

where $G^*(\omega a_T, T_0)$ denotes the modulus at the reference temperature T_0 and shifted frequency ωa_T (Dealy and Plazek, 2009). The shift factor a_T represents the horizontal shift along the frequency axis and describes the temperature dependence of the material. The correlation between a_T and T can be described by either the Arrhenius equation or Williams-Landel-Ferry (WLF) equation. Early literature reports (Dealy and Plazek, 2009) of the temperature dependence of liquid viscosity birthed the empirical Arrhenius equation:

$$a_T(T) = \exp \left[\frac{E_a}{R} \left(\frac{1}{T} - \frac{1}{T_0} \right) \right], \quad (2.24)$$

where E_a is the flow activation energy, and R is the universal gas constant. Equation (2.24) is more suitable for polymer solutions, and for polymer melts when T is well above the glass transition temperature T_g . The WLF equation is applicable for concentrated polymer solutions, and polymer melts at test temperatures less than $T_g + 100$ K (Ferry, 1970):

$$\log a_T = \frac{-c_1(T - T_0)}{c_2 + (T - T_0)}, \quad (2.25)$$

where c_1 and c_2 are empirical constants, derived from curve fitting. The quality of superposition is dependent on experimental data and material response. Poor experimental

data resulting from instrument effects, noise at low frequency or systematic errors at high frequency lead to poor superposition. The nonlinearity in material response affect the superposition since nonlinear viscoelasticity alters the temperature dependence of the relaxation times (Ferry, 1970, Dealy and Plazek, 2009).

TCS is a similar concept to the TTS, resulting not from temperature-dependent properties (such as friction and chain density), but from a change in the connectivity (Adolf and Martin, 1990, Schausberger and Ahrer, 1995, Daga and Wagner, 2006). It can be used to determine the rheological properties at experimentally inaccessible frequencies. TTS is a useful tool for studying the viscoelastic materials at critical limits, such as the gel point, at which the bond probability reaches the critical value and an infinite cluster spans a macroscopic sample, inducing a transition from liquid- to solid-like characteristics (Martin et al., 1988).

2.4 Polymer adsorption and electrophoresis

Adsorption is a complex surface mechanism that allows two contacting particles to be bonded by hydrogen bonds or van der Waals forces. Adsorption allows for the control of a variety of interfacial processes important in many industrial and biological applications such as flocculation, solid-liquid separation, blood clotting, and soil stability. The mechanisms governing the adsorption process are influenced by several factors, such as the physical and chemical nature of the surface and solvent, the interactions of the solute with the solvent, and the nature of the interactions between the surface and the adsorbed solute, and temperature. Some parameters that influence adsorption include molecular weight, particle concentration, pH, conductivity, temperature, surface, and ionic charge density.

The polymer chain conformation is forced to change near the particle surface due to the intermolecular interactions between the polymer chains and the interface (Jones and Richards, 1999). This conformational structure is composed of trains, loops, and tails as shown in Figure 2.9. Trains are segments all adsorbed at the surface, loops are the unbound segments in between two trains, and tails are free ends of the adsorbed polymer chains. To fully grasp the behaviour of polymers at interfaces, it is important to first understand the behaviour in solution. The dimensions of a linear polymer molecule is determined by the freely jointed chain model, giving rise to the mean-square end-to-end distance (Rubinstein

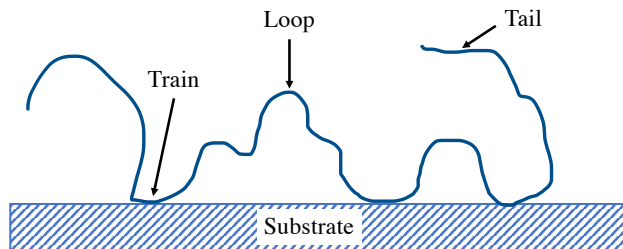


Figure 2.9: Schematic of an adsorbed polymer chain.

and Colby, 2003)

$$\langle R^2 \rangle = Nl^2, \quad (2.26)$$

where N is the number of bonds, and l is the bond length. For an ideal long polymer chain however, the mean-square distance is

$$\langle R^2 \rangle = C_\infty Nl^2 = Nb^2, \quad (2.27)$$

where C_∞ is the Flory's characteristic ratio, and b is the effective bond length or Kuhn length. For an ideal chain, $\langle R^2 \rangle$ is expressed as a mean square radius of gyration $\langle R_g^2 \rangle = \langle R^2 \rangle / 6$. The reader is referred to Rubinstein and Colby (2003) for dimensions of other types of polymer chains in solution.

The polymer-solvent interaction can be described by the temperature-dependent free energy parameter known as the Flory-Huggins chi (χ) parameter. When $\chi > 0$, the polymer-polymer and solvent-solvent interactions are more favourable compared to polymer-solvent interactions. When $\chi < 0$, polymer-solvent interactions are preferred. A solution with $\chi = 0$ is called an athermal solution, the polymer-solvent interactions are identical to the polymer-polymer interactions. The quality of the solvent depends on both the chemical compositions of the polymer and solvent molecules and the solution temperature. The solvent could be either good solvent ($\chi < 0.5$, polymer chains avoid contact with each other to maximize contact with the solvent) (Zhao and Brittain, 2000), poor solvent ($\chi > 0.5$, polymer chains agglomerate with other chains and precipitate from solution), or theta solvent ($\chi = 0.5$, polymer chains dissolve in the solvent at all concentrations). For a non-solvent, χ increases and the solvent is unable to disperse the polymer.

The amount of polymer adsorbed or bounded on a substrate can be determined using thermogravimetric analysis. TGA experiment requires that a small amount of the sample

is placed on a crucible, and the temperature is ramped up from room temperature with simultaneous measurement of the mass. The components in the sample are expected to burn at different well-defined temperatures, which will be evident from the mass changes as the temperature increases. Thus, enabling the determination of weight percentages of the components in the sample. The amount adsorbed can be calculated based on the mass loss due to the polymer and the mass of the residual material, which would contain only silica after heating, and the specific surface area of silica:

$$\Gamma = \frac{\Delta w}{(1 - \Delta w)A}, \quad (2.28)$$

where Γ is the adsorbed amount in mg of polymer adsorbed per m^2 of surface, Δw is the mass fraction of polymer in the sample, and A is the specific surface area ($\text{m}^2 \text{g}^{-1}$) of the substrate.

A non-invasive approach to determining the influence of an adsorbed polymer on a particle surface is by measuring the ζ -potential. The ζ -potential for silica nanoparticles in solution with solubilized PA chains is determined using electroacoustic spectroscopy (ESA) by measuring the electrophoretic mobility μ_e , defined as the ratio of the particle velocity ν_p to the electric field strength E ,

$$\mu_e = \frac{\nu_p}{E}. \quad (2.29)$$

This mobility depends on the ζ -potential according to

$$\mu_e = \frac{4\pi\epsilon_0\epsilon_r\zeta}{\eta}f(\kappa R), \quad (2.30)$$

where η is the viscosity of the suspending medium, ϵ_r is the dielectric constant, and κR is the ratio of the particle radius R to the thickness of the electrical double layer, κ^{-1} . For $\kappa R \ll 1$, $f(\kappa R) = 1$, applicable in dilute electrolyte (Delgado et al., 2007). ζ -potentials have been used extensively to characterize the stability of colloidal suspensions. The higher the ζ -potential, the stronger the repulsion between particles with equal signed ζ and sometimes the more stable the colloidal material. ζ -potential, however, cannot be used to determine the adsorption on the colloidal surface, but can provide useful information about the thickness of an adsorbed layer. The polymer can introduce a steric repulsion, thus enhancing colloidal stability.

Adsorption of polyacrylamide onto silica nanoparticles: Role of particle-polymer interactions

3.1 Preface

This chapter is motivated by inconsistencies in literature data regarding the adsorption of polyacrylamide (PA) onto colloidal silica, and a need to better understand the interactions between the polymer, solvent, and nanoparticles. Here, the adsorbed amount is measured using thermogravimetric analysis for two PA molecular weights. Rheology and electroacoustic measurements are adopted to help understand the influence of the polymer on colloidal stability, structure, and mechanical properties. The PA-coated silica NPs synthesized and characterized in this chapter are used as physical cross-linkers in polymer solutions and weak chemically cross-linked hydrogels in chapters 4 and 5.

Abstract

Understanding particle stability, surface modification, and polymer-solvent interactions is critical to improving the performance of silica nanoparticles (NPs) in numerous applications. Here, the interactions of colloidal silica with polyacrylamide (PA) are studied. The use of thermogravimetric analysis was motivated by differences in the literature regarding PA adsorption onto colloidal silica. The results, correlating experimental data to a modified Langmuir isotherm, show that adsorption is concentration dependent. The optimal adsorption amounts for 150 kDa and 40 kDa PA on colloidal silica are 0.25 and 0.13 g m⁻², respectively. Noninvasive electroacoustic characterization of the bare and PA-coated silica NPs was adopted to determine the ζ -potential, adsorbed layer thickness, and mobility of the bare and PA-coated NPs in reverse-osmosis water at pH values 3, 6, and 9, showing that the adsorbed-layer thickness increases with pH. The polymer coatings decrease the electrophoretic mobility

due to shifting the electrokinetic shear plane. Rheological data for the 150 kDa PA solution at 21°C furnished a critical overlap concentration $c^* \approx 19 \text{ mg ml}^{-1}$ and Huggins coefficient $k_H \approx 0.96$ and 0.82 for a conventional and quadratic Huggins equation, respectively. Despite water easily dissolving PA, the results suggest that water is not a good solvent for PA. Based on the rheology, interactions of unentangled PA with varying amounts of colloidal silica reveal that silica NPs enhance PA-solution viscosity.

3.2 Introduction

Nanoparticles (NPs) are of interest in numerous industrial applications. Their unique properties, such as small size, high surface-to-volume ratio, and chemical and optical responses, contribute to their relevance in these industries. However, the stability and interactions of these particles still pose significant challenges in many applications. For instance, [Adibnia et al. \(2017b\)](#) reported chemical interactions occurring between silica and ions in solution when colloidal silica was used to form hydrogel nanocomposites. There is a need to modify the particle surface to control the particle size, minimize undesirable chemical effects, and enhance polymer adsorption.

Functionalization of colloidal silica with polymeric substances is studied extensively by various authors, because the polymer coating affects dispersion stability, thereby altering the interfacial properties of silica while enhancing several tailored properties that make these materials important. Polymer functionalized NPs are used in a wide range of applications, such as improving oil displacement ([Fossati et al., 2018](#)), facilitating the controlled release of drugs ([Yavuz et al., 2009](#)), and as coatings and adhesives ([Dastjerdi et al., 2019](#)). Polymers prevent aggregation and rapid surface oxidation that may occur at the surface of NPs. Coating NPs with polymers such as polyethylene glycol (PEG) has become a popular method. PEGylation of a nanoparticle (NP) increases its colloidal stability and size. It tends to reduce its effective surface charge ([Pelaz et al., 2015](#)). [Glorani et al. \(2017\)](#) synthesized silica NPs coated with PEG with varying molecular weights, and studied their interaction with different biological environments. They showed that PEG layers improved the properties of silica NPs for use in biomedical applications. Other polymers, such as polyvinyl alcohol (PVA) and polyacrylamide (PA), have gained widespread attention for their use as nanoparticle coatings.

Polyacrylamide, derived from the controlled polymerization of acrylamide, is a synthetic

polymer with a high capacity to absorb water, with a long history of use in gel electrophoresis. It has found widespread applications in different fields, for instance as biomaterials in drug delivery, enzyme immobilization, soft-tissue fillers, and smart materials (Yang, 2008). PA has been widely used as an additive for wastewater treatment (Xiong et al., 2018), as a friction reducer or thickening agent in oil recovery (Li et al., 2017), as a soil conditioner in agricultural applications (Fijałkowska et al., 2021), and as a stabilizing or binding agent in cosmetics (Anderson, 2005).

Polyacrylamide polymers are employed in a wide range of industrial, agricultural, and environmental applications, with increasing interest in their behaviour at solid-liquid interfaces. These polymers are adsorbed on the surface of colloidal particles to alter their properties. Their interactions with colloidal particles have been useful in many industrial processes, such as enhanced oil recovery (EOR), cosmetics, biotechnology, and water treatment. For instance, Maurya and Mandal (2016) characterized the rheological properties of silica/PA suspensions for use in a high-temperature, high-saline reservoir. The adsorption of the PA on the silica was due to the formation of hydrogen bonds, resulting in an increase in apparent viscosity (1.5 times higher) and suspension stability at high temperature and salinity compared to bare silica suspension. Hu et al. (2017) reported a considerable increase in the polymer solution viscosity with the addition of silica at temperatures up to 85°C and NaCl concentrations up to 8 wt%.

Polymer adsorption on colloidal silica depends on the type of solvent, the nature and structure of the adsorbing polymer (dispersity, molecular weight, ionic strength, solution pH and temperature), and the particle surface (size, shape, ionic strength, pH value, and composition) (Russel et al., 1989). The interaction between the polymer-modified particles may be one of attraction or repulsion between the polymers, depending on the type and quality of the solvent. Good solvents yield repulsive interactions between polymer chains, whereas poor solvents drive attraction (Russel et al., 1989).

Gu et al. (2014) reported improved stability and better dispersibility of PA modified acidic colloidal silica compared to the un-modified colloidal silica in aqueous environment by studying the thermal stability, ζ -potential and particle-size distribution. The size of PA-coated silica was reported slightly smaller, and ζ -potential was more negative in the pH range 3–7.5 compared to bare silica, which was attributed to the surface silanol groups becoming ionized by negatively charged PA. However, at pH in the range 7.5–10, ζ -potential was less

negative, possibly due to a weak chemical effect arising from reactions of the negatively charged PA via hydrogen bonds with the negatively charged silica (Gu et al., 2014).

Literature data on PA adsorption onto silica nanoparticles varies from zero to limited adsorption (Bessaies-Bey et al., 2018). In many cases, adsorption is strongly parameter-dependent, and reported to occur by hydrogen bonding between the hydroxyl groups on the silica surface and the amide groups of the PA (Bessaies-Bey et al., 2018). Figure 3.1 shows a schematic of the interaction of PA with colloidal silica. Other important parameters that influence the apparent adsorbed amount are the resolution of the detection technique used, and the presence of impurities (Bessaies-Bey et al., 2018). Using Fourier transform infrared spectroscopy (FTIR), Hu et al. (2017) reported adsorption as occurring from the formation of hydrogen bonds between the silanol groups on the NP surface and the carbonyl groups in partially hydrolyzed polyacrylamide (HPAM). M. Bjelopavlic (2001) reported zero adsorption for a 10 kDa PA and $6 \text{ m}^2 \text{ g}^{-1}$ silica NPs in 0.01 M sodium nitrate at $\text{pH} = 3$ using total organic carbon (TOC) method. The reader is referred to Bessaies-Bey et al. (2018) for extensive literature on adsorption or not of PA on siliceous materials at different compositions, using a variety of experimental conditions and techniques.

This study measures the adsorption of polyacrylamide onto colloidal silica, seeking to better understand how the polymer influences colloidal stability, structure, and rheology properties of silica dispersions. Many researchers have explored the interactions of PA and colloidal silica in water. However, few have reported how PA coating affects the hydrodynamic size, double layer thickness, ζ -potential, and mobility of the colloidal silica in the pH range 3–9. None of the established literatures on polymer adsorption on colloidal silica have explored the use of thermogravimetric analysis (TGA) to measure adsorption. It is therefore of interest to compare how the results from this technique differ from those previously reported in the literature.

The following techniques were employed. First, adsorbed amounts are measured using TGA for two PA molecular weights. TGA is a characterization method widely used for the quantitative analysis of polymer adsorption, experimentally derived from changes in mass while heating in an inert gas. Experiments were conducted using PA with molecular weights 40 and 150 kDa to establish how these affect adsorption. Second, a non-invasive approach to determine the influence of an adsorbed polymer was undertaken by measuring the ζ -potential, hydrodynamic diameter, and electrophoretic mobility. The ζ -potential for bare

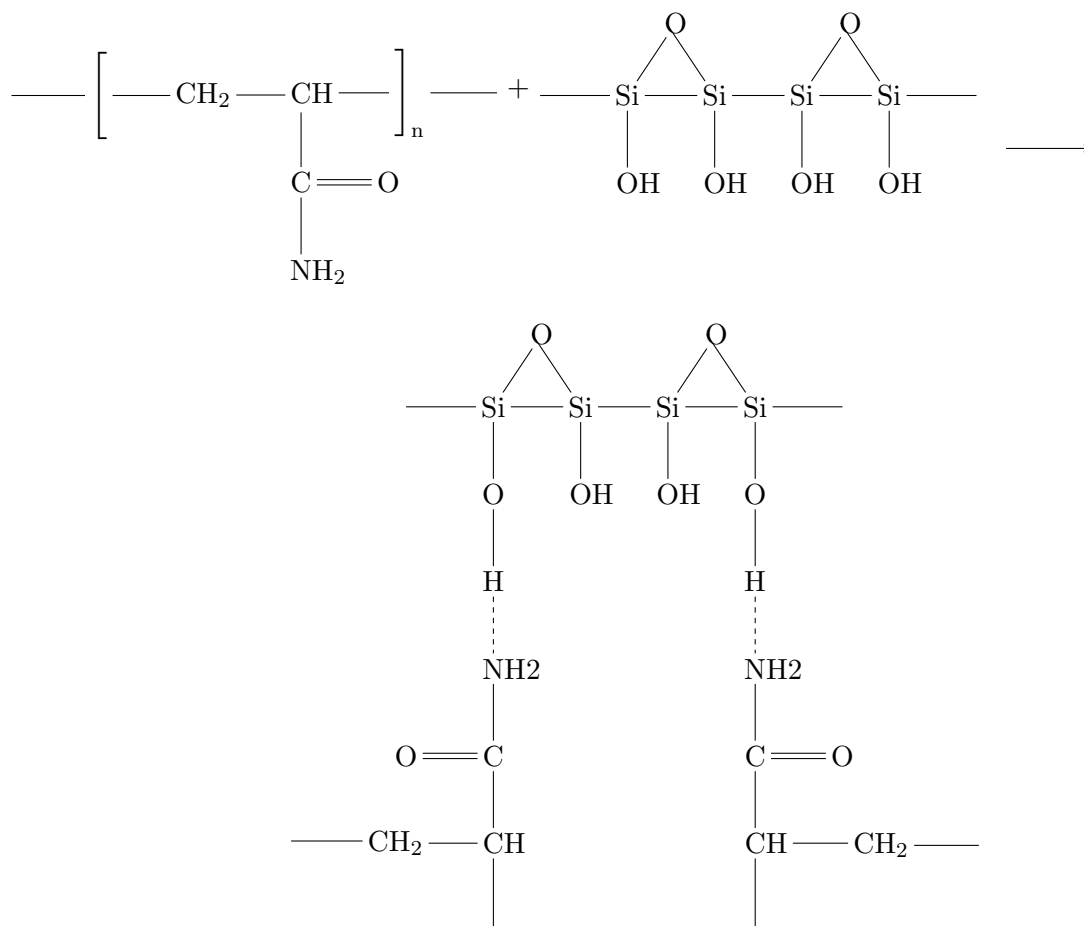


Figure 3.1: Structural mechanism of PA-modified colloidal silica. Adapted from [Gu et al. \(2014\)](#).

and PA-coated silica nanoparticles was determined using the electrokinetic sonic amplitude (ESA), which furnishes the (complex valued) dynamic electrophoretic mobility, defined as the ratio of the particle velocity to the electric field. Zeta-potentials have been used extensively to characterize the stability of colloidal suspensions. The higher the ζ -potential, the stronger the electrostatic repulsion between the particles, and sometimes the more stable the colloid. Zeta-potential, however, cannot be used to determine the adsorbed amount, but still provides indirect information on the hydrodynamic thickness of the adsorbed layer. Polymers can impart steric repulsion between NPs, thus, enhancing dispersion stability. Adsorbed polymers can likewise bridge the particles, leading to flocculated suspensions. Finally, the rheological properties of PA and PA-coated silica NPs are studied to investigate the flow behaviour, the interactions of PA in aqueous solvent, and the effect of varying the silica volume fraction.

3.3 Materials and methods

3.3.1 Materials

Negatively charged sodium-stabilized colloidal silica (Ludox[®] TM-50, 50 wt% colloidal suspension, Sigma-Aldrich Inc., USA) with particle diameter $d \approx 30$ nm was used as received. According to the supplier, the density and specific surface area are 1.4×10^3 kg m⁻³ and 140 m² g⁻¹, respectively. Polyacrylamide (PA) with an average number molecular weight $M_n \approx 150$ kDa was supplied by Sigma-Aldrich (in powder form) and used as received. A stock solution of 10 wt% PA was prepared by dissolving the required amount of polymer powder in reverse-osmosis (RO) water (Type 1, $\sigma \approx 5.6$ μ S m⁻¹, $\Omega \approx 18$ MOhm cm at 25°C) and gently stirring on a magnetic stirrer for 6–8 h at room temperature to achieve complete dissolution. PA/silica suspensions were prepared by adding the desired amounts of each component at room temperature, stirred on magnetic stirrer for 24 h. Suspensions were left for 10 h to equilibrate following the procedures described by [Maurya and Mandal \(2016\)](#) before carrying out further studies. Varying pH values of bare and PA-coated silica suspensions for ESA analysis were achieved by the addition of 2 M HCl solution.

3.3.2 TGA

Thermogravimetric analysis (TGA) was used to determine the amount of adsorbed PA on the silica nanoparticles. PA/silica suspensions were prepared with a constant silica volume fraction $\phi = 10$ v%, varying PA concentration from $c = 5$ to 75 mg ml⁻¹. PA of molecular weights 40 kDa and 150 kDa were used to establish the effects of chain length on adsorption. TGA samples were prepared by centrifuging the PA/silica suspensions at 200,000 g for 90 min using a Thermo Scientific Sorvall MTX 150 micro-ultracentrifuge. The PA-coated particles formed a solid mass at the bottom of the centrifuge tube, and the excess solution containing non-adsorbed PA and solvent was removed. The remaining particles were washed with solvent and mixed thoroughly using a vortex mixer for 2 min to remove excess unbound/non-adsorbed polymer. Suspensions were centrifuged again, and the process repeated 3 times. A small portion of the particles (manufacturer’s recommendation 3–10 mg) was transferred to a TGA platinum pan, and the analysis was carried out using a TGA model Q50 (TA Instruments Inc.) at a ramp rate of 20 °C min⁻¹ to 100 °C (boiling point of water) under

nitrogen to remove excess water, and then held at 100 °C for 10 min to remove residual water. Further heating was undertaken with a ramp rate of 20 °C min⁻¹ to 550 °C under nitrogen (so the sample only reacts to temperature during decomposition) with a purge rate of 40 ml min⁻¹ and subsequently to 700 °C using air for complete thermal degradation accompanied by oxidation. Sample degradation with temperature change is reported by the instrument software. Details of the TGA procedure (time versus weight and temperature) and a plot of the resulting temperature versus weight loss (in %) are available in Appendix 3.A (Figures 3.A.1 and 3.A.2).

TGA data were used to calculate the adsorbed amount:

$$\Gamma = \frac{m_p \rho_s V_s}{m_s A_s}, \quad (3.1)$$

where, m_p and m_s are obtained from the TGA data at 700°C, representing the relative mass of the PA and the residual mass of silica NPs, respectively. $V_s = 4\pi a^3/3$ is the volume of a single particle, with a the particle radius from ESA, $A_s = 4\pi a^2$ is the surface area per particle, thus assuming silica particles are spherical, and $\rho_s = 2.2 \text{ g cm}^{-3}$ is the bulk density of silica (Rumble, 2017). The expected amount of polymer M_p in the bulk per unit total sample mass M is estimated as

$$\frac{M_p}{M} = \frac{(1 - \phi)c}{\phi \rho_s + (1 - \phi) \rho_p}, \quad (3.2)$$

where $\phi \approx 0.64$ is the volume fraction of silica based on random close packing, and c is the mass of polymer per unit volume in the bulk solution. The adsorbed amounts (surface coverage) are therefore reported as the direct TGA amount [Eqn. (3.1)] minus the amount of polymer estimated in the interstitial voids by Eqn. (3.2).

A modified Langmuir isotherm (Mohammadi et al., 2012) was used to correlate the adsorption data:

$$\Gamma = \frac{\Gamma_{\max} K c^n}{1 + K c^n}, \quad (3.3)$$

where Γ_{\max} , K and n are fitting parameters, representing maximum adsorption, equilibrium constant and exponent, respectively. This equation is empirically modified from the well-known Langmuir isotherm with an exponent n to account for the dependency of surface coverage on polymer concentration (Mohammadi et al., 2012). A value $n < 1$ signifies weaker concentration dependence, *i.e.*, less polymer is required to achieve the same surface coverage, while $n > 1$ indicates that the PA/NPs isotherm have a stronger concentration

dependence. [Mohammadi et al. \(2012\)](#) applied this modified Langmuir isotherm to the adsorption of asphaltenes onto mineral surfaces to identify multilayer adsorption.

The adsorption data were also analyzed using the Brunauer-Emmett-Teller (BET) isotherm ([Brunauer et al., 1938](#)), which is a theoretical model addressing multilayer adsorption, widely used for gases. The BET isotherm adapted for solute/polymer adsorption from a solvent

$$\Gamma = \frac{\Gamma_{\max} c_{\text{BET}} c}{(1 - c/c_0)[c_0 + c(c_{\text{BET}} - 1)]}, \quad (3.4)$$

where Γ_{\max} , c_{BET} and c_0 are fitting parameters, representing maximum adsorption (mg m^{-2}), BET adsorption constant related to the interaction energy with the surface, and adsorbate monolayer saturation concentration (mg ml^{-1}), respectively. [Ebadi et al. \(2009\)](#) proposed a modification for Eqn. (3.4) written

$$\Gamma = \frac{\Gamma_{\max} K_S c}{(1 - K_L c)(1 - K_L c + K_S c)}, \quad (3.5)$$

where K_S and K_L are the equilibrium adsorption constant for the first layer in the BET and Langmuir isotherms (ml mg^{-1}) and equilibrium adsorption constant for upper layers in the BET isotherm (ml mg^{-1}), respectively. These give $c_{\text{BET}} = K_S/K_L$. Eqn. (3.5) gives the equilibrium constants and eliminates the use of c_0 , which is not defined for most materials, considered to lose its physical meaning if adopted as a fitting parameter ([Ebadi et al., 2009](#), [Sobolčiak et al., 2021](#)). Nevertheless, Eqns. (3.4) and (3.5), we have $c_0 = 1/K_L$.

3.3.3 Electroacoustic measurements

An AcoustoSizer II instrument (Colloidal Dynamics LLC, USA) and its integrated software (AcoustoSizer IIX, version 3.28) provide the magnitude and phase angle of the dynamic mobility spectrum of bare and PA-coated colloidal silica suspensions. The instrument provides hydrodynamic diameter and ζ -potential, also drawing on acoustic attenuation. Reported values are the average of measurements from three separately prepared samples. Following instrument calibration, 30 ml of sample was injected into the ESA cell. The instrument provides the ESA at frequencies in the range 1–20 MHz and subsequently converts the spectrum to dynamic mobility according to

$$\text{ESA} = A \frac{z_s z_e}{z_s + z_e} \phi \frac{\rho_p - \rho}{\rho} M, \quad (3.6)$$

where M is the particle volume-averaged dynamic mobility, ϕ is the particle volume fraction, ρ_p and ρ are the particle and solvent density (2200 kg m⁻³ and 998 kg m⁻³, respectively), and z_s and z_e are the acoustic impedances of the suspension and the electrode backing material, respectively. A is an instrumental frequency-dependent function that is obtained by calibration using a potassium tungstosilicate (KSiW) electrolyte.

The dynamic mobility is a complex-valued quantity, being the ratio of particle velocity to the electric field strength (V/E). It is particularly useful for characterizing particle dispersions (Hunter, 1998). In a Newtonian solvent, M is a function of the solvent and particle properties, calculated as (O'Brien et al., 1995)

$$M = \frac{2\epsilon\zeta}{3\eta} G\left(\frac{\omega a^2}{\nu}\right) [1 + f(\lambda, \omega')] \quad (3.7)$$

for $\kappa a \gg 1$ and $\phi < 0.05$, where a is the particle radius, κ is the reciprocal Debye length, ϵ is the solvent dielectric permittivity, η is the shear viscosity, and ζ is the ζ -potential. The function G captures inertia forces, and is a complex-valued function of a , angular frequency ω , and the kinematic viscosity of the solvent ν . For spherical particles with thin double layers (O'Brien et al., 1995, Carasso et al., 1997),

$$G(\alpha) = \frac{1 + (1+i)\sqrt{\alpha/2}}{1 + (1+i)\sqrt{\alpha/2} + i(\alpha/9)(3 + 2(\Delta\rho/\rho))}, \quad (3.8)$$

where $\alpha = \omega a^2/\nu$. The factor $1 + f$ accounts for dynamics of the diffuse double layer, and is a frequency-dependent function of $\lambda = K_s/(aK)$, where K is the electrolyte conductivity, and K_s is the surface conductance, $\omega' = \omega\epsilon/K$, and (O'Brien et al., 1995, Carasso et al., 1997)

$$f(\lambda, \omega') = \frac{1 + i\omega' - (2\lambda + i\omega'(\epsilon_p/\epsilon))}{2(1 + i\omega') + (2\lambda + i\omega'(\epsilon_p/\epsilon))}, \quad (3.9)$$

where ϵ_p is the particle dielectric permittivity.

3.3.4 Rheology

An ARES-G2 strain-controlled rheometer (TA Instruments, USA) was used to measure the rheological properties of the PA solutions and PA-coated colloidal silica dispersions. A parallel-plate geometry with a 25 mm diameter top plate was used for all experiments. Samples were pipetted onto the lower plate, and the upper plate lowered to achieve a 0.5 mm gap.

The temperature was set to 21°C during measurements controlled with a ThermoCube 10–300 thermoelectric chiller (Solid State Cooling Systems). An “evaporation blocker” (provided by the manufacturer) was used to minimize evaporation. Steady shear viscosity measurements were repeated for accuracy using a stainless steel 34 mm diameter cup and a recessed end-bob geometry. The viscosity measurements using this geometry deviated by only $\approx 2\%$ from those using a parallel-plate geometry.

Steady shear viscosity at strain rates in the range $\dot{\gamma} \approx 0.1\text{--}1000 \text{ s}^{-1}$ was measured with maximum equilibration time 60 s and sample period 30 s. This was followed by a frequency sweep, performed in the range $\omega \approx 0.1\text{--}100 \text{ rad s}^{-1}$ with a strain amplitude $\gamma \approx 100\%$, within the linear viscoelastic regime, as identified by the moduli being independent of strain from a strain sweep at $\omega \approx 10 \text{ rad s}^{-1}$.

All measurements were repeated on $n = 3$ separately prepared samples, subsequently averaged. The sample-averaged data were reported and in some figures the error bars were provided. The error bars represent standard error σ/\sqrt{n} , where σ is the sample standard deviation.

3.4 Results and discussion

3.4.1 Properties of colloidal silica

Suspensions were diluted with RO water to achieve the desired volume fractions $\phi = 5, 10, 15$ and $20 \text{ v}\%$. The pH of each sample following dilution remained ≈ 9 . The ζ -potential and conductivity at room temperature ($T \approx 21^\circ\text{C}$) versus ϕ at $\text{pH} = 9$ are shown in Figure 3.2(a).

The magnitude of the ζ -potential decreases with increasing ϕ while the conductivity K increases almost linearly with ϕ . The double layer thickness/Debye length is

$$\kappa^{-1} = \sqrt{\frac{\epsilon_s \epsilon_0 k_B T}{2I e^2}}, \quad (3.10)$$

where ϵ_0 and ϵ_s are the permittivity of vacuum and dielectric constant of the solvent, $k_B T$ is the thermal energy, $I = (1/2) \sum_{j=1}^N z_j^2 n_j^\infty$ is the bulk ionic strength, n_j^∞ are the bulk ion concentrations with z_j the valences and e the elementary charge.

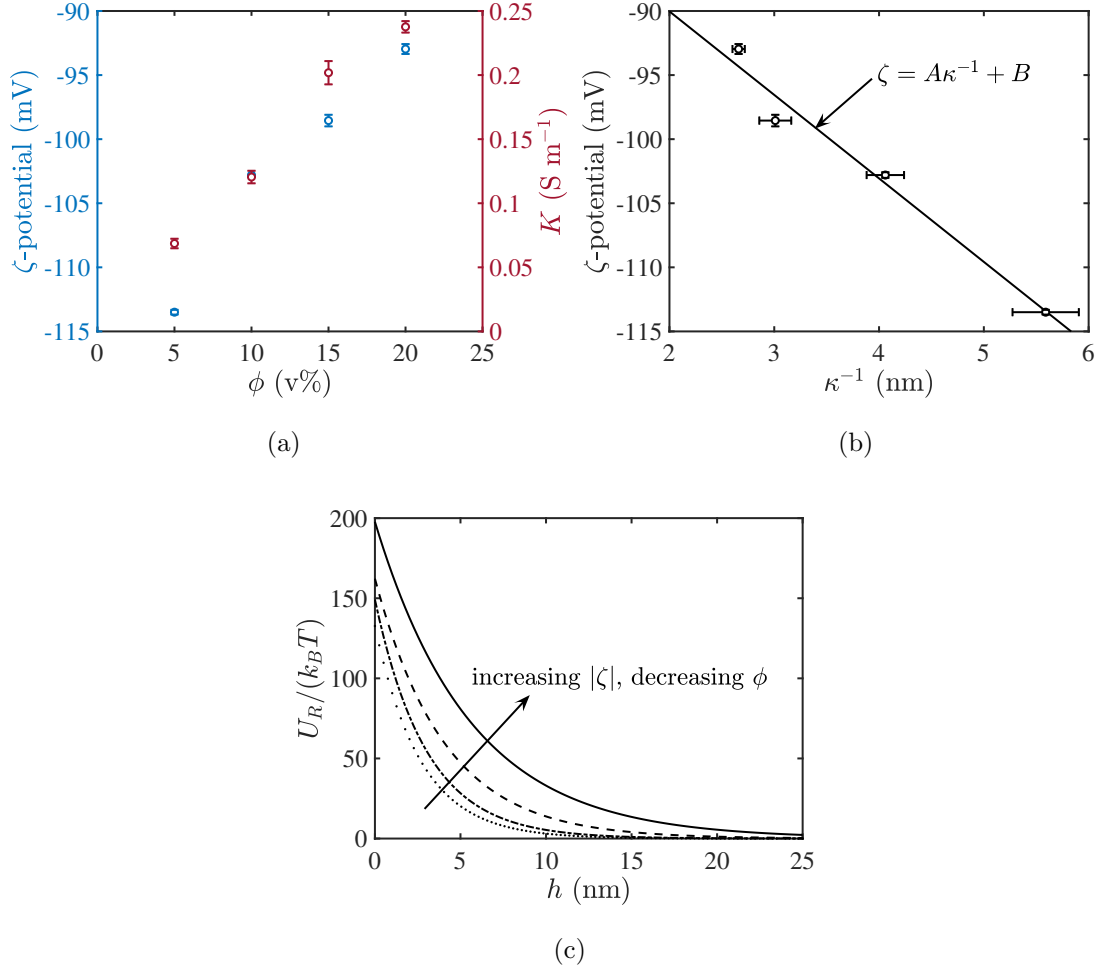


Figure 3.2: (a) ζ -potential of colloidal silica dispersions (from the ESA) versus the silica volume fraction ϕ adjusted by dilution in RO water at $T \approx 21^\circ\text{C}$ and $\text{pH} \approx 9$. (b) ζ -potential versus the double layer thickness κ^{-1} (from Eqns. (3.11) and (3.12)) with $\phi = 5, 10, 15,$ and 20 v% (κ^{-1} decreases with increasing ϕ). Line is $\zeta = A\kappa^{-1} + B$ with empirical fitting parameters $A \approx -6.5\ \text{mV}\ \text{nm}^{-1}$ and $B \approx -77\ \text{mV}$. (c) Electrostatic interaction energy according to Eqn. (3.13) with $a = 28\ \text{nm}$ for the four particle volume fractions in (a). Error bars are the standard error σ/\sqrt{n} from $n = 3$ samples.

Note that Eqn. (3.10) furnishes κ^{-1} for silica NPs in RO water if n_j^∞ for all the ion species are known. However, the bulk ion concentrations are from the NP counterions, so their concentrations are unknown. Thus, an alternative measure, proposed by [Dukhin and Goetz \(2017\)](#), is based on the measured dispersion conductivity K_∞ :

$$\kappa^{-1} \approx \sqrt{\frac{\epsilon_s \epsilon_0 D_{\text{eff}}}{K_\infty}}, \quad (3.11)$$

where D_{eff} is the effective diffusion coefficient furnished by the Nernst-Heckell equation ([Mostinsky, 2011](#))

$$D_{\text{eff}} = \frac{k_B T}{N_A e^2 \sum_{j=1}^N (z_j^2 / \lambda_j)} \quad (3.12)$$

with λ_j the limiting molar conductivities ($\text{S cm}^2 \text{ mol}^{-1}$) of ions in the solution.

The ζ -potential is plotted versus κ^{-1} on the basis of Eqn. (3.12) (by varying ϕ) in the top-right panel of Figure 3.2. Assuming H^+ and OH^- ions in solution, the limiting molar conductivities at $T = 25^\circ\text{C}$ are 349.6 and 199.1 $\text{S cm}^2 \text{ mol}^{-1}$, respectively ([Atkins and de Paula, 2010](#), [Rumble, 2017](#)). The electrostatic interaction energy U_R of two identical NPs with sufficiently thin double layers ($\kappa a > 10$), assuming the Stern potential equals the ζ -potential, is ([Hunter, 1981](#))

$$U_R \approx 2\pi\epsilon_s\epsilon_0 a \zeta^2 e^{-\kappa h}, \quad (3.13)$$

where h is the separation distance. This potential is plotted in Figure 3.2(c) for each of the measured ζ -potentials and their corresponding Debye length. Accordingly, the repulsive electrostatic interaction decreases with increasing ϕ due to compression of the double layer with increasing NP counter-ion concentration.

3.4.2 Properties of polyacrylamide

The present study focuses on polyacrylamide (see Appendix 3.B, Table 3.B.1 for properties), an uncharged, water soluble polymer.

3.4.3 Adsorption isotherms of PA on colloidal silica using TGA

The adsorbed amounts Γ of PA on colloidal silica from TGA according to Eqn. (3.1) are plotted in Figure 3.3 (circles) versus PA concentration c for molecular weights 40 (blue) and

150 kDa (red). The increase in Γ with concentration is attributed to the increasing chemical potential of the polymer in the bulk solution. Increasing the molecular weight increases the decrease in free energy upon adsorption, accounting for configurational chain entropy and enthalpic interactions between silica, polymer and solvent.

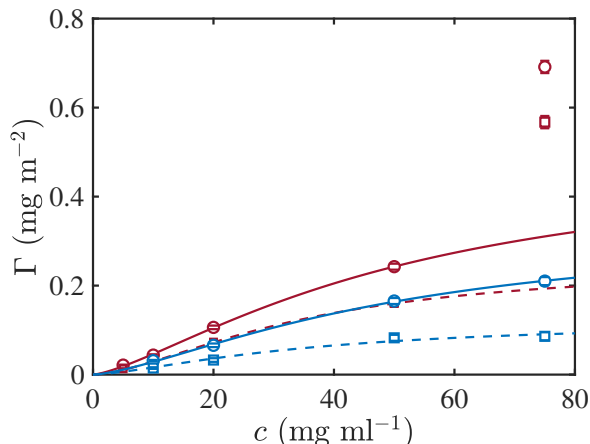


Figure 3.3: Adsorbed amount Γ versus PA concentration c for molecular weights 150 kDa (red) and 40 kDa (blue). The data obtained directly from TGA (circles) are compared with counterparts (squares) obtained by subtracting the amount of polymer in interstitial voids of the silica pellets. Error bars are the standard error σ/\sqrt{n} from $n = 3$ samples. Lines are modified Langmuir isotherms with optimal fitting parameters in Table 3.1. Data at 75 mg ml^{-1} for the 150 kDa polymer were not included in the fitting, since doing so furnished negative values of the equilibrium constant K , prompting use of the BET isotherm (3.5).

Note that a significant amount of the mass change registered by TGA can be attributed to PA in the interstitial regions of the silica pellets, as shown in Figure 3.3 by Γ (squares) corrected by subtracting the amount of PA captured in the interstitial voids, albeit based on an assumption of random close packing. The lines in Figure 3.3 are the modified Langmuir isotherm Eqn. (3.3) with optimal fitting parameters. The modified Langmuir coefficients, Γ_{\max} and K , obtained by prescribing the exponent n in the range 1–2 are shown in Figure 3.4.

The maximum coefficient of determination R^2 is achieved with $n \approx 1.5$ (optimal fitting parameters are provided in Table 3.1), which is comparable to the value $n \approx 1.6$ from Mohammadi et al. (2012) for the adsorption of asphaltenes onto Hematite. Although, $R^2 > 0.98$ for all samples, $\Gamma_{\max} \approx 5.4 \text{ mg m}^{-2}$ with $n = 1$ for 150 kDa PA is larger than reported in the literature for PA adsorption on siliceous materials with similar sample composition,

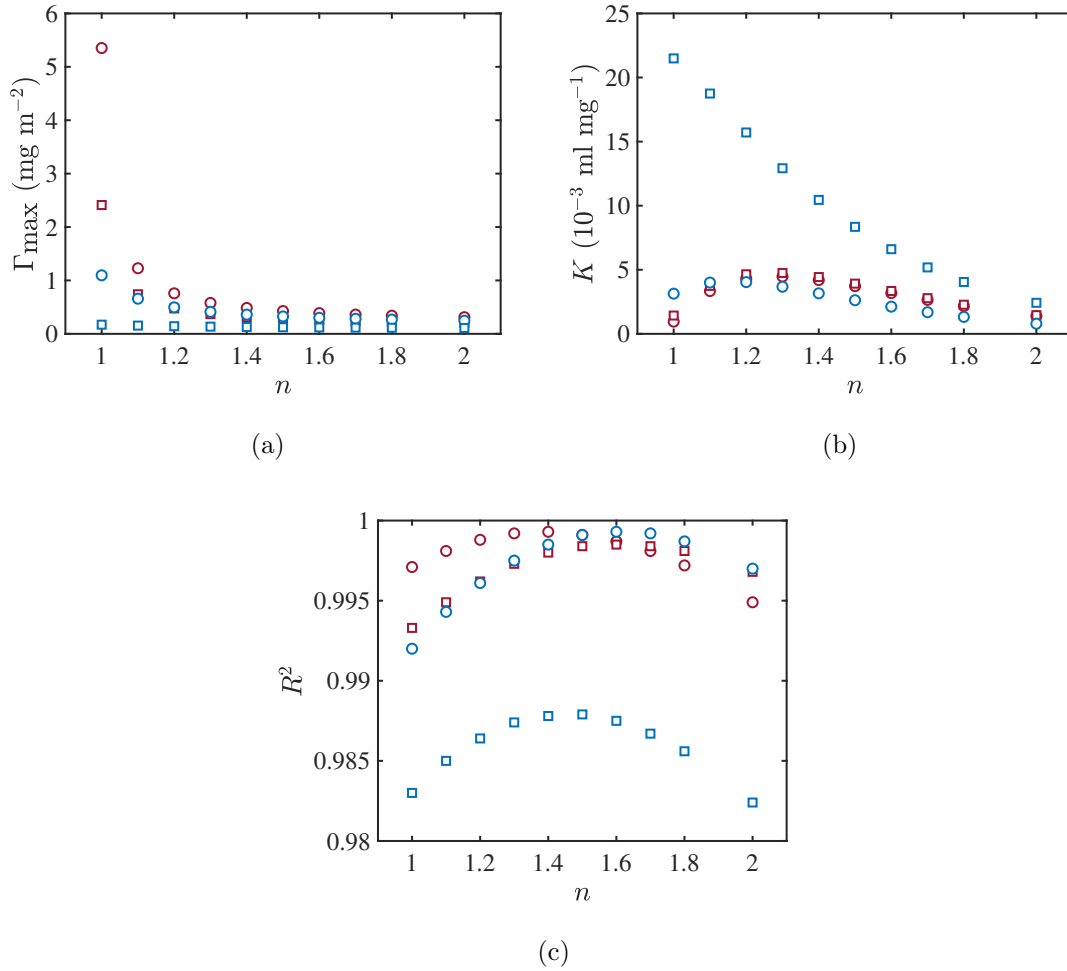


Figure 3.4: (a) Theoretical maximum adsorbed amount Γ_{\max} , (b) equilibrium constant K , and (c) R^2 versus the isotherm exponent n from non-linear fitting of Eqn. (3.3) to data (identified by the symbols and colors in Figure 3.3).

Table 3.1: Optimal modified-Langmuir isotherm parameters (maximizing R^2 with respect to n) from Figure 3.4.

PA MW (kDa)	n	Γ_{\max} (mg m^{-2})	K ($10^{-3} \text{ ml mg}^{-1}$)	R^2
150	1.389	0.493	4.237	0.9993
40	1.455	0.328	3.378	0.9991
150 ^a	1.607	0.250	3.305	0.9985
40 ^a	1.459	0.125	9.167	0.9879

^aSubtracting from the TGA measurement the estimated amount of PA in the interstitial voids of the silica pellets.

albeit using different measurement techniques (Bessaies-Bey et al., 2018). Whereas some researchers have reported zero adsorption of PA on siliceous materials, others have reported adsorption amounts $< 1 \text{ mg m}^{-2}$, subject to varying experimental conditions. Fitting the three parameters produces the same graph as Figure 3.3.

For example, Guévellou et al. (1995) showed that, at a fixed PA (MW 7,500 kDa) concentration in solution, the adsorbed amount on sand (99% silica) measured using a total and inorganic carbon analyzer at $T = 30^\circ\text{C}$ decreases with pH from $\Gamma_{\max} = 0.35$ at pH = 9 to $\Gamma_{\max} = 0 \text{ mg m}^{-2}$ at pH = 12.5. They attributed the decrease in PA adsorption to electrostatic forces arising from the polymer undergoing hydrolysis when pH $\gtrsim 10$.

Bessaies-Bey et al. (2018) reported no adsorption of neutral PA (MW 470 kDa) on synthetic silica particles ($1.1 \text{ m}^2 \text{ g}^{-1}$) in water at pH = 2 using TOC at $T = 22^\circ\text{C}$, but obtained a plateau $\Gamma_{\max} = 0.45 \text{ mg m}^{-2}$ on natural quartz under the same experimental conditions. The ionic strength, pH, and polymer anionicity were factors highlighted as critical to controlling polymer adsorption on siliceous materials (Bessaies-Bey et al., 2018).

Wiśniewska (2012) determined the temperature dependence of the adsorption of hydrolyzed PA (MW 10 kDa, anionicity 14.4%) on silica NPs ($326 \text{ m}^2 \text{ g}^{-1}$) in 0.01 M NaCl solution (pH = 6) using a spectrophotometric method. They obtained adsorbed amounts ($\Gamma_{\max} = 0.2\text{--}0.4 \text{ mg m}^{-2}$) that decrease with an increase in temperature in the range 15–35°C. This temperature dependence was attributed to structural changes of the polymer chains. At higher temperatures, the polymer coils expand, forming a thicker adsorbed layer, whereas at a lower temperatures the adsorbed layers are thinner, comprising loosely entangled polymer

coils ([Wiśniewska, 2012](#)).

As quantified by the optimal modified Langmuir parameters in Table 3.1, Γ_{\max} increased with the PA molecular weight. [Lee and Schlautman \(2015\)](#) reported an increase in the adsorbed amount of neutral PA on kaolinite in aqueous solution when increasing the MW from 1.5 to 6,000 kDa. [Petit et al. \(2014\)](#) obtained $\Gamma_{\max} = 1 \text{ mg m}^{-2}$ and $K = 30 \text{ ml mg}^{-1}$ for the adsorption of poly(N,N-dimethylacrylamide) (PDMA) on silica nanoparticles in water at $T = 20^\circ\text{C}$ using TOC for PDMA concentrations in the range 0–1.5 mg ml^{-1} . They interpreted these adsorption constants in terms of a strong binding energy for PDMA on silica. When compared to values in Table 3.1, it may be concluded that the binding energy for PA on silica is relatively weak.

The adsorption data interpreted using the BET isotherm Eqn. (3.5) are shown in Figure 3.5 with fitting parameters provided in Table 3.2. The maximum adsorption capacity Γ_{\max} for the 40 kDa PA is similar to that obtained with the modified Langmuir isotherm. This isotherm presents a very different adsorbed amount for the 150 kDa PA at higher concentrations, extrapolating to much higher adsorbed amounts than the modified Langmuir model above, which, recall, does not capture such an increase in the adsorbed amount at higher concentrations. The K_S values measure equilibrium concentrations for monolayer saturation, while K_L values relate to the superficial adsorbate solubility ([Piccin et al., 2017](#)). [Samiey and Abdollahi Jonaghani \(2015\)](#) claimed the fitting parameters in Eqn. (3.5) for adsorption from the liquid phase do not have any physical significance due to solvent interactions with adsorbate molecules. Moreover, according to ([Ebadi et al., 2009](#)), the critical assumptions of the BET equation for gas phase adsorption are not valid for liquid phase adsorption. For instance, it is impossible to assume that adsorption will be infinite when liquid phase concentration equals the saturation concentration of the adsorbate.

3.4.4 Effect of pH on the particle/polymer suspension

Zeta-potential and particle size

The interrelations of the ζ -potential, hydrodynamic particle diameter d and pH are explored in Figure 3.6. These experiments were conducted on suspensions containing (i) 5 v% bare silica and (ii) 5 v% silica with 1.25 w% PA. This PA concentration is in the dilute, unen-

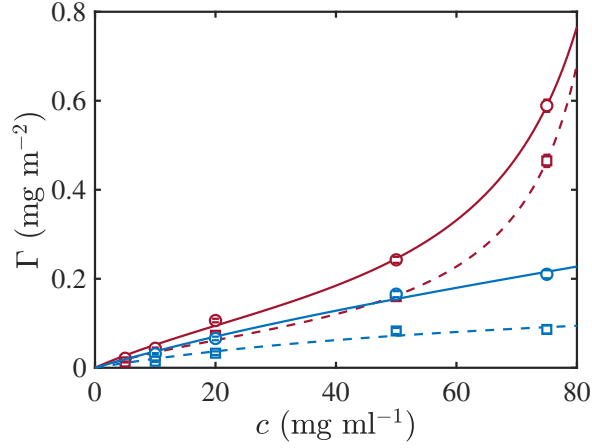


Figure 3.5: The same as Figure 3.3, but lines are BET isotherms Eqn. (3.5) with fitting parameters Γ_{\max} , K_S and K_L in Table 3.2.

Table 3.2: BET isotherm parameters accompanying Figure 3.5, with $c_{\text{BET}} = K_S/K_L$ and $c_0 = 1/K_L$.

PA MW (kDa)	Γ_{\max} (mg m^{-2})	c_{BET}	c_0 (mg ml^{-1})	K_S (ml mg^{-1})	K_L (ml mg^{-1})	R^2
150	0.149	3.97	98.1	0.0405	0.0102	0.9989
40	0.351	4.70	421	0.0112	0.00238	0.9906
150 ^a	0.0873	4.41	91.3	0.0483	0.0109	0.9984
40 ^a	0.153	14.5	957	0.0152	0.00105	0.9473

^aSubtracting from the TGA measurement the estimated amount of PA in the interstitial voids of the silica pellets.

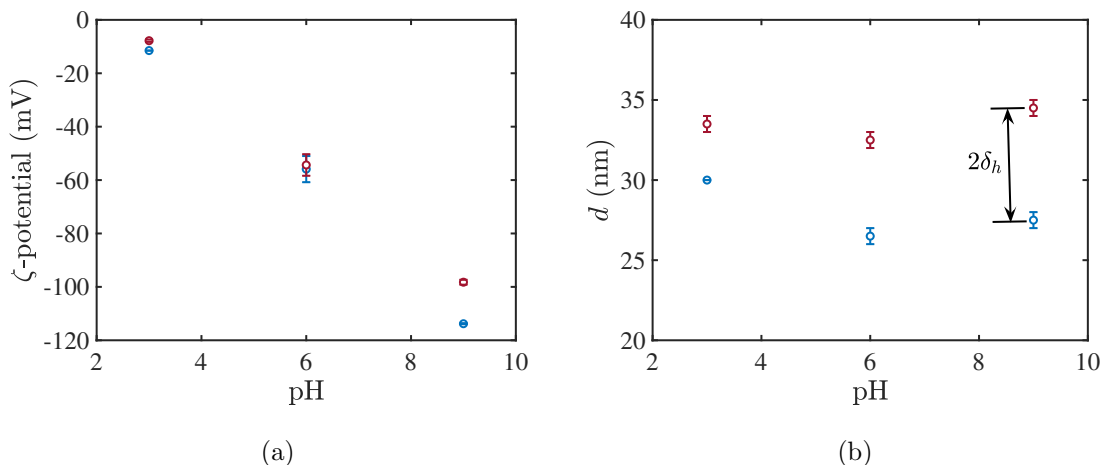


Figure 3.6: (a) ζ -potential (b) hydrodynamic diameter of bare (blue) and PA-coated silica NPs (red) versus pH (3, 6 and 9): silica volume fraction 5 v%, $T \approx 21^\circ\text{C}$. Error bars are the standard error σ/\sqrt{n} from $n = 3$ samples. δ_n is the hydrodynamic polymer layer thickness.

tangled regime. Three separately prepared samples of each suspension were analyzed, and the average and standard error (as error bars) are reported. The ζ -potential of the bare and PA-coated NPs were obtained directly from the model implemented in the AcoustoSizer II software. The initial pH ≈ 9 was adjusted by the addition of 2 M HCl solution dropwise to achieve pH ≈ 3 and 6. As a result of PA adsorption, the ζ -potential of silica NPs in the silica/PA suspension at pH ≈ 9 is less negative (-98.9 mV) than for bare silica (-113.8 mV). The absolute values of ζ -potential for both bare and PA-coated silica increase with increasing pH due to protonation of negatively charged surface moieties.

Note that the bulk PA concentration increases the effective solvent shear viscosity by a factor of ≈ 2.4 at strain rates in the range $\dot{\gamma} \approx 10\text{--}1000$ s $^{-1}$, as will be shown in Figure 3.11. Fitting parameters to the dynamic mobility data will reveal that the polymer contribution to the solvent viscosity is small at high (MHz) frequencies. Therefore, the shear viscosity used for calculating the ζ -potential from the dynamic mobility is that of water for both the bare silica in pure electrolyte and the PA-coated silica in PA solutions.

Kim et al. (2009) reported qualitatively similar results for silica/PVA suspensions: -25 and -23 mV at pH ≈ 9 for silica and silica/PVA suspensions, respectively, and ascribed the decrease in the absolute value to the screening effect of non-ionic polymer on the charged particle surface (Kim et al., 2009). The ζ -potential approaches zero at low pH, which indicates

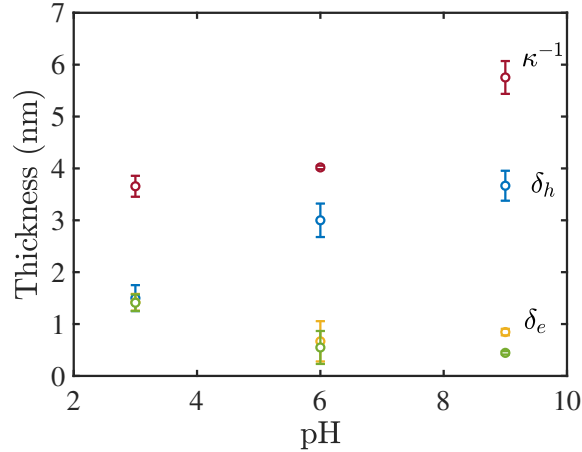


Figure 3.7: Variation of double layer thickness [κ^{-1} , red, Eqn. (3.11)], hydrodynamic coating thickness (δ_h , blue) and electrophoretic layer thickness [δ_e , yellow, Eqn. (3.14) and green, Eqn. (3.15)] versus pH: silica volume fraction 5 v%, $T \approx 21^\circ\text{C}$. Error bars are the standard errors propagated from the standard error σ/\sqrt{n} of 3 sample measurements of ζ , d , and K_∞ .

instability in both systems. The isoelectric point (IEP, pH at which $\zeta = 0$) of silica cited in the literature ([Alves Júnior and Baldo, 2014](#), [Lazaro et al., 2018](#)) is $\text{pH} \approx 2$. PA is uncharged, as so its adsorption does not change the surface charge. It decreases the magnitude of the ζ -potential by shifting the shear plane, also increasing the hydrodynamic size.

Compared to the bare silica NPs, the PA-coated silica NPs have a larger diameter (as measured from the ESA) at all pH values. The diameter of the bare silica NPs at $\text{pH} \approx 9$ was measured 27.5 ± 0.5 nm, close to 30 nm from the manufacturer. The hydrodynamic diameter of the bare and PA-coated silica is only slightly pH dependent, suggesting colloidal stability. The hydrodynamic thickness of the adsorbed layer δ_h is derived from the difference in the hydrodynamic size of the coated and bare silica NPs in Figure 3.6. The values increase with pH, as plotted in Figure 3.7 (blue circles).

Note that $\delta_h \ll a$ at all pH values considered, suggesting a thin polymer coating within the double layers, *i.e.*, $\kappa\delta_h < 1$. [Wiśniewska \(2012\)](#) determined the temperature and MW dependence of δ_h from the adsorption of hydrolyzed PA (MW 1.5 kDa, anionicity 9.3% and MW 10 kDa, anionicity 14.4%) on silica NPs ($326 \text{ m}^2 \text{ g}^{-1}$) in 0.01 M NaCl solution ($\text{pH} = 6$). They found δ_h to increase with temperature (15–35°C), with values in the range 2.8–3.6 nm for the lower MW PA and 4.5–5.5 nm for the higher MW PA. These were

Table 3.3: Conductivity at the beginning (K_0) and end (K_∞) of ESA experiments. κ^{-1} are calculated from Eqns. (3.11) and (3.12). K_0 and K_∞ have standard errors σ/\sqrt{n} from $n = 3$ samples, while for κ^{-1} , $\text{SE}_{\kappa^{-1}} = |\kappa^{-1}/(2K_\infty)| \text{SE}_{K_\infty}$.

Sample	pH	K_0 (S m ⁻¹)	K_∞ (S m ⁻¹)	κ^{-1} (nm)
silica 5%	9	0.0681 ± 0.0037	0.0686 ± 0.0037	5.75 ± 0.15
	6	0.133 ± 0.001	0.134 ± 0.001	4.02 ± 0.03
	3	0.164 ± 0.010	0.159 ± 0.010	3.66 ± 0.10
PA-silica 5%	9	0.0696 ± 0.0017	0.0695 ± 0.0017	5.56 ± 0.13
	6	0.139 ± 0.002	0.139 ± 0.002	3.93 ± 0.05
	3	0.186 ± 0.006	0.185 ± 0.006	3.41 ± 0.09

attributed to structural changes of the polymer chains as a result of temperature and MW changes (Wiśniewska, 2012).

The double layer thicknesses κ^{-1} calculated from Eqns. (3.11) and (3.12) at pH = 3, 6 and 9 are also shown in Figure 3.7 (red circles). The double layer thicknesses are much smaller than the particle radius, furnishing $\kappa a \gg 1$. The instrument software reports a ζ -potential and Smoluchowski ζ -potential. The first is what is reported in this work, whereas Smoluchowski's solution is expected to break down for $\kappa a < 50$ and large ζ -potential. The decrease in κ^{-1} with pH is attributed to the accompanying change in ionic strength. Note that suspension conductivities, measured at the start (K_0) and end (K_∞) of ESA experiments, for the bare and PA-coated silica NPs are shown in Table 3.3 with the corresponding κ^{-1} at pH = 3, 6 and 9.

Another thickness, which depends on the ζ -potential of the bare and PA-coated particles, is known as the electrophoretic layer thickness δ_e . This is calculated using the Gouy-Chapman theory for the equilibrium distribution of ions and potential in the diffuse double layer (Hunter, 1981, Stuart and Mulder, 1985):

$$\tanh\left(\frac{ze\zeta}{4k_B T}\right) = \tanh\left(\frac{ze\psi_d}{4k_B T}\right)e^{-\kappa\delta_e}, \quad (3.14)$$

where δ_e is the double-layer thickness spanning the Stern layer and shear plane, ψ_d is the diffuse-layer potential, and $\zeta = \zeta(\delta_e)$ is the ζ -potential with adsorbed polymer. Eqn. (3.14) is based on the assumption that (i) $\psi_d \approx \zeta_0$ (ζ_0 is the ζ -potential without adsorbed poly-

Table 3.4: Total adsorbed layer thickness, as defined by [Carasso et al. \(1997\)](#), dimensionless thickness, and dimensionless particle radius. Errors are the standard errors propagated from the standard error σ/\sqrt{n} of 3 sample measurements of ζ , d , and K_∞ .

pH	$\delta_h + \delta_e$ (nm)	$\kappa\delta_h$	κa (bare)	κa (PA coated)
9	4.51 ± 0.34	0.64 ± 0.05	2.38 ± 0.08	3.12 ± 0.14
6	3.67 ± 0.71	0.74 ± 0.08	3.30 ± 0.06	4.13 ± 0.11
3	2.92 ± 0.40	0.41 ± 0.07	4.10 ± 0.13	4.92 ± 0.27

mer), and (ii) the principal effect of polymer adsorption is to displace the shear plane outward ([Carasso et al., 1997](#), [Barany, 2015](#)). For low values of the ζ -potential ($\zeta \leq 50$ mV, Debye-Hückel approximation) ([Stuart and Mulder, 1985](#)), Eqn. (3.14) reduces to

$$\zeta = \psi_d e^{-\kappa\delta_e}. \quad (3.15)$$

As shown in Figure 3.7 (yellow and green circles, respectively), δ_e from Eqns. (3.14) and (3.15) are very close. At pH = 6 and 9, both notably smaller than δ_h , suggesting that electro-osmotic flow permeates the periphery of the adsorbed polymer layers. At pH = 3, however, $\delta_e \approx \delta_h$, suggesting that the polymer layer is much more compact and uniform, as might be expected based on the notably smaller value of δ_h .

[Carasso et al. \(1997\)](#) defined a total adsorbed layer thickness of poly(vinyl alcohol) (PVA) on silica particles as $\delta_h + \delta_e$, which they found to increase with polymer concentration (due to δ_h), implying longer tails and loops for PVA concentrations in the range 0.06–1.1 μM . However, δ_e was only slightly dependent on PVA concentration and molecular weight. As shown in Table 3.4, $\delta_h + \delta_e$ increases with pH due to the changes in δ_h and δ_e .

Mobility magnitude and argument

Mobility magnitude $|M|$ spectra for silica NPs in RO water and PA solution are compared in Figure 3.8(a) at pH = 3, 6 and 9. These experiments were conducted on suspensions containing (i) 5 v% silica NPs in RO water and (ii) 5 v% silica NPs in 1.25 w% PA (150 kDa MW). At pH = 9, the silica NPs in RO water have a notably higher mobility magnitude ($\approx 12\%$) than in PA solution. The lower mobility magnitude from PA adsorption may be

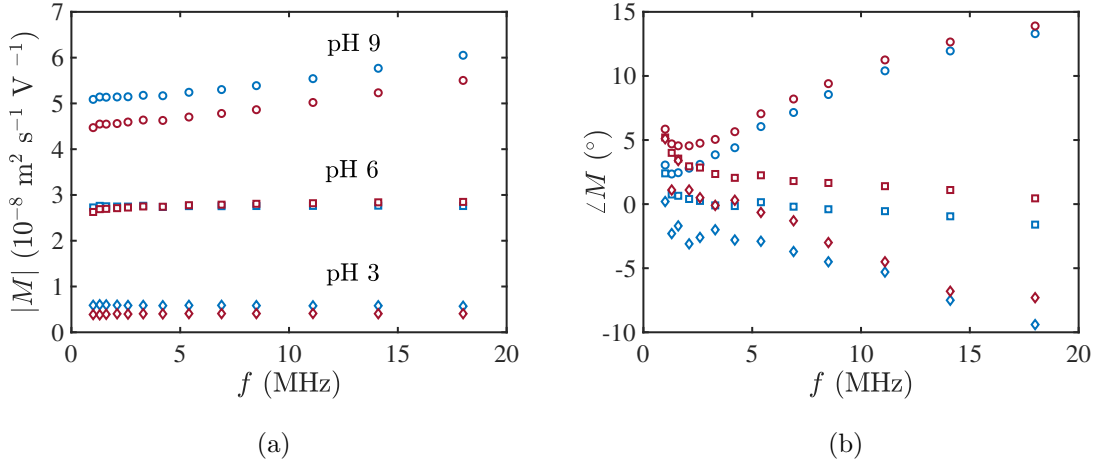


Figure 3.8: Dynamic mobility magnitude (left) and argument spectra (right) for silica NPs in RO water (blue) and in PA solution (red) at pH = 3 (\diamond), 6 (\square) and 9 (\circ): silica volume fraction $\phi = 5 \text{ v\%}$, $T \approx 21^\circ\text{C}$. K_∞ and κ^{-1} are provided in Table 3.3.

due to viscoelastic stresses brought about by the polymer and/or the PA adsorption. The accompanying ζ -potentials are -98.9 mV and -113.8 mV for NPs in PA solution and RO water, respectively. [Adibnia et al. \(2017a\)](#) observed similar behaviour brought about by the addition of acrylamide monomer to silica and Laponite dispersions. [Hill et al. \(2003\)](#) attributed the lower mobility for particles coated with uncharged polymer to a decrease in the net charge behind the shear surface and an increase in the drag force. The mobility magnitude of silica particles in RO water and PA solution both decrease with decreasing pH, which corresponds to increasing κa , as shown in Table 3.4.

The mobility argument $\angle M$ (phase) spectra are plotted in Figure 3.8(b) at pH = 3, 6 and 9. Note that, according to the phase-angle convention of the AcoustoSizer II, a positive (negative) phase angle corresponds to the particle velocity leading (lagging) the applied electric field. For the most highly charged particles at pH = 9, the phase lead is customarily attributed to polarization of the diffuse double layer, whereas for the weakly charged particles, a negative phase angle, corresponding to a phase lag, reflects particle inertia. Note also that visco-elastic coupling of the polymer to the electro-osmotic flow can also affect the dynamic mobility ([Carasso et al., 1997](#), [O'Brien, 2002](#)). At pH = 9, the distinct phase lead correlates with an increase in δ_h , as shown in Figure 3.7. Note that polymer segments adsorbed as trains may become transformed or redistributed into tails and loops, as reported by [Carasso et al. \(1997\)](#). [Carasso et al. \(1997\)](#) claimed that adsorption

is less favourable at high pH such that the polymer segments adsorbed as trains become redistributed into tails and loops leading to increased thickness of the adsorbed layer and accounting for increase in phase lead. At low pH, more polymer segments adsorb in trains, and the layer contracts.

Figure 3.9 compares the theory of O'Brien et al. (1995), Eqn. (3.7), with experimental data at pH = 9 with the prescribed value of κ^{-1} (from Table 3.3), here varying particle diameter d (available in Figure 3.9). Other parameters in Eqns. (3.7)–(3.9) were prescribed according to values in the caption of Figure 3.9. The dynamic mobility magnitude and phase angle better fit the ESA data at higher frequencies. The values of d are comparable to those furnished by the instrument (shown in Figure 3.6) in the frequency range 1–18 MHz at $T \approx 21^\circ\text{C}$. The instrument software report page contains two size analysis: ESA and Attenuation. According to Colloidal dynamics, the ESA method can only be used for particle size in the range 70–10000 nm. The size analysis on the report page used in this work are those from the attenuation method.

A theoretical analysis was undertaken by replacing the Newtonian fluid viscosity in Eqns. (3.7) and (3.8) with a complex shear viscosity for the NPs in PA solution following Wang and Hill (2009) with the form

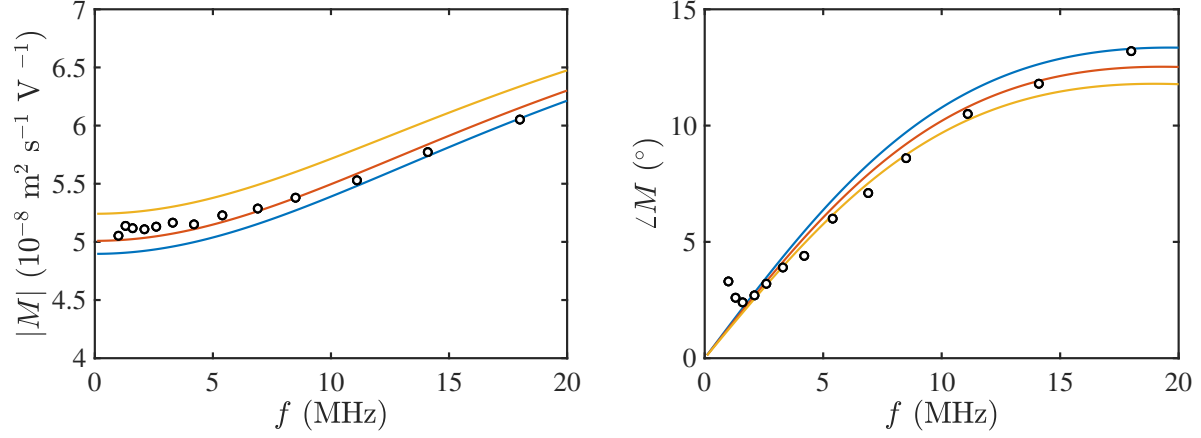
$$\eta^* = \eta + i\mu^*\omega^{-1} = \eta + \eta' + i\mu'\omega^{-1}, \quad (3.16)$$

where η is the solvent viscosity and

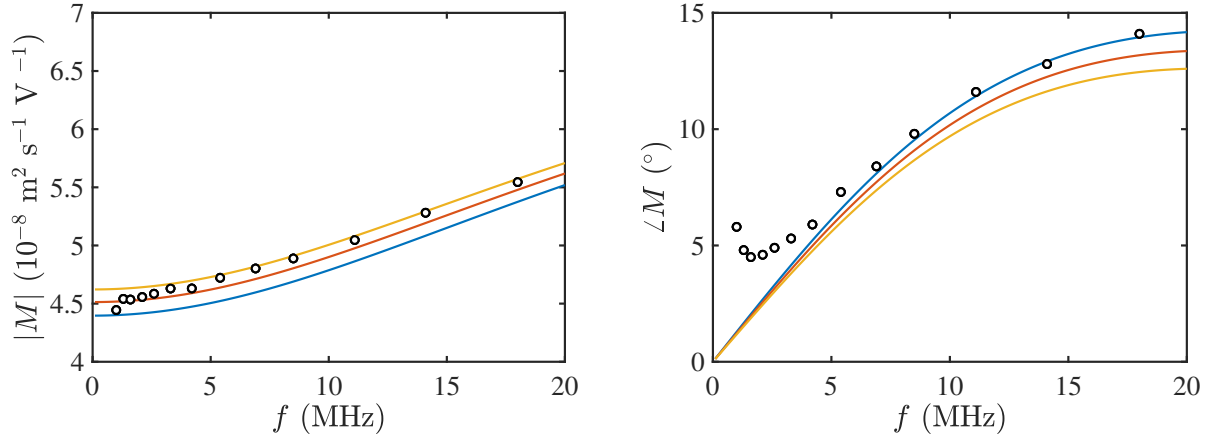
$$\mu^* = \mu' - i\eta'\omega$$

is a complex shear modulus for the PA/silica suspension. Note that η' is the polymer contribution to the shear viscosity, ω is the angular frequency, and μ' is the shear modulus.

Wang and Hill (2009) theory is applicable for spherical colloids embedded in uncharged gels, with no-slip between the colloidal particle and gel. It can be applied to interpret the PA/silica suspension mobility experiments to determine the polymer contribution to the shear viscosity. The theory defines shear modulus as the single independent gel parameter that affects particle dynamics for large particles at MHz frequencies, valid when κ^{-1} is small compared to the polymer mesh size. Accordingly, NP mobility in polymer solution/gel depends on four model parameters: double layer thickness κ^{-1} , ζ -potential, and the real and imaginary parts of the complex shear viscosity Eqn. (3.16).



(a) Bare silica: $\kappa a = 2.2$ ($d = 25$ nm, blue), 2.3 ($d = 26.5$ nm, red) and 2.6 ($d = 30$ nm, yellow).



(b) Silica + PA: $\kappa a = 2.8$ ($d = 31$ nm, blue), 3 ($d = 33$ nm, red) and 3.2 ($d = 35$ nm, yellow).

Figure 3.9: Dynamic mobility magnitude (left) and argument (right) spectra for (a) NPs in reverse-osmosis water with $\zeta = -113.8 \pm 0.20$ mV, and (b) NPs in PA solution with $\zeta = -98.2 \pm 0.65$ mV (from the ESA software) at pH = 9. Circles are experimental data, and lines are Eqn. (3.7) for various particle diameters d . Other prescribed parameters: solvent viscosity $\eta = 9 \times 10^{-4}$ Pa s, temperature $T = 294.15$ K, solvent density $\rho = 998$ kg m $^{-3}$, particle density $\rho_p = 2200$ kg m $^{-3}$.

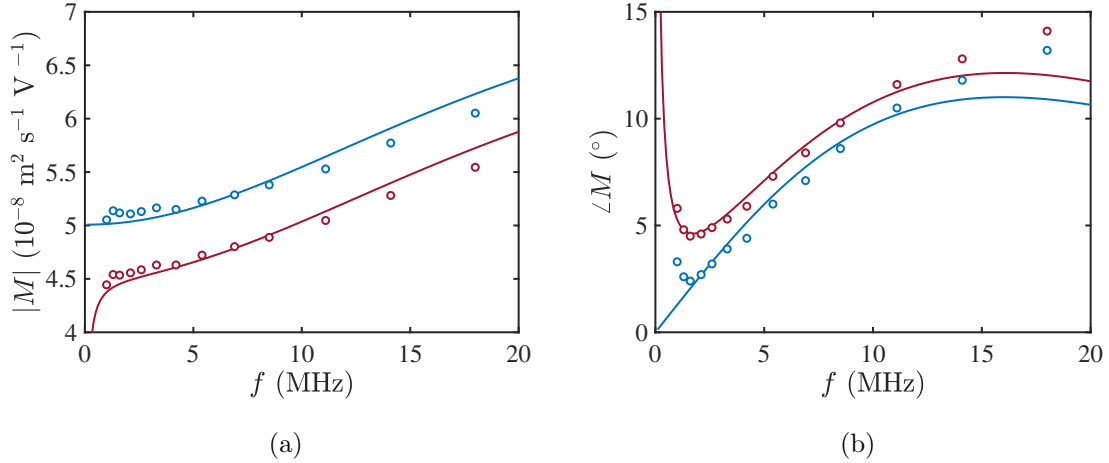


Figure 3.10: Dynamic mobility magnitude (left) and argument (right) spectra for NPs in reverse-osmosis water (blue), and (b) NPs in PA solution (red) at pH = 9. Circles are experimental data, and solid lines are O’Brien’s theory (Eqns. (3.7)–(3.9)). The shear viscosity for the PA-coated NPs is replaced with the theory of Wang and Hill (2009) (Eqn. (3.16)). Fitting parameters (4 for the PA/silica and 2 for the bare silica) are provided in Table 3.5 with prescribed parameters: solvent viscosity 0.9 mPa s, $T = 294.15$ K, solvent density $\rho = 998$ kg m⁻³, particle density $\rho_p = 2200$ kg m⁻³.

Results of non-linear least-squares fitting of the theory of O’Brien et al. (1995), Eqns. (3.7)–(3.9) to the mobility spectra at pH = 9 for NPs in solvent and polymer solution with two and four variables as fitting parameters (available in Table 3.5), respectively are shown in Figure 3.10. The shear viscosity is the viscosity of water for the bare NPs, hence the absence of two additional fitting parameters: real and imaginary parts of μ^* . Other parameters in Eqns. (3.7)–(3.9) were prescribed according to values in the caption of Figure 3.10.

The resulting hydrodynamic diameter and ζ -potential from the fitting are compared with data obtained from the ESA experiment, where shear viscosity prescribed is the viscosity of water η for both NPs in reverse-osmosis water and in PA solution. The polymer contribution to the shear viscosity η' is low compared to $\eta \approx 0.9$ mPa s. These did not reflect significant changes in the ζ -potential and hydrodynamic diameter obtained from fitting. The shear modulus at MHz frequencies, *i.e.* $\mu' \sim 30$ Pa when $\omega \sim 10^6$ rad s⁻¹. This contribution from the elastic stress is expectedly small.

Table 3.5: Model parameters for the O’Brien’s theory (Eqns. (3.7)–(3.9)) in Figure 3.10 and measurements from Acoustosizer II instrument software. Shear viscosity is the viscosity of water. It is replaced with Eqn. (3.16) (Wang and Hill, 2009) for the silica NPs in polymer solution in Figure 3.10.

Sample	Figure 3.10				Instrument software	
	μ' (Pa)	η' (mPa s)	$-\zeta e/kT$ –	d (nm)	$-\zeta e/kT$ –	d (nm)
Bare silica	-	-	4.22	27.7	4.49	27.3
Silica/PA	31.3	0.028	4.07	35.1	3.88	34.7

3.4.5 Rheology

Steady shear rheology of PA solutions

Steady shear rheology was applied to characterize PA solutions, providing insights to better understand how the polymers interact with NPs in NP composites. Non-Newtonian steady-shear viscosity is captured by a power-law model (Macosko and Larson, 1994)

$$\eta = m\dot{\gamma}^{n-1}, \quad (3.17)$$

where η is the apparent viscosity, $\dot{\gamma}$ is the shear rate, n is the power-law index, and m is the flow consistency index. A log-log plot of η versus $\dot{\gamma}$ furnishes a slope $n - 1$. Newtonian rheology corresponds to $n = 1$ with shear thickening $n > 1$ and shear thinning $n < 1$.

The shear-rate dependence of η is shown in Figure 3.11(a) for PA concentrations $c = 0.2$ –10 wt%. These data reveal Newtonian shear rheology at all polymer concentrations, expediting the plot of specific viscosity η_{sp} versus PA concentration in Figure 3.11(b). Note that η_{sp} is defined as (Rubinstein and Colby, 2003)

$$\eta_{sp} = \frac{\eta - \eta_s}{\eta_s}, \quad (3.18)$$

where η_s is the solvent viscosity ($\approx 10^{-3}$ Pa s for water) and η is the Newtonian solution viscosity obtained by averaging the steady shear viscosity across the range of shear rates studied. The overlap concentration c^* , defined by the transition between dilute and semi-dilute regimes, was obtained by plotting the specific viscosity η_{sp} of each PA solution versus

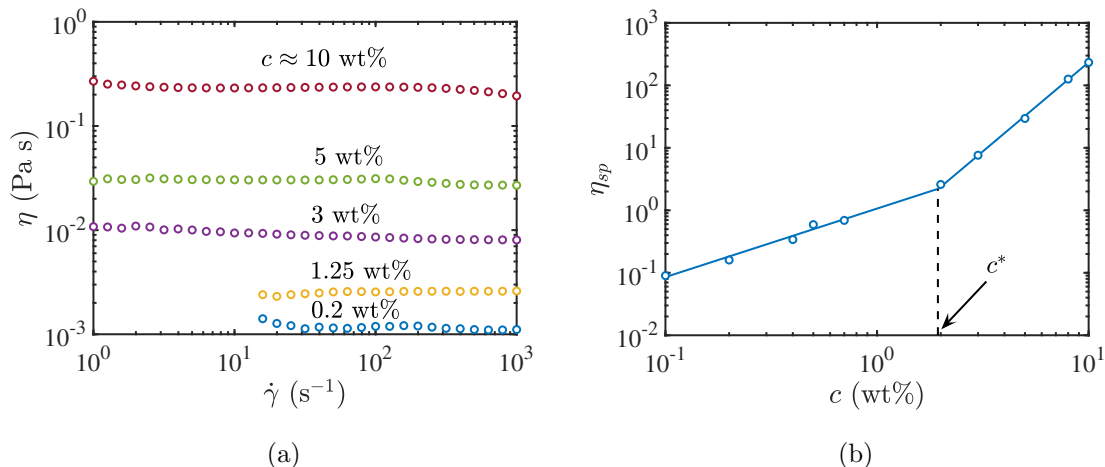


Figure 3.11: (a) Steady-shear viscosity η versus shear rate $\dot{\gamma}$ for various 150 kDa PA concentrations in RO water. (b) Specific viscosity versus 150 kDa PA concentration in RO water ($T \approx 21^\circ\text{C}$). Lines are power-law fits with exponents ≈ 1.10 (when $c < c^*$) and ≈ 2.85 (when $c > c^*$) for the dilute and semi-dilute unentangled regions, respectively, with intersection identifying an overlap concentration $c^* \approx 1.94$ w%.

concentration, from which the two regimes are identified using power-law scaling relationships $\eta_{sp} \sim c^n$. The intersection of these power-laws in Figure 3.11(b) furnishes $c^* \approx 1.9$ wt% for this PA in RO water at 21°C . The power-law exponents are approximately 1.1 and 2.8 for the dilute and semi-dilute unentangled solutions, respectively. These values are in close agreement with the theoretical scaling values of 1 and 2 reported for polymers in a θ -solvent (Rubinstein and Colby, 2003).

From these data, an estimate of the molecular weight of the PA was calculated according to the Mark-Houwink equation (Rubinstein and Colby, 2003)

$$[\eta] = KM^a, \quad (3.19)$$

where $[\eta]$ is the intrinsic viscosity obtained in the limit of reduced viscosity (η_{sp}/c) for very low polymer concentrations, $[\eta] = \lim_{c \rightarrow 0} \eta_{sp}/c$. The Mark-Houwink parameters, K and a , for PA in water at $T \approx 25^\circ\text{C}$ are available from literature (Kulicke et al., 1982) as 0.00631 ml g⁻¹ and 0.8 respectively. Plotting reduced viscosity versus polymer concentration in the dilute regime, as shown in Figure 3.12(a), $[\eta]$ can be estimated by extrapolating to zero concentration or from the y -intercept of a linear fit using the Huggins equation (Rubinstein

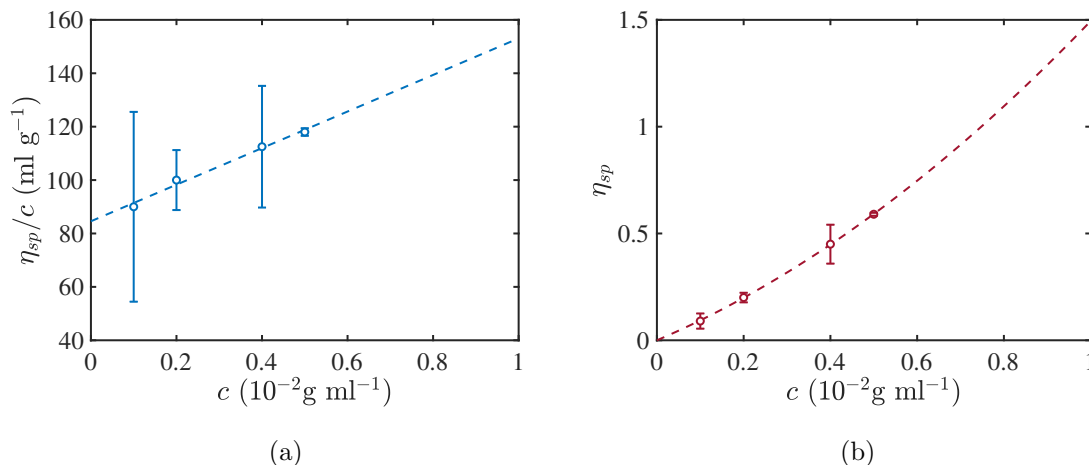


Figure 3.12: (a) Reduced viscosity η_{sp}/c versus PA concentration c and (b) specific viscosity η_{sp} versus c ($T = 21^\circ\text{C}$). Dashed lines in (a) and (b) are linear and quadratic fits, respectively, to the data (averaged η over all shear rates) with standard errors ($\text{SE}_{\eta_{sp}/c} = |1/c| \text{SE}_{\eta_{sp}}$). When the fits are compared to the Huggins Eqns. (3.20) and (3.21), they furnish the intrinsic viscosity and Huggins coefficients presented in Table 3.6.

and Colby, 2003, Huggins, 1942)

$$\frac{\eta_{sp}}{c} = [\eta] + k_H[\eta]^2 c, \quad (3.20)$$

where k_H is the Huggins coefficient obtained by dividing the slope by $[\eta]^2$.

Note that the foregoing method introduces significant errors at low concentrations from dividing η_{sp} by c (Fanood and George, 1987, Kozicki and Kuang, 1996, Harding, 2011). Another way of obtaining $[\eta]$ and k_H , which eliminates extrapolation outside the range of data required by the conventional Huggins approach, is plotting η_{sp} versus c in the dilute regime, as shown in Figure 3.12(b). According to the quadratic form of the Huggins equation (Huggins, 1942, Fanood and George, 1987, Rubinstein and Colby, 2003)

$$\eta_{sp} = [\eta]c + k_H[\eta]^2 c^2, \quad (3.21)$$

where

$$[\eta] = \left. \frac{d\eta_{sp}}{dc} \right|_{c=0} \quad (3.22)$$

is the limiting slope at $c = 0$ and k_H is obtained by dividing the quadratic term by $[\eta]^2$. The constant k_H provides information about the intermolecular interactions between polymer chains in solution (Wu and Shanks, 2003, Jouenne and Levache, 2020). Fanood and George

Table 3.6: The Huggins coefficient k_H , intrinsic viscosity $[\eta]$, and molecular weight M for nominal 150 kDa PA in RO water at $T = 21^\circ\text{C}$.

Huggins	$[\eta]$ (ml g ⁻¹)	k_H	R^2	M (kDa)
Conventional	84.6	0.96	0.9875	144.2
Quadratic	87.1	0.82	0.9999	149.6

(1987) determined $[\eta]$ and k_H for PA in water using the conventional and quadratic Huggins equations, demonstrating higher precision when using the latter approach.

The fitting parameters give $[\eta]$, k_H and molecular weight M from Eqn. (3.19). Note that α is the same as the Mark-Houwink parameter a already defined above. Many texts use a , including Rubinstein and Colby (2003). I used a value defined in literature for PA/water because it was impossible for me to determine the exact value. A log-log plot of $[\eta]$ versus M would furnish a as slope. However, PA standards of known M would be needed. The exponent a is a function of polymer geometry. Typically, $a = 0.5$ represent a hard sphere in a θ -solvent; $0.5 < a < 0.8$ reflect a random coil in a good solvent; and $0.8 < a < 2$ are those from stiff chains (Rubinstein and Colby, 2003, Alberto Masuelli, 2014), as shown in Table 3.6. Whereas the molecular weights are very close to the value prescribed by the manufacturer, k_H indicates that water is not a good solvent for PA. I didn't find a clear-cut relationship between k_H and a in the literature.

For example, Wu and Shanks (2003) determined $k_H \approx 0.99$ for 10 kDa PA in pure water at $T = 25^\circ\text{C}$. This decreased with the addition of NaCl. They reported $k_H \approx 0.47$ with NaCl concentration 0.099 g ml⁻¹, suggesting that, although PA easily dissolves in water, it is not a thermodynamically good solvent for PA. Higher ionic strength and dipole interactions between the amide groups of PA and NaCl cause chain expansion, indicating improved solvent quality (lower k_H) than in pure water (Wu and Shanks, 2003). Pamies et al. (2008) reported typical ranges of k_H values for flexible chains, globular and non-globular particles, polyelectrolytes, *etc.*

Typical values of k_H for flexible chain polymers range from 0.3 in good solvents to 0.5 in poor solvents and 0.7 in theta solvents. Values of k_H previously reported by Fanoos and George (1987) for a PA in water at $T = 25^\circ\text{C}$ vary between 0.50 and 0.53, which are somewhat lower than values in table 3.6. However, for PA and some other water-soluble polymers like

poly(vinyl alcohol) (PVA), k_H may be affected by solution conditions (history, solvent quality and temperature), molecular weight distribution, branching, and ionic strength (Fanood and George, 1987, Lewandowska et al., 2001, Wu and Shanks, 2003).

Lewandowska et al. (2001) further attributed $k_H > 0.5$ for aqueous solutions of PVA to the association of PVA molecules through formation of hydrogen bonds between hydroxyl OH groups of the polymer chains, despite water being a moderate solvent for PVA. The existence of intramolecular hydrogen bonds between the amide groups of PA chains may be used to explain the high k_H values for aqueous solutions of PA, among other possible factors, although not proven here.

The Flory-Huggins polymer-solvent interaction parameter for PA in water at infinite dilution, $\chi = 0.495$ at $T = 25^\circ\text{C}$ (Day and Robb, 1981). χ affects the size of a polymer coil in solution, and provides a measure of solvent quality. In a good solvent ($\chi < 0$), polymer chains form expanded coils in solution, whereas in a poor solvent ($\chi > 0$), polymer chains contract to minimize solvent contact, thus forming compact globules. Du and Hill (2019a) reported $\chi \approx 0.484$ and 0.487 at $T \approx 22.5^\circ\text{C}$ for a chemically cross-linked PA gel swollen in RO water and phosphate buffered saline (PBS), respectively. Polymer adsorption is more favourable in theta solvents than good solvents, since the latter promote solubilization. Laurens et al. (2020) reported the impact of solvent type on polymer adsorption onto silica, finding that the adsorbed amount was higher in a theta solvent than in an athermal solvent.

Note that water could be theta solvent based on the value of k_H . Only the value of a from the Mark-Houwink equation and addition of salt supports this.

There are three parameters that define the kind of solvent (a , χ , and k_H). Literature-reported value of $a = 0.8$ at $T = 25^\circ\text{C}$ for PA/water suggests that the random coil is in a good solvent. The Huggins coefficient $k_H > 0.8$ obtained here suggests a polymer chain in a theta solvent. Lastly, $\chi = 0.495$ at $T = 25^\circ\text{C}$ for PA/water is reported to be closer to $\chi = 0.5$ in a theta solvent. I didn't find any direct relationship between all three parameters in the literature. All three are affected by temperature, solvent quality, and molecular weight.

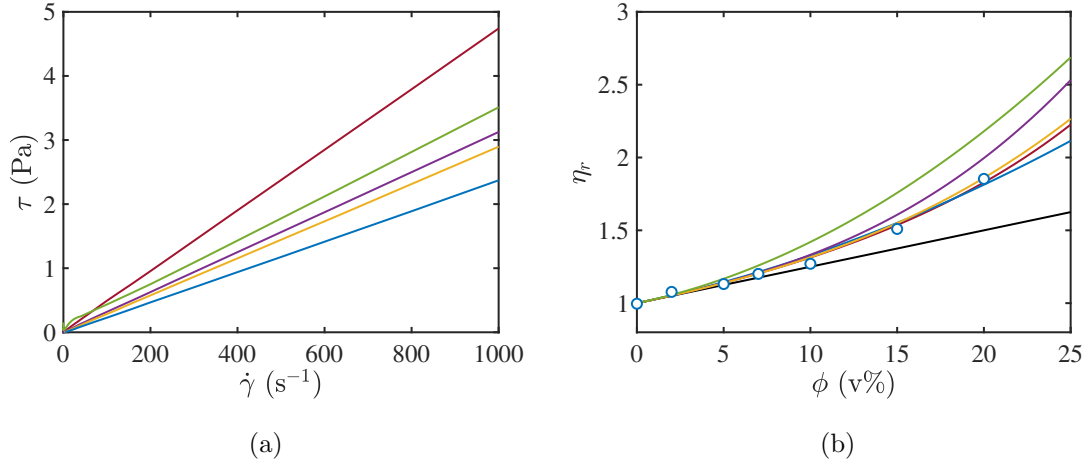


Figure 3.13: (a) Steady-shear stress versus shear rate for 150 kDa PA concentration $c = 1.25$ w% with various colloidal silica concentrations 2, 5, 10, 15 and 20 v% (increasing blue to red) ($T = 21^\circ\text{C}$). (b) Relative viscosity η_r versus colloidal silica volume fraction ϕ (blue circles). Solid lines are the fit to the data [blue, Eqn. (3.25)], Einstein [black, Eqn. (3.23)] and Krieger-Dogherty [red, Eqn. (3.24)] models, Afuwape and Hill (2021) [green, Eqn. (3.26)], rheological virial expansions Eqns. (3.27) (purple) and Eqns. (3.28) (yellow) for, respectively, low and high Péclet numbers.

Rheology of PA-coated colloidal silica dispersions

Using a PA concentration in the dilute regime ($c < 1.9$ wt%) with varying amounts of colloidal silica, rheological measurements were performed to study changes from the unentangled PA. The relationship between the shear stress and shear rate for the PA/silica suspension at varying silica volume fractions and fixed PA concentration $c = 1.25$ wt% is shown in Figure 3.13(a). The flow is Newtonian at all silica volume fractions, and the shear stress increases with silica volume fraction over the entire range of shear rates considered.

The viscosity relative to that of a PA solution with concentration $c = 1.25$ wt% is plotted versus the silica concentration in Figure 3.13(b). The experimental data are compared with theories for the dispersion of spherical solids in a viscous fluid. One of these is the Einstein equation

$$\eta/\eta_0 = 1 + 2.5\phi, \quad (3.23)$$

where $\eta/\eta_0 = \eta_r$ is the relative viscosity, η_0 is the viscosity of the $c = 1.25$ wt% PA solution, and ϕ is the silica NP volume fraction. As shown in Figure 3.13(b) (black line), Equa-

tion (3.23) under-predicts the viscosity at higher NP volume fractions because the theory neglects hydrodynamic and other interactions leading to clustering, for example.

Another model employed is the Krieger and Dougherty equation ([Krieger and Dougherty, 1959](#))

$$\eta_r = \left(1 - \frac{\phi}{\phi_m}\right)^{-2.5\phi_m}, \quad (3.24)$$

where ϕ_m is the maximum concentration, depending on the particle shape and degree of filling. For random close packing of spheres, $\phi_m \approx 0.64$ is commonly used. Equation (3.24) is expected to provide a semi-empirical correlation for the relative viscosity of spherical solids in a viscous fluid up to close packing. As shown in Figure 3.13(b) (red line), the Krieger and Dougherty model successfully captures the experimental dependence of η_r on ϕ . This suggests that the particles are well dispersed.

A quadratic fit to the data with the slope of the linear term equal to Einstein Eqn. (3.23) gives

$$\eta_r = 1 + 2.5\phi + (7.8 \pm 1.8)\phi^2 \quad (R^2 = 0.9878). \quad (3.25)$$

The coefficient of the $O(\phi^2)$ term is much smaller than the value reported by [Afuwape and Hill \(2021\)](#) for emulsion droplets in (elastic) hydrogels:

$$G/G_0 = 1 + 2.5\phi + (17 \pm 6)\phi^2. \quad (3.26)$$

At low volume fractions $\phi \ll 1$, limiting shear viscosities for a variety of dispersions have been found to take the forms ([de Kruif et al., 1985](#))

$$\eta_r = 1 + (5/2)\phi + (4 \pm 2)\phi^2 + (42 \pm 10)\phi^3 + \dots \quad (\text{Pe} \rightarrow 0) \quad (3.27)$$

and

$$\eta_r = 1 + (5/2)\phi + (4 \pm 2)\phi^2 + (25 \pm 7)\phi^3 + \dots \quad (\text{Pe} \rightarrow \infty). \quad (3.28)$$

These indicate that shear thickening (microstructural deformation) is due to three-body interactions, as evidenced by the first deviation occurring at $O(\phi^3)$; the $O(\phi^2)$ terms are the same, indicating that two-body (pairwise) hydrodynamic interactions do not alter the microstructure. Here, the particles are supposed to interact only hydrodynamically—often, however, electrostatic, dispersive and steric forces play a role. As shown in Figure 3.13(b), plotting Eqns. (3.27) and (3.28) with the data confirm that the Péclet number is indeed small:

$$\text{Pe} = \frac{\dot{\gamma}a^2}{k_B T / (6\pi\eta_0 a)} \lesssim 0.003,$$

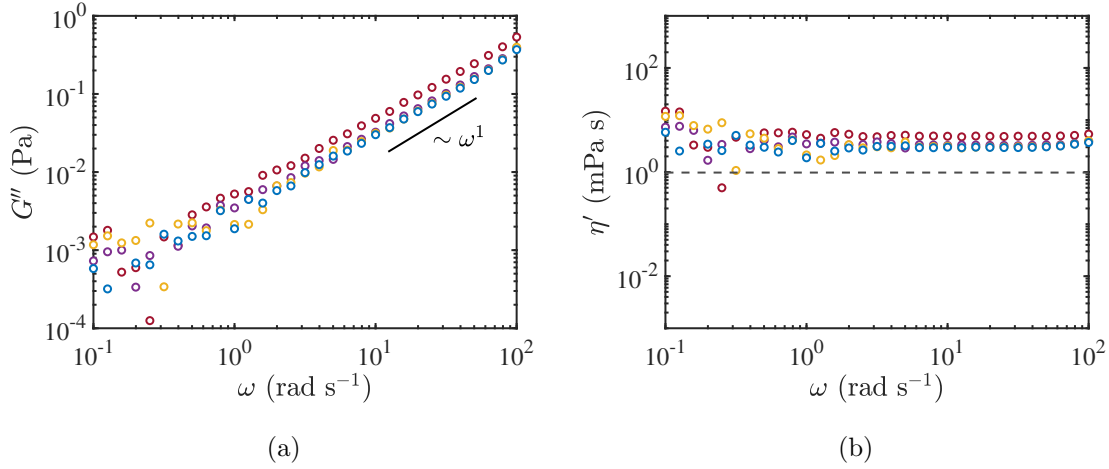


Figure 3.14: (a) Loss modulus and dynamic viscosity (b) spectra for $c = 1.25$ w% 150 kDa PA solutions with varying colloidal silica concentrations 2, 5, 10, and 20 v% (same as Figure 3.13) ($T = 21^\circ\text{C}$). The dashed line shows the viscosity of water at 21°C .

where a is the partial radius, $\dot{\gamma} \lesssim 100 \text{ s}^{-1}$ is the shear rate, η_0 is the polymer-solution shear viscosity, and $k_B T$ is the thermal energy. However, the data with $\phi \geq 0.15$ are better described by Eqn. (3.28), except at the lower bounds of Eqn. (3.27). This might be attributed to error in the volume fraction, the impact of non-hydrodynamic interactions, or the finite size of the polymer chains.

Figure 3.14 shows loss modulus G'' and dynamic viscosity η' spectra for dilute PA/NP suspensions with various NP volume fractions ϕ . The loss modulus has a power-law scaling of the form $G'' \sim \omega^1$ for $\omega = 1\text{--}100 \text{ rad s}^{-1}$, indicating a constant shear viscosity, consistent with

$$\eta' = G''/\omega$$

and the foregoing steady-shear experiments (Figure 3.13). The suspensions do not exhibit any appreciable elasticity, hence the storage modulus G' is negligibly small, below the instrument sensitivity. Despite instrumental noise at low frequencies, the spectra still indicate a Newtonian viscosity over the full frequency range of the rheometer, also pointing to an absence of silica NP clustering.

3.5 Conclusions

Adsorption of polyacrylamide (PA) on silica nanoparticles (NPs) in an aqueous solution was studied. Thermogravimetric (TGA), electrophoretic (ESA), and rheological analyses were used to study the effect of PA on silica stability, structure, and rheological properties. The interaction of polymer molecules, particles, and solvent were studied to understand how these factors may influence their performance as an adsorbent.

The adsorbed amount was measured using TGA for PA molecular weights 40 and 150 kDa, accounting for the amount of non-adsorbed PA in the interstitial voids of the centrifuged solids, assuming random close packing (RCP). Optimal parameters in a modified Langmuir isotherm revealed a strong concentration dependence. Adsorption was higher for the 150 kDa PA, and PA is generally weakly adsorbed onto silica at bulk polymer concentrations in the dilute regime. The adsorbed amount of PA was expectedly lower after subtracting the non-adsorbed amount of PA in the interstitial voids.

At all investigated pH values, the ζ -potential and hydrodynamic diameter of silica with adsorbed PA were higher than for bare silica. The neutral polymer, however, did not contribute significantly to the increase in the ζ -potential, especially at lower pH. The theory of Wang and Hill (2009) was fitted to the dynamic mobility spectra for NPs in PA solution, using the complex viscosity, ζ -potential, and hydrodynamic diameter as fitting parameters. This suggests that PA concentration was low enough to not significantly influence the NP dynamics at MHz frequencies. The polymer contribution to the viscosity obtained from the fitting is small compared to the solvent viscosity.

The double-layer thickness was much smaller than the particle radius, *i.e.*, $\kappa a \gg 1$, but larger than the sum of the hydrodynamic coating thickness and electrophoretic layer thickness. Likewise, κa increases with increasing pH. Due to a significant decrease in effective charge and viscoelastic stress, the coating reduces the mobility magnitude at pH = 9, whereas negligible changes were observed at pH = 3 and 6. Higher absolute values of ζ -potential at pH = 9 indicated that the PA-coated silica is stable, and so subsequent analyses were conducted at this pH.

Steady shear rheological measurements of PA at concentrations ranging from 0.1–10 wt% yielded an overlap concentration $c^* \sim 1.9$ wt%. A viscosity-averaged molecular weight $M = 144$ – 149 kDa from the Mark-Houwink equation compared well with the number-averaged

molecular weight 150 kDa provided by the manufacturer. Fitting the Huggins equation to a plot of reduced viscosity versus concentration yielded the intrinsic viscosity. The resulting Huggins coefficient was $k_H = 0.82\text{--}0.96$, which suggests water is not a good solvent for PA. However, a literature value of the Flory-Huggins χ -parameter for PA in water suggests a theta solvent. Although water easily dissolves PA, according to [Wu and Shanks \(2003\)](#), it cannot be considered a good solvent for PA, which, however, favours adsorption onto silica. This can be attributed to increased intramolecular interactions between the amide groups of PA chains, causing the chains to contract in the solvent.

The addition of 1.25 wt% PA (dilute, unentangled) to colloidal silica shows Newtonian shear rheology at silica volume fractions in the range 2–20 v%. Hydrodynamic interactions at higher NP volume fractions were evident by comparing the reduced shear viscosity with theoretical and semi-empirical formulas for spherical solids in a viscous fluids. The loss modulus spectra of the PA/NP suspensions increased with NP loading and showed a steady-shear viscosity behaviour in the frequency range studied (respecting the Cox-Merz rule).

Appendix

3.A TGA

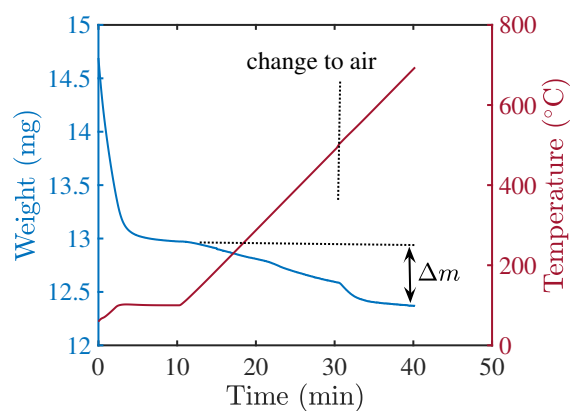


Figure 3.A.1: Raw TGA data for a mixture of 5 wt% PA and 10 v% colloidal silica.

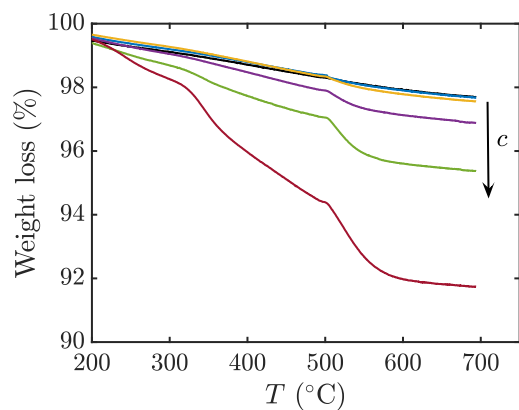


Figure 3.A.2: TGA curves of bare and PA-coated colloidal silica with increasing PA concentration in the range $c = 0\text{--}75 \text{ mg ml}^{-1}$ and silica concentration 10 v%.

3.B Polyacrylamide properties

Table 3.B.1: Polyacrylamide properties from (Du and Hill, 2019a) for molecular weights 150 and (40) kDa.

Characteristic ratio	C_∞	8.5
Bond angle	θ	68°
Repeat unit	l_o	0.154 nm
MW per repeat-unit	M_o	35.6 g mol ⁻¹
Kuhn length	b	1.58 nm
Kuhn MW	M	440 g mol ⁻¹
Radius of gyration	R_g	12 (6.2) nm

Silica nanoparticle cross-linking of polyacrylamide: Linear viscoelasticity

4.1 Preface

Nanocomposite synthesis by physical cross-linking of polymer solutions with NPs is an exciting field of research with a growing number of new technological applications. In this chapter, bare and PA-coated silica NPs are used to cross-link polyacrylamide solutions. The role of silica as a physical cross-linker is studied, spanning a broad range of viscoelastic properties. Time-concentration superposition and time-temperature superposition are used to investigate the microstructure from its rheological response to systematic variations in temperature and polymer and nanoparticle concentration.

Abstract

Nanoparticle (NP)-cross-linked polymer networks have received widespread attention due to their “self-healing” properties, which arise from the junctions having a finite lifetime. These dynamics are desirable for biomedical applications. For example, the solubility and ability to mimic native structures contribute to their use as scaffolds and supports for cell proliferation and migration. Here, we use NP-cross-linked polyacrylamide (PA) to better understand how bare and PA-coated silica NPs influence nanocomposite viscoelasticity over a range of temperatures. Using the principle of time-temperature superposition, dynamic moduli spectra at frequencies $\omega = 0.1$ – 100 rad s^{-1} and temperatures $T = 21$ – 56°C furnish the apparent activation energy for NP junctions. With a silica NP loading 5 v%, pre-PA-coated NPs enhanced the nanocomposite storage modulus relative to their bare NP counterparts by approximately 30%. Bare NPs increased the relaxation time of the polymer by a factor of 4, increasing to a factor of 6 with pre-PA-coating. The temperature-dependent linear

viscoelastic properties of the nanocomposites reveal thermodynamic simplicity and reversibility at low-temperature ranges. Beyond these temperature ranges, the resulting enhanced stiffness and exponential divergence of relaxation time are identified by a phase transformation, indicative of a binary solution having a lower critical transition temperature.

4.2 Introduction

Polymer nanocomposites (PNCs) have gained attention due to the uniqueness of properties arising from the polymer-nanoparticle (NP) interaction, and the ability to tailor these properties by changing the composition. For example, [Haraguchi et al. \(2011b\)](#) added hydrophilic inorganic clay to *N,N*-dimethylacrylamide (DMAA) monomer to produce PNCs by in situ redox-initiated free-radical polymerization in water. This exhibited self-healing, enhanced mechanical properties, and withstood high degrees of deformation, including bending, compression, and elongation ([Haraguchi et al., 2011b](#)). Other unique properties obtainable from PNCs include thermal stability, enhanced barrier properties, increased electrical stability, optical and magnetic properties ([Gao, 2012](#), [Vera et al., 2020](#)). PNCs therefore employed in a wide variety of applications, such as coatings, adhesives, packaging, drug delivery, tissue engineering scaffolds, water treatment, and electronic devices ([Mai et al., 2003](#), [Gao, 2012](#), [Chaurasia et al., 2015](#)). In contrast to studies of chemically cross-linked PA gels, little attention has been given to the effects of time and temperature on the rheological properties of PNCs. Insights from such studies may help to further expand and optimize the application of PNCs.

Rheological characterization of nanocomposites provides valuable insights into the physicochemical interactions between the components, as shown schematically in Figure 4.2.1. Viscoelastic properties provide information about NP dispersion, structure, shear thinning, and phase behaviour. The polymer-polymer interaction is mainly due to chain entanglements and/or cross-linking networks. The particle-polymer interaction can be attributed to bridging polymer chains joined to the particles by several means, one of which is trapped entanglements at the particle-polymer interface ([Isono and Aoyama, 2013](#)). This often leads to an interphase having properties that are different from those of each component. In composites, particle-particle interactions may induce aggregation, as demonstrated for spherical nanoparticles ([Hári and Pukánszky, 2011](#)). One way of controlling aggregation and improv-

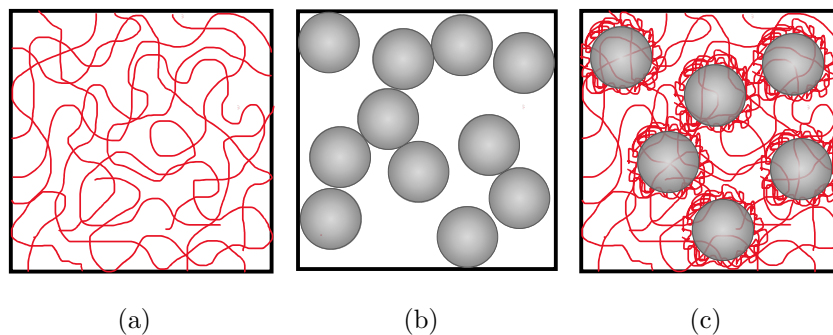


Figure 4.2.1: Schematic representation of (a) polymer network, (b) particle network and (c) polymer-particle network. Adapted from [Isono and Aoyama \(2013\)](#).

ing the colloidal stability is coating the particle surfaces, as achieved in the present study by pre-adsorbing PA onto silica NPs.

[Sujan et al. \(2020\)](#) prepared silica-PA hydrogels and silica-polyacrylic acid (PAA) hydrogels by functionalizing silica NPs with acrylic and amine groups to serve as cross-links in the free-radical polymerization of acrylamide and acrylic acid, respectively. The dual functions of the cross-linker enhanced the mechanical properties relative to chemically cross-linked gels. Their bifunctional cross-linker was capable of forming pseudo-cross-linking and typical covalent cross-linking with PA and PAA ([Sujan et al., 2020](#)). [Yang et al. \(2013\)](#) reported a significant improvement in mechanical properties for PAA nanocomposite hydrogels cross-linked by chemically-modified silica NPs with respect to their bare-NP cross-linked counterparts. They attributed these enhancements to the formation of trapped entanglements and an immobilized glass layer from covalent bonds of adsorbed chains with the NP surface. However, without surface modification, they ascribed the interaction between silica NPs and PAA to hydrogen bonding ([Yang et al., 2013](#)).

Although silica NPs are known to interact weakly with PA ([Bessaies-Bey et al., 2018](#)), they still impart significant changes to polymer viscoelasticity because of the high surface area to volume ratio and size similarity ([Daga and Wagner, 2006](#)). In the present study, bare and PA-coated silica NPs serve as the physical cross-linker for PA nanocomposites. Understanding the flow behaviour, and time and temperature dependence of these composites is becoming increasingly important in many industrial and bioengineering applications. For example, temperature plays a significant role in the hydrophilic/hydrophobic transition of polymers and PNCs used for cell adhesion and detachment ([Haraguchi et al., 2011a](#), [Nagase](#)

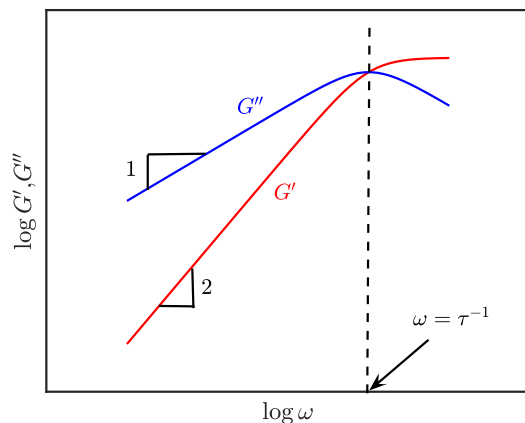


Figure 4.2.2: Maxwell (single-relaxation time) viscoelastic model furnishing dynamic storage G' and loss G'' moduli spectra with power-law regimes $G' \sim \omega^2$ and $G'' \sim \omega^1$ in the terminal region.

et al., 2018). Senses et al. (2015) studied the temperature-dependent dynamic confinement and coupling of silica NPs with an adsorbed layer of high-glass transition temperature (T_g) polymer dispersed in a low- T_g polymer matrix. They reported an unusual thermo-reversible stiffening response that is dependent on the mobility of the high- T_g polymer, driven by large differences in the T_g of the polymers in the interphases. Such properties have application in flexible electronics (Senses et al., 2015).

Many materials behave as liquid or solid, depending largely on the timescale of their deformation. The time-dependent shear properties of polymeric materials have been widely studied. This phenomenon was described by Emri and Gergesova (2010) as resulting from the second law of thermodynamics, which explains why the deformation energy may be stored and dissipated. Polymeric materials are, however, described as viscoelastic, since their time-dependent behaviour lies between purely elastic and purely viscous. For example, Figure 4.2.2 shows the time-dependent storage and loss moduli for dilute polymer solution in the terminal region with $G' \sim \omega^2$ and $G'' \sim \omega^1$ at very long times. The viscoelastic response is usually maintained even with the addition of nanoparticles to form polymer nanocomposites. It is important to probe the effect of mixing linear chain dynamics with colloidal silica of similar size, and to investigate the role of the additional entanglements on the terminal relaxation at different temperatures.

According to [Isono and Aoyama \(2013\)](#), the temperature dependence of viscoelastic polymer materials can be determined from the segmental frictional coefficient of the polymer matrix, and is independent of molecular weight. Thus, particle-polymer interactions and cross-linking and/or entanglement are not expected to affect the temperature dependence of segmental friction ([Isono and Aoyama, 2013](#)). However, [Xu et al. \(2007\)](#) attributed a change of microstructure with respect to temperature in polydimethylsiloxane (PDMS) polymers containing calcium carbonate (CaCO_3) filler to an increase in filler concentration above the critical value. This provided a “pseudo solid-like” behaviour resulting from filler-polymer and filler-filler interactions ([Xu et al., 2007](#)).

The time-temperature superposition (TTS) principle captures the equivalence of changes in frequency and temperature on the rheology of viscoelastic materials. TTS helps determine the thermorheological character ([Choong et al., 2013](#)) by extending spectra, also furnishing an activation energy that sheds light on entanglement/disengagement ([Du and Hill, 2019a](#)). A TTS master curve is obtained by superposing rheological properties at varying frequencies (reciprocal deformation times) and temperatures relative to a reference temperature. This is achieved through the application of shift factors. A horizontal shift factor results from the temperature dependence of relaxation times, relative to a reference temperature, while a vertical shift factor results from the temperature dependence of viscoelastic properties arising from a change in sample density with respect to temperature ([Rubinstein and Colby, 2003](#)).

The present study investigates the interactions of silica NPs and PA to understand how they may affect the temperature-dependence of rheological properties, the homogeneity of the polymer/NP network, and the reversibility of the rheological properties with respect to temperature. Accordingly, the temperature dependence of the rheological properties in the linear viscoelastic regime were measured. These materials were synthesized by in situ free-radical polymerization of acrylamide with/without silica NPs (bare and PA-coated). The role of silica as a physical cross-linker on the rheology of the pure polymer was investigated. It is not known a priori how the coating of silica with PA would affect the viscoelasticity of the nanocomposites. Cole-Cole and Han plots provide new insights into the miscibility and relaxation times at higher temperatures. The effects of varying monomer concentration on the relaxation modes using time-concentration superposition (TCS) were explored. TCS, similarly to TTS, extends the frequency range of the experiments by shifting spectra with respect to changes in concentration ([Sun et al., 2012](#)), thus assuming that NP concentration

controls micro-structural relaxation times in a similar manner to temperature. The rheological properties are characterized using temperature sweeps and TTS analysis, furnishing apparent activation energies.

4.3 Materials and methods

Acrylamide (AAm) solution (40 w/v%, Fisher Scientific, U.S.A.), ammonium persulfate (APS) powder ($\geq 98\%$, Fisher Scientific, U.S.A.) and N,N,N',N' -tetramethylethylenediamine (TEMED, 99%, GE Healthcare Life Science, Germany) are monomer, initiator and catalyst, respectively. Silica NPs, available as Ludox[®] TM50 (50 w% colloidal suspension, Sigma-Aldrich Inc., U.S.A.) with diameter $d \approx 30$ nm, serve as a physical cross-linker. All were used as provided by the manufacturers. Polyacrylamide (PA)-coated silica NP dispersions, as prepared and characterized in Chapter 3, containing 1.25 w/v% PA and 5 w/v% colloidal silica (Ludox[®] TM50) were used as a physical cross-linker.

Three series of samples were synthesized: (i) solutions of free-radical polymerized acrylamide having concentrations $c_a \approx 0.7 \text{ mol l}^{-1}$ (5 w/v%), 1.1 mol l^{-1} (8 w/v%) and 1.4 mol l^{-1} (10 w/v%); (ii) solutions of free-radical polymerized acrylamide with bare silica NPs as the physical cross-linker; and (iii) PA-coated silica NPs serving as the physical cross-linker. The polymerized acrylamide samples are identified as A_x , where x is the concentration of acrylamide monomer (w/v%) in the pre-gel solution; NP-cross-linked samples are identified as A_xN_y and A_xC_y for bare and PA-coated NPs, respectively. Subscripts y identify NP volume fraction based on the total volume of the pre-gel solution.

Nanoparticle cross-linked polyacrylamide gels were synthesized by mixing AAm, 10 μl of freshly prepared APS solution, bare silica NP suspension or PA-coated silica NP dispersion, and reverse-osmosis (RO) water (Type 1, $\sigma \approx 5.6 \mu\text{S m}^{-1}$, $\Omega \approx 18 \text{ MOhm cm}$ at $T = 25^\circ\text{C}$) in a centrifuge tube, such that the final bare silica (or PA-coated silica) concentration in the pre-gel solution was ≈ 5 w/v% for all samples. Pure polyacrylamide (PAAm) solutions were synthesized without adding NPs. Nitrogen gas was bubbled through the mixtures for 5 min to remove dissolved oxygen, which inhibits the polymerization, before adding 3 μl TEMED per ml of total pre-gel solution.

Bare silica NPs (5 w/v%) and PA-coated silica NPs were characterized using an Acous-

Table 4.3.1: ζ -potential, acoustic-attenuation diameter, conductivity and pH of bare and PA-coated silica NPs dispersed in reverse-osmosis water (Type 1, $\sigma \approx 5.6 \mu\text{S m}^{-1}$, $\Omega \approx 18 \text{ MOhm cm}$ at 25°C) at $\approx 21^\circ\text{C}$. These were measured using an AcoustoSizer II instrument (Colloidal Dynamics LLC, USA).

	Bare SiO ₂	PA-coated SiO ₂
ζ -potential (mV)	-114.0 ± 0.2	-98.0 ± 0.7
Diameter d_{50} (nm)	28.0 ± 0.5	35.0 ± 0.5
Conductivity (mS cm^{-1})	0.65 ± 0.03	0.69 ± 0.03
pH	9.0	9.0

toSizer II instrument (Colloidal Dynamics LLC, U.S.A.). The hydrodynamic diameter $d \approx 28 \text{ nm}$ measured using the acoustic-attenuation sizing capability of this instrument is consistent with $d = 27 \text{ nm}$ reported by (Adibnia et al., 2017a) using the same instrument, also agreeing with diameters from scanning electron microscopy ($d \approx 29 \text{ nm}$) (Rose et al., 2013) and dynamic light scattering ($d \approx 30 \text{ nm}$) (Bhosale et al., 2011). The ζ -potential, acoustic-attenuation diameter, conductivity and pH for these bare and PA-coated silica NPs at $\approx 21^\circ\text{C}$ are summarized in Table 4.3.1.

4.3.1 Rheology

Rheological properties were measured using an ARES-G2 rheometer (TA Instruments, U.S.A.) with parallel-plate geometry under oscillatory shear. Pregel mixtures were pipetted directly onto the bottom plate, and the 25 mm diameter top plate was carefully lowered so that the gap between the plates was 0.5 mm. An “evaporation blocker” provided by the manufacturer, and silicone oil were used to minimize evaporation. The following experiments were conducted sequentially: a time-sweep experiment, where the gelation kinetics were monitored at 21°C with angular frequency $\omega = 10 \text{ rad s}^{-1}$ and strain amplitude $\gamma = 0.2$. At steady-state, a frequency-sweep in the range $\omega = 0.1\text{--}100 \text{ rad s}^{-1}$ was undertaken with $\gamma = 0.2$ at temperatures from 21 to 56°C in increments of 2.5°C . Temperature was controlled using a thermoelectric chiller (ThermoCube 300, Solid State Cooling Systems) attached to the rheometer. All measurements were repeated on $n = 3$ separately prepared samples, subsequently averaged. The sample-averaged data were reported and in some figures the error

bars were provided. The error bars represent standard error σ/\sqrt{n} , where σ is the sample standard deviation.

4.4 Results and discussion

4.4.1 Polymerization time series

Time series of the storage G' and loss G'' moduli during polymerization for various monomer concentrations (increasing from top to bottom) at $T \approx 21^\circ\text{C}$ are shown in Figure 4.4.1. The samples share the same qualitative behaviour: moduli increase rapidly during the early stage and reach a steady-state plateau. The physically cross-linked samples (red and green) have higher storage and loss moduli than the polymer solutions (blue), and the extent to which the moduli increase varies with the monomer concentration and whether the NPs are bare or PA-coated. For example, with $c_a \approx 1.4 \text{ mol l}^{-1}$, 5% bare NP loading increases G' by $\approx 89\%$ and G'' by $\approx 35\%$, whereas 5% PA-coated NP loading increases G' by $\approx 143\%$ and G'' by $\approx 62\%$. Such increases reflect entanglements and cross-links increasing the resistance to flow.

The stiffening of physically cross-linking polymer solutions with increasing NP loading is in qualitative agreement with hydrogel nanoparticle composites (HNC) for which chemical (bisacrylamide) and physical cross-linking (silica NPs) are active (Adibnia et al., 2017b). Adibnia et al. (2017b) noted an increase in G' by two orders of magnitude for lightly chemically cross-linked PAAm with varying NP loadings $\leq 20 \text{ v}\%$. In the absence of NPs, Du and Hill (2019a) observed a systematic increase in G' for DNA-only cross-linked gels when varying the DNA-cross-linker ratio with $c_a \approx 1.4 \text{ mol l}^{-1}$ (similar to those reported here), whereas G'' was independent of the DNA-cross-linker ratio.

The visual appearance of the samples with monomer concentration $c_a \approx 1.4 \text{ mol l}^{-1}$ after 6 hours at $T \approx 21^\circ\text{C}$ are shown in Figure 4.4.2. Silica NP loading changes the solutions from clear and colourless to a thick, cloudy white paste. The as-provided Ludox[®] TM50 colloidal silica is a cloudy dispersion of silica particles. Flow behaviour, observed by inverting the vials, revealed the PAAm sample immediately flowing freely, whereas the samples containing bare and PA-coated NPs maintained their solid-like state for several days. This again reflects the role of NPs in increasing the viscosity and stiffness. After a week of observation in the

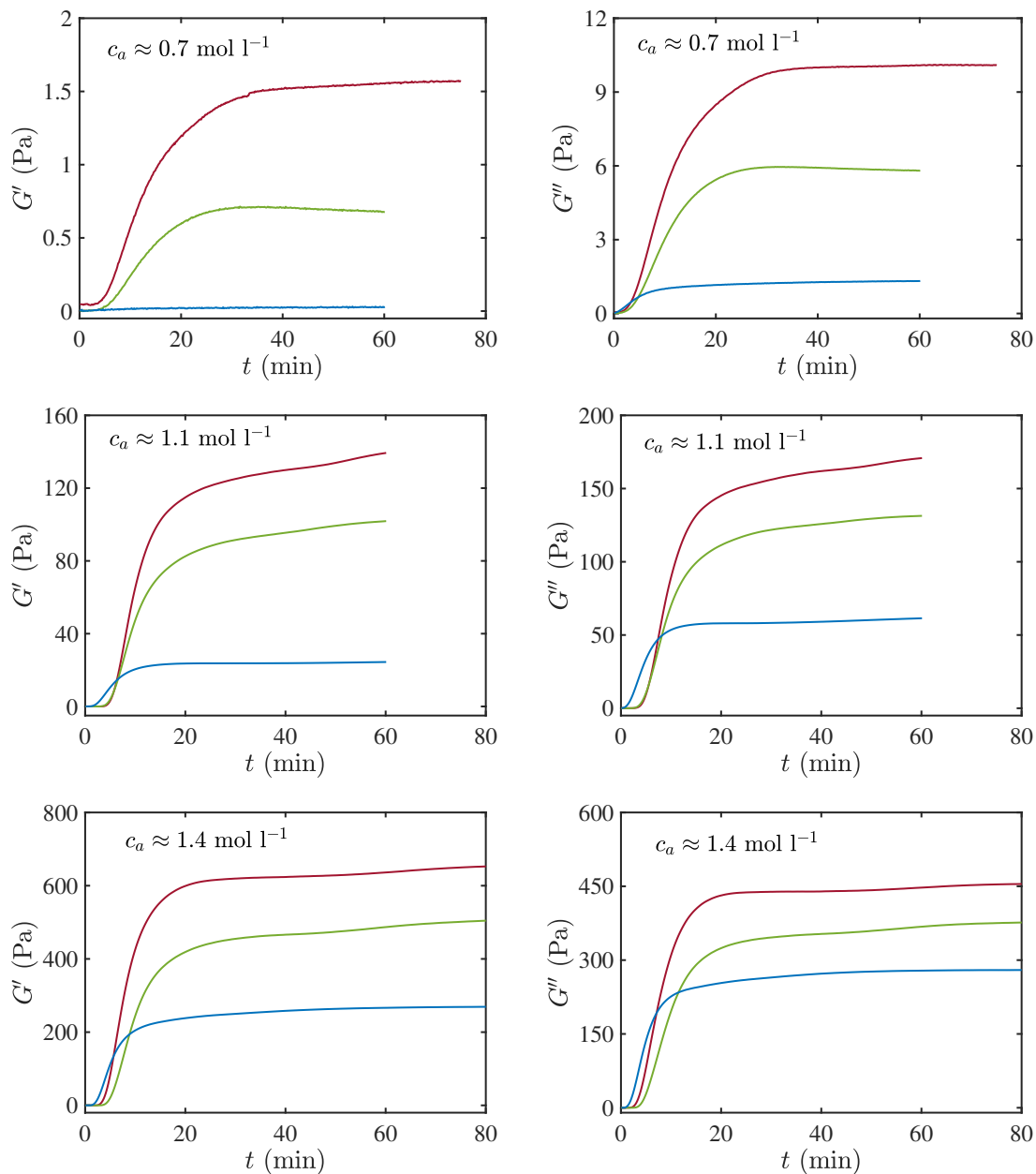


Figure 4.4.1: Storage (left) and loss (right) moduli time series during polymerization at $\omega \approx 10 \text{ rad s}^{-1}$ and $\gamma \approx 0.2$ for samples A_x (blue), A_xN_5 (green) and A_xC_5 (red) at $T \approx 21^\circ\text{C}$. Subscripts x identify the monomer concentrations in w/v% ≈ 5 (0.7 mol l^{-1}), 8 (1.1 mol l^{-1}) and 10 (1.4 mol l^{-1}), as indicated in each panel.



Figure 4.4.2: Samples A_{10} , $A_{10}N_5$ and $A_{10}C_5$ after degassing and polymerization, stored in airtight glass tubes at 21°C .

inverted position, deformation or flow of the nanocomposite samples as seen with the naked eye were very minimal. The yielding process is very slow under gravity. The nanocomposite gels, despite appearing solid like, dissolved in water, forming a thin film at the bottom of the glass tube. This property has found use in some agricultural applications, such as soil surface coating to prevent or reduce erosion (Lentz et al., 1996, Sojka and Lentz, 1997, Sojka et al., 1998).

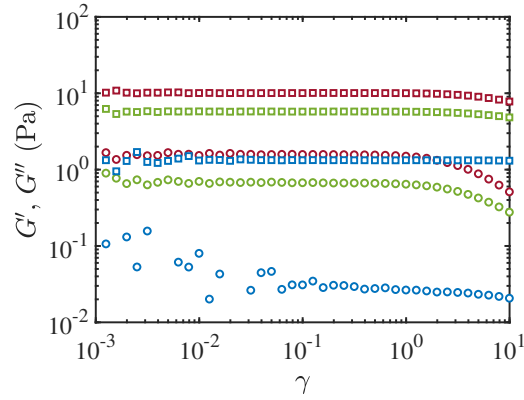
The effects of bare and PA-coated silica NPs on the viscoelastic rheology as a function of strain amplitude are shown in Figure 4.4.3. At higher γ , the moduli deviate from linearity, identified as the independence of storage and loss moduli as a function of strain. The value of γ at which this deviation occur for each samples is different.

4.4.2 Complex viscosity spectra

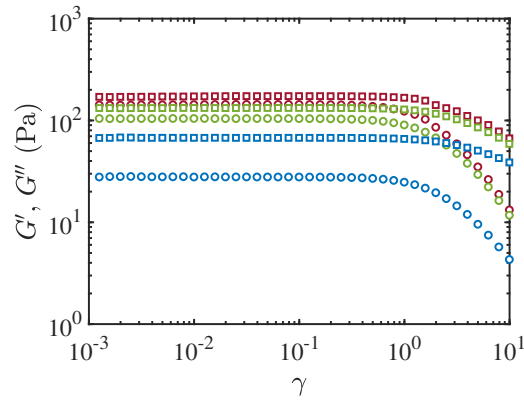
Strain-controlled frequency sweeps were conducted at temperatures in the range $21\text{--}56^\circ\text{C}$ with strain amplitude $\gamma \approx 0.2$ in the linear-viscoelastic regime. The complex viscosity is

$$\eta^*(\omega) = \eta' - i\eta'', \quad (4.1)$$

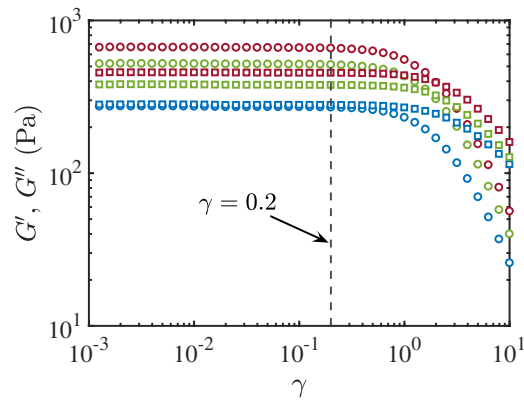
where $\eta' = G''/\omega$ and $\eta'' = G'/\omega$. Spectra of the complex viscosity magnitude $|\eta^*|$ are shown in Figure 4.4.4 at temperatures 21 and 51°C . As to be expected from the dynamic moduli time series above, NP loading increases $|\eta^*|$. However, in striking contrast to the monodisperse 150 kDa PA solutions in Chapter 3, which were Newtonian with a steady-shear viscosity $\eta \approx 0.2 \text{ Pa s}$ at PA concentration $c \approx 10 \text{ wt}\%$, these PAAm solutions are notable



(a) $c_a = 0.7 \text{ mol l}^{-1}$



(b) $c_a = 1.1 \text{ mol l}^{-1}$



(c) $c_a = 1.4 \text{ mol l}^{-1}$

Figure 4.4.3: Storage (circles) and loss (squares) moduli versus strain amplitude at $\omega \approx 10 \text{ rad s}^{-1}$ for samples A_x (blue), A_xN_5 (green) and A_xC_5 (red) at $T \approx 21^\circ\text{C}$. Subscripts x identify the monomer concentrations in $w/v\% \approx 5$ (0.7 mol l^{-1}), 8 (1.1 mol l^{-1}) and 10 (1.4 mol l^{-1}), as indicated in each panel. The strain amplitude $\gamma \approx 0.2$ is used to define a linear viscoelastic regime for experiments reported here.

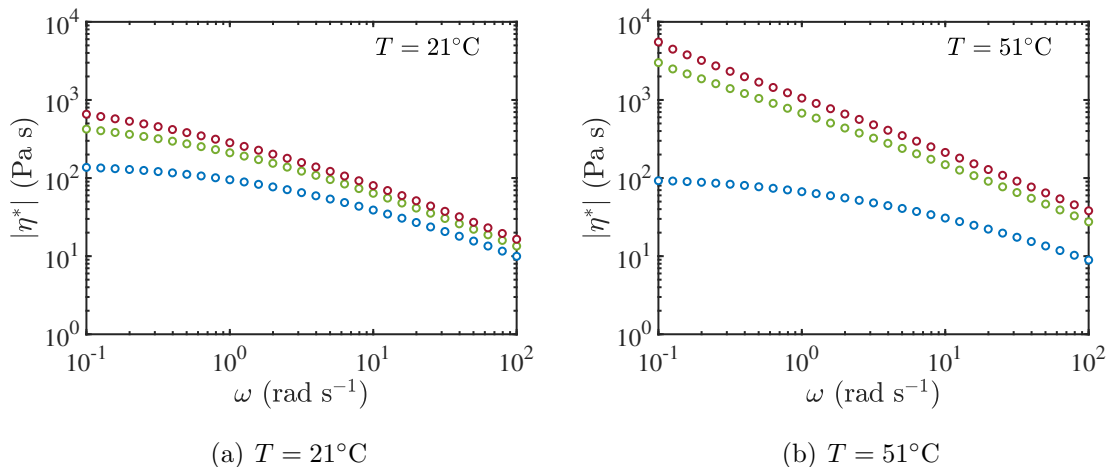


Figure 4.4.4: Complex viscosity $|\eta^*|$ spectra at $T = 21$ and 51°C for PAAm sample A_{10} (blue), and silica NP loaded PAAm samples $A_{10}N_5$ (green) and $A_{10}C_5$ (red). $\gamma \approx 0.2$ in the linear viscoelastic regime.

shear thinning, and the viscosity *increases* significantly with silica NP loading, particularly at the higher temperature. Whereas silica NPs in 150 kDa PA solutions behaved as passive spherical fillers, increasing the shear viscosity a small $O(\phi) \ll 1$ amount, here they may enhance the viscosity by more than an order of magnitude, depending on the shear rate and temperature. For example, with $c_a = 10$ w/v%, $|\eta^*| \approx 100$ Pa s at $\omega = 0.1$ rad s^{-1} , increasing to $|\eta^*| \approx 3000$ Pa s with the addition of only 5 w/v% silica NPs.

Note that increasing the temperature and adding NPs appear to shift the spectra to the left along the frequency axis, as expected by increasing the relaxation time, while simultaneously shifting the spectra upward along the shear viscosity axis, as might be achieved by increasing the effective cross-link number density. Therefore, increasing the temperature and NP-loading slow the relaxation and increase the entanglement density. Note that the relaxation slows even though an increase in temperature decreases the solvent viscosity, reducing polymer-solvent friction, and, therefore, facilitating chain relaxation.

Overall, the foregoing observations suggest that the in situ free-radical polymerization leads to a much higher molecular weight compared to the 150 kDa PA solutions in Chapter 3, placing the solutions in an entangled regime. The much higher molecular weight may also increase the entropic driving force for polymer chains to adsorb onto the silica NPs, all increasing the number of chains taking part in physical cross-links and slowing the relaxation.

A consequence of these may be the formation of star-like structures with NPs as the centres. Such structures have exponentially diverging relaxation times, and plausibly explaining the large increases in shear viscosity with NP loading, possibly enhanced by polymer-coil expansion as the polymer-solvent and polymer-NP interaction energies vary with temperature. These inferences will be tested below by turning to dynamic moduli, and time-concentration and time-temperature superposition.

The nanocomposites with bare and PA-coated silica exhibit stronger shear thinning than the neat polymer over the entire frequency range. This behaviour can be analyzed using the power-law model (Shaw, 2011):

$$|\eta^*| = K\omega^{n-1}, \quad (4.2)$$

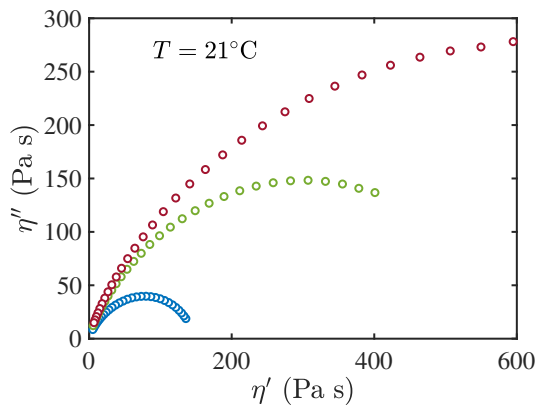
where n is the flow behaviour index or relaxation exponent, and K is the flow consistency index. These parameters were obtained by fitting the power-law model to the data in Figure 4.4.4 in the low- and high-frequency ranges. The values of n and K are provided in Tables 4.4.1. These confirm power-law scaling $|\eta^*| \sim \omega^{-2/3}$ at high frequency.

The complex viscosities of the polymer solution and nanocomposites were further examined using Cole-Cole plots (Cole and Cole, 1941) of the η'' versus η' , as shown in Figure 4.4.5. These have been used to interpret the partial miscibility of polymer blends (Chen et al., 2013, Hoseini et al., 2017). A smooth and semicircular curve identifies monodisperse homogeneous microstructures (indicating compatibility), otherwise reflecting phase separation. Hári and Pukánszky (2011) used such observation to interpret the effect of composition on network formation in a polymer/layered silicate nanocomposite. Increasing the polymer content up to ≈ 20 v% increased the viscosity and changed the shape of the Cole-Cole plot, suggesting the formation of silicate networks.

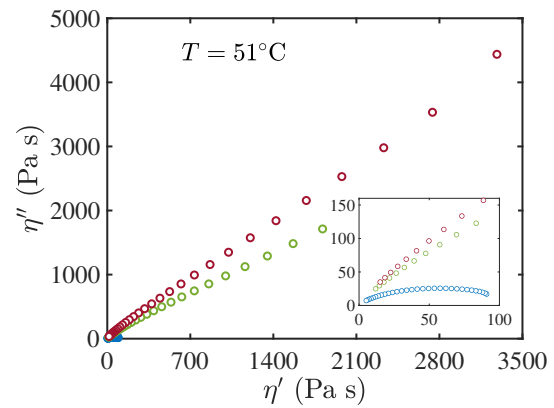
As shown in Figure 4.4.5(a), the Cole-Cole plots at $T = 21^\circ\text{C}$ for the neat polymer and the nanocomposites are smooth and semi-circular, suggesting miscibility and compatibility of the polymer and silica NPs. The semi-circle diameter increases with NP loading, confirming an increase in the relaxation time. As confirmed by Figure 4.4.5(b), at $T = 51^\circ\text{C}$, the effect of temperature is not significant on the neat polymer. Whereas the nanocomposites at 21°C present semi-circles, indicating miscibility, at 51°C the very weak curvature indicates an heterogeneous two-phase mixture, suggesting a liquid-liquid phase separation and very long relaxation times. Indeed, these samples appeared more cloudy with a notably inhomogeneous texture.

Table 4.4.1: Fitting parameters for the power-law model [Eqn. (4.2)] for the neat polymer solutions and nanocomposites shown in Figure 4.4.4 in the specified temperature and angular frequency ω range.

Sample	ω (rad s ⁻¹)	K (Pa s ^{n})	n	R^2
$T = 21^\circ\text{C}$				
A ₁₀	0.1–0.3	109.8	0.90	0.991
	10–100	157.2	0.41	0.998
A ₁₀ N ₅	0.1–0.3	247.8	0.77	0.997
	10–100	310.5	0.32	0.999
A ₁₀ C ₅	0.1–0.3	324.4	0.69	0.999
	10–100	397.4	0.31	0.999
$T = 51^\circ\text{C}$				
A ₁₀	0.1–0.3	77.6	0.92	0.967
	10–100	109.8	0.46	0.997
A ₁₀ N ₅	0.1–100	664.0	0.33	0.999
A ₁₀ C ₅	0.1–100	1054.9	0.29	0.999



(a) $T = 21^\circ\text{C}$



(b) $T = 51^\circ\text{C}$

Figure 4.4.5: Cole-Cole plots accompanying Figure 4.4.4.

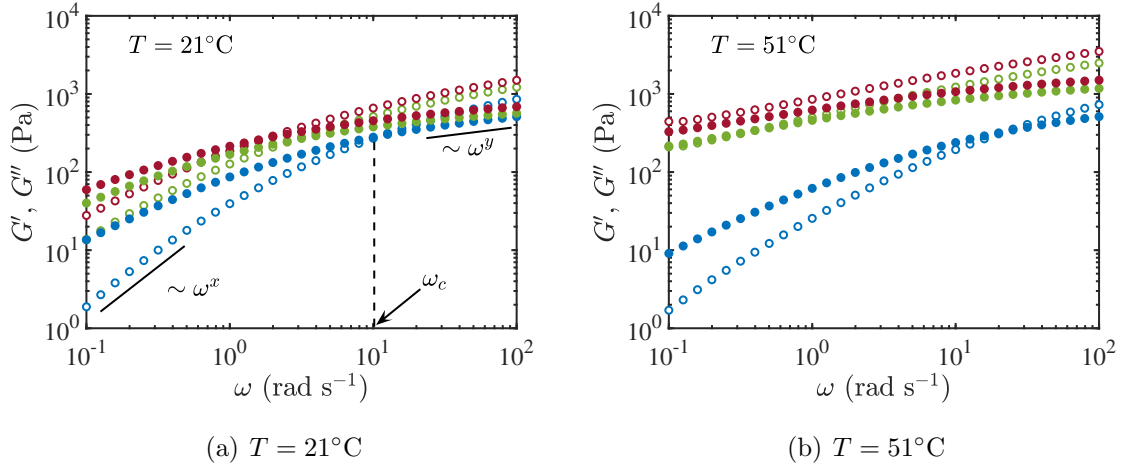


Figure 4.4.6: Storage (open) and loss (filled) moduli spectra accompanying Figure 4.4.4.

4.4.3 Dynamic moduli spectra

The storage and loss moduli spectra of the neat polymer and nanocomposites are shown in Figure 4.4.6 at 21 (a) and 51°C (b). All the samples at $T = 21^\circ\text{C}$ are demonstrated to be viscoelastic liquids with $G'' > G'$ at low frequency, crossing over to solid-like rheology at high frequency with $G'' < G'$. At $T = 51^\circ\text{C}$, however, the cross-over frequency of the nanocomposites almost vanishes (in the available frequency range) for the bare silica NP sample, and completely vanishes for the PA-coated silica NP sample. The cross-over frequency, identified in Figure 4.4.6(a) by $\omega_c = 1/\tau$, where τ is termed the terminal relaxation time, shifts to lower frequencies with NP loading, as previously suggested when interpreting the dynamic viscosity spectra above. Note that parallel storage and loss moduli spectra are a rheological hallmark of a percolation threshold (Adibnia and Hill, 2016). For the PA-coated silica NP sample in Figure 4.4.6(b) (red), $G' \sim G'' \sim \omega^{1/3}$, which is considerably smaller than the value obtained by Adibnia and Hill (2016) for cross-linking of polyacrylamide hydrogels ($\approx 0.68 \pm 0.05$). However, the exponent is not universal, because it reflects the cross-linking mechanism underlying the the percolating cluster at the threshold.

More generally, slope of the dynamic moduli spectra varies over the entire frequency range. These were quantified by fitting power-laws ω^x and ω^y at low and high frequency. The exponents, crossover modulus G_c , and cross-over time τ are provided in Table 4.4.2.

Exponents at low frequency for all three samples at $T = 21^\circ\text{C}$ furnish $G' \sim \omega^{0.9-1.3}$ and

Table 4.4.2: Power-law fitting parameters for the neat polymer solutions and nanocomposites in Figure 4.4.6(a) at $T \approx 21^\circ\text{C}$, where G' or $G'' \sim \omega^x$ at low frequency and G' or $G'' \sim \omega^y$ at high frequency.

	τ (ms)	G_c (Pa)	G'			G''				
			x	R^2	y	R^2	x	R^2	y	R^2
A ₁₀	87	292	1.48	0.999	0.50	0.995	0.88	0.999	0.26	0.990
A ₁₀ N ₅	345	247	1.09	0.999	0.37	0.996	0.71	0.999	0.17	0.990
A ₁₀ C ₅	556	269	0.91	0.999	0.36	0.997	0.63	0.999	0.18	0.994

$G'' \sim \omega^{0.6-0.9}$. Exponents at lower frequencies for the PA-coated nanocomposite are similar to those obtained for weak chemically cross-linked PA gels with bis to acrylamide ratio of 0.1 mmol mol⁻¹, reported by [Du and Hill \(2019b\)](#) as $G' \sim \omega^{0.77}$ and $G'' \sim \omega^{0.61}$. [Du and Hill \(2019b\)](#) attributed these lower exponents (as compared to the single-relaxation time Maxwell model), to chain relaxation being hindered by chemical cross-linking. Thus, silica NPs in this context, appear to play a similar role to chemical cross-linker, with physical cross-linking promoting entanglements from hydrogen bonding between polymer and NPs ([Jia et al., 2019](#)).

The dynamic moduli spectra are further interpreted using Han plots of G' versus G'' , as shown in Figure 4.4.7 at $T = 21$ and 51°C . The Han plot was originally proposed by [Han and Chuang \(1985\)](#) to investigate the rheological miscibility of polymer blends. This yields linear and temperature-independent correlations for homogeneous microstructures ([Han and Chuang, 1985](#), [Chen et al., 2013](#)). [Hoseini et al. \(2017\)](#) employed the technique to investigate the effect of increasing silica loading on miscibility of two immiscible polymers. Compatibility required the logarithmic slopes obtained from each plot to be independent of the NP volume fraction, furnishing exponents/slopes ≈ 2 for a monodisperse polymer ([Chen et al., 2013](#)). As shown in Figure 4.4.7, bare and PA-coated silica NPs do not significantly influence the slope ≈ 2 of the neat polymer solution at $T = 21^\circ\text{C}$, but there is a notable departure at 51°C , consistent with inferences drawn from the Cole-Cole analysis.

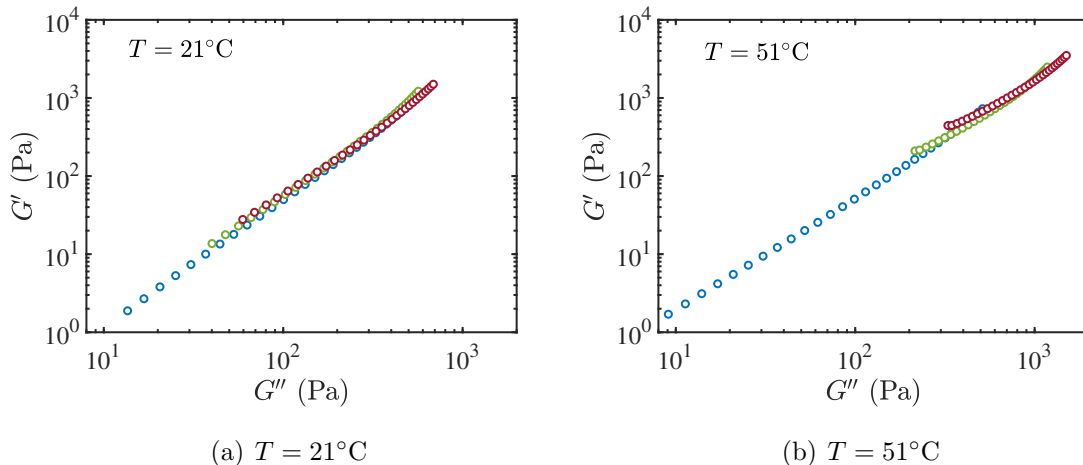


Figure 4.4.7: Han plots accompanying Figure 4.4.4.

4.4.4 Time-concentration superposition

Storage and loss moduli spectra for samples A_x , A_xN_5 and A_xC_5 with monomer concentration x ranging from 3 to 10 w/v% at 21°C are shown in the left panels of Figure 4.4.8. The power-law exponent for $G'' \sim \omega^n$ at low frequencies ranges from 0.88–1 for sample A_x , 0.71–1 for sample A_xN_5 , and 0.63–1 for sample A_xC_5 . Horizontal and vertical shifting of the spectra produces the spectra in right panels of Figure 4.4.8, hereafter referred to as time-concentration superposition (TCS) (Daga and Wagner, 2006, Larsen and Furst, 2008, Adibnia and Hill, 2017).

The horizontal and vertical shift factors (a , b) may be correlated with changes in τ and G_c according to scaling relations of the form $a \sim \tau$ and $b \sim G_c^{-1}$ (Adibnia and Hill, 2017). Here, the spectra are manually shifted relative to the sample with $c_a \approx 10$ wt%, which has a well defined cross-over τ and G_c . The shift factors a and b are plotted versus the monomer concentration c_a in Figure 4.4.9, similarly to Adibnia and Hill (2017) for silica NP-filled PA solutions with varying NP volume fraction. Their shift factors a and b were found to depend exponentially and linearly on the silica volume fraction, respectively, qualitatively similar to the shift factors in Figure 4.4.9. As seen in table 4.4.3, c_1 and c_2 for the nanocomposites are equal, showing that the PA pre-coating does not affect the relaxation time. However, the PA pre-coating has a significant impact on the vertical shift (c_3 and c_4).

The shift factors for the PA solutions (A_x , top panel, Figure 4.4.8) may be correlated using

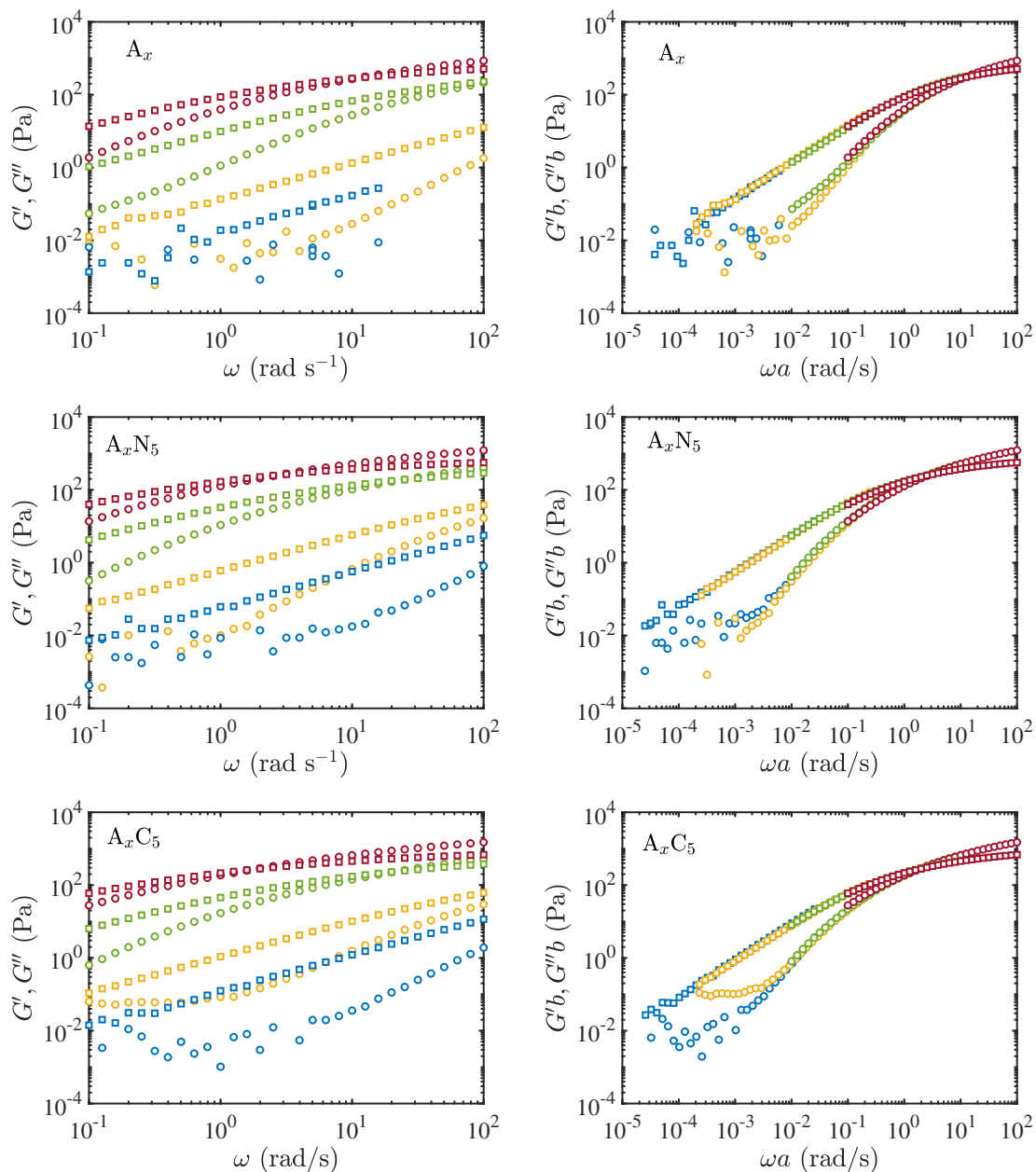


Figure 4.4.8: Left: Storage (circles) and loss (square) moduli spectra of samples A_x , A_xN_5 and A_xC_5 with $c_a = 3, 5, 8, 10$ w/v% (blue, yellow, green, red) at $T = 21^\circ\text{C}$. Right: TCS spectra referenced to the sample with $c_a = 10$ w/v% (red).

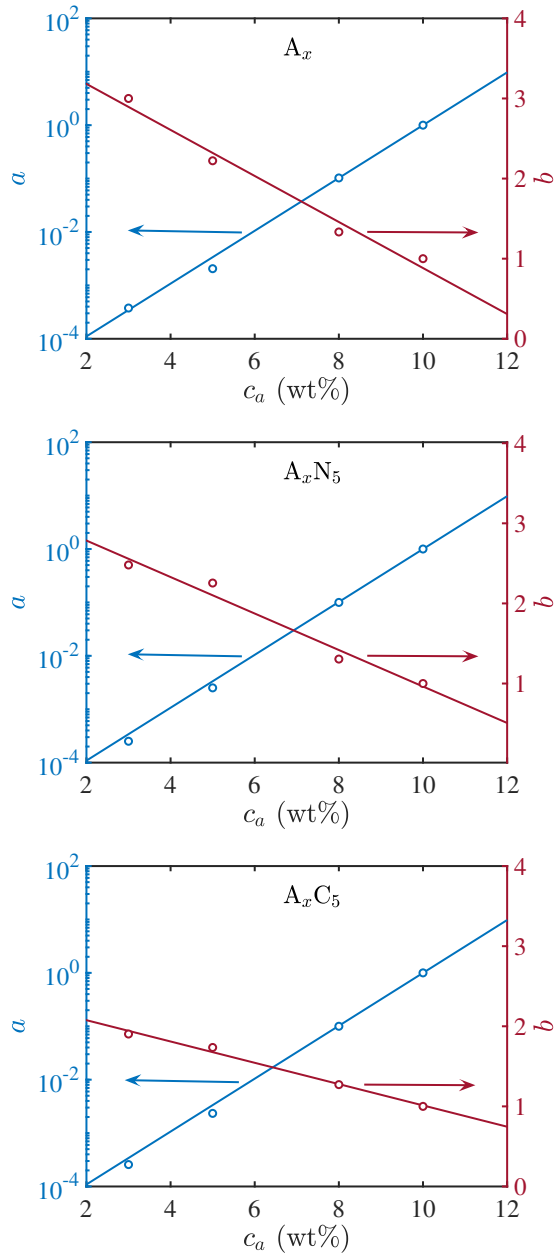


Figure 4.4.9: Horizontal a (blue) and vertical b (red) shift factors versus monomer concentration c_a (wt%) from dynamic moduli spectra in Figure 4.4.8. Lines are fits $a = c_1 e^{c_2 x}$ and $b = c_3 x + c_4$ with $x = c_a$, where the fitting parameters c_1 – c_4 are in table 4.4.3.

Table 4.4.3: Fitting parameters for the lines in Figure 4.4.9. Shift factors $a = c_1 e^{c_2 x}$ and $b = c_3 x + c_4$ with $x = c_a$.

Samples	$c_1 (\times 10^{-6})$	c_2	R^2	c_3	c_4	R^2
A_x	9.00	1.15	0.999	-0.287	3.76	0.980
$A_x N_5$	7.00	1.19	0.999	-0.228	3.24	0.972
$A_x C_5$	7.00	1.19	0.999	-0.133	2.34	0.990

a power-law scaling, as shown in Figure 4.4.10(a). This permits a direct comparison with the scaling for ideal Gaussian chains from [Baumgärtel and Willenbacher \(1996\)](#): $a \sim c^{3.5}$, $b \sim c^{-2.2}$, where c is the polymer concentration. From the data and power-law fits in Figure 4.4.10, the shift factors for samples A_x are

$$a \sim c_a^\alpha = 1.5 \times 10^{-7} c_a^{6.6} \text{ and } b \sim c_a^\beta = 8.7 c_a^{-0.9}. \quad (4.3)$$

[Daga and Wagner \(2006\)](#) attributed differences in the scaling exponents to solvent quality, furnishing $\alpha = 4.2$ and $\beta = -0.72$ from TCS from poly(ethylene oxide)(PEO)-water solutions with varying PEO concentrations 2.2–6.5 wt% at $T = 25^\circ\text{C}$. More importantly, the difference $\alpha - \beta = 4.92$ was related to the scaling exponent for the concentration dependence of the zero shear viscosity $\eta_0 \propto c^\delta$ with $\delta = 5.0$. Similarly, for PA samples A_x , the power-law exponent from the plot of η_0 versus c_a at $T = 21^\circ\text{C}$ in Figure 4.4.10(b) is

$$\delta = 7.45 \pm 1.12,$$

which compares very well with

$$\alpha - \beta = 7.48 \pm 1.15$$

from Eqns. (4.3).

The larger scaling exponent for a ($\alpha = 6.57 \pm 1.04$, Eqn. (4.3)) compared to ideal solutions (3.5) can be related to specific interactions within the polymer segment limited by hydrogen bonding, increasing molecular friction as the polymer concentration increases ([Daga and Wagner, 2006](#)). Moreover, the difference of scaling exponent for b ($\beta = -0.91 \pm 0.11$, Eqn. (4.3)) compared to ideal solutions (-2.2) can be explained as a weak concentration dependence of the plateau modulus, which [Daga and Wagner \(2006\)](#) related to solvent quality, approaching the theta condition with increasing polymer concentration for PEO-water solutions, which reduces the coil size, so that additional polymer has no effect on chain overlap.

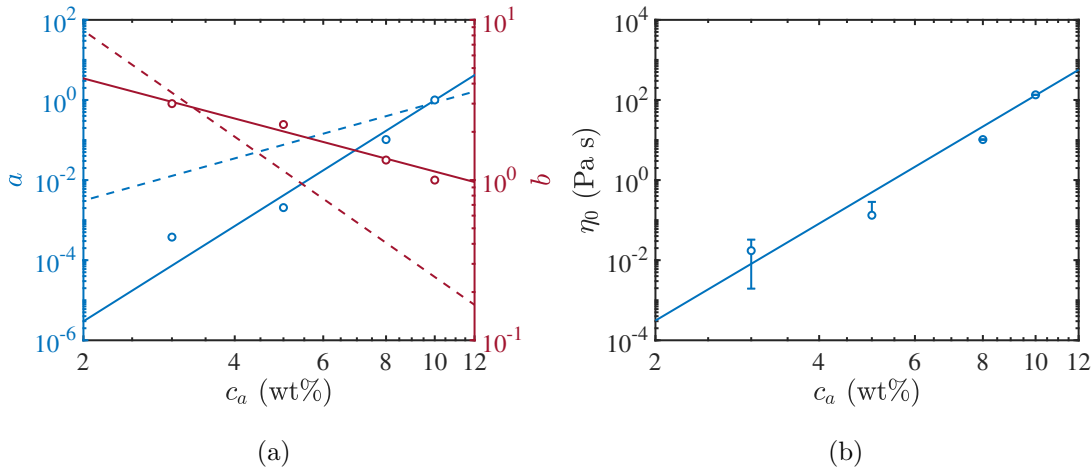


Figure 4.4.10: (a) Horizontal and vertical shift factors versus monomer concentration for PA samples A_x from TCS in Figure 4.4.8. Solid lines are power-law fits [Eqns. (4.3)] and dashed lines are the scaling for ideal solutions (Baumgärtel and Willenbacher, 1996). (b) Zero-shear viscosity versus monomer concentration for samples A_x at $T = 21^\circ\text{C}$. Data from averaging $|\eta^*(\omega)|$ as $\omega \rightarrow 0$. Line is $\eta_0 = 2 \times 10^{-6} c_a^{7.45}$, $R^2 = 0.9873$. Error bars are the standard error of the mean.

Daga and Wagner reported water to be a good solvent for PEO at 25°C with Flory-Huggins interaction parameter $\chi = 0.12$ at 30°C for PEO concentration (MW = 2.3 kDa) in the range 5–40 wt%. This is significantly smaller than that for PA in water at infinite dilution: e.g., $\chi = 0.495$ at 25°C (Day and Robb, 1981) and $\chi \approx 0.484$ – 0.487 at $T \approx 22.5^\circ\text{C}$ (Du and Hill, 2019a).

4.4.5 Time-temperature superposition

The storage and loss moduli spectra for the polymer solution and its nanocomposites at temperatures from $T = 21$ to 56°C are shown in the left panels of Figures 4.4.11 and 4.4.12. The top panel for the neat polymer sample A_{10} confirms conclusions drawn from Figures 4.4.4–4.4.7 that the moduli have a weak dependence on temperature. For the nanocomposites $A_{10}N_5$ and $A_{10}C_5$, however, the moduli *increase* by more than an order of magnitude.

The TTS function of the Trios software (TA Instruments), referenced to $T_0 = 21^\circ\text{C}$, produce the TTS spectra in the right panels of Figures 4.4.11 and 4.4.12.

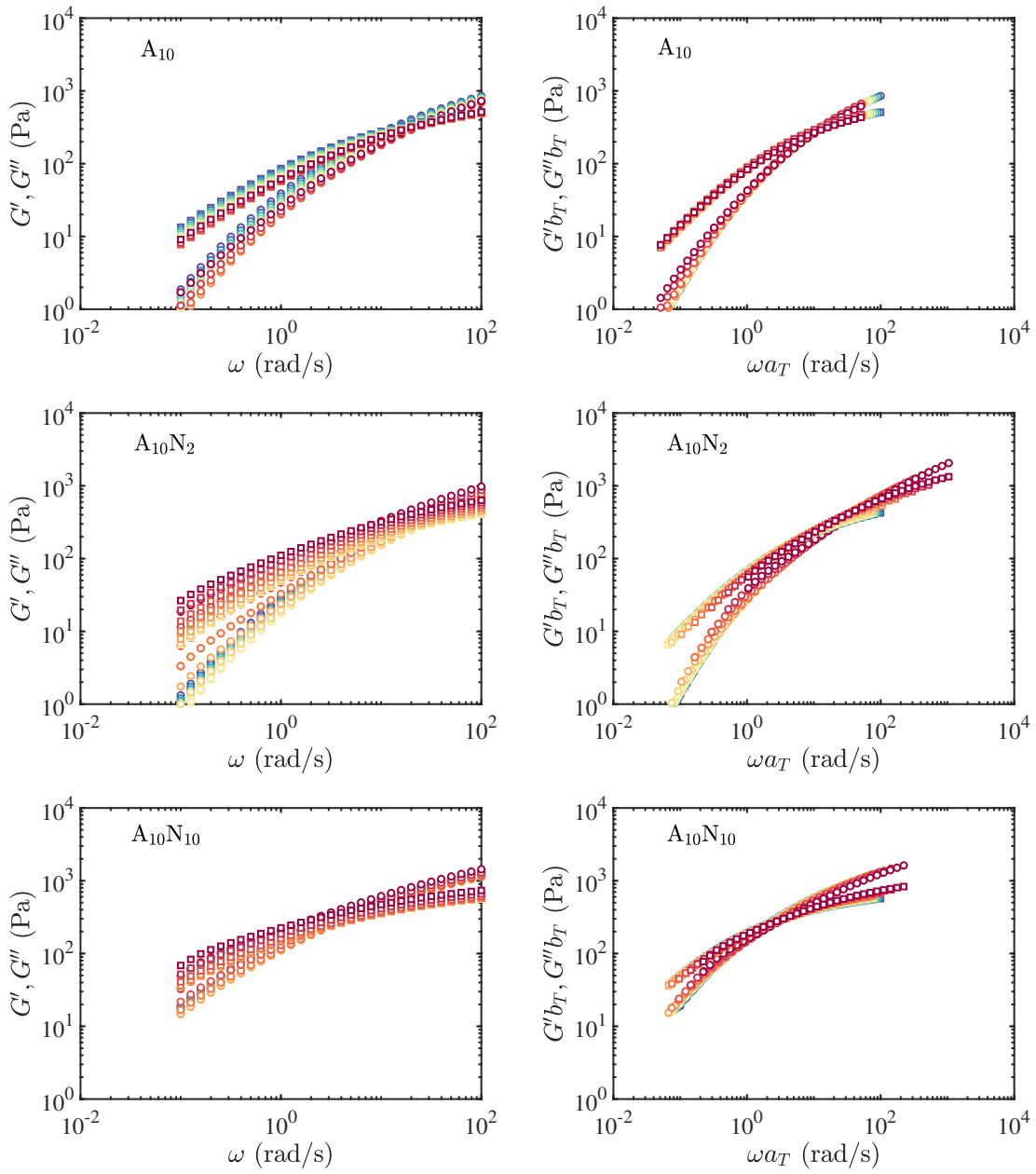


Figure 4.4.11: Left: Storage (circles) and loss (square) moduli spectra for samples A_{10} , $A_{10}N_2$ and $A_{10}N_{10}$ ($c_a = 10$ w/v%) at temperatures in the range $T = 21\text{--}56^\circ\text{C}$ (increasing blue to red). Right: TTS spectra referenced to $T = 21^\circ\text{C}$.

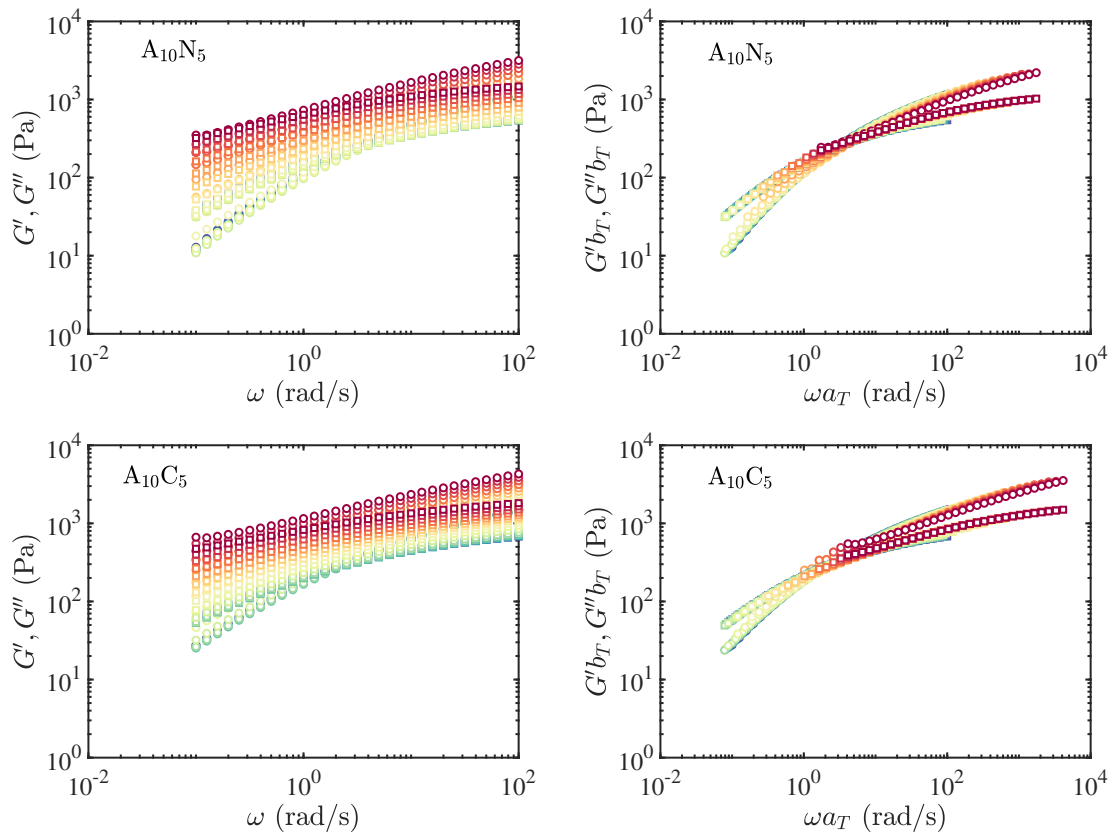


Figure 4.4.12: Left: Storage (circles) and loss (square) moduli spectra for samples A₁₀N₅ and A₁₀C₅ ($c_a = 10$ w/v%) at temperatures in the range $T = 21$ – 56°C (increasing blue to red). Right: TTS spectra referenced to $T = 21^\circ\text{C}$.

The horizontal shift factor a_T for the frequency shift may be related to the temperature according to the Williams-Landel-Ferry equation (Williams et al., 1955),

$$\log a_T = \frac{-C_1(T - T_0)}{C_2 + (T - T_0)}, \quad (4.4)$$

where C_1 and C_2 are constants to be determined by fitting Eqn. (4.4) to the horizontal shift factor. The vertical and horizontal shift factors b_T and a_T at T_0 are related to those at absolute temperature T by

$$b_T G^*(T, \omega) = G^*(T_0, \omega a_T). \quad (4.5)$$

Since the moduli are ideally proportional to the product of temperature and density for unentangled polymer melts and solutions (Dealy and Plazek, 2009), b_T may be interpreted as $b_T = T_0 \rho_0 / (T \rho)$, where ρ and ρ_0 are the polymer solution concentration at T and T_0 respectively.

Although TTS furnishes reasonable overlap of the dynamic moduli over the full range of frequencies in Figures 4.4.11 and 4.4.12, the quality of overlap is not as high as for the (weakly) chemically cross-linked PAAm hydrogels of Du and Hill (2019b). Thus, the nanocomposites may not be considered as thermorheologically simple, as defined by all relaxation times exhibiting the same temperature dependence (Dealy and Plazek, 2009). Nevertheless, the TTS still provides insights into how the the linear viscoelastic response extends comfortably beyond the kilohertz range. Such information is not just of academic interest, but is directly relevant to interpreting the ionic conductivity of hydrogels, customarily measured in the kilohertz range (Wu, 2022). The high-frequency response is also relevant to ultra-sound imaging and electro-kinetic-sonic amplitude diagnostics (Adibnia et al., 2020).

4.4.6 Apparent activation energy and effective cross-link density

The temperature dependence of the horizontal and vertical shift factors obtained from TTS for each of the samples are shown in Figures 4.4.13(a) and (b), respectively. The temperature dependence of the vertical shift factors b_T is generally weak, practically negligible at low temperature, whereas the horizontal shift factors undergo a notable thermal transition at temperatures that change with the NP loading. At low temperature, all samples reflect a similar apparent activation energy E_a , plotted in Figure 4.4.13(b) from local Arrhenius fits to data triplets in Figure 4.4.13(a). This temperature dependence is captured by fitting the WLF Eqn. (4.4) to the data for the PAAm sample A₁₀, shown as the line in Figure 4.4.13(a).

Table 4.4.4: Fitting parameters in the WLF Eqn. (4.4) for the samples in Figure 4.4.13(a) for the specified temperature range.

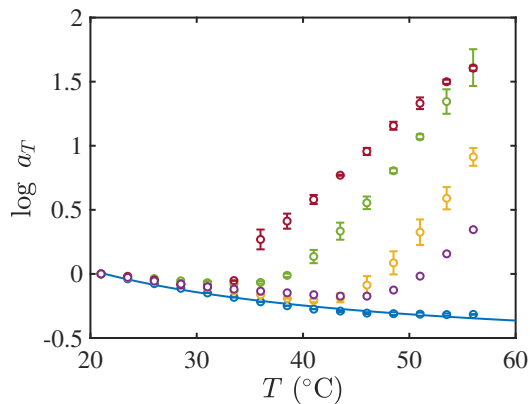
	T ($^{\circ}\text{C}$)	C_1	C_2 K	T_0 K	R^2
A ₁₀	21–56	0.66	31.12	294.45	0.989
A ₁₀ N ₂	21–44	0.73	55.15	294.35	0.983
A ₁₀ N ₁₀	21–46	0.38	27.92	294.29	0.998
A ₁₀ N ₅	21–36	0.14	12.06	294.35	0.963
A ₁₀ C ₅	21–34	0.13	6.84	294.35	0.742

The fitting parameters are provided in Table 4.4.4 for each sample. The lines for the other samples are not shown since they are slight variations of the blue line in the temperature range specified in Table 4.4.4. Increasing the temperature causes the nanocomposites to depart significantly from their parent polymer.

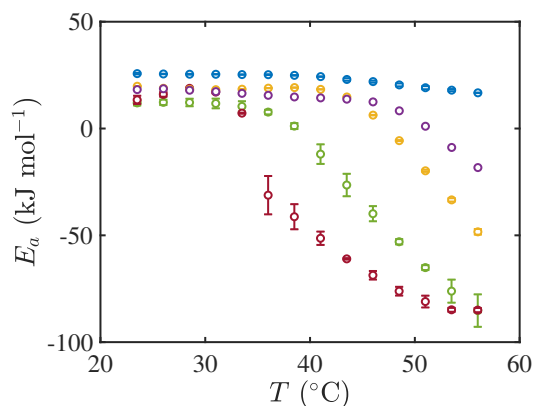
The non-Arrhenius behaviour of the nanocomposites is related to the TTS data not perfectly superposing at higher temperatures, as shown in Figure 4.4.11. [Dealy and Plazek \(2009\)](#) ascribe such a failure of TTS to thermorheological complexity. [Handge and Pötschke \(2007\)](#) reported a failure of the TTS for polycarbonate/multi-walled carbon nanotube (2 wt%) composites resulting from the different temperature dependence of the relaxation process of the pure polymer and the nanocomposite. They attributed the particle interactions to being more influenced by the entropic polymer melt elasticity than the temperature ([Handge and Pötschke, 2007](#)).

The apparent activation energy in the temperature range for which the WLF model is valid is lower for the nanocomposites compared to the neat polymer. These results contrast to chemically cross-linked gels ([Du and Hill, 2019b](#)), where E_a was associated with a free-energy barrier for disentanglement. Their reported values of E_a increased systematically with the chemical cross-linker ratio in the range $E_a \approx 15\text{--}60 \text{ kJ mol}^{-1}$ ($\approx 6\text{--}25k_B T$) ([Du and Hill, 2019b](#)). Figure 4.4.13(b) shows that E_a for the neat polymer slightly decreases with increasing temperature, spanning the range $E_a \approx 18\text{--}25 \text{ kJ mol}^{-1}$ ($\approx 7\text{--}10k_B T$). These are comparable to activation energies for terminal relaxation in polymer melts, $E_a \approx 2\text{--}20k_B T$ ([Rubinstein and Colby, 2003](#), [Du and Hill, 2019b](#)).

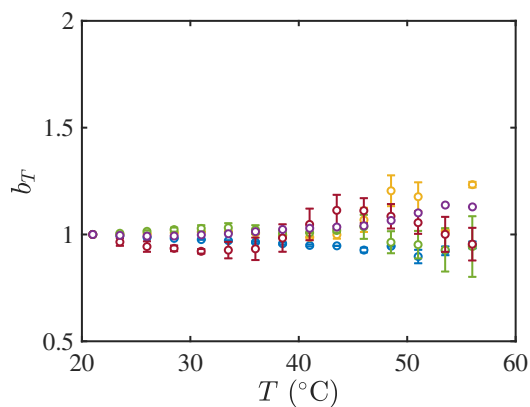
In contrast to the foregoing hydrogels and polymer melts, E_a for the nanocomposites in



(a)



(b)



(c)

Figure 4.4.13: Temperature dependence for samples A_{10} (blue), $A_{10}N_2$ (yellow), $A_{10}N_{10}$ (purple), $A_{10}N_5$ (green) and $A_{10}C_5$ (red). (a) Logarithm to base 10 of the horizontal shift factor a_T . Line is a fit of Eqn. (4.4). (b) Apparent activation energy E_a from local Arrhenius fits to data triplets in (a). (c) Vertical shift factor b_T . Error bars are the standard error σ/\sqrt{n} from $n = 3$ samples.

Figure 4.4.13 decreases significantly with temperature, even changing sign. The transition to negative apparent activation energies suggest that the nanocomposites are undergoing a spontaneous phase transition involving the silica NPs interacting with the polymer. Sample with $\phi = 10\%$ undergo this transition at a higher temperature than for the samples with $\phi = 5\%$ bare and PA-coated NPs. Such a transition, from the perspective of registering negative activation energies, has not been previously reported (to the best of our knowledge) for nanocomposites. Nevertheless, negative and non-constant activation energies have been identified for temperature-induced protein aggregation and unfolding. These were attributed to chemical modifications or structural changes within dimers or larger oligomers (Oliveberg et al., 1995, Andrews and Roberts, 2007, Wang and Roberts, 2013). Large negative activation energies have also been reported for crystallization of polymer melts, brought about by a decrease in the free energy of nucleation induced by cooling (Mandelkern et al., 1954, Vyazovkin and Sbirrazzuoli, 2002, Vyazovkin, 2020).

Another way of verifying the TTS principle, focussing specifically on b_T , is to plot the phase angle δ versus $|G^*|$. Termed a van Gorp-Palmen plot (van Gorp and Palmen, 1998), this excludes the frequency shift a_T . Such curves are expected to superpose perfectly if TTS is valid over the entire temperature range (Dealy and Plazek, 2009, Chen et al., 2013). As expected from the TTS above, such superposition is not the case. Van Gorp-Palmen plots for six temperatures in the low-temperature range 21–33.5°C (increasing by 1.5°C) for all samples are shown in Figure 4.4.14. These data superpose almost perfectly without shifting, suggesting that the effect of b_T on $|G^*|$ is negligible for the neat polymer (Figure 4.4.14(a)) and bare silica NPs (Figures 4.4.14(b)-(d)), but perhaps not quite so well for the pre-coated PA silica NPs (Figure 4.4.14(e)). Overall, these data correspond with the TTS quality and inferences drawn with respect to mixture homogeneity at low temperature. Note that the phase angle decreases with increasing $|G^*|$ for all three samples. The addition of NPs to the polymer produces significant decrease in the phase angle in the low frequency range, which can be attributed to enhanced elasticity.

As shown in Figure 4.4.15, much larger departures from superposition are revealed from van Gorp-Palmen plots in the high-temperature range, again consistent with Cole-Cole and Han plots above.

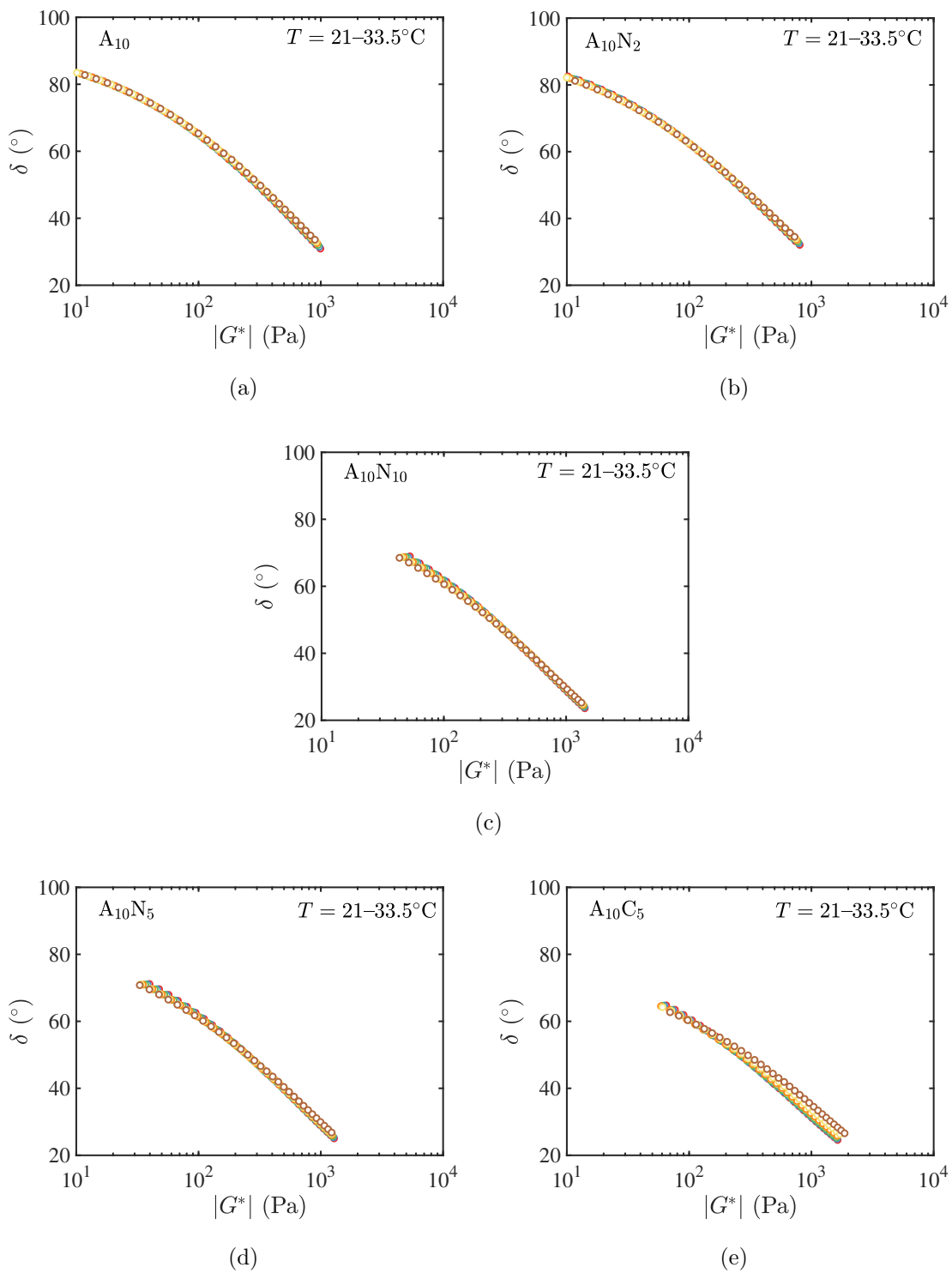


Figure 4.4.14: van Gurp-Palmen plots in the low-temperature range $T = 21-33.5^\circ\text{C}$ (increasing blue to red) for samples (a) A_{10} , (b) $A_{10}N_2$, (c) $A_{10}N_{10}$, (d) $A_{10}N_5$ and (e) $A_{10}C_5$.

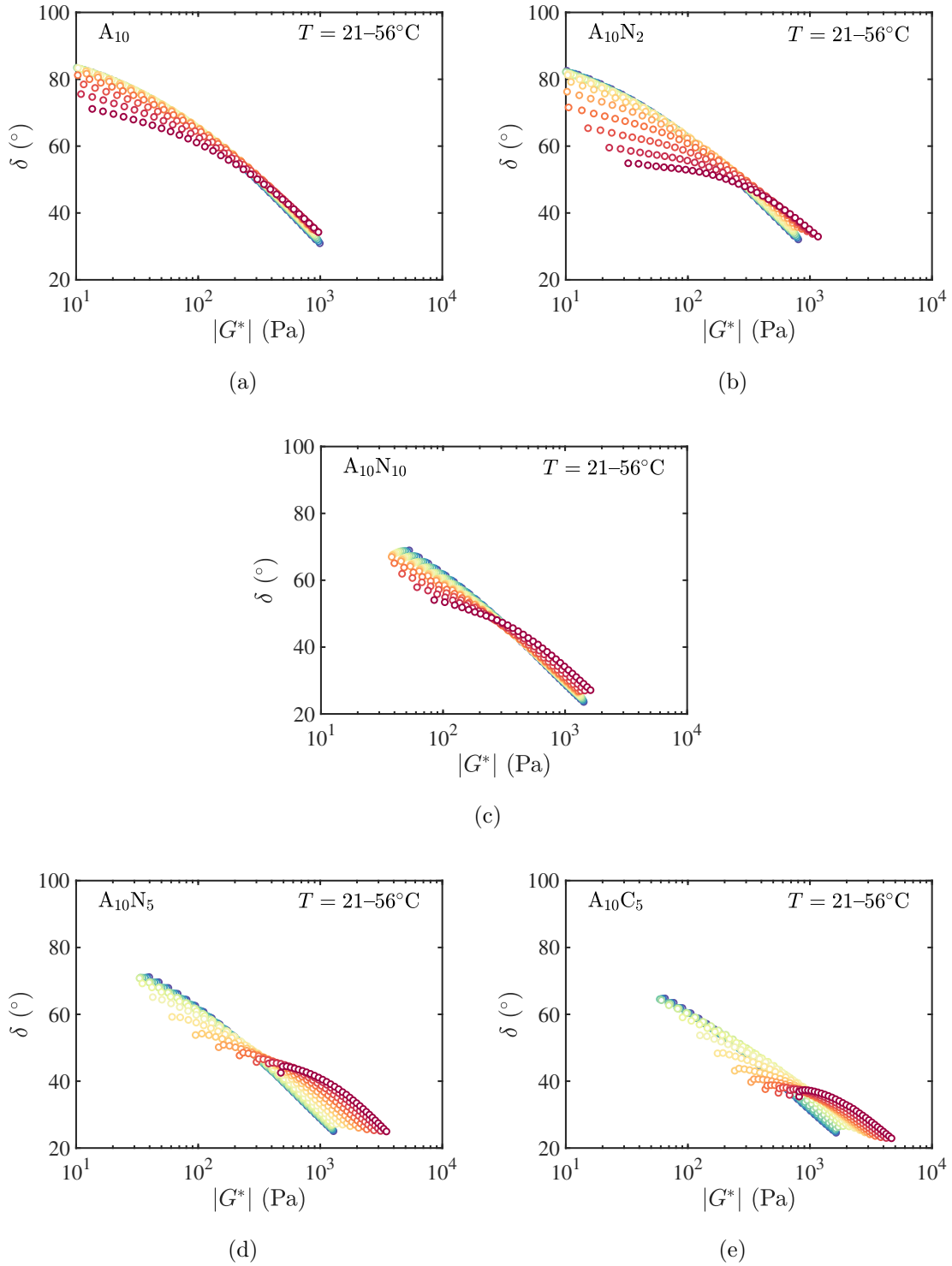


Figure 4.4.15: The same as Figure 4.4.14, but in the high-temperature range $T = 21-56^\circ\text{C}$ (increasing blue to red).

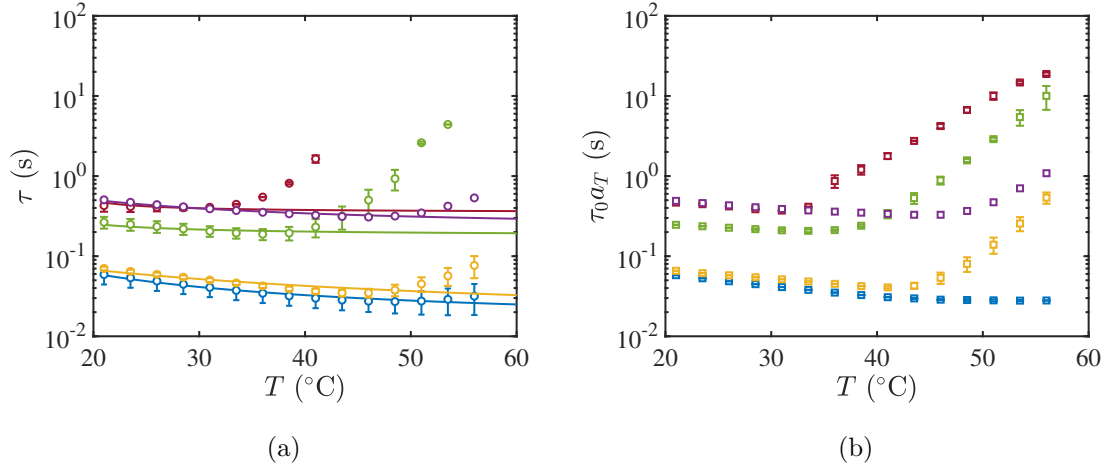


Figure 4.4.16: (a) Relaxation time $\tau = \omega_c^{-1}$ versus temperature T at temperatures for which there exists a cross-over angular frequency ω_c in the experimental range. Lines are fits of Eqn. (4.6) with C_1 , C_2 and T_0 from Table 4.4.4, and τ_0 in Table 4.4.5. (b) $\tau = \tau_0 a_T$ versus temperature T . Samples A_{10} (blue), $A_{10}N_2$ (yellow), $A_{10}N_{10}$ (purple), $A_{10}N_5$ (green) and $A_{10}C_5$ (red). Error bars are the standard error σ/\sqrt{n} from $n = 3$ samples.

4.4.7 Relaxation times

The horizontal shift factor a_T may be related to the relaxation time τ of polymeric materials by setting $a_T = \tau/\tau_0$ in the WLF Eqn. (4.4):

$$\log \frac{\tau}{\tau_0} = \frac{-C_1(T - T_0)}{C_2 + (T - T_0)}, \quad (4.6)$$

where the relaxation time $\tau = \omega_c^{-1}$ (from the crossing of G' and G'' when such a crossing exists in the experimental frequency range) and T is the absolute temperature.

Figure 4.4.16(a) shows $\tau \approx \omega_c^{-1}$ for the samples at temperatures for which there is a crossing of G' and G'' in the experimental frequency range. The lines are Eqn. (4.6) with τ_0 for each sample adjusted to fit the data at low temperature (Arrhenius regimes). These values of τ_0 are listed in Table 4.4.5 with the WLF fitting parameters C_1 , C_2 and T_0 in Table 4.4.4. Figure 4.4.16(b) shows $\tau = \tau_0 a_T$, which extends the experimental temperature range for which cross-over frequencies are available to ascertain τ .

As inferred above from the shear viscosities and dynamic moduli, NPs give rise to significant increase in the relaxation time. The relaxation times in Figure 4.4.16 clarify how

Table 4.4.5: Fitting parameter τ_0 in the WLF Eqn. (4.6) for the samples in Figure 4.4.16 over the prescribed temperature range.

	T ($^{\circ}\text{C}$)	τ_0 (s)	R^2
A ₁₀	21–51	0.05	0.992
A ₁₀ N ₂	21–44	0.05	0.992
A ₁₀ N ₁₀	21–46	0.49	0.967
A ₁₀ N ₅	21–36	0.23	0.937
A ₁₀ C ₅	21–34	0.53	0.886

this counter-intuitive slowing of dynamic with increasing temperature is effective at the high temperatures for which effective activation energies are negative. These data reveal an exponential divergence of the nanocomposite relaxation times with respect to temperature, whereas the relaxation time of the parent polymer solution decreases monotonically with respect to increasing temperature. Secondary entanglements resulting from adsorbed and non-adsorbed polymer on nearby particles are suggested to slow the relaxation of the nanocomposites (Anderson and Zukoski, 2009).

Further insights are gleaned from the temperature dependence of the dynamic moduli, loss tangent $\tan \delta = G''/G'$ and shear viscosity plotted in Figure 4.4.17. These show that G' and G'' have similar dependence on temperature, thus producing a nanocomposite loss tangent $\tan \delta < 1$ that is weakly dependent on temperature. In principle, $\tan \delta < 1$ implies an elastic solid-like character, and $\tan \delta > 1$ signifies viscous liquid-like character. The $\tan \delta$ values for the nanocomposites are lower than for the neat polymer solution, as expected over the temperature range studied, since NPs enhance the elasticity by forming physical cross-links that restrict chain motion.

Increasing the temperature is expected to enhance the mobility of chain segments, due to an increase in the kinetic energy of molecules. This leads to an increase in the free volume between the segments (Lodge and Hiemenz, 2020) and a reduction in G' for single-phase polymers. As the chains move more freely, G'' increases, reaches a peak and then decreases (Kalogeris, 2016, Lodge and Hiemenz, 2020). Although, $G' \sim nk_B T$ (statistical theory of rubber elasticity, where n is the cross-link density (Ferry, 1970, Rubinstein and Colby, 2003)) suggest a linear increase in G with T , this is not true for many polymers.

This equation represents shear modulus of entropic elasticity, and does not account for the enthalpic elasticity. The moduli of the parent polymer solution decrease slightly with temperature. The nanocomposites behave similarly to the parent polymer solution up to a certain temperature, and then the moduli increase with temperature. The increases in the moduli may be attributed to a phase change or the contribution of intermolecular resistance. Sample with $\phi = 10\%$ have a qualitatively similar temperature dependence with the parent polymer solution in the range 21–46°C, much wider range than samples with $\phi = 5\%$. The increases in moduli and shear viscosity with temperature beyond this range are lower compared to samples with $\phi = 5\%$. Therefore, at higher silica volume fraction ($\phi = 10\%$), there may be insufficient monomer to form a network or the absence of significant phase change, and the storage modulus does not increase significantly.

[Senses et al. \(2015\)](#) reported increases in moduli with temperature for poly(methyl methacrylate) (PMMA)-coated silica in PEO solutions, which they attributed to large differences between the glass transition temperatures T_g of PMMA and PEO. At $T < T_g$ for PMMA, PEO chains are confined to glassy PMMA loops, dynamically decoupling from polymer on the surface. At $T > T_g$, the adsorbed polymer becomes mobile and dynamically coupled with matrix chains. The stiffening at higher temperatures was due primarily to NPs adsorbed with long polymer chains. However, in the absence of NPs or in the use of bare NPs, the material softens at high temperatures ([Senses et al., 2015](#)).

[Petit et al. \(2007\)](#) reported thermothickening behavior (increase in the viscoelastic properties: G' , G'' , and $|\eta^*|$) for a hybrid mixture of silica and copolymer based on polyacrylamide grafted with PNIPA side chains (PAM-co-PANa-g-PNIPA) at high temperatures for silica concentration ranging from 0–140 g l⁻¹. This was attributed to coupling between the two physical cross-links: silica/PNIPA and PNIPA/PNIPA aggregates present in the mixture, and the strong interactions between PNIPA and silica surfaces ([Petit et al., 2007](#)).

4.5 Hysteresis

When heating in the range $T = 21$ –56°C, as shown in the left panels of Figure 4.5.1, viscoelastic characteristics of the nanocomposites are revealed not to return to their initial as-prepared values upon cooling. Interestingly, whereas the high-temperature dynamic moduli, as shown in the right panels of Figure 4.5.1, identify viscoelastic fluid rheology, cooling

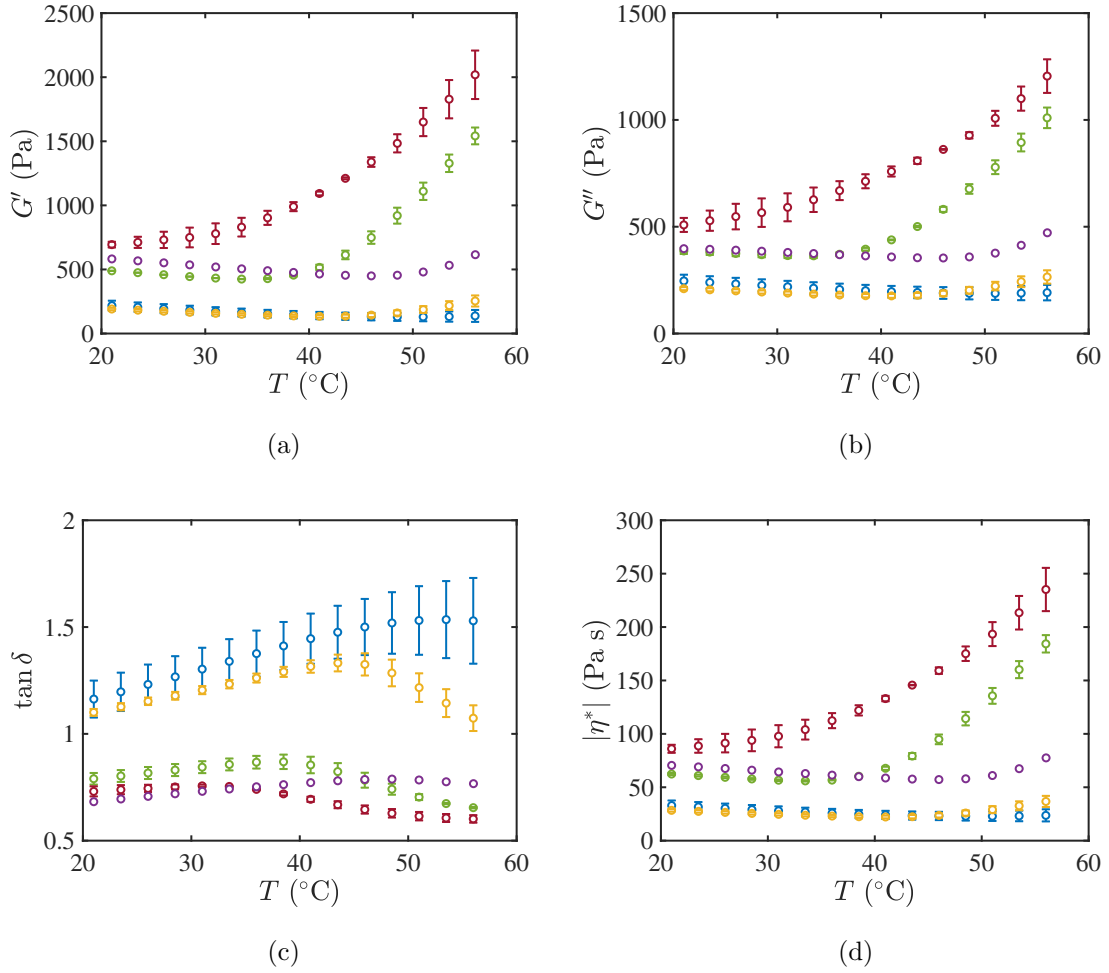


Figure 4.4.17: Temperature dependence of (a) storage modulus G' , (b) loss modulus G'' , (c) loss tangent at $\omega \approx 10 \text{ rad s}^{-1}$ and (d) Shear viscosity $|\eta^*|$ with $\gamma \approx 0.2$ in the linear viscoelastic regime ($\omega \approx 10 \text{ rad s}^{-1}$). Samples A₁₀ (blue), A₁₀N₂ (yellow), A₁₀N₁₀ (purple), A₁₀N₅ (green) and A₁₀C₅ (red). Error bars are the standard error σ/\sqrt{n} from $n = 3$ samples.

produces dynamic moduli that are indicative of a critical state that separates percolating and non-percolating elastic networks, i.e., power-law scaling or the storage and loss moduli with equal exponents. This suggests that heating above the critical temperature for the nanocomposites precipitates a nanoparticle rich phase that is kinetically trapped in the high-temperature state. As expected for binary mixture with a lower-critical phase transition temperature, the amount of the nanoparticle-rich phase, and therefore, the degree of hysteresis, is expected to increase with the degree of superheating.

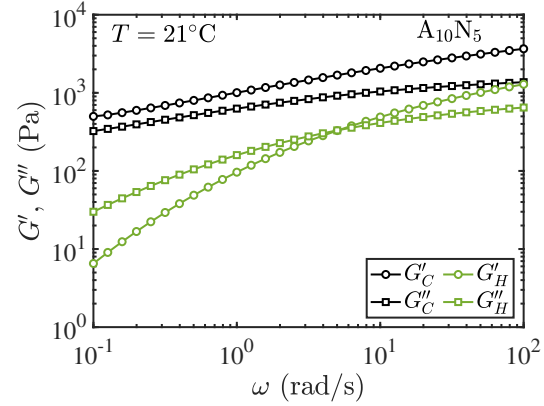
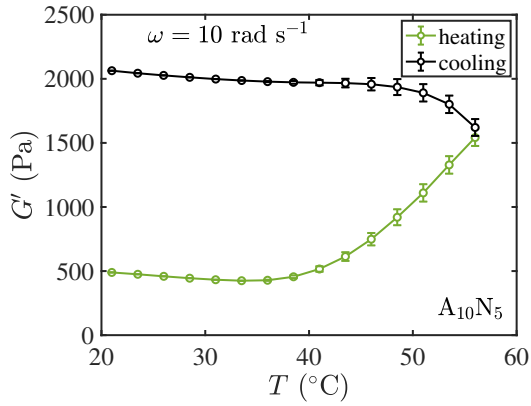
For example, as shown in Figure 4.5.2, the storage modulus of the parent polymer solution A_{10} returns to its initial as-prepared value, even after heating to the maximum temperature. The cooling runs were carried out immediately after the heating runs. The difference at the transition may be due to sampling or instrument errors. Sampling errors especially at higher temperatures may have contributed to the unequal values for heating and cooling in the range 21–56°C.

As shown in Figure 4.5.3(a) for nanocomposite $A_{10}N_5$, for example, heating and cooling within a restricted temperature range $T = 21\text{--}36^\circ\text{C}$ produced no evidence of hysteresis. For this sample, the critical temperature T_c , e.g., from Figures 4.4.16 and 4.5.3(b), is $T_c \approx 38^\circ\text{C}$, so the heating did not bring the sample into the two-phase region.

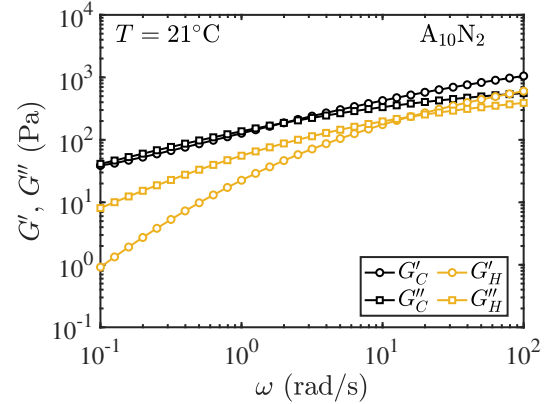
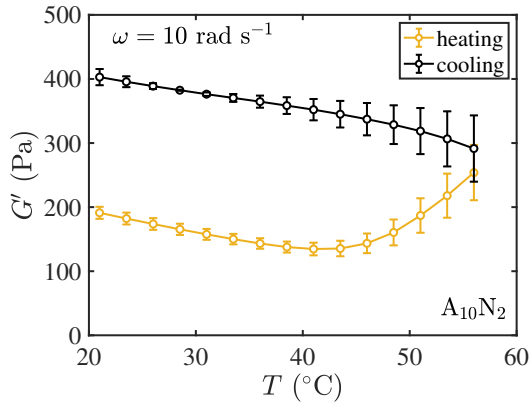
On the other hand, [Petit et al. \(2007\)](#) reported reversible thermothickening properties for a hybrid mixture of silica and PAM-co-PANa-g-PNIPA in the temperature range $T = 20\text{--}60^\circ\text{C}$, with some hysteresis observed around the critical temperature. However, no hysteresis was reported for the copolymer without silica. The cooling run returned the viscoelastic properties to their initial state. These were ascribed to an irreversible adsorption of PNIPA on silica that decreased their tendency to phase separate at high temperatures ([Petit et al., 2007](#)).

4.6 Conclusions

In situ polymerized polyacrylamide solutions doped with bare and pre-polyacrylamide-coated silica nanoparticles were examined from the perspective of their linear viscoelastic rheology. While this study focussed on samples with a limited range of polymer concentrations $c_a \approx 10 \text{ w/v}\%$ and silica NP concentrations $\lesssim 10 \text{ w/v}\%$, new insights were gleaned from



(a) Nanocomposite $A_{10}N_5$.



(b) Nanocomposite $A_{10}N_2$.

Figure 4.5.1: Left: Heating and cooling temperature dependence of the storage modulus G' at $\omega = 10 \text{ rad s}^{-1}$. Right: Storage and loss moduli spectra at $T = 21^\circ\text{C}$ prior the heating cycle (subscript H) and after the subsequent cooling cycle (subscript C). Error bars are the standard error σ/\sqrt{n} from $n = 3$ samples.

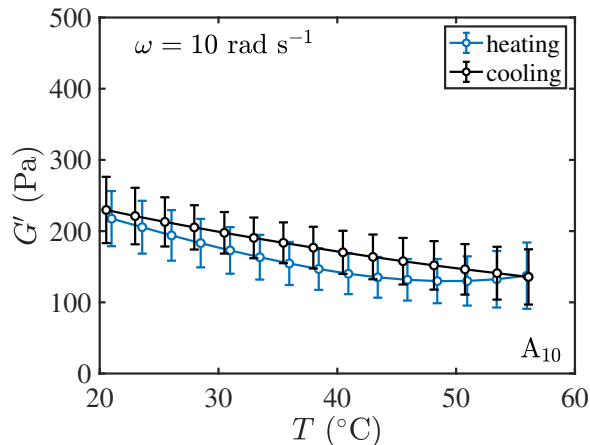


Figure 4.5.2: Heating (blue) and cooling (black) temperature dependence of the storage modulus G' for polymer solution A_{10} over the maximum temperature range 21–56°C. Error bars are the standard error σ/\sqrt{n} from $n = 3$ samples.

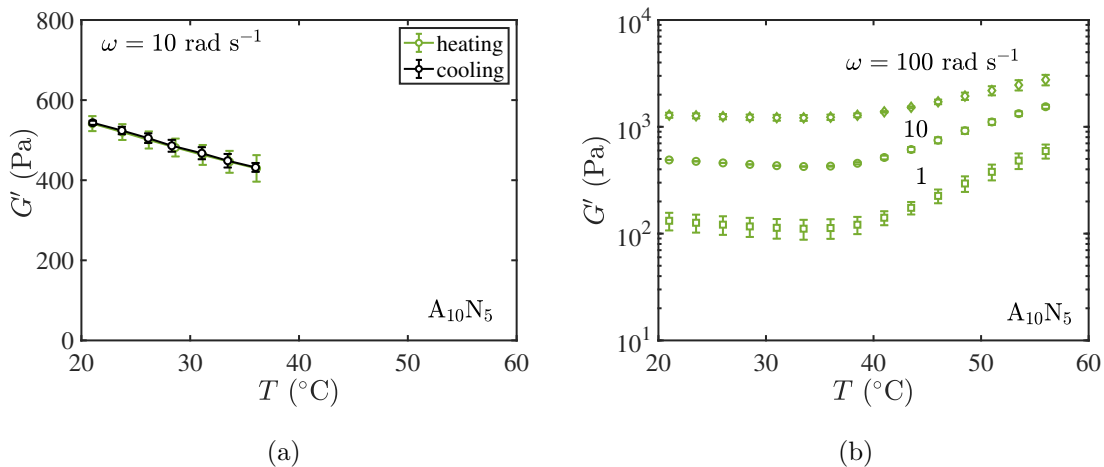


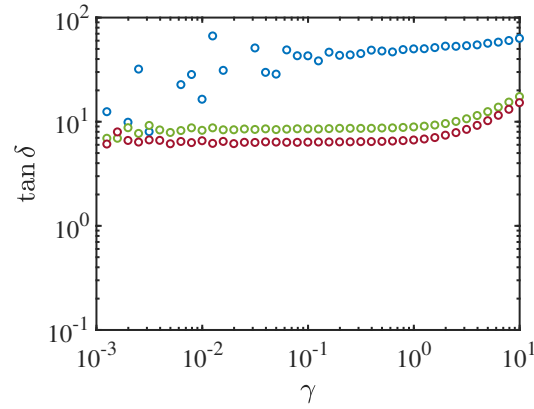
Figure 4.5.3: (a) Heating (blue) and cooling (black) temperature dependence of storage modulus G' for nanocomposite sample $A_{10}N_5$ within a reduced temperature range 21–36°C not exceeding the critical temperature for this sample ($\approx 38^\circ\text{C}$, Figure 4.4.16). (b) Temperature dependence of the storage modulus G' at $\omega = 1, 10,$ and 100 rad s^{-1} . Error bars are the standard error σ/\sqrt{n} from $n = 3$ samples.

systematic changes in temperature, namely evidence of thermal phase transitions from the nanoparticle-polymer and polymer-solvent interaction energy. Whereas the shear viscosity of the parent polymer solutions decrease slightly with temperature, nanoparticle doping furnished an exponential divergence of the rheological relaxation times with respect to temperature, similarly increasing the storage and loss moduli. Time-temperature superposition furnished apparent activation energies that transition to large negative values when heating beyond critical phase-transition temperatures. Note, however, that such transitions were irreversible, so that, upon cooling, the nanocomposite dynamic moduli may continue to increase. Interestingly, the degree of hysteresis increased with the maximum temperature. This suggests a nanoparticle enriched phase emerging from the heating into a quasi-binary phase diagram having a lower-critical-transition-temperature. As might be expected if the kinetics of the phase transition increased with temperature, the higher the maximum temperature above the phase transition the greater the degree of stiffening maintained or gained upon cooling/quenching.

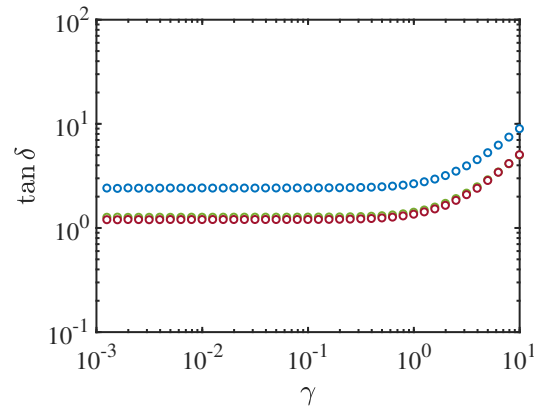
Appendix

4.A Loss tangent

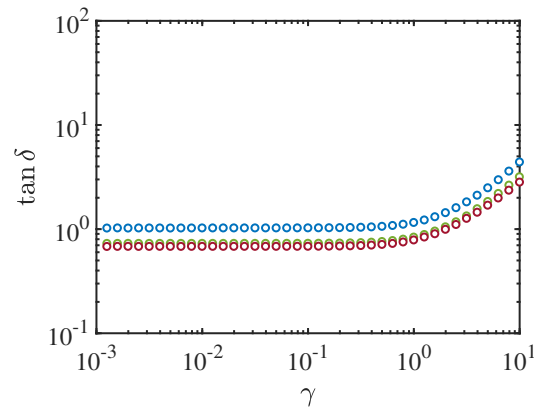
The loss tangent as a function of strain amplitude are shown in Figure 4.A.1. At higher γ , $\tan \delta$ varies significantly with γ . These variations are identified as nonlinear viscoelastic response of the polymer solutions and nanocomposites.



(a) $c_a = 0.7 \text{ mol l}^{-1}$



(b) $c_a = 1.1 \text{ mol l}^{-1}$



(c) $c_a = 1.4 \text{ mol l}^{-1}$

Figure 4.A.1: Loss tangent versus strain amplitude at $\omega \approx 10 \text{ rad s}^{-1}$ and $T \approx 21^\circ\text{C}$ for samples A_x (blue), $A_x N_5$ (green) and $A_x C_5$ (red). Subscript x represents the monomer concentration in w/v% ≈ 5 (0.7 mol l^{-1}), 8 (1.1 mol l^{-1}) and 10 (1.4 mol l^{-1}) as indicated in each panel.

Linear viscoelasticity of weakly cross-linked hydrogel nanocomposites

5.1 Preface

Soft nanocomposites with beneficial characteristics can be synthesized by embedding nanoparticles into a polymeric hydrogel network. It is of fundamental importance to understand how pre-coating the NPs with a polymer that is identical to that of the hydrogel matrix might affect the nanocomposite rheology. In this chapter, bare and polyacrylamide-coated silica NPs are used to physically cross-link polyacrylamide (PA) hydrogels that are weakly cross-linked with chemical cross-linker. The effect of temperature and varying chemical cross-linker concentration on the rheological properties are investigated. Time-concentration superposition is used to study the gelation dynamics and obtain critical relaxation exponents. The enhancement of linear viscoelastic properties is studied for hydrogels with different chemical cross-linker concentrations, and the significance of bare and PA-coated silica NP interactions on the enhancement is reported. The rheological response of the hydrogels to systematic variations in temperature are studied using time-temperature superposition.

Abstract

This paper studies how modifying the surface of an inorganic nanoparticle filler with an adsorbing polymer influence the linear viscoelastic rheology of its hydrogel nanocomposites, systematically varying the chemical cross-linker concentration and temperature. The experiments are conducted with bare and polyacrylamide (PA)-coated silica nanoparticles (NP) in PA hydrogels with acrylamide monomer concentration $c_a \approx 10\%$ and (low) chemical cross-linker-to-acrylamide monomer ratio $c_{\text{bis}}/c_a \approx 0.1$ – $0.6 \text{ mmol mol}^{-1}$. Dynamic moduli increase with NP volume fractions $\phi \leq 0.10$ and cross-linker ratio c_{bis}/c_a , and pre-coating the silica with adsorbed PA further enhances

the moduli. Time-cross-linker-concentration superposition (TCS) yields lower critical relaxation exponents ($0.2 \leq \Delta \leq 0.4$) compared to universal scaling from percolation theory ($0.6 \leq \Delta \leq 0.8$). This may be attributed to the low chemical cross-link density, high monomer concentration, and structural complexity brought about by the NP filler, which acts as a physical cross-linker. Time-temperature superposition (TTS) provides insight into how these materials behave in the temperature range 21–56°C, furnishing apparent activation energy that is temperature-dependent, and lower for the pre-PA-coated NP loading. The temperature dependence of the linear viscoelastic properties for the hydrogel nanocomposites suggests the role of chemical cross-linking in kinetically arresting the thermal phase transition in the temperature range 21–56°C.

5.2 Introduction

Polyacrylamide (PA) hydrogels with a wide range of monomer and cross-linker concentrations have been studied extensively, being one of the most widely used hydrophilic polymers. These materials are synthesized by free-radical polymerization of acrylamide (monomer) with bis-acrylamide (bis) as the cross-linker. Properties can be tuned, by varying the acrylamide and bis concentrations, to optimize water retention capacity for agricultural purposes (Sojka et al., 1998, Green et al., 2004), stiffness and pore size for separations (Skidmore and Turnbull, 2005, Stringer, 2005, Büyükköroğlu et al., 2018) and bioengineering applications (Vincent and Engler, 2017, Funaki and Janmey, 2017). The sol-gel transition (Larsen and Furst, 2008), gelation kinetics (Calvet et al., 2004, Savart and Dove, 2010, Adibnia and Hill, 2016), degree of cross-linking (Du and Hill, 2019b), swelling (Lira et al., 2009) and mechanical properties (Denisin and Pruitt, 2016) of PA hydrogels have been widely covered in literature.

Various types of nanoparticle (NP) have been embedded in hydrogels, forming hydrogel nanocomposites. The high surface-to-volume ratio makes these desirable fillers for polymeric materials (Sasaki and Akiyoshi, 2010). When added to a pre-gel solution, NPs modify the structure of the resulting network. This imparts unique properties and often enhances properties of the unfilled polymer (Manias, 2007, Gaharwar et al., 2014), beneficial in a wide range of agricultural (Vundavalli et al., 2015), biomedical (Sasaki and Akiyoshi, 2010, Gaharwar et al., 2014, Rafeian et al., 2019, Barrett-Catton et al., 2021), reservoir engineering (Singh et al., 2018, Pereira et al., 2020), food processing and packaging (Nile et al., 2020) applications. Some of these properties include adhesion strength, stiffness, and

stimuli responsiveness (Rafeian et al., 2019). For example, a nano fly ash-polyacrylamide nanocomposite—with high-temperature stability, gel strength, and plugging capacity—was synthesized by Singh et al. (2018) to reduce excessive water production and improve oil recovery from heterogeneous reservoirs.

Adibnia and Hill (2016) studied the gelation kinetics and rheological properties of polyacrylamide (PA) hydrogels with a low monomer concentration $c_a \approx 0.4 \text{ mol l}^{-1}$, varying the bis-to-acrylamide ratio in the range $c_{\text{bis}}/c_a \approx 0\text{--}46 \text{ mmol mol}^{-1}$. They identified an optimum $c_{\text{bis}}/c_a \approx 25 \text{ mmol mol}^{-1}$, above which the storage modulus G' and loss modulus G'' both plateau, with c_a . Adibnia and coworkers (Adibnia et al., 2017b, Adibnia and Hill, 2017) extended this work silica-polyacrylamide hydrogel nanocomposites with $c_a \approx 0.4\text{--}1.4 \text{ mol l}^{-1}$ and $c_{\text{bis}}/c_a \approx 2\text{--}46 \text{ mmol mol}^{-1}$, to understand the effect of silica nanoparticles on the gel point (Adibnia and Hill, 2017) and the roles of physical and chemical cross-linking (Adibnia and Hill, 2017) on storage and loss moduli. The polymerization and cross-linking of acrylamide were slowed by silica NPs, which act as a multifunctional cross-linker capable of producing ≈ 50 elastically active bis (chemical) cross-links. This was attributed to radical localization at the silica surface. They revealed that dynamic scaling at the gel point does not change with the addition of NPs. However, a significantly lower ratio c_{bis}/c_a was required to gel the PA (Adibnia and Hill, 2017).

Jia et al. (2019) synthesized silica-polyacrylamide hydrogel nanocomposites with fixed c_a and c_{bis} , but varying the NP volume fraction. They used Fourier transform infrared (FTIR) spectroscopy to identify hydrogen bonding between PA and silica, achieving a nanocomposite tensile strength twice that of the the parent PA hydrogel, with a larger equilibrium swelling ratio in simulated seawater. Okay and Oppermann (2007) employed rheometry to monitor the gelation of Laponite[®] clay modified with pyrophosphate ions (so the edges and faces bear negative charge) in acrylamide solutions with bis as a chemical cross-linker. The nanocomposite hydrogels formed were more viscous than conventional hydrogels, having $G' \approx 3\text{--}10 \text{ kPa}$, lower loss tangent $\tan \delta \sim 0.01$, and rubber-like elasticity at Laponite[®] concentrations in the range 2–7 w/v%. They attributed the increase in the storage modulus to nanoparticle cross-linking, and an increase in the loss modulus to friction from polymer adsorption/desorption at the NP surface.

Ye et al. (2014) modified the NP surfaces, using aluminum (with a positively charged surface) and sodium stabilized (with negatively charged surface) colloidal silica (both with

20 wt% concentration), to synthesize silica-polyacrylamide hydrogel nanocomposites. The modified colloidal silica significantly enhanced the mechanical properties of the nanocomposites compared to pure PA solutions ($c_a \approx 1 \text{ mol l}^{-1}$) with G' increasing by a factor of ≈ 500 for the nanocomposites with aluminium stabilized silica and by a factor of ≈ 5 for the sodium stabilized silica at $\omega \approx 10 \text{ rad s}^{-1}$. Note that such large increases in G' reflect the reference having a very low, or practically zero, shear modulus G' . The positively charged silica NPs revealed stronger attraction to PA, as indicated by the hydrodynamic layer thicknesses from dynamic light scattering (DLS) on both kinds of silica NPs. Using DLS, they ascertained the maximum adsorbed amount of PA (at 80 mg l^{-1}) on the aluminum- and sodium-stabilized silica NPs (0.1 wt%) to be ≈ 0.5 and 0.2 mg m^{-2} , respectively. The weak interactions of sodium-stabilized silica NPs were in good agreement with the Guth-Gold model (Guth, 1945):

$$G'/G'_0 \approx 1 + 2.5\phi + 14.1\phi^2, \quad (5.1)$$

where G' and G'_0 are the steady-state storage moduli in the presence and absence of filler particles, respectively, and ϕ is the particle volume fraction. Equation (5.1) models the passive elastic disturbances and interactions similarly to the viscous hydrodynamic counterparts of particulate dispersions. For silica NPs with $\phi \approx 5 \text{ v\%}$ in PA hydrogels with $c_a \approx 0.4 \text{ mol l}^{-1}$, Adibnia et al. (2017b) reported an enhancement $G'/G'_0 \approx 20$ and 2 for $c_{\text{bis}}/c_a \approx 5$ and 12 mmol mol^{-1} , respectively. Note that these reflect the effect that c_{bis}/c_a has on increasing G'_0 as much, or more so, than the degree to which ϕ increases G' .

NP enhancements of hydrogel properties are not limited to mechanical properties, but extend to thermorheological properties, among others. Time-temperature superposition (TTS) and time-concentration superposition (TCS) have been used to obtain master rheological spectra curves shifted at a reference temperature and concentration, respectively. These probe the microstructure over a wide frequency range. Du and Hill (2019a) applied the TTS principle to chemically cross-linked polyacrylamide hydrogels with similar acrylamide concentration $c_a \approx 1.4 \text{ mol l}^{-1}$ adopted in the present study, and low chemical cross-linker to acrylamide ratios in the range $c_{\text{bis}}/c_a \approx 0.2\text{--}0.9 \text{ mmol mol}^{-1}$. They obtained vertical and horizontal shift factors, related to the effective cross-link number density, that were weakly temperature independent, and an apparent activation energy that decreased with temperature but increased with the cross-linker ratio. These changes were attributed to the nature of the cross-links, since permanent chemical cross-linked networks hinder entanglement release, thus affecting viscoelastic properties (Du and Hill, 2019a). TCS was used by Adibnia and Hill (2017) to study the effect of chemical cross-linking during the sol-gel transition of silica-

polyacrylamide hydrogel nanocomposites with $c_a \approx 0.4 \text{ mol l}^{-1}$ and silica volume fraction $\phi \approx 9.5 \text{ v\%}$. They obtained critical relaxation exponents at the gel point, independent of NP loading.

Despite extensive research on the rheological properties of silica-polyacrylamide hydrogel nanocomposites, little is known about how bare or PA-coated silica NPs affect weakly cross-linked polyacrylamide gels, particularly their rheological response to temperature, frequency, and concentration. This study uses TCS and TTS principles to examine the interactions of NPs as a physical cross-linker in very weak chemically cross-linked PA hydrogels.

In the previous study (Chapter 4), we examined the silica-PA interaction using the viscoelastic properties in the absence of chemical cross-linking. In those materials, the NPs transform concentrated polymer solutions to viscoelastic fluids that behave as solids/hydrogels on short enough time scales. We identified reversible rheological properties of these gels at low temperatures (21–34°C), beyond which we identified a phase transformation, indicative of a binary solution having a lower critical transition temperature, above which a silica-rich phase imparted significantly enhanced stiffness and viscosity. In the present study, we seek to examine how a low concentration of chemical cross-linker affects the resulting nanocomposites. Therefore, based on the previous study, we hypothesize that cross-linking may kinetically suppress the high-temperature phase transition that we identified in the absence of chemical cross-linker. This may potentially improve microstructural homogeneity, but suppress the gains in stiffness and viscosity arising from the thermal phase transition.

Accordingly, the present study probes the viscoelastic response of dual-cross-linked gels with weak chemical cross-linker to monomer concentration ratio $c_{\text{bis}}/c_a \approx 0\text{--}0.6 \text{ mmol mol}^{-1}$, varying the concentration of bare and PA-coated silica NPs. Rheological analysis in the linear viscoelastic regime is used to ascertain how temperature and chemical cross-linker concentration affect dynamic moduli spectra, and, therefore, how chemical cross-linking might control or suppress the NP-induced thermal phase transition identified in our previous thermorheological study without chemical cross-linker. TCS provides critical relaxation exponents, and how these vary with the addition of bare and PA-coated silica. TTS yields shift factors, from which apparent activation energy and the effective number of cross-links of the gels are determined.

5.3 Materials and methods

Acrylamide (AAM) solution (40 w/v%, Fisher Scientific, U.S.A.), *N,N'*-methylene (bis) acrylamide powder (Fisher Scientific, U.S.A.), ammonium persulfate (APS) powder ($\geq 98\%$, Fisher Scientific, U.S.A.) and *N,N,N',N'*-tetramethylethylenediamine (TEMED, 99%, GE Healthcare Life Science, Germany) were monomer, chemical cross-linker, initiator and catalyst, respectively. Silica NPs, available as Ludox[®] TM50 (50 w% colloidal suspension, Sigma-Aldrich Inc., U.S.A.) with diameter $d \approx 30$ nm, served as a physical cross-linker. All were used as provided by the manufacturers. Polyacrylamide (PA)-coated silica NP dispersions, prepared as described in a previous study (1.25 w/v% PA and 5 w/v% Ludox[®] TM50), were used as a physical cross-linker.

The dual-cross-linked gels were prepared by mixing a fixed volume of acrylamide solution (40 w/v%), varying volumes of bis-acrylamide solution (0.5 w/v%), and silica NPs in a centrifuge tube, diluted using reverse-osmosis (RO) water (Type 1, $\sigma \approx 5.6 \mu\text{S m}^{-1}$, $\Omega \approx 18 \text{ MOhm cm}$ at 25°C). NP volume fractions and chemical cross-linker concentrations are listed in table 6.4.1. A constant monomer concentration $c_a \approx 1.4 \text{ mol l}^{-1}$ was used for all samples. Samples are identified using nomenclature B_xN_y for bare silica NP loaded hydrogels, and B_xC_y for PA-coated silica NP loaded hydrogels, where x is the ratio of bis-acrylamide cross-linker c_{bis} (mmol l^{-1}) to acrylamide c_a (mol l^{-1}) concentrations, and y is the bare NP (or PA-coated NP) volume fraction. All the concentrations are based on the total volume (5 ml) of the pre-gel solution. Dissolved oxygen was removed following addition of 50 μl of freshly prepared APS solution (0.44 mol l^{-1}) by bubbling N_2 gas through the solutions for ≈ 5 min. TEMED catalyst (50 μl) was added immediately before conducting rheological measurements.

Bare silica NPs (5 w/v%) and PA-coated silica NPs were characterized using an AcoustoSizer II instrument (Colloidal Dynamics LLC, U.S.A.). The hydrodynamic diameter $d \approx 28$ nm measured using the acoustic-attenuation sizing capability of this instrument is consistent with $d = 27$ nm reported by (Adibnia et al., 2017a) using the same instrument, also agreeing with diameters from scanning electron microscopy ($d \approx 29$ nm) (Rose et al., 2013) and dynamic light scattering ($d \approx 30$ nm) (Bhosale et al., 2011). The ζ -potential, acoustic-attenuation diameter (d_{50}), conductivity and pH for these bare and PA-coated silica NPs at $\approx 21^\circ\text{C}$ are summarized in Table 5.3.2.

Table 5.3.1: Compositions of bis- and dual-cross-linked gels, where c_a , x , and y denote acrylamide concentration, bis-acrylamide-to-acrylamide ratio, and NP volume fraction in the pre-gel solution.

Sample	c_a (mol l ⁻¹)	x (mmol mol ⁻¹)	y (w/v%)
B _x N ₀	1.4	0.1	0
	1.4	0.2	0
	1.4	0.4	0
	1.4	0.6	0
B _x N ₅	1.4	0.1	5
	1.4	0.2	5
	1.4	0.4	5
	1.4	0.6	5
B _x N ₁₀	1.4	0.1	10
	1.4	0.2	10
	1.4	0.4	10
	1.4	0.6	10
B _x C ₅	1.4	0.1	5
	1.4	0.2	5
	1.4	0.4	5
	1.4	0.6	5

Table 5.3.2: ζ -potential, acoustic-attenuation diameter, conductivity and pH of bare and PA-coated silica NPs dispersed in reverse-osmosis water (Type 1, $\sigma \approx 5.6 \mu\text{S m}^{-1}$, $\Omega \approx 18 \text{ MOhm cm}$ at 25°C) at $\approx 21^\circ\text{C}$. These were measured using an AcoustoSizer II instrument (Colloidal Dynamics LLC, USA).

	Bare SiO ₂	PA-coated SiO ₂
ζ -potential (mV)	-114.0 ± 0.2	-98.0 ± 0.7
Diameter, d_{50} (nm)	28.0 ± 0.5	35.0 ± 0.5
Conductivity (mS cm ⁻¹)	0.65 ± 0.03	0.69 ± 0.03
pH	9.0	9.0

5.3.1 Rheology

Rheological properties were measured using an ARES-G2 rheometer (TA Instruments, U.S.A.) with parallel-plate geometry under oscillatory shear. Pregel mixtures were pipetted directly onto the bottom plate, and the 25 mm diameter top plate was carefully lowered so that the gap between the plates was 0.5 mm. An “evaporation blocker” provided by the manufacturer, and silicone oil were used to minimize evaporation. The following experiments were conducted sequentially: a time-sweep experiment, where the gelation kinetics were monitored at 21°C with angular frequency $\omega = 10 \text{ rad s}^{-1}$ and strain amplitude $\gamma = 0.02$. At steady-state, a frequency-sweep in the range $\omega = 0.1\text{--}100 \text{ rad s}^{-1}$ was undertaken with $\gamma = 0.02$ at temperatures from 21 to 56°C in increments of 2.5°C. Temperature was controlled using a thermoelectric chiller (ThermoCube 300, Solid State Cooling Systems) attached to the rheometer.

5.4 Results and discussion

5.4.1 Dual cross-linking: chemical and NP

Storage and loss moduli time series during gelation at $\omega \approx 10 \text{ rad s}^{-1}$ and $\gamma \approx 0.02$ are shown in Figure 5.4.1 for gels with varying bis-to-acrylamide concentration ratios $x \approx 0, 0.1, 0.2, 0.4$ and $0.6 \text{ mmol mol}^{-1}$, varying bare silica volume fractions $\phi = 0, 5$ and 10 v\% , and a PA-coated silica volume fraction $\phi = 5 \text{ v\%}$. NP cross-linking alone increases the storage modulus (blue lines, $c_{\text{bis}}/c_a = 0$), but the effect is amplified with chemical cross-linking. These effects, which are non-additive, are quantified below.

Note that several previous studies ([Okay and Oppermann, 2007](#), [Abdurrahmanoglu et al., 2008](#), [Adibnia et al., 2017b](#)) have shown that NP cross-linking in PA-clay nanocomposites is sufficient to form gels that are less stiff than bis-acrylamide cross-linked PA. As expected, the moduli increases with NP volume fraction.

Samples with $c_{\text{bis}}/c_a \approx 0.6 \text{ mmol mol}^{-1}$ (red) consistently have the highest storage moduli and the lowest loss moduli, reflecting more efficient cross-linking and, thus, fewer network defects.

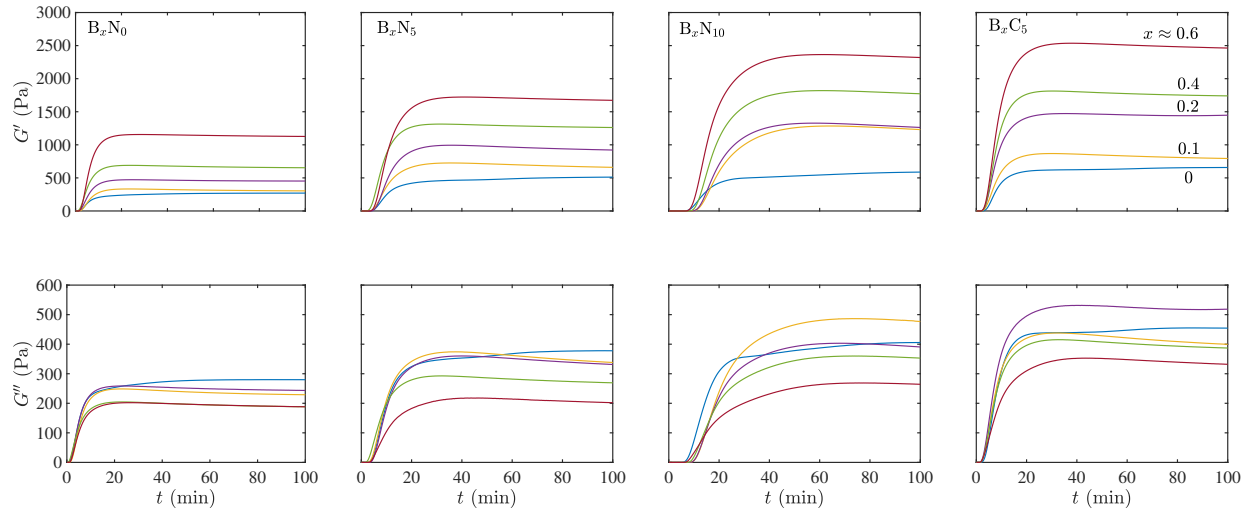


Figure 5.4.1: Storage (top) and loss moduli (bottom) time series ($\omega \approx 10 \text{ rad s}^{-1}$, $\gamma \approx 0.02$, $T \approx 21^\circ\text{C}$) for samples with acrylamide concentration $c_a \approx 1.4 \text{ mol l}^{-1}$, bis-to-acrylamide concentration ratios $x = 0\text{--}0.6$ (colors identified in the top right panel), bare silica volume fractions 5 and 10 v%, and a PA-coated silica concentration $\phi = 5 \text{ v}\%$.

5.4.2 Synergistic NP enhancements

The qualitative enhancements identified above are quantified by drawing on enhancement factors $G'_\infty/G'_{0\infty}$ and $G''_\infty/G''_{0\infty}$ for the storage and loss moduli, respectively, where subscript ∞ identifies the steady-state plateaus from Figure 5.4.1, and 0 denotes the parent polymer without NPs. These are compared with the Guth-Gold model Eqn. (5.1), which captures elastic enhancement for passive NPs (Adibnia et al., 2017b), as shown by the dashed curves in Figures 5.4.2(a) and (b).

The nanocomposites with and without chemical cross-linker are distinguished in Figures 5.4.2(a) and (b) by the positive and negative curvature of the enhancement factors with respect to NP loading ϕ . Moreover, with chemical cross-linking ($x > 0$), there is a systematic change in the degree to which NPs and chemical-cross-linking enhance the storage and loss moduli of the parent polymer. Interestingly, however, this appears to diverge as $x \rightarrow 0$, suggesting a discontinuous change when x is small enough and ϕ is large enough. Such a change may reflect the percolation threshold for the chemically cross-linked network.

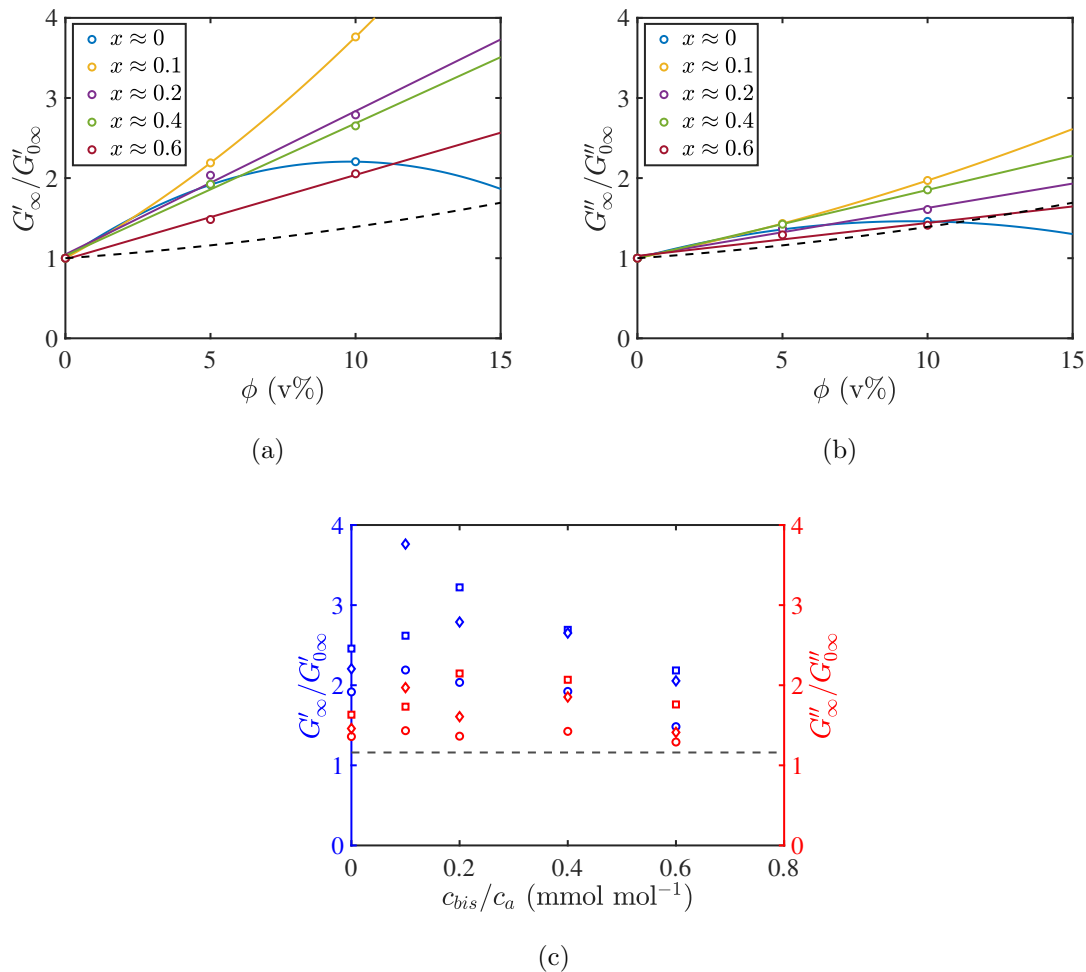


Figure 5.4.2: Scaled (a) storage and (b) loss moduli versus silica NP volume fraction for samples B_xN_0 , B_xN_5 , and B_xN_{10} . (c) Scaled moduli versus chemical cross-linker ratio for samples B_xN_5 (circles), B_xC_5 (squares), and B_xN_{10} (diamonds). $\gamma \approx 0.02$, $\omega \approx 10 \text{ rad s}^{-1}$, $T \approx 21^\circ\text{C}$. $G'_{0\infty}$ and $G''_{0\infty}$ are the steady state storage and loss moduli in the absence of NPs. Dashed line is the enhancement for passive NPs according to Eqn. (5.1). Solid lines are to guide the eye. The steady-state moduli G'_{∞} and G''_{∞} versus chemical cross-linker ratio at $\omega \approx 10 \text{ rad s}^{-1}$ is shown in Figure 5.A.1.

5.4.3 Dynamic moduli spectra and TCS

Steady-state dynamic moduli spectra are shown in the left panels of Figure 5.4.3. Note that the colors identify the chemical cross-linker concentration, consistent with Figure 5.4.2. All the samples, except the weakly cross-linked polymer B_{0.1}N₀ and the solutions with no cross-linking, are viscoelastic solids with $G' > G''$ over the entire frequency range. Vertical and horizontal shifting the spectra produces the time-concentration-superposed spectra in the right panels of Figure 5.4.3. These do not superpose perfectly, but they do produce master spectra that are characteristic of elastic solids when $\phi > 0$ and x is large enough. Note that the samples with the lowest chemical cross-linker concentration ($x = 0.1$, yellow) indicate a percolation threshold (Adibnia and Hill, 2017) (parallel power-law scaling of both moduli) in the MHz frequency range. Note that the master curves identify a significant increase in stiffness (above the low-frequency plateau modulus) at high frequencies, accompanied by an increase in the loss tangent.

The horizontal and vertical shift factors a and b are plotted versus the bis-to-acrylamide concentration ratio c_{bis}/c_a in the insets. The shift factors have power-law scaling $a \sim \tau \sim (c_{\text{bis}}/c_a)^y$ and $b \sim G^{-1} \sim (c_{\text{bis}}/c_a)^z$ (Adolf and Martin, 1990, Adibnia and Hill, 2017). As shown in table 5.4.1, the power-law exponents are in the range $|y| \approx 6.2\text{--}7.4$ and $|z| \approx 1.5\text{--}2.4$. Adibnia and Hill (2017) reported scaling exponents $|y| \approx 3$ and $|z| \approx 2$ for dual-cross-linked hydrogels by shifting moduli spectra above the gel point ($c_{\text{bis}}/c_a \approx 1.6 \text{ mmol mol}^{-1}$) for samples with $c_a \approx 0.4 \text{ mol l}^{-1}$ and $\phi \approx 9.5 \text{ v\%}$. Adibnia and Hill (2016) obtained similar scaling exponents for bis-cross-linked polyacrylamide hydrogels, concluding that NPs do not change the critical exponents $\Delta = z/y$ (Adibnia and Hill, 2017). On the contrary, the critical exponents from the scaling exponents from Figure 5.4.3 span the range $\Delta = z/y \approx 0.22\text{--}0.39$ with respect to changes in NP concentration. Note that Martin et al. (1988) used scaling analysis from percolation theory, furnishing $0.6 \leq \Delta \leq 0.8$, so the values furnished by TCS for the nanocomposites in Figure 5.4.3 are ostensibly smaller.

The low-frequency power-law scaling exponents of the storage and loss moduli in Figure 5.4.3 are plotted versus bis-cross-link density in Figure 5.4.4. Du and Hill (2019b) reported a low-frequency scaling exponent ~ 0.31 (increases to 0.38 near the percolation threshold) for TCS plot of loss moduli well above the percolation threshold for bis-cross-linked polyacrylamide gels with similar monomer concentration and bis-to-acrylamide ratios $c_{\text{bis}}/c_a \approx 0.2\text{--}0.9$. The exponent for the storage moduli in Figure 5.4.4(a) vanishes as the

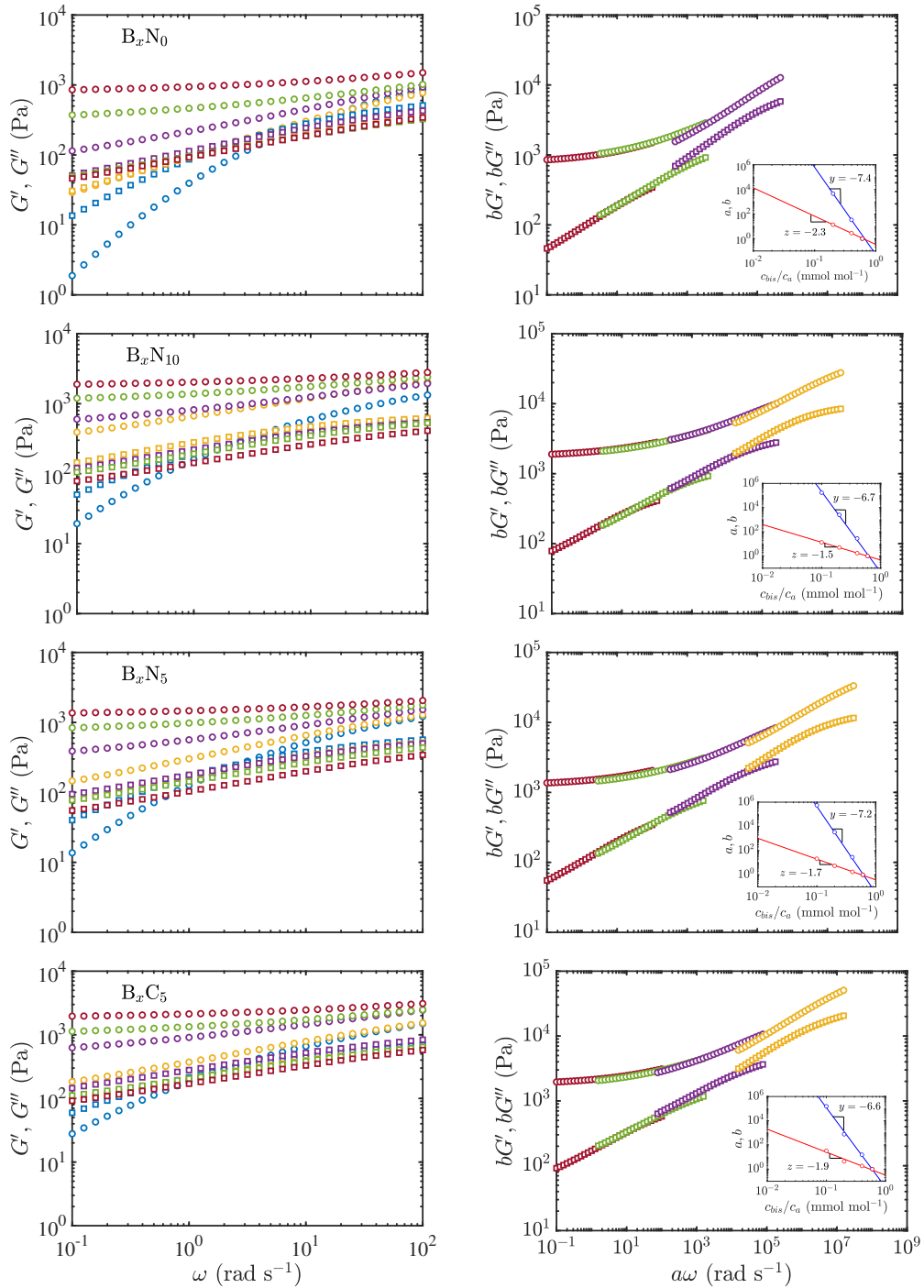


Figure 5.4.3: Storage (circles) and loss moduli (squares) spectra for dual-cross-linked gels with bis-to-acrylamide ratio $x = 0$ (blue), $x = 0.1$ (yellow), 0.2 (purple), 0.4 (green) and $0.6 \text{ mmol mol}^{-1}$ (red) at $T \approx 21^\circ\text{C}$. Time-concentration superpositions (TCS) are on the right, referenced to the sample with $x = 0.6 \text{ mmol mol}^{-1}$ (red). Shift factors a (blue) and b (red) for scaling the frequency and moduli are provided in the insets, plotted versus the bis-to-acrylamide concentration ratio c_{bis}/c_a with power-law fits and their exponents.

Table 5.4.1: Fitting parameters for the shift factors in the inset of Figure 5.4.3 of the form $a \approx Ax^y$ and $b \approx Bx^z$. $\Delta = z/y$ is the critical relaxation exponent. Acrylamide concentration for all samples is $c_a \approx 1.4 \text{ mol l}^{-1}$.

	A	y	B	z	Δ
B_xN_0	0.05	-6.2	0.29	-2.4	0.39
B_xN_5	0.03	-7.2	0.39	-1.7	0.24
B_xC_5	0.03	-6.6	0.32	-1.9	0.29
B_xN_{10}	0.05	-6.7	0.47	-1.5	0.22

bis-to-acrylamide ratio increases, evidence of ideal elastic-solid rheology in this limit.

A plateau modulus G_N^0 has been defined (Ferry, 1970) as the value of G' at the frequency where G'' has a local minimum. However, because no such minima exist for the samples in Figure 5.4.3, Figure 5.4.5 shows $G'_{0.1} \equiv G'(\omega = 0.1 \text{ rad s}^{-1})$ versus the bis-to-acrylamide ratio. Using this, Du and Hill (2019b) identified a percolation threshold as the value of c_{bis}/c_a when $G_N^0 = 0$ from a linear plot of G_N^0 versus c_{bis}/c_a for bis-cross-linked polyacrylamide gels, thus furnishing a percolation bis-to-acrylamide ratio $c_{\text{bis}}/c_a \approx 0.127 \text{ mmol mol}^{-1}$ (with similar $c_a \approx 1.4 \text{ mol l}^{-1}$). The critical percolation threshold for the bis-cross-linked sample with $\phi = 0 \text{ v\%}$ is $c_{\text{bis}}/c_a \approx 0.116$ from Figure 5.4.5. This is close to the value of Du and Hill (2019b), and higher than for the samples containing silica: $c_{\text{bis}}/c_a \approx 0.04 \text{ mmol mol}^{-1}$ for $\phi = 5 \text{ v\%}$ bare and PA-coated silica NPs, and $c_{\text{bis}}/c_a \approx 0 \text{ mmol mol}^{-1}$ for $\phi = 10 \text{ v\%}$ bare silica NPs.

Loss tangent $\tan \delta$ spectra with varying bis-cross-linker (increasing from top to bottom, red to green) for the nanocomposites are shown in Figure 5.4.6. $\tan \delta$ decreases with increasing bis cross-link density. These show, as expected, that the samples are elastic solids, and become increasingly ideal elastic solids as the bis-cross-linker concentration increases.

5.4.4 Time-temperature superposition

Dynamic moduli spectra for samples $B_{0.4}N_0$, $B_{0.4}N_5$, $B_{0.4}C_5$, and $B_{0.4}N_{10}$ with $c_a \approx 1.4 \text{ mol l}^{-1}$ at temperatures in the range $T = 21\text{--}56^\circ\text{C}$ are shown in the left panels of Figure 5.4.7. The

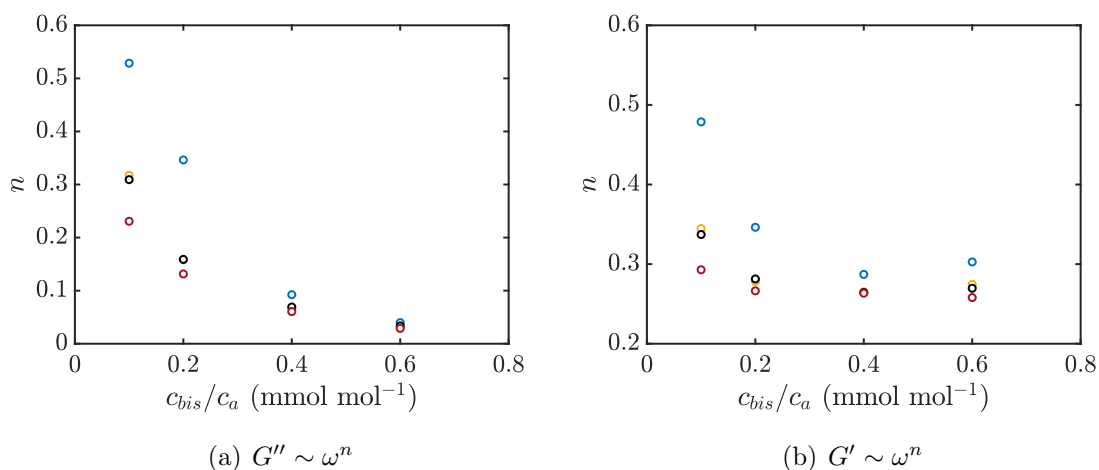


Figure 5.4.4: Low frequency power-law exponents versus bis-to-acrylamide concentration ratio from loss (a) and storage (b) moduli for gels with NP volume fractions $\phi = 0\%$ (blue), 5% (bare silica, yellow), 5% (PA-coated silica, black) and 10% (bare silica, red). Exponents were obtained from power-law fits to spectra in the left panel of Figure 5.4.3 at angular frequencies in the range $\omega \approx 0.1\text{--}0.7 \text{ rad s}^{-1}$ at various c_{bis}/c_a .

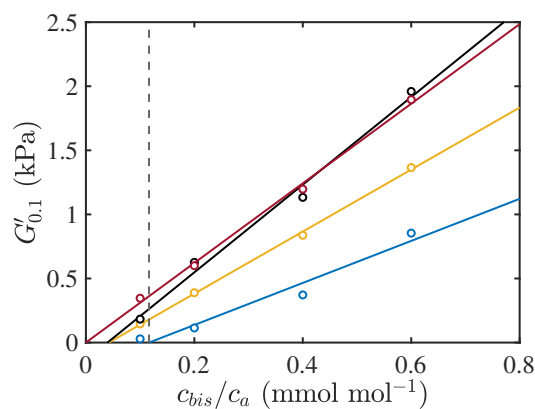


Figure 5.4.5: Storage modulus G' at $\omega = 0.1 \text{ rad s}^{-1}$ and $T = 21^\circ\text{C}$ versus bis-to-acrylamide concentration ratio for gels with NP volume fractions $\phi = 0$ (blue), 5 (bare silica, yellow), 5 (PA-coated silica, black) and 10 v% (bare silica, red). Solid lines are linear fits to the data. Dashed line identifies the apparent percolation threshold where $G'_{0.1} = 0$ for the bis-only cross-linked gel, $c_{\text{bis}}/c_a \approx 0.12 \text{ mmol mol}^{-1}$. Increasing the silica NP loading decreases the bis-cross-linking percolation limit, vanishing when $\phi \approx 10 \text{ v}\%$.

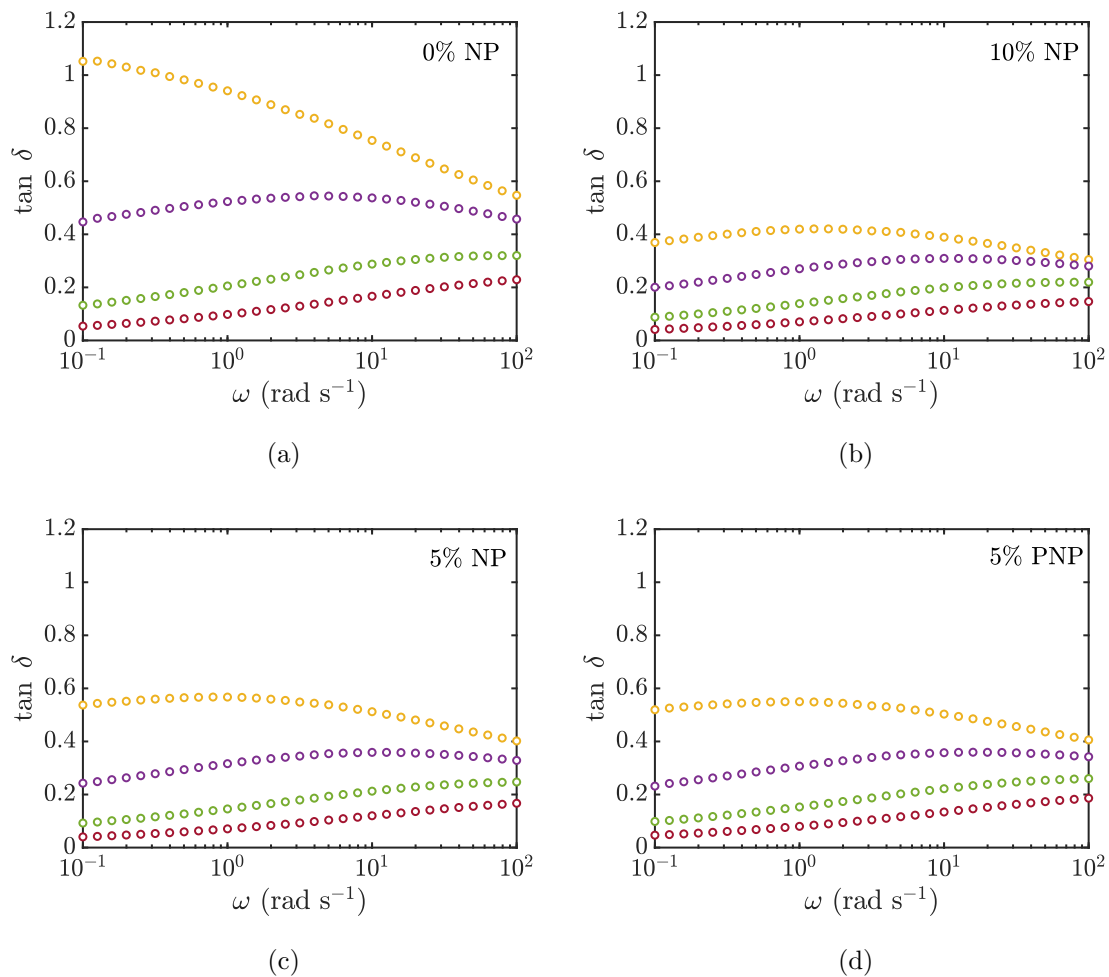


Figure 5.4.6: Loss tangent spectra for dual cross-linked gels with varying NP concentration, as indicated at $T = 21^\circ\text{C}$ and $\gamma = 2\%$. The bis-to-acrylamide concentration varies from 0.1 (yellow), 0.2 (purple), 0.4 (green) and 0.6 mmol mol⁻¹ (red).

accompanying loss tangent spectra are in Figure 5.4.8. The TTS function of the Trios software (TA Instruments) was used to apply vertical and horizontal shifts to the moduli, producing master curves referenced to temperature $T_0 = 21^\circ\text{C}$, as shown in the right panels of Figure 5.4.7. The horizontal and vertical shift factors a_T and b_T , respectively, are related by

$$b_T G^*(T, \omega) = G^*(T_0, \omega a_T). \quad (5.2)$$

When the moduli are assumed proportional to the product of temperature and density, as is customary for unentangled polymer melts and solutions (Dealy and Plazek, 2009), $b_T = T_0 \rho_0 / (T \rho)$, where ρ and ρ_0 are the density at T and T_0 respectively. Temperature clearly has a weak influence on the spectra. Nevertheless, these small changes furnish valuable insights on the polymer-polymer and polymer-NP interactions when turning to the apparent activation energies furnished by the temperature dependence of the shift factors. Note, for example, that the samples with $\phi = 5$ v% are distinguished by the others (with $\phi = 0$ and 10 v%) for the failure of their spectra to superpose at low frequencies.

5.4.5 Apparent activation energy and effective cross-link density

The top panel of Figure 5.4.9 shows the temperature dependence of the horizontal shift factors a_T , and apparent activation energy obtained from TTS for samples $B_{0.4}N_0$, $B_{0.4}N_5$, $B_{0.4}C_5$, and $B_{0.4}N_{10}$. The relationship between a_T and absolute temperature T is captured by the Williams-Landel-Ferry (WLF) equation (Williams et al., 1955)

$$\log a_T = \frac{-C_1(T - T_0)}{C_2 + (T - T_0)}, \quad (5.3)$$

where T_0 is the reference temperature, C_1 and C_2 are constants. The three fitting parameters T_0 , C_1 and C_2 for each sample are presented in Table 5.4.2, and Eqn. (5.3) is plotted in Figure 5.4.9(a). The systematic change in $\log a_T$ with ϕ is qualitatively similar to manner in which $\log a_T$ for bis-cross-linked polyacrylamide gels vary with cross-link density (Du and Hill, 2019b). Moreover, the systematic change with respect to temperature furnishes an apparent activation energy E_a , which is calculated here from local Arrhenius fits to data triplets in Figure 5.4.9(a)

$$\frac{d \log a_T}{dT} = \frac{E_a}{2.303RT^2}, \quad (5.4)$$

and plotted in Figure 5.4.9(b) with (Shangguan et al., 2017)

$$E_a = RT \frac{2.303C_1C_2T}{(C_2 + T - T_0)^2} \quad (5.5)$$

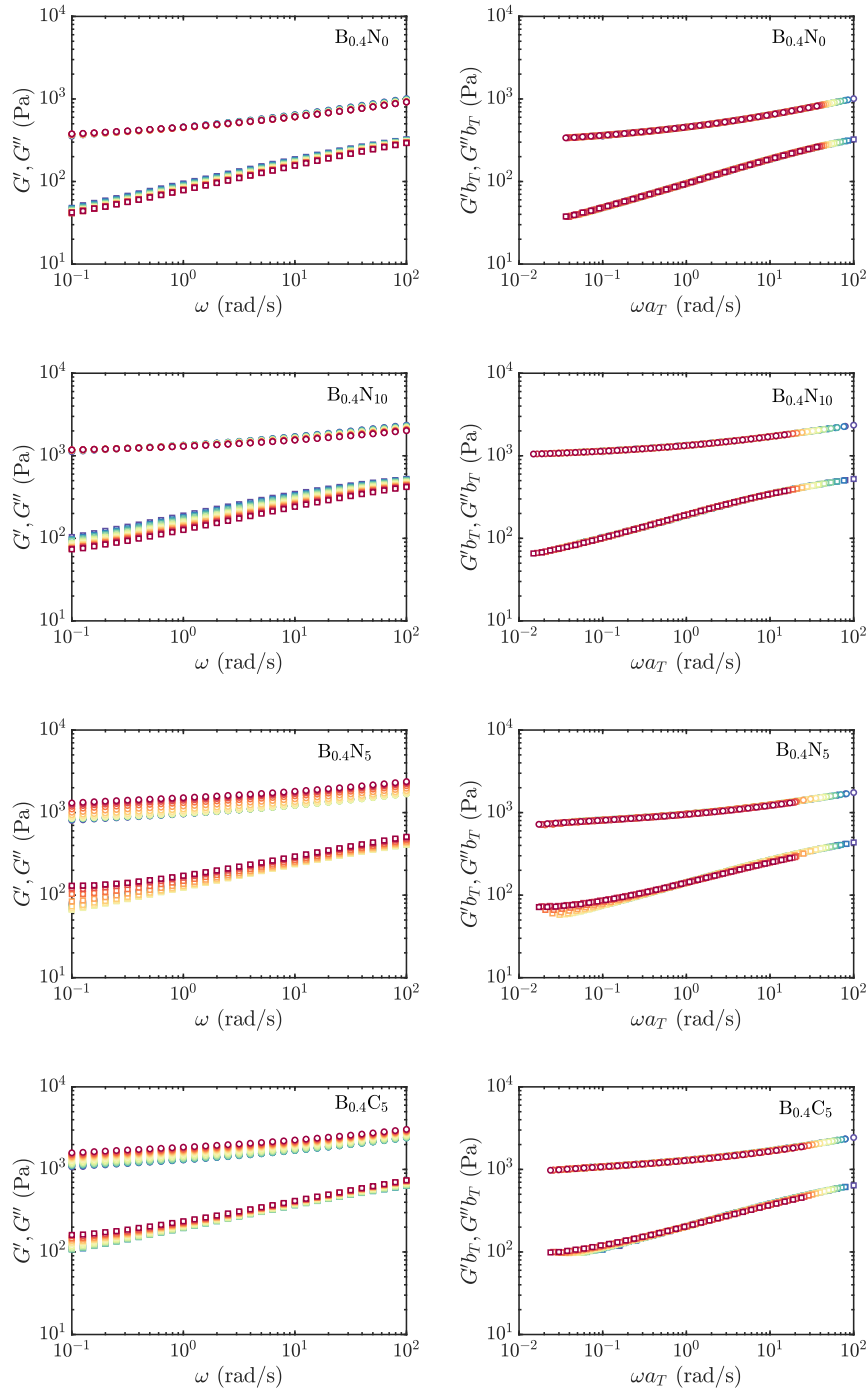


Figure 5.4.7: Storage (circles) and loss moduli (squares) spectra for dual-cross-linked gels following time-temperature superposition (TTS) with temperature ranging from $T = 21 - 56^\circ\text{C}$, increasing from blue to red, referenced to $T = 21^\circ\text{C}$.

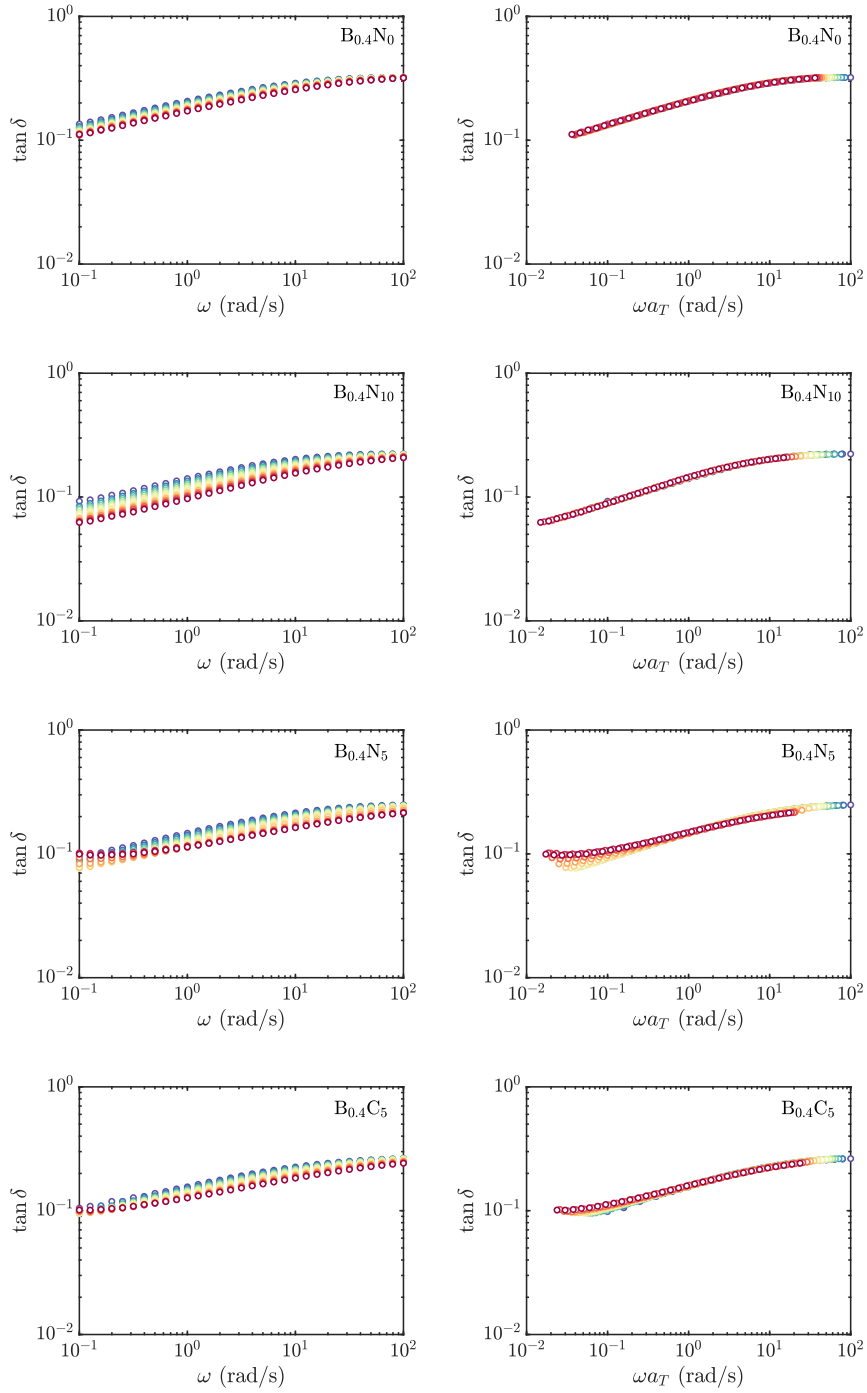


Figure 5.4.8: Loss tangent spectra for dual-cross-linked gels following time-temperature superposition (TTS) with temperature ranging from $T = 21 - 56^\circ\text{C}$, increasing from blue to red, referenced to $T = 21^\circ\text{C}$.

Table 5.4.2: Fitting parameters in WLF Eqn. (5.3) for the pure polymer and nanocomposites shown in Figure 5.4.9(a) in the temperature T range specified.

	C_1	C_2 (K)	T_0 (K)	R^2
$B_{0.4}N_0$	0.86	35.08	293.99	0.999
$B_{0.4}N_5$	3.11	109.9	293.82	0.994
$B_{0.4}C_5$	3.08	136.3	293.25	0.989
$B_{0.4}N_{10}$	2.39	57.81	294.02	0.999

from Eqn. (5.3).

The exclusively positive, weakly temperature dependent values of E_a revealed here contrast significantly with the strong temperature dependence of E_a for the same silica NPs in PAAm solutions without bis-cross-linker (Chapter 4), which furnished $E_a < 0$ at high temperature. This confirms the hypothesis that bis-cross-linking provides a kinetic barrier to suppress demixing that would deposit a silica-rich phase. Recall, such a transition was posited to arise from depletion-attraction (Parola and Reatto, 2015), reflecting a higher temperature increasing the solvent quality, thus favouring PAAm coil swelling and desorption from silica when increasing the temperature.

The vertical shift factor b_T is related to the effective number of cross-links according to (Dealy and Plazek, 2009)

$$\frac{N}{N_0} = \frac{VT_0}{b_TV_0T}, \quad (5.6)$$

where $V/V_0 \approx 1 + \beta(T - T_0)$, β is the volume expansion of water, and $N_0 = N(T_0)$. N and V are defined as the effective cross-linker number and sample volume at each temperature, and N_0 and V_0 are the cross-linker number and sample volume at T_0 . The ratio N/V is the effective cross-linker number density. T and T_0 are absolute temperatures. Equation (5.6) is plotted versus temperature in Figure 5.4.9(c). Samples with $\phi = 5\%$ bare silica (red) and PA-coated silica (black) have a notably larger and significant increase in N/N_0 with temperature. While this suggests an increase in the number of effective cross-links, it is not yet clear why a similar increase is absent when $\phi = 10\%$.

Figures 5.4.10(a) and (b) show $G'/(RT)$ and $G''/(RT)$ versus T for samples $B_{0.4}N_0$, $B_{0.4}N_5$, $B_{0.4}C_5$, and $B_{0.4}N_{10}$ at $\omega = 10 \text{ rad s}^{-1}$. Note that $G'/(RT)$ may be interpreted as

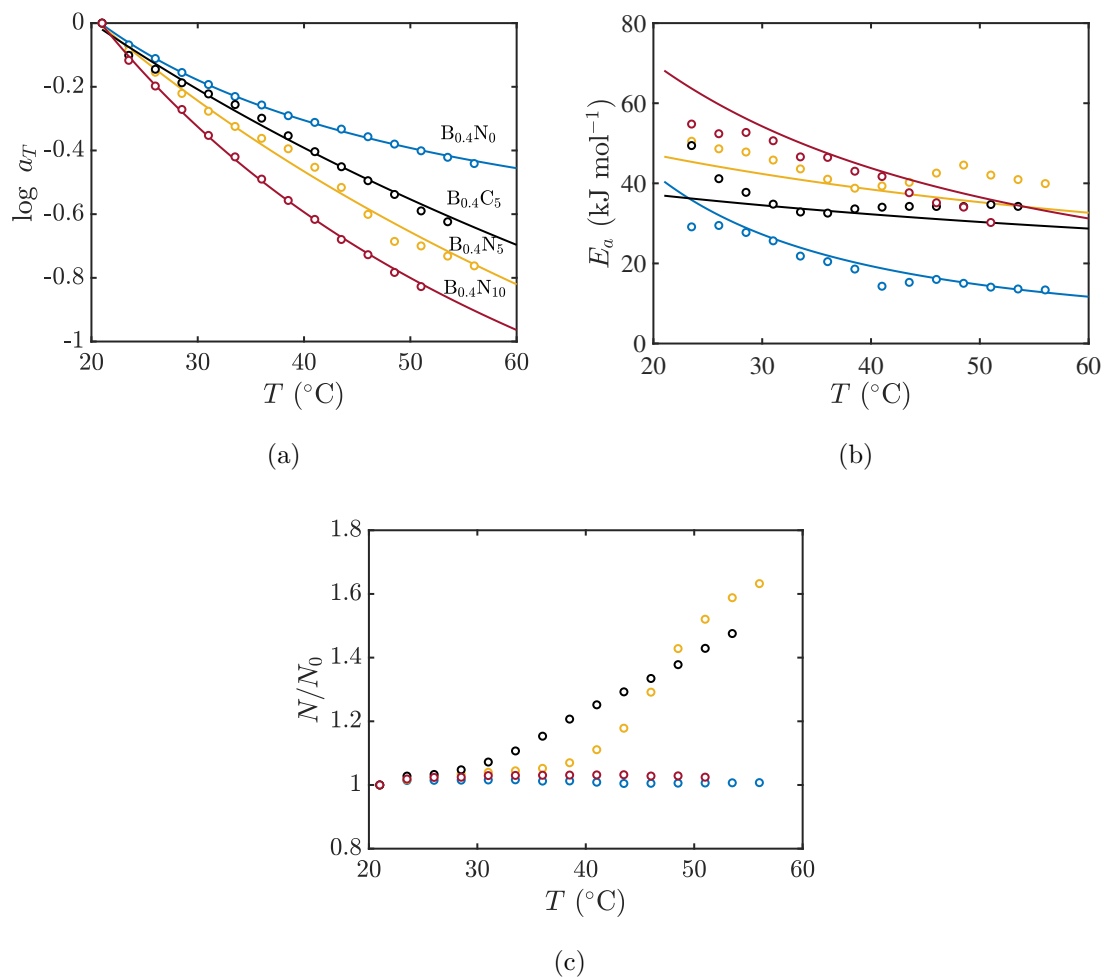


Figure 5.4.9: Temperature dependence of (a) horizontal shift factor a_T (solid lines are fits of the WLF Eqn. (5.3), (b) apparent activation energy E_a (calculated from local Arrhenius fits to data triplets in (a) (solid lines are Eqn. (5.5)), and (c) vertical shift factor b_T , for samples $B_{0.4}N_0$ (blue), $B_{0.4}N_5$ (yellow), $B_{0.4}C_5$ (black), and $B_{0.4}N_{10}$ (red).

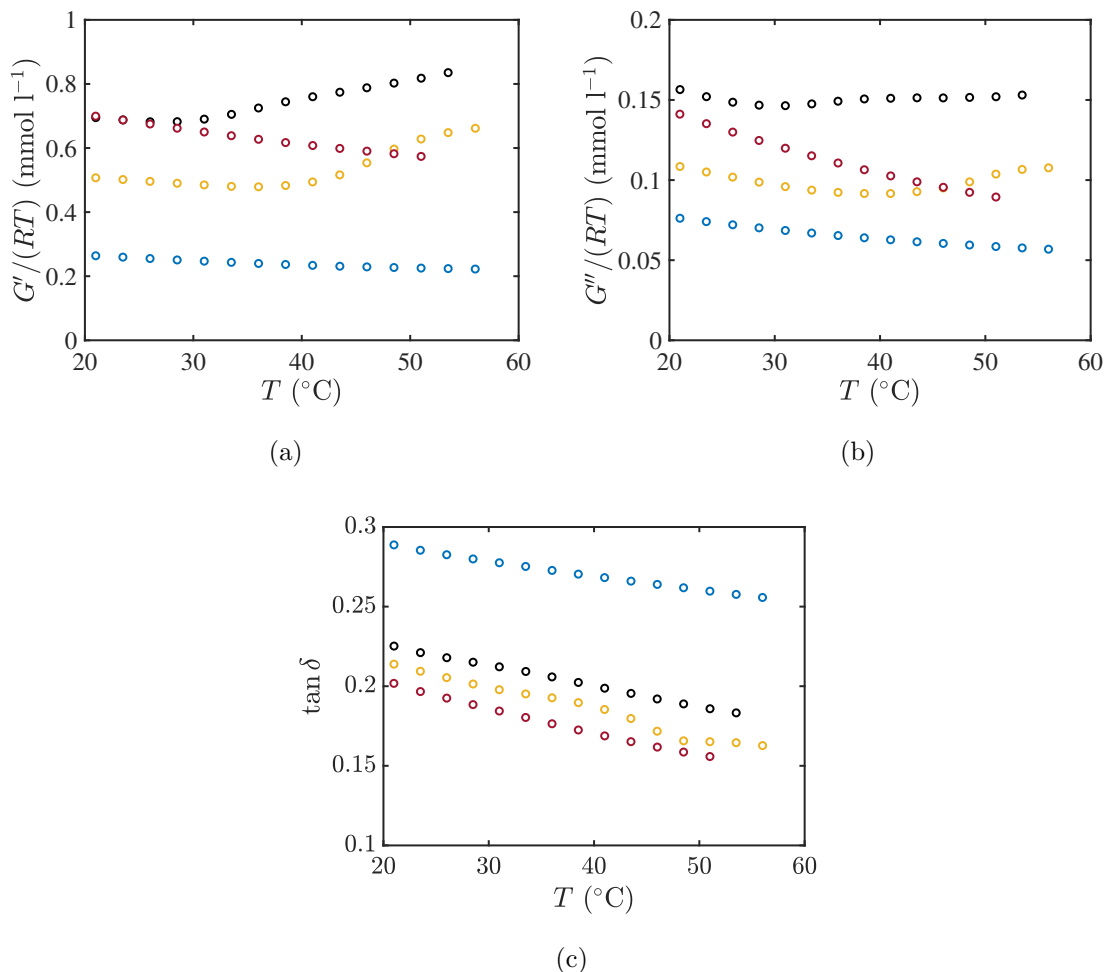


Figure 5.4.10: Temperature dependence of (a) storage G' , (b) loss moduli G'' , and (c) loss tangent $\tan \delta$, for samples B_{0.4}N₀ (blue), B_{0.4}N₅ (yellow), B_{0.4}C₅ (black), and B_{0.4}N₁₀ (red) at $\omega \approx 10 \text{ rad s}^{-1}$ with $\gamma \approx 2\%$.

an effective cross-linking number density. Similarly to Figure 5.4.9(c), and more subtly in Figure 5.4.9(b), the samples with $\phi = 5 \text{ v}\%$ are readily distinguished from the others, here by distinct changes in the sign of the derivative of $G'/(RT)$ and $G''/(RT)$ with respect to T .

The changes at low temperature for the nanocomposite samples are typical of homogeneous polymer systems in the terminal viscoelastic regime (Jeon et al., 2000). The low-temperature changes in Figures 5.4.10(a) and (b) suggest that terminal flow is controlled by both polymer/NPs and chemical covalent bonds as temperature increases. Significant increases in $G'/(RT)$ at higher temperatures for samples B_{0.4}N₅ (yellow) and B_{0.4}C₅ (black), may be attributed to a phase change at the temperatures at which the sign of the derivatives

of $G'/(RT)$ and $G''/(RT)$ with respect to T change (≈ 37 and 27°C , respectively). Note that, despite these changes, the loss tangents in Figure 5.4.10(c) for all the samples decrease with increasing temperature without presenting evidence of a phase change.

In summary, evidence of a thermal phase transition in the samples with silica volume fraction $\phi = 5\%$ is present from their temperature dependence of horizontal and vertical shift factors a_T and b_T . Of these two nanocomposites, the silica NPs pre-coated with PA undergo a transition at a lower temperature than for the initially bare silica NPs. This is consistent with the previous study for these NPs in non-cross-linked PAAm solutions. No evidence of a transition exists in the absence of NPs ($\phi = 0$). More surprising, perhaps, is that nanocomposites with a higher silica volume fraction $\phi = 10\%$ present no ostensible evidence of a transition. Experiments in non-cross-linked PAAm solutions (Chapter 4) conducted with $\phi = 10\%$ have a qualitatively similar temperature dependence with the parent polymer solution in the range $21\text{--}46^\circ\text{C}$, much wider range than samples with $\phi = 5\%$. This may be related to the percolation threshold for the nanocomposites with $\phi = 10\%$ (Figure 5.4.5).

5.5 Conclusions

Linear viscoelastic oscillatory shear responses of dual cross-linked polyacrylamide hydrogels using bare and PA-coated silica NPs as the physical cross-linker and bis-acrylamide as the chemical cross-linker have been studied. The effects of pre-coating the silica with PA, varying chemical cross-linker concentration, and varying temperature on the rheological properties were investigated.

NP-doping enhanced the storage and loss moduli of the parent-chemically cross-linked hydrogels by factors that are significantly greater than the passive enhancement predicted by the elastic analogue of Einstein's viscosity with hydrodynamic interactions. This is evidence that bare silica changes the in situ free-radical polymerization and cross-linking, here increasing the effective cross-linking efficiency/concentration. Moreover, pre-coating the silica systematically enhanced the effect, suggesting, perhaps, that the PA-pre coating enhances entanglement/coupling between the silica and hydrogel network.

Time-concentration superposition of dynamic moduli spectra was undertaken on samples for which the spectra presented viscoelastic solid rheology, i.e., not crossing of the storage

and loss moduli in the experimental frequency range. The superposition produced universal dynamic moduli spectra, representing viscoelastic solids, extending the frequency range from $\omega = 0.1 \text{ rad s}^{-1}$ to more than 10^7 rad s^{-1} . Scaling of the horizontal and vertical shift factors with respect to the chemical cross-linker concentration furnished power-law scaling exponents that varied only quantitatively with respect to silica concentration and PA pre-coating. The universal exponents $\Delta = z/y \approx 0.22\text{--}0.29$ for nanocomposites were somewhat smaller than predicted by percolation theory and measured for similar hydrogels without silica nanoparticles. For example, without nanoparticles, but the same monomer and bis-cross-linker concentration, the analysis furnished $\Delta \approx 0.39$.

The role of temperature on the rheology of these soft nanocomposites was of particular interest in this study, since our previous study, conducted without chemical cross-linker, suggested a thermal phase transition when increasing the temperature. Such a transition appeared to promote demixing of a silica enriched phase, significantly increasing stiffness and viscosity of the nanocomposites, possibly due to depletion-attraction induced by an increase in solvent quality with increasing temperature. The central hypothesis tested in the present study was that chemical cross-linking would immobilize nanoparticles in the as-prepared state, thus kinetically arresting the thermal phase transition.

Accordingly, time-temperature superposition of dynamic moduli spectra was undertaken, furnishing an apparent activation energy that decreased monotonically with temperature, in a qualitatively similar manner to the parent hydrogel. Moreover, with chemical cross-linker, while the activation energies remained positive, they revealed a discontinuous change in slope with respect to temperature when loaded with silica at volume fraction $\phi \approx 5 \text{ v\%}$. Interestingly, with an increase of the silica loading to $\phi \approx 10 \text{ v\%}$, the temperature dependence of the activation energy reverted back to that of the parent hydrogel. The same high concentration of silica, but without bis-cross-linking yields similar result in the range 21–46°C (Chapter 4). This was attributed to excessive NPs or insufficient monomer for network formation.

Overall, this study demonstrate that a small degree of chemical cross-linking can be adopted to arrest the thermal demixing of silica at high temperatures. Such a strategy might be adopted to improve microstructural homogeneity, albeit at the cost of transforming low-frequency fluid-like dynamics to solid-like viscoelasticity.

Appendix

5.A Steady state storage and loss moduli

The steady state storage and loss moduli following polymerization time series in Figure 5.4.1 are shown in Figure 5.A.1.

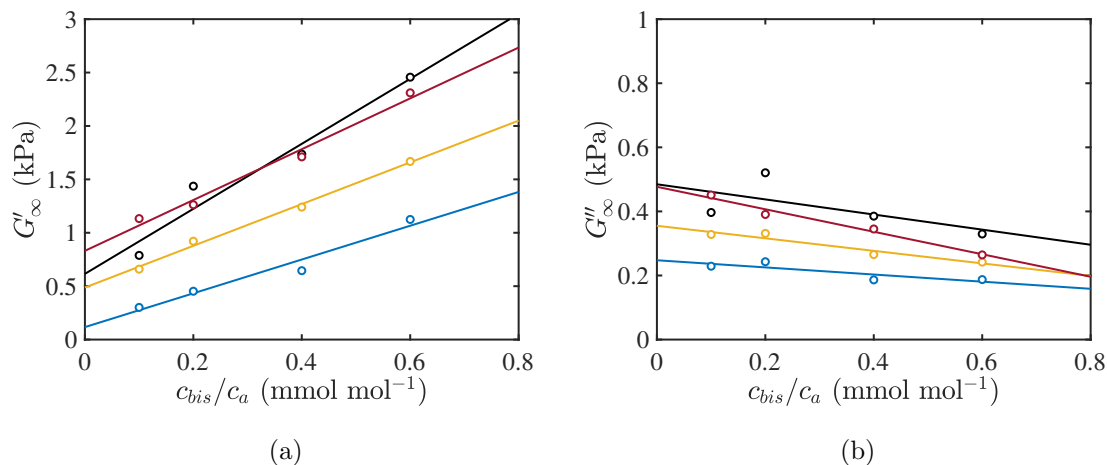


Figure 5.A.1: Steady state storage (a) and loss (b) moduli at $\omega = 10 \text{ rad s}^{-1}$ and $T = 21^\circ\text{C}$ versus bis-to-acrylamide concentration ratio for gels with NP volume fractions $\phi = 0$ (blue, $G'_{0\infty}$ and $G''_{0\infty}$), 5 (bare silica, yellow), 5 (PA-coated silica, black) and 10 v% (bare silica, red). $G'_{0\infty}$ and $G''_{0\infty}$ are the steady state storage and loss moduli in the absence of NPs. Solid lines are linear fits to the data.

5.B Oscillatory sweep response

The effects of bare and PA-coated silica NPs on the viscoelastic rheology as a function of strain amplitude are shown in figures 5.B.1 and 5.B.2. These data were used to set the strain amplitude for experiments reported in the main text, helping to ensuring a linear-viscoelastic response.

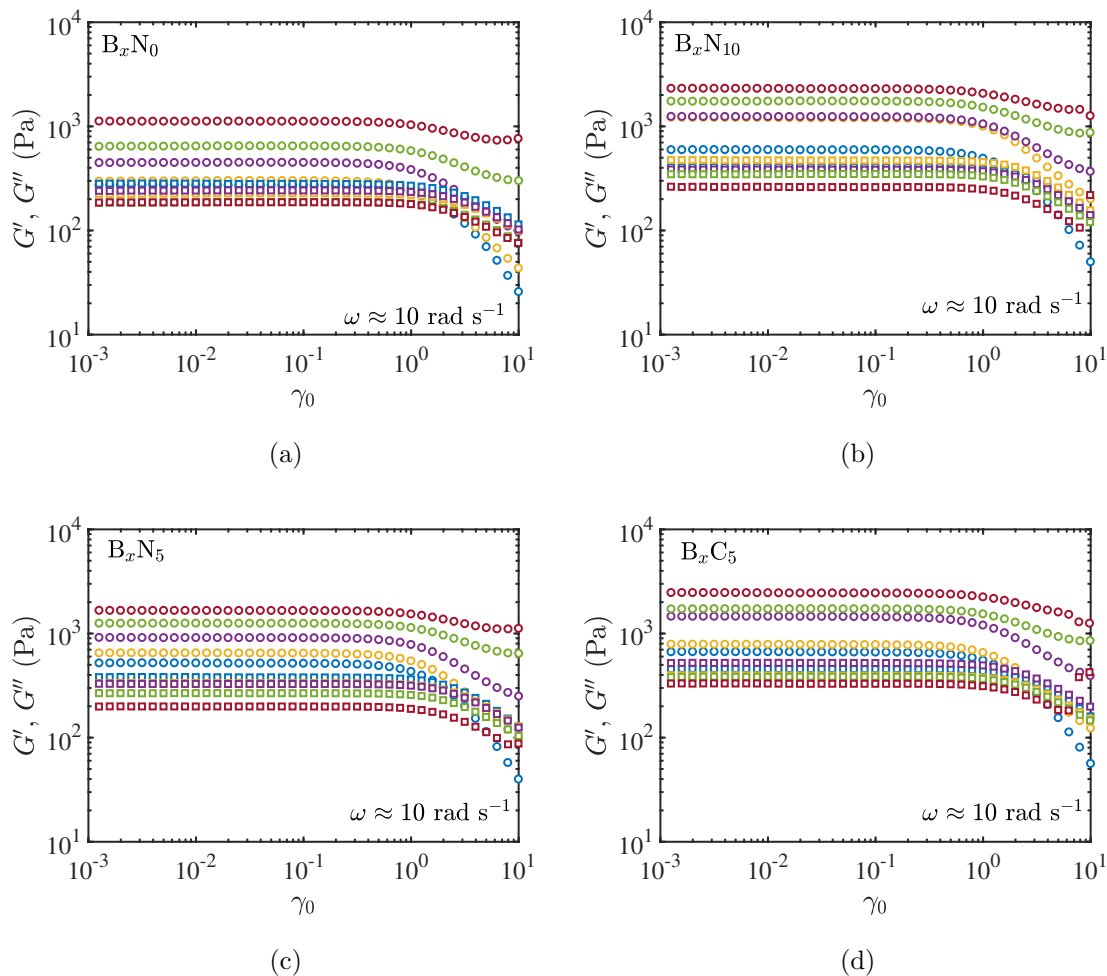
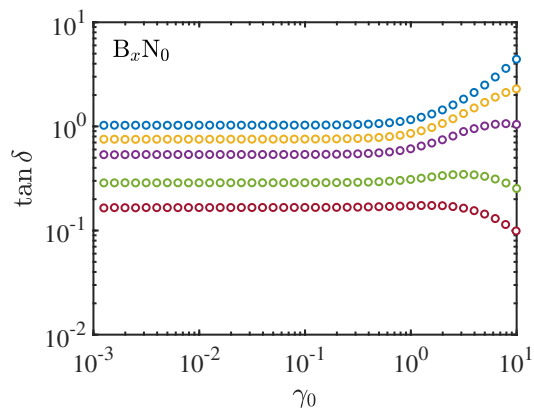
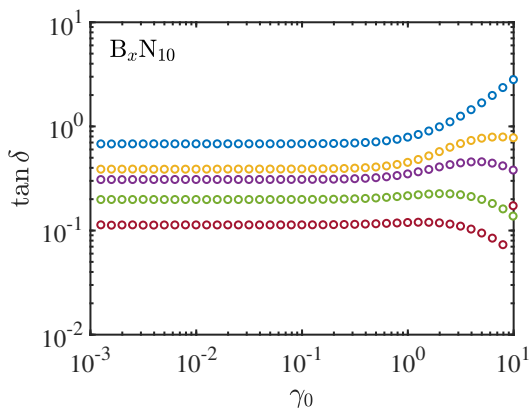


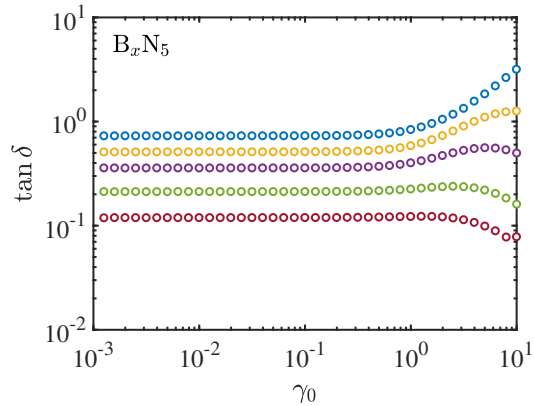
Figure 5.B.1: Storage (circles) and loss (squares) moduli versus strain amplitude (at $\omega \approx 10 \text{ rad s}^{-1}$) for bis-to-acrylamide ratios 0 (blue), 0.1 (yellow), 0.2 (purple), 0.4 (green) and 0.6 mmol mol^{-1} (red).



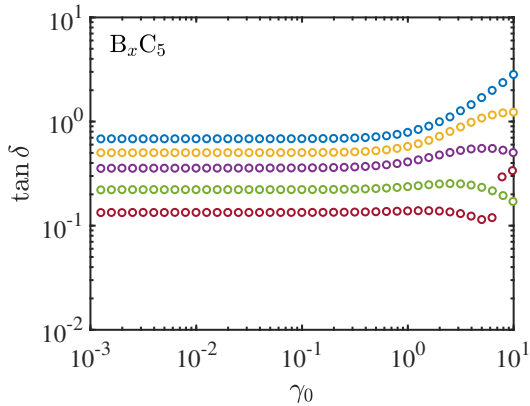
(a)



(b)



(c)



(d)

Figure 5.B.2: Loss tangent accompanying the dynamic moduli in Figure 5.B.1.

Nonlinear rheology of silica-doped polyacrylamide hydrogels under large amplitude oscillatory shear (LAOS)

6.1 Preface

The response of soft matter to deformation is often nonlinear, even under small strain. In many cases, the nonlinearity is due to changes in the microstructure. Some soft materials are subjected to high deformation rates during their production and processing, and this response is therefore of high practical relevance. In this Chapter, the nonlinear response of polyacrylamide and silica nanoparticle cross-linked polyacrylamide hydrogels is probed by conducting oscillatory shear experiments beyond their region of linear viscoelasticity. Such experiments are referred to as large-amplitude oscillatory shear (LAOS). LAOS test methods integrate well-known material measurements, including linear viscoelastic storage and loss moduli with nonlinear viscoelastic properties in a systematic way, allowing for the characterization of linear and nonlinear viscoelasticity. Inter/intracycle strain stiffening parameters, Lissajous-Bowditch curves, and relative harmonic intensities are used to depict the large-deformation responses.

Abstract

Whereas the linear viscoelasticity of polyacrylamide (PA) hydrogels cross-linked with silica nanoparticles (NPs) has been studied in detail, little is known of how NPs affect energy storage and dissipation at large strain. Indeed, deformation in practical applications can be large and rapid, limiting insights furnished by linear viscoelasticity. In this study, large amplitude oscillatory shear (LAOS) is adopted to study the effects of silica NPs on the elastic and viscous nonlinearities of “soft” and “stiff” PA hydrogels

are investigated and compared with the neat PA hydrogels. At large strain amplitudes ($\gamma_0 > 3$), the third harmonic relative intensity $I_{3/1}$ reveals that silica NPs have an effect on the nonlinear rheological response, suggesting heterogeneous deformation. The addition of PA-coated NPs to soft hydrogels suppresses the nonlinearity onset, as identified by the critical strain amplitude $\gamma_{0,c}$. In the range $\gamma_0 = 0.001$ – 10 , “soft” and “stiff” hydrogels exhibit (type II) strain hardening and (type III) weak strain overshoot, respectively. LAOS quantified the onset and degree of nonlinearity, distinguishing the viscoelastic responses of “soft” and “stiff” hydrogels in the strain amplitude range $\gamma_0 = 0.001$ – 10 , and revealing the effect of silica NPs on the flow-induced microstructure under large-strain deformation.

6.2 Introduction

Many industrial processes subject materials to large-strain deformation, and hence the rheological response is often nonlinear. For example, in injection processes and porous media flow through converging/diverging pores, [Aliabadian et al. \(2018\)](#) characterized the nonlinear viscoelastic properties of hybrid solutions of hydrolyzed polyacrylamide (HPAM) polymer and fumed silica nanoparticles (NPs) using large amplitude oscillatory shear (LAOS). They reported intracycle shear-thinning at large deformation that was not present under small amplitude oscillatory shear (SAOS). [Kamkar et al. \(2021\)](#) investigated the nonlinear viscoelastic response of a gelatin-based hydrogel used for tissue engineering, with capability to undergo large deformation. They reported inter/intracycle strain-stiffening using LAOS. Generally, most materials employed in tissue engineering tend to be subjected to large deformation, where the viscoelastic properties are nonlinear. The nonlinearity can be attributed to several factors, such as cell expansion, composition of extracellular matrices, combination and distribution of different cell types ([Abbasi M. et al., 2020](#)), and cell-wall structure ([Kamkar et al., 2021](#)).

Polyacrylamide (PA) hydrogels have been used extensively in many biological and tissue-engineering applications. For example, [Christensen et al. \(2016\)](#) implemented PA hydrogels as tissue scaffolds in the treatment of osteoarthritis, [Christensen et al. \(2013\)](#) used PA hydrogels as fillers in cosmetic surgery, and [Sokol et al. \(2014\)](#) used PA hydrogel as an injectable material for the treatment of female-stress incontinence. The ability of these gels to deform linearly when subjected to a wide range of stress, completely recover upon stress removal,

and the precise control of stiffness make them suitable materials for cell substrates, among other properties (Beningo et al., 2002, Kandow et al., 2007, Norris et al., 2021). In many of these applications, the hydrogels typically undergo transitions from the linear to the nonlinear regime with increasing strain amplitude. The behaviour of the hydrogels, when subjected to large deformation, can influence their performance. However, it is imperative to precisely evaluate and quantify the limit of the material deformation and the degree of non-linearity. The shear-thinning/thickening and self-healing capabilities of viscoelastic materials are important mechanical properties to drive biological responses (Winer and Oake, 2009, Chaudhuri et al., 2020). Boudou et al. (2009) investigated the nonlinear elastic properties of PA gels for applications in cell biology, determining the extent to which nonlinearity impacts the accuracy of cellular force measurement in traction-force microscopy (TFM). They reported an improvement in the accuracy of TFM data from the nonlinear elastic response of PA.

Large amplitude oscillatory shear (LAOS) is a commonly used rheological characterization that analyzes the non-sinusoidal stress response at large strain amplitudes (Hyun et al., 2002, Sim et al., 2003, Hyun et al., 2011). Viscoelastic parameters obtained from LAOS quantify microstructural changes, such as strain softening or hardening (Hyun et al., 2002). LAOS reveals the mechanical response of the material under large deformation, otherwise not readily measured under small amplitude oscillatory shear (SAOS). A wide range of conditions can be studied under LAOS within the capability of a rotational rheometer (Mackay, 1998) by independently controlling frequency and strain amplitude. LAOS has been extensively used in recent years to characterize nonlinear viscoelasticity of a variety of complex materials, including hydrogels (Abbasi M. et al., 2020, Kamkar et al., 2021), polymer nanocomposites (Lim et al., 2013, Kamkar et al., 2018, Aliabadian et al., 2018), suspensions (Ma et al., 2017), and polymer solutions (Goudoulas et al., 2017, Goudoulas and Germann, 2018).

Materials undergo a transition from linear to nonlinear rheology when subjected to increasing strain at a prescribed angular frequency ω . The stress response transitions from a single harmonic sinusoid in the linear region to a non-sinusoidal stress with higher harmonics. Several methods have been proposed to analyze and quantify the nonlinear rheological response, including Fourier transform rheology (FT-rheology) (Wilhelm, 2002), decomposition into characteristic waveforms (Klein et al., 2007), and stress decomposition (Cho et al., 2005). Ewoldt et al. (2008) reported several new measures derived from higher harmonic contributions and Chebyshev stress decomposition calculated from the odd, integer Fourier

coefficients. These complement widely used first-order Fourier coefficients, and provide interesting new insights into the nonlinear rheology (Ewoldt et al., 2008).

The linear viscoelastic rheology of PA hydrogels and nanocomposite hydrogels with varying monomer, chemical cross-linker, and NP concentrations have been studied extensively. The oscillatory response measured with SAOS is typically represented using dynamic storage G' and loss moduli G'' . Although the rheological analysis based on SAOS is widely used to investigate hydrogel microstructure, it provides limited understanding compared to LAOS because the stress response includes only the first harmonic. Large deformation provides a better understanding of the gel stiffness, since the nonlinear material response appears to include higher harmonics, providing new insights into the material response (Ewoldt et al., 2008).

In the present study, bare silica NPs and PA-coated silica NPs were used as fillers to modify the viscoelastic properties of neat PA hydrogels. Silica NPs are known for their unique properties, which stem from the dissociation of surface silanol groups to form negatively charged ions in water. In our previous study, we showed that by coating the NPs with PA before gelation, the storage and loss moduli could be increased. To evaluate and compare the microstructural changes of the neat PA hydrogels and silica-PA hydrogel nanocomposites under large deformation, several methods of quantifying the nonlinear viscoelastic properties were investigated. We adopted concentrations of pregel components representing “soft” and “stiff” gels. The effects of bare and PA-coated silica NPs on the nonlinear behaviour were compared with the neat hydrogels. The large deformation responses are mainly presented using inter/intracycle strain stiffening parameters, stress waveforms, and Lissajous–Bowditch curves, and other FT-rheology parameters: relative harmonic intensities and the nonlinear material coefficient. With the data accumulated, it was possible to quantitatively determine the onset/degree of nonlinearity, differentiate between the viscoelastic behaviour of the “soft” and “stiff” hydrogels within the strain range 0.001–10, and determine the effect of silica NPs on the flow-induced microstructure resulting from large strain deformation. The Lissajous–Bowditch curves provide an excellent visual description of the viscoelastic response of the samples as a function of both strain amplitude and frequency.

Slip is an important factor which can affect the rheology of complex soft materials. The presence of wall-slip, like LAOS, can result in nonlinear, nonsinusoidal waveforms. The slip phenomena is evaluated by testing the same sample using a sandblasted and cone-plate

geometry, in place of the parallel plate geometry. A reliable approach for checking slip is to use vane or roughened surface geometries (Walls et al., 2003). The application of large strain-high frequency combinations using smooth parallel plate geometries have been reported to cause significant slip (Yazar et al., 2019, Kamkar et al., 2021). Slip versus no-slip conditions were checked by comparing the nonlinear rheological data under the same conditions of frequency and strain amplitude. Identical stress waveforms from the three geometries is an indication of the absence of slip, so that the nonlinear response at large strains may be attributed to the sample.

6.3 LAOS and FT-rheology theory

A strain sweep performed at a fixed frequency generally reveals a linear and nonlinear regime. The linear regime occurs at a small amplitude, termed small amplitude oscillatory shear (SAOS), and can be characterized by rheological properties that are independent of strain amplitude. The viscoelastic moduli G' , G'' are precisely defined only in this regime. The nonlinear regime begins where the viscoelastic properties vary with strain amplitude. To implement this condition, the large amplitude oscillatory shear (LAOS) strain is applied, which is commonly quantified using Fourier transform (FT) rheology (Wilhelm, 2002). FT-rheology provides a physical and visual interpretation of the nonlinear viscoelastic response using the stress response and Lissajous-Bowditch curves, which represent the stress as a function of time and strain, respectively. The viscoelastic properties can be determined by imposing an oscillatory shear strain, $\gamma(t) = \gamma_0 \sin(\omega t)$, where γ_0 is the strain amplitude, ω is the oscillation frequency, and t is time. The shear stress response $\sigma(t)$ can be expressed as a Fourier series:

$$\sigma(t) = \sum_{n=1, \text{odd}} \sigma_n(\omega, \gamma_0) \sin[n\omega t + \delta_n(\omega, \gamma_0)], \quad (6.1)$$

where σ_n and δ_n are the harmonic stress magnitude and phase angle, respectively. Factoring out γ_0 , Eqn. (6.7) can be written as in- and out-of-phase components with the strain input:

$$\sigma(t) = \gamma_0 \sum_{n, \text{odd}} [G'_n(\omega, \gamma_0) \sin(n\omega t) + G''_n(\omega, \gamma_0) \cos(n\omega t)]. \quad (6.2)$$

Each component can be resolved using a Fourier transform. For small strains (SAOS), only the first harmonic $n = 1$ will be included in the stress response. At larger strains, the nonlinear material response produces an increasing number of harmonics, but only the odd

harmonics contribute to the stress response. This is because the material response remains unchanged upon reversing the coordinate system, *i.e.*, the stress response takes on odd symmetry with respect to the shear strain orientation (Ewoldt et al., 2008).

Several methods have been employed to interpret and quantify nonlinear viscoelasticity. One is the first harmonic coefficient of the elastic modulus

$$G'_1 = \frac{\omega}{\pi\gamma_0^2} \int \sigma(t)\gamma(t)dt, \quad (6.3)$$

which reduces to $G'(\omega)$, uniquely defined in the linear regime, but diverges under LAOS. Ewoldt et al. (2008) reported the inability of G'_1 to markedly capture the local elastic response at small and large instantaneous strains, thus defining new geometric elastic moduli:

$$G'_M = \left. \frac{d\sigma}{d\gamma} \right|_{\gamma=0} = \sum_{n, \text{odd}} nG'_n = e_1 - 3e_3 + \dots, \quad (6.4)$$

$$G'_L = \left. \frac{\sigma}{\gamma} \right|_{\gamma=\pm\gamma_0} = \sum_{n, \text{odd}} nG'_n (-1)^{(n-1)/2} = e_1 + e_3 + \dots, \quad (6.5)$$

where the minimum-strain modulus G'_M and large-strain modulus G'_L are equivalent to G' in the linear viscoelastic regime. G'_M captures the minimum-strain elastic response using the slope of the stress response at the point where $\gamma = 0$, whereas G'_L is equivalent to the stress response at maximum strain. The coefficient e_n is the elastic Chebyshev coefficient, related to the Fourier coefficient in the time domain by (Ewoldt et al., 2008)

$$e_n = G'_n (-1)^{(n-1)/2} \quad n : \text{odd}, \quad (6.6)$$

where the sign of the third-order component e_3 is used to indicate the degree of intracycle elastic nonlinearities: $e_3 > 0$ implies strain stiffening, $e_3 < 0$ strain softening, and $e_3 = 0$ signifies linear elastic response. Intercycle stiffening, on the other hand, is determined from a plot of the first component $e_1 = G'_1$ against γ_0 (Ewoldt et al., 2008). Another measure quantifying elastic intracycle nonlinearities is the strain-stiffening ratio (Ewoldt et al., 2008):

$$S \equiv 1 - \frac{G'_M}{G'_L} = \frac{4e_3 + \dots}{e_1 + e_3 + \dots}. \quad (6.7)$$

Similarly to e_3 , $S > 0$ corresponds to intracycle strain stiffening, $S < 0$ indicates intracycle strain softening, and $S = 0$ signifies linear elastic response. Inter/intracycle strain stiffening/softening parameters quantitatively differentiate the nonlinear viscoelastic response and the accompanying microstructural changes (Ewoldt et al., 2008, Hyun et al., 2011, Kamkar et al., 2021).

Another way of representing experimental data obtained from LAOS, and to qualitatively distinguish material response, are Lissajous-Bowditch curves and stress waveforms. The Lissajous-Bowditch curve is a parametric plot of the periodic shear stress response $\sigma(t)$ against the oscillatory shear strain $\gamma(t)$ at specified ω and γ_0 . For a linear viscoelastic material, the curve is an ellipse. A distortion in the curve reveals the contribution of higher harmonics in the shear stress waveform output.

An example is shown in Figure 6.3.1 for “soft” and “stiff” PA hydrogels with monomer concentration $c_a \approx 0.4 \text{ mol l}^{-1}$ at $\omega \approx 10 \text{ rad s}^{-1}$ with $\gamma_0 \approx 6$, and $c_a \approx 0.7 \text{ mol l}^{-1}$ at $\omega \approx 1 \text{ rad s}^{-1}$ with $\gamma_0 \approx 0.4$, both in the nonlinear regime, respectively. The shapes of the stress waveforms and Lissajous-Bowditch curves in both models are distinctively different, which means the flow-induced microstructure resulting from large strain deformation is greatly affected by the composition of the PA hydrogel.

The area enclosed by the Lissajous-Bowditch curve can be interpreted as the energy dissipated per unit volume in a complete cycle of imposed oscillatory strain (Ewoldt et al., 2010)

$$E_d = \oint \sigma d\gamma = \pi G_1'' \gamma_0^2. \quad (6.8)$$

Although the shape of the Lissajous-Bowditch curve depends on all harmonics, Eqn. (6.8) is only a function of G_1'' . The Lissajous-Bowditch curve for the corresponding perfectly plastic reference material is rectangular, enclosing the measured stress-strain response shown in Figure 6.3.2. The energy dissipated per cycle by a perfect plastic material in LAOS is (Ewoldt et al., 2010)

$$(E_d)_p = 4\gamma_0\sigma_{\max}, \quad (6.9)$$

where σ_{\max} is the maximum stress. The actual dissipated energy is normalized by the perfect plastic dissipation energy to give the energy dissipation ratio proposed by Ewoldt et al. (2010)

$$\phi_E \equiv \frac{E_d}{(E_d)_p} = \frac{\pi G_1'' \gamma_0}{4\sigma_{\max}}, \quad (6.10)$$

where $\phi_E \rightarrow 1$ implies a perfectly plastic material response, $\phi_E \rightarrow 0$ signifies purely elastic material response, and $\phi_E \approx \pi/4$ corresponds to a material that behaves as a Newtonian fluid. This ratio provides a comparison of the unknown material response with a perfect plastic model with the maximum possible energy dissipation.

The degree of nonlinearity can be quantified by relative intensity, defined as the ratio of the intensity of the higher harmonics to the first, $I_{n/1} \equiv I(n\omega_1)/I(\omega_1)$. The third harmonic

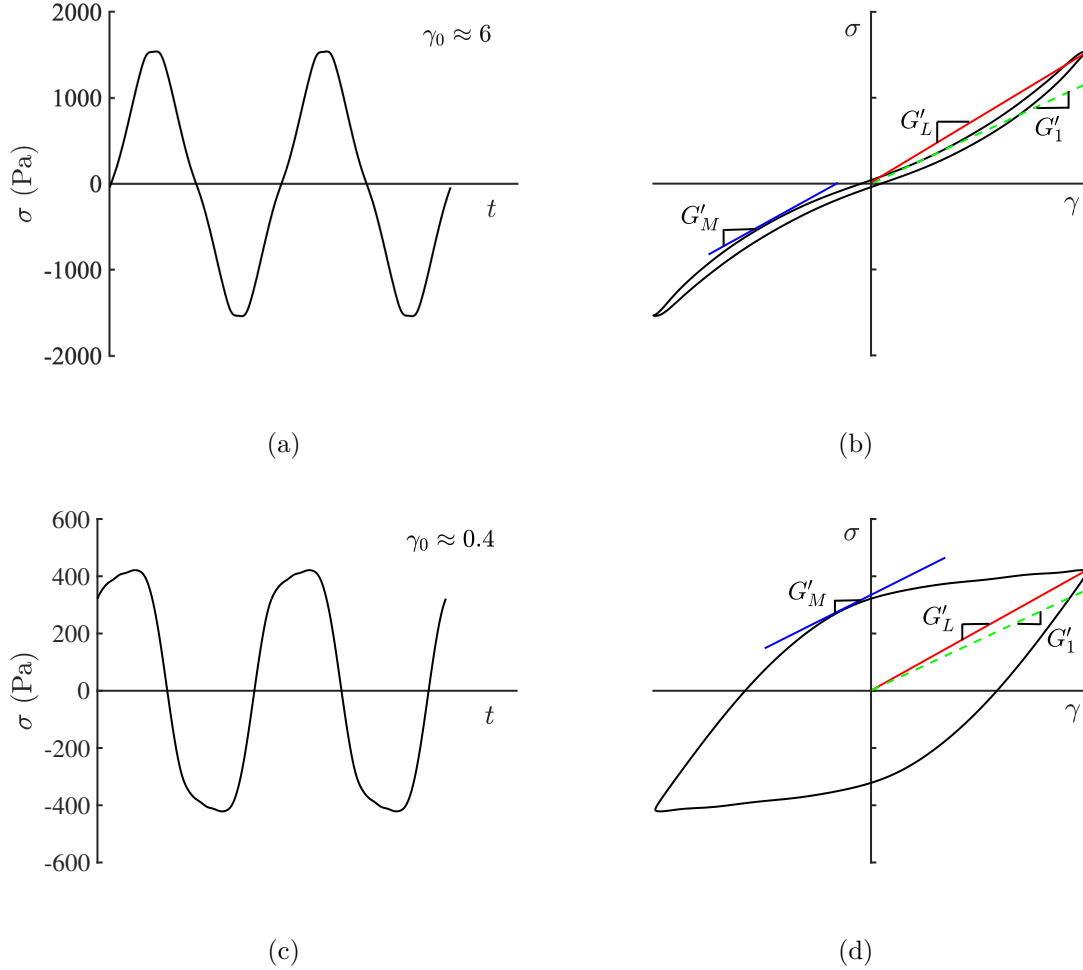


Figure 6.3.1: Stress waveforms (left) and Lissajous-Bowditch plots for the nonlinear viscoelastic response of “soft” PA hydrogel with 3 w% acrylamide and 2.6 w% bis-acrylamide to acrylamide ratio in the pregel solution at $\gamma_0 \approx 6$ and $\omega \approx 10 \text{ rad s}^{-1}$ (top); and “stiff” PA hydrogel with 5 w% acrylamide and 5.3 w% bis-acrylamide to acrylamide ratio in the pregel solution at $\gamma_0 \approx 0.4$ and $\omega \approx 1 \text{ rad s}^{-1}$ (bottom). The first harmonic modulus G'_1 , minimum-strain modulus G'_M and the large-strain modulus G'_L are distinctly defined on each Lissajous-Bowditch curve.

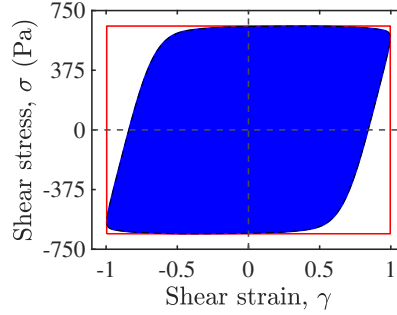


Figure 6.3.2: Lissajous-Bowditch plot for the nonlinear viscoelastic response of a “stiff” PA nanocomposite hydrogel with 5 w% acrylamide, 5.3 w% bis-acrylamide to acrylamide ratio and 2 v% silica NPs in the pregel solution at $\omega \approx 1 \text{ rad s}^{-1}$ and $\gamma_0 \approx 1$ (blue curve). This is enclosed by a rectangle representing a perfect plastic model response with $\gamma_0 \approx 1.0$ and maximum stress $\sigma_{\text{max}} \approx 653 \text{ Pa}$. The energy dissipation ratio $\phi_E = 0.813$.

contribution provides the highest relative intensity $I_{3/1}$ at a given frequency and strain amplitude, compared with the other odd harmonics ($I_{5/1}, I_{7/1}, \dots$), which decay very fast. Hence, $I_{3/1}$ is most important in quantifying nonlinear response. Under SAOS, $I_{3/1}$ is expected to scale quadratically with strain amplitude $I_{3/1} \propto \gamma_0^2$ (Wilhelm, 2002). Under LAOS, however, there is a crossover of the $I_{3/1}$ dependence from γ_0^2 to a general power-law behaviour, described by (Wilhelm, 2002, Neidhöfer et al., 2003)

$$I_{3/1} = A \left[1 - \frac{1}{1 + (B\gamma_0)^C} \right]. \quad (6.11)$$

where A is the maximum $I_{3/1}$ for large γ_0 , and $B = 1/\gamma_{0,c}$ is the reciprocal critical strain amplitude, which depends strongly on material structure, topology and nonlinearity (Filipe et al., 2008). The critical strain amplitude is the strain above which the amplitude of the stress decays. The parameter C is the power-law dependence. Expanding Eqn. (6.11) in a Taylor series in γ_0 , neglecting higher order terms, the scaling relationship can be written (Neidhöfer et al., 2003, Hyun et al., 2007, 2011)

$$\log(I_{3/1}) = K + C \log \gamma_0, \quad (6.12)$$

where K and C are the intercept and slope obtained from a log-log plot of $I_{3/1}$ versus γ_0 , respectively. Equation (6.12) is reported to be valid when $0.1 < \gamma_0 < 2$ for polymer melts, with $C = 2$ for linear polydisperse polypropylene (Hyun et al., 2006), linear monodisperse, and comb polystyrene (Hyun et al., 2007). However, Hyun et al. (2007) reported

$C < 2$ for several branched polymers and polymers with strain hardening behaviour, such as branched polypropylenes ($C \approx 1.60$), high-density polyethylene (HDPE, $C \approx 1.59$), low-density polyethylene (LDPE, $C \approx 1.63$), polylactic acid (PLA)/Epoxy ($C \approx 1.74$). These suggest that C is effective for determining the extent of chain branching and strain hardening. [Hyun et al. \(2006, 2007, 2011\)](#) concluded that C is unaffected by the polymer molecular weight, molecular weight distribution, and certain experimental conditions, such as temperature and frequency. The intercept K , on the other hand, is affected by the degree of shear thinning, frequency and temperature ([Hyun et al., 2007](#)).

Another measure of nonlinearity is the nonlinear coefficient ([Hyun and Wilhelm, 2008](#), [Hyun and Kim, 2011](#))

$$Q(\omega, \gamma_0) \equiv I_{3/1}/\gamma_0^2, \quad (6.13)$$

which at small strain amplitude becomes ([Hyun and Wilhelm, 2008](#))

$$Q_0(\omega) = \lim_{\gamma_0 \rightarrow 0} Q(\omega, \gamma_0). \quad (6.14)$$

Q and Q_0 tell a lot more about the stress curve than $I_{3/1}$, and provide useful information on molecular structure. The parameter Q_0 is strongly dependent on frequency, and can be used to quantify the intrinsic nonlinear response of complex fluids ([Hyun et al., 2011](#)). For a linear polymer melt, Q is expected to be constant at small and medium strain amplitude, which reduces as the strain amplitude increases. [Hyun and Wilhelm \(2008\)](#) investigated the influence of polymer topology on Q and Q_0 by comparing FT-rheology for linear and comb polystyrene melts. They reported an increasing Q with γ_0 for the comb PS with entangled branches, attributing this to long-chain branching and entanglement. [Lim et al. \(2013\)](#) proposed a mathematical model, similar to the ‘‘Carreau-Yasuda’’ viscosity equation, for fitting to γ_0 :

$$Q = Q_0[1 + (C_1\gamma_0)^{C_2}]^{(C_3-1)/C_2}, \quad (6.15)$$

where Q_0 , C_1 , C_2 and C_3 are fitting parameters, from which other interesting quantities to describe nonlinearity can be obtained, *e.g.*, $C_1 = 1/\gamma_{0,c}$ is the reciprocal critical strain amplitude and C_3 is the degree of strain thinning.

To further investigate the extent of nonlinearity and effect of NP doping, [Lim et al. \(2013\)](#) defined the nonlinear viscoelastic ratio (NLR), which provides a comparison between the linear and nonlinear behaviour of the NP-doped hydrogels. It determines which of SAOS or LAOS parameters provide more sensitivity to morphological changes. NLR relates the

normalized Q_0 in LAOS to the complex modulus G^* in SAOS for nanocomposite hydrogels relative to the neat counterparts (Lim et al., 2013):

$$\text{NLR} = \frac{Q_0(\phi)/Q_0(0)}{G^*(\phi)/G^*(0)}, \quad (6.16)$$

where ϕ is the NP volume fraction. When $\text{NLR} = 1$, the addition of NPs changes the nonlinear viscoelasticity in the same manner as the linear viscoelasticity. When $\text{NLR} > 1$, the morphology of the composite hydrogel amplifies the nonlinear properties more than the linear properties, while the reverse is applicable when $\text{NLR} < 1$.

In this work, we describe the nonlinear rheology of hydrogels and nanocomposite hydrogels using LAOS and FT-rheology by comparing “soft” and “stiff” gel samples, and analyzing the influence of bare and PA-coated NPs on the nonlinear response.

6.4 Materials and methods

6.4.1 Materials

Acrylamide (AAM) solution (40 w/v%, Fisher Scientific, U.S.A.), N,N' -methylene (bis) acrylamide (2 w/v%, Fisher Scientific), ammonium persulfate (APS) powder ($\geq 98\%$, Fisher Scientific, U.S.A.) and N,N,N',N' -tetramethylethylenediamine (TEMED, 99%, GE Healthcare Life Science, Germany) were used as monomer, chemical cross-linker, initiator and catalyst, respectively. Silica NPs, available as Ludox[®] TM50 (50 w% colloidal suspension, Sigma-Aldrich Inc., U.S.A.) with diameter $d \approx 30$ nm, served as a physical cross-linker. All were used as provided by the manufacturers. Polyacrylamide (PA)-coated silica NPs (as prepared in Chapter 3) containing 1.25 w/v% PA and 5 w/v% colloidal silica (Ludox[®] TM50) were used as a physical cross-linker.

The hydrogels were prepared by mixing acrylamide solution, bis-acrylamide solution, and silica NPs (in the case of nanocomposite hydrogels) in a centrifuge tube with dilution using reverse-osmosis (RO) water (Type 1, $\sigma \approx 5.6 \mu\text{S m}^{-1}$, $\Omega \approx 18 \text{ MOhm cm}$ at 25°C). The concentrations are shown in Table 6.4.1. Dissolved oxygen was removed after adding $10 \mu\text{l}$ of freshly prepared APS solution (0.44 mol l^{-1}) by bubbling N_2 gas for 5 min. TEMED ($3 \mu\text{l}$ per ml of total pre-gel solution) was added immediately before rheological measurements. The nomenclature $\text{A}_x\text{B}_y\text{N}_\phi$ (or $\text{A}_x\text{B}_y\text{C}_\phi$ for the samples with PA-coated NPs) is adopted to

Table 6.4.1: Compositions and steady-state linear viscoelastic properties of PA hydrogels and nanocomposite hydrogels at $\omega \approx 10 \text{ rad s}^{-1}$ (for the soft gels), $\omega \approx 1 \text{ rad s}^{-1}$ (for the stiff gels), with $\gamma_0 \approx 0.02$.

Sample	c_a (mol l ⁻¹)	c_{bis}/c_a (w%)	ϕ (v%)	G'_∞ (Pa)	G''_∞ (Pa)
“Soft”					
A ₃ B _{2.6}	0.42	2.6	0	131	1.3
A ₃ B _{2.6} N ₅	0.42	2.6	5	204	1.6
A ₃ B _{2.6} C ₅	0.42	2.6	5	288	6.3
“Stiff”					
A ₅ B _{5.3}	0.71	5.3	0	2890	1.1
A ₅ B _{5.3} N ₂	0.71	5.3	2	3630	4.5

identify the samples, where x is the monomer concentration, y is the ratio of bis-acrylamide cross-linker to acrylamide ratio, and ϕ is the NP (or PA-coated NP) volume fraction. All the concentrations are based on the total volume of the pre-gel solution in a centrifuge tube.

6.4.2 Methods

Rheometry

All rheological measurements were performed using an ARES-G2 strain-controlled type rotational rheometer (TA Instruments, U.S.A), mostly using a 25 mm diameter titanium smooth parallel plate-plate (PP) geometry. The test modes were carried out with the sample sandwiched between the plates. Temperature control was achieved with a Peltier plate system, and the gap was maintained at 1 mm to minimize sample inertia. The surface around the sample was coated with silicone oil with an evaporation blocker provided by the manufacturer to minimize evaporation.

The torque response for the plate-plate geometry in the LAOS regime is governed by nondimensional parameters; relative magnitude of yield strain and strain amplitude at the plate edge $\gamma_0 = R\theta_0/h$, where θ_0 is the plate maximum angular displacement, R is the

plate radius, and h is the gap. [Ewoldt et al. \(2010\)](#) attributed torque response from a plate-plate geometry in LAOS to inhomogenous shear deformation, with the tendency to smoothen the linear-to-nonlinear transitions without the introduction of any new qualitative features. They reported close resemblance of the characteristic shapes of the Lissajous curves in LAOS for the plate-plate and cone-plate geometries, and small overestimation of stresses for yield stress or shear-thinning materials. In an attempt to limit or eradicate wall-slip effects, parallel plate geometry (PP) was replaced with a 25 mm, 0.04 rad cone-plate (CP) and 25 mm diameter sandblasted plate (SP) geometries. Rheological tests on sample A₅B_{5.3}, using these three geometries were compared.

Small amplitude oscillatory shear

Gelation dynamics were monitored at an angular frequency $\omega \approx 10 \text{ rad s}^{-1}$ for the “soft” gels ($c_a \approx 3 \text{ w\%}$) and $\omega \approx 1 \text{ rad s}^{-1}$ for the stiff gels ($c_a \approx 5 \text{ w\%}$) with strain amplitude $\gamma_0 \approx 0.02$. When the properties reached a steady state ($\approx 60 \text{ min}$ for the soft gels and $\approx 30 \text{ min}$ for the stiff gels), strain sweep tests were performed in the range $\gamma_0 \approx 0.001$ –1 to determine the onset of nonlinearity (identified as the critical strain amplitude value after which the moduli vary non-linearly with amplitude). Then, frequency sweeps in the range $\omega \approx 0.1$ –100 rad s^{-1} at temperature $T \approx 21^\circ\text{C}$ and $\gamma_0 \approx 0.02$ were performed to determine the steady-state response in the linear viscoelastic regime.

Large amplitude oscillatory shear

Strain sweep experiments were conducted in the range $\gamma_0 \approx 0.001$ –10 in a strain-controlled mode at 21°C and $\omega \approx 10$ and 1 rad s^{-1} for the hydrogels with $c_a \approx 3$ and 5 w\% , respectively. The samples remained intact (no rupture) despite undergoing deformation with $\gamma_0 = 10$. The data acquisition mode in the ARES-G2 rheometer software (TRIOS) was set to “transient”, to allow for FT-rheology evaluations of the raw data using the FT-rheology software package incorporated into TRIOS. This package allows for the transformation of the raw stress and strain functions to the power and phase spectra, from which the fundamental and harmonic frequencies are extracted. Fourier coefficients (G'_n , G''_n), intensity ratio ($I_{n/1}$), and the Chebyshev coefficient (e_n) can be calculated from the odd harmonics n , from which other nonlinear measures, such as G'_M , G'_L , Q , *etc*, are calculated.

6.5 Results and discussion

6.5.1 Linear viscoelastic response

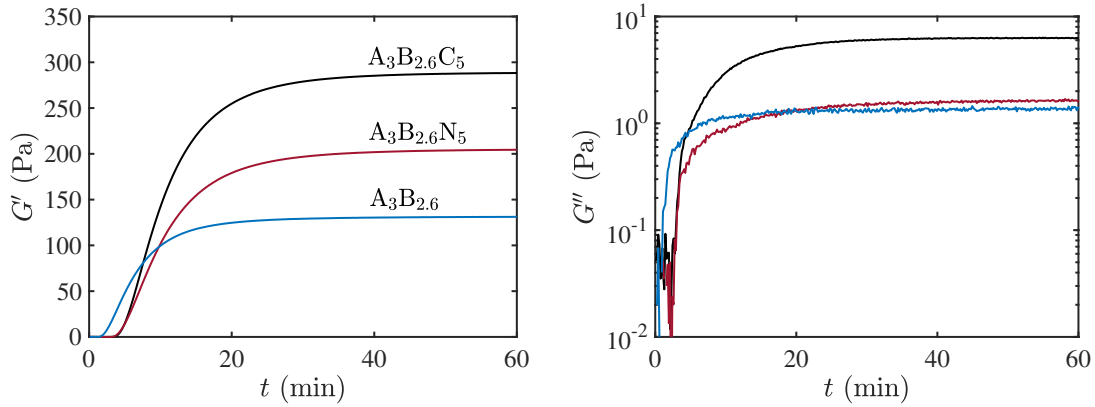
Polymerization and cross-linking time series

Storage and loss moduli time series during gelation of the samples at $\omega \approx 10$ and 1 rad s^{-1} for the hydrogels with $c_a \approx 3$ and 5 w\% , respectively, are shown in Figure 6.5.1. These are typical responses for PA hydrogels and nanocomposite hydrogels (Adibnia et al., 2017b). After an initial incubation period t_i , defined by Adibnia et al. (2017b) as the time during which the moduli are below the instrument sensitivity, the moduli increase rapidly until they reach their steady-state values. Nanocomposite hydrogels have longer incubation times and higher steady-state storage and loss moduli than the neat hydrogels. This implies that the addition of NPs not only increases the stiffness, but likewise increases the viscosity $\eta' = G''/\omega$. Adibnia et al. (2017b) attributed the increase in G'' for nanocomposites to adsorption/desorption and friction at the NP surface. The PA-coated NPs in sample $A_3B_{2.6}C_5$ increase G' by a factor 2.2, whereas the bare NPs in sample $A_3B_{2.6}N_5$, with the same volume fraction, increase G' by a factor 1.6.

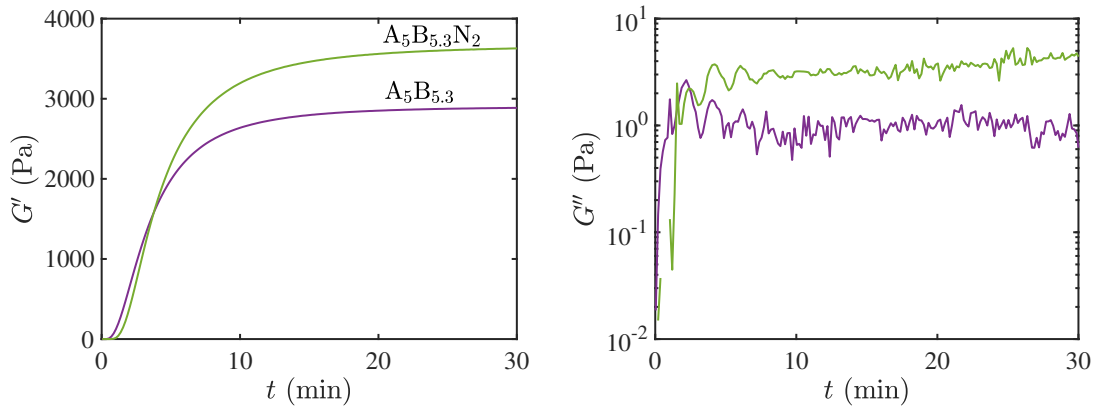
The low signal to noise ratio may be attributed to the low response of G'' at $\gamma_0 \approx 0.02$ or the strongly elastic hydrogel with $G'' < 0.1\%$ of the G' values.

Dynamic moduli spectra

Dynamic moduli spectra in the linear viscoelastic regime provide useful benchmarks with which to distinguish the microstructures. The top panel of Figure 6.5.2 compares storage and loss moduli spectra with $\gamma_0 \approx 0.02$ and $T = 21^\circ\text{C}$ for the samples listed in Table 6.4.1. These are all viscoelastic solids for which G' is constant, and $\tan \delta \ll 1$ over the entire frequency range. The nanocomposite moduli are increased by NP loading due to PA cross-linking promoted by silica (Chapters 4 and 5). Moreover, the PA coating of silica for sample $A_3B_{2.6}C_5$ further increases G' due to improved interfacial coupling (Chapters 4 and 5). The stiffer hydrogels present a loss modulus G'' that is weak and frequency independent, whereas soft hydrogels have power-law scaling, increasing approximately as $G'' \sim \omega^{2/3}$. Similarly to their effect on G' , NPs increase G'' for both types of hydrogels.

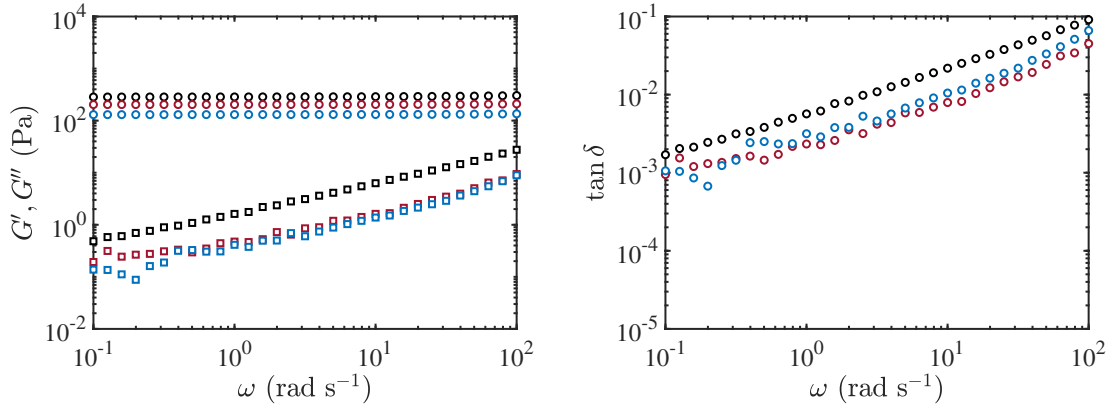


(a) “Soft” samples.

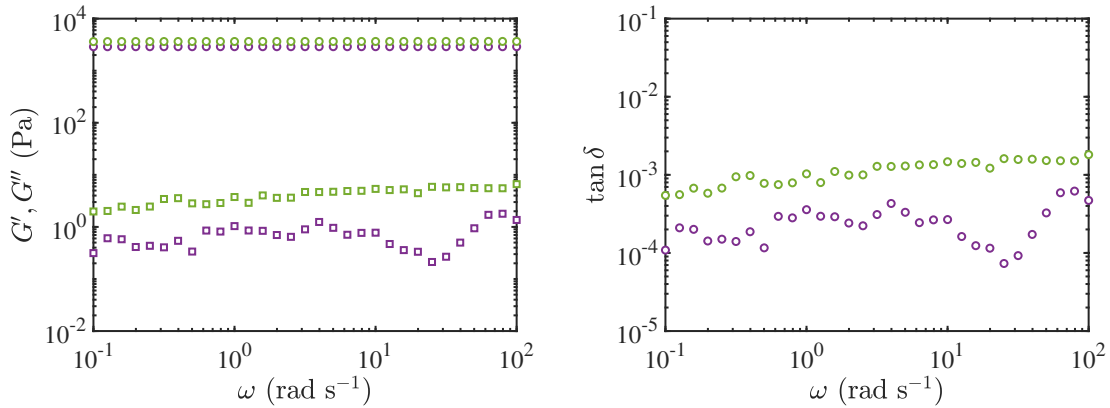


(b) “Stiff” samples.

Figure 6.5.1: Storage (left) and loss (right) moduli time series during polymerization and cross-linking with $\gamma_0 \approx 0.02$ and $\omega \approx 10 \text{ rad s}^{-1}$ for samples $A_3B_{2.6}$, $A_3B_{2.6}N_5$, and $A_3B_{2.6}C_5$ (a) and $\omega \approx 1 \text{ rad s}^{-1}$ for samples $A_5B_{5.3}$, $A_5B_{5.3}N_2$ (b).



(a) “Soft” samples.



(b) “Stiff” samples.

Figure 6.5.2: Steady-state storage (circles) and loss (squares) moduli spectra, loss tangent spectra accompanying the time series in Figure 6.5.1, in the linear-viscoelastic regime ($\gamma_0 \approx 0.02$).

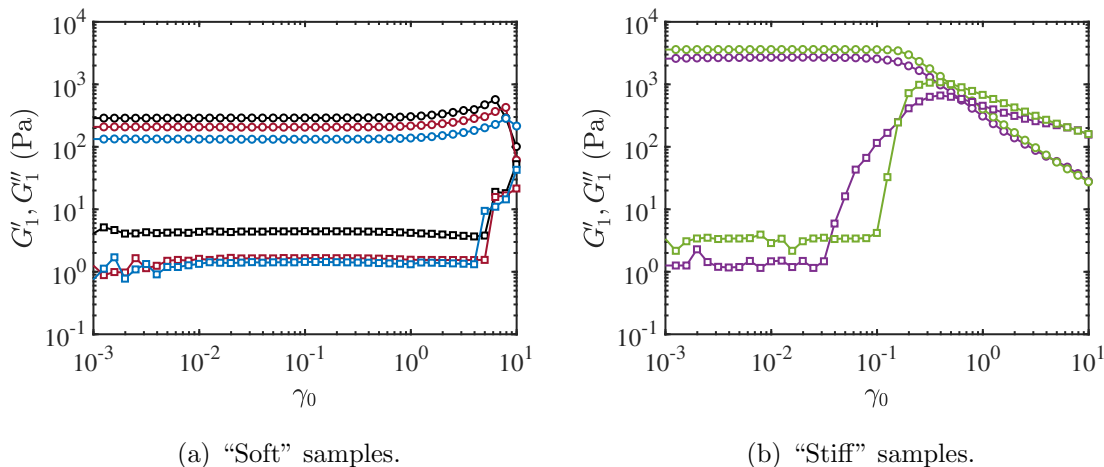


Figure 6.5.3: First-harmonic elastic G'_1 (circles) and loss G''_1 (squares) moduli versus strain amplitude γ_0 at $\omega = 10 \text{ rad s}^{-1}$ for “soft” gels (a) and $\omega = 1 \text{ rad s}^{-1}$ for the “stiff” gels (b). Colors are the same as in Figure 6.5.1.

6.5.2 LAOS test and FT-rheology

The elastic and loss moduli, captured by the first harmonic coefficient G'_1 and G''_1 , plotted against strain amplitude γ_0 in Figure 6.5.3. The linear viscoelastic region, identified by values of G'_1 and G''_1 that are independent of γ_0 , varies according to the sample composition, extending to much larger γ_0 for soft samples compared to stiff samples. Above this critical strain, both G'_1 and G''_1 increased for the soft samples. For the stiff gels ($A_5B_{5.3}$ and $A_5B_{5.3}N_2$), G'_1 decreased, whereas G''_1 increased, reaches a maximum and then decreased.

These nonlinear responses are classified by [Hyun et al. \(2002, 2011\)](#) as type II or strain hardening (G'_1 and G''_1 increase) and type III or weak strain overshoot (G'_1 decreases, G''_1 increases followed by a decrease), respectively. The type II behaviour has been identified for a poly(vinyl alcohol) (PVA)/borax solution ([Hyun et al., 2002](#)) and a gelatin-based hydrogel ([Kamkar et al., 2021](#)). Strain hardening in these materials was attributed to gelation or shear-induced network formation ([Hyun et al., 2002](#)). Weak strain overshoot (type III) was observed for carbon black filled natural rubber ([Roland, 1990, Fan et al., 2019](#)), silica-filled styrene-butadiene rubber ([Ramier et al., 2007](#)), polyethylene oxide (PEO)-protected silica particles ([Derec et al., 2003](#)), fumed silica suspension ([Raghavan and Khan, 1997, Yziquel et al., 1999, Ma et al., 2017](#)), and Xantham gum ([Hyun et al., 2002](#)). It is described to have originated from several sources, including energy dissipation from chain friction at

the filler surface (Ramier et al., 2007), destruction of filler network (Roland, 1990, Yziquel et al., 1999), and interaction of side chains (Hyun et al., 2002).

The existence of weak strain overshoot is characterized by a local maximum in the loss modulus (right panel of Figure 6.5.3). Sim et al. (2003) related the increase of G_1'' , followed by a decrease, to the destruction of microstructure resulting from imposed strain, and the reformation of clusters, respectively. Parthasarathy and Klingenberg (1999) attributed the overshoot of G_1'' to slight rearrangements of unstable clusters, followed by larger-scale structural rearrangements as the strain amplitude is further increased. Hyun et al. (2002) explained the increase of G_1'' at large strains to be due to the destruction of the complex structure, with a subsequent decrease the result of chain alignment with the flow. In general, the overshoot is material-dependent, thus motivating further investigation of the nonlinear viscoelasticity from the higher harmonics.

The first harmonic viscoelastic moduli are not sufficient to characterize the nonlinear stress response. Higher harmonic contributions that capture small and large instantaneous strains are considered, according to Eqns. (6.4) and (6.5). Figure 6.5.4 shows a plot of first harmonic modulus G_1' , large-strain modulus G_L' , and minimum-strain modulus G_M' as functions of strain amplitude γ_0 . These intercycle variations of the elastic moduli converge in the SAOS regime, although G_M' appears to show significant variations at very low strain amplitudes (< 0.01) for the soft gels ($A_3B_{2.6}$, $A_3B_{2.6}N_5$, and $A_3B_{2.6}C_5$), possibly due to experimental noise. In these gels, G_1' and G_L' increases significantly with γ_0 at large strains, compared to G_M' with barely noticeable changes. This is an indication of intracycle strain stiffening. For the stiff gels ($A_5B_{5.3}$ and $A_5B_{5.3}N_2$), G_1' appear to have values that fall between G_L' and G_M' at large γ_0 (> 0.2). This supports the definition of G_1' by Ewoldt et al. (2008) as an average measure of elasticity throughout the oscillatory cycle. The elastic moduli follow the order $G_M' < G_1' < G_L'$.

The type III behaviour in Figure 6.5.3(b) is related to the higher elasticity of the stiff gel compared to the soft gel, among other factors. The occurrence or not of wall-slip effect at large γ_0 was investigated by varying the rheometer plate geometry. Figure 6.5.5 shows the nonlinear viscoelastic parameters as a function of strain amplitude using smooth parallel plate (PP, circles), cone-plate (CP, squares), and sandblasted plate (SP, diamonds) geometries for “stiff” sample $A_5B_{5.3}$. Varying the plate geometry did not change the weak strain overshoot response. The yield points (where the two moduli cross) with different plate

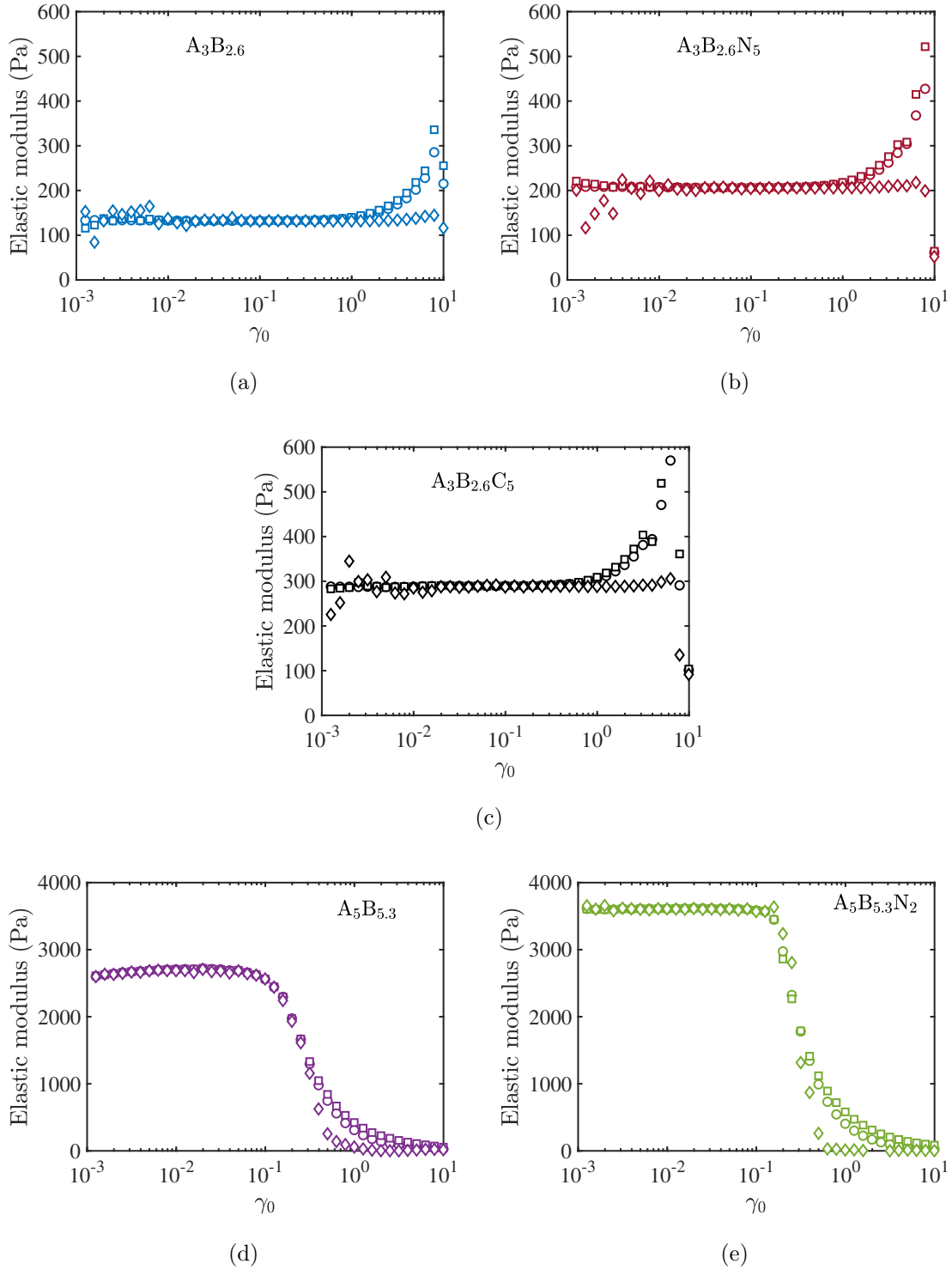


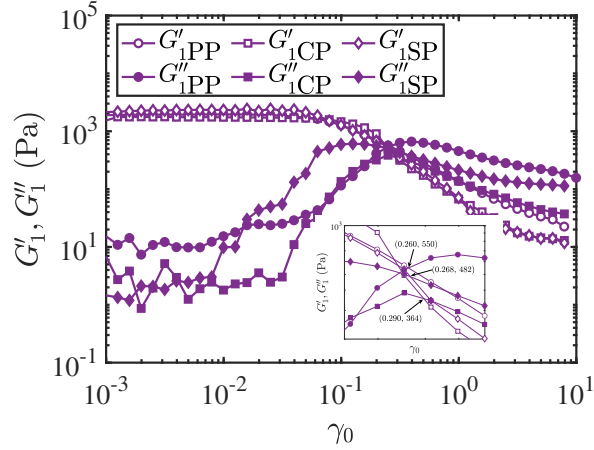
Figure 6.5.4: Comparison of the first harmonic elastic modulus G'_1 (circles), large-strain modulus G'_L (squares), and minimum-strain modulus G'_M (diamonds).

geometries do not have distinctly different values of γ_0 . [Kamkar et al. \(2021\)](#) investigated the wall slip effect in the viscoelastic behaviour of gelatin-based hydrogels at large strain amplitudes using glass slides, with and without sandpaper as rheometer plate geometries. They attributed the type III nonlinear response (sudden decline in G'_1) in their moduli versus strain plot to the existence of wall-slip, rather than yielding.

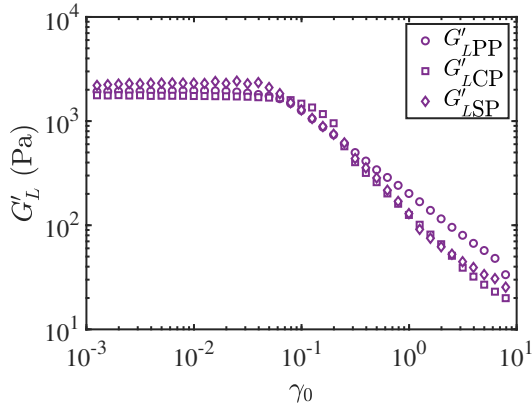
The fundamental differences in the large amplitude response were further investigated using the elastic Chebyshev coefficient e_3 from Eqn. (6.6) and strain-stiffening ratio S from Eqn. (6.7). These describe the intracycle elastic nonlinearities as shown in Figure 6.5.6. In the linear regime ($0.001 < \gamma_0 < 0.3$ for the soft gels, and $0.001 < \gamma_0 < 0.1$ for the stiff gels), $e_3 \approx 0$ and $S \approx 0$. The noisy S data at extremely low strain values ($0.001 < \gamma_0 < 0.03$) for the soft gels correspond to G'_M in the same γ_0 range, shown in Figure 6.5.4(a).

At large strain amplitudes, both e_3 and S take on positive values, indicating intracycle strain stiffening. [Aliabadian et al. \(2018\)](#) attributed the strain-stiffening behaviour in polymer solutions containing fumed silica NPs to deformation-induced network restructuring and the breakup of large NP agglomerates. The latter explains the slightly higher peaks obtained for the nanocomposites. Figure 6.5.7 shows the comparison of e_3 and S using different plate geometries for the “stiff” gel A₅B_{5.3}. The peaks appear at lower strains with the cone plate and sandblasted plate geometries. However, there is no qualitative difference in the response from the three plate geometries. The observed decrease in both e_3 and S (> 0) at large strain amplitudes follows the complete breakup of the gel network structures, and such behaviour was considered by [Aliabadian et al. \(2018\)](#) as an indication of slippage at the gel interface.

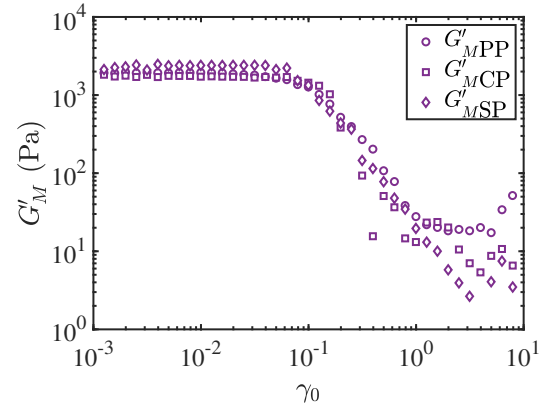
The shear stress waveform and the corresponding Lissajous-Bowditch curves for $\gamma_0 \approx 0.05, 0.2, 1, \text{ and } 6$, which show the transition from the SAOS to LAOS regimes, are shown in Figures 6.5.8 and 6.5.9 for the soft gels at $\omega \approx 10 \text{ rad s}^{-1}$ and for the stiff gels at $\omega \approx 1 \text{ rad s}^{-1}$, respectively. The Lissajous-Bowditch curves provide an excellent visual description of the viscoelastic response of these samples as a function of both strain amplitude and frequency. In the SAOS regime, the stress response is sinusoidal and the Lissajous-Bowditch curve appears as an ellipse ([Ewoldt et al., 2008](#)). At constant ω , the elliptical curves are independent of imposed strain amplitudes in the linear regime, but change with the maximum stress magnitude. The changes in the shapes of the Lissajous-Bowditch curves and distortion of the stress response curves represent the material nonlinearity at large strain. The stress amplitude at each strain amplitude increases for the nanocomposite hydrogels due to their



(a)



(b)



(c)

Figure 6.5.5: First-harmonic moduli G'_1 , G''_1 (top), large-strain elastic modulus G'_L , and minimum-strain elastic modulus G'_M (bottom) versus strain amplitude γ_0 at $\omega = 1 \text{ rad s}^{-1}$ for sample $A_5B_{5.3}$. Different rheometer plate geometries (indicated) are reported to investigate the existence or not of wall-slip. The cross-over amplitude and modulus for each plate geometry are shown in the inset of (a).

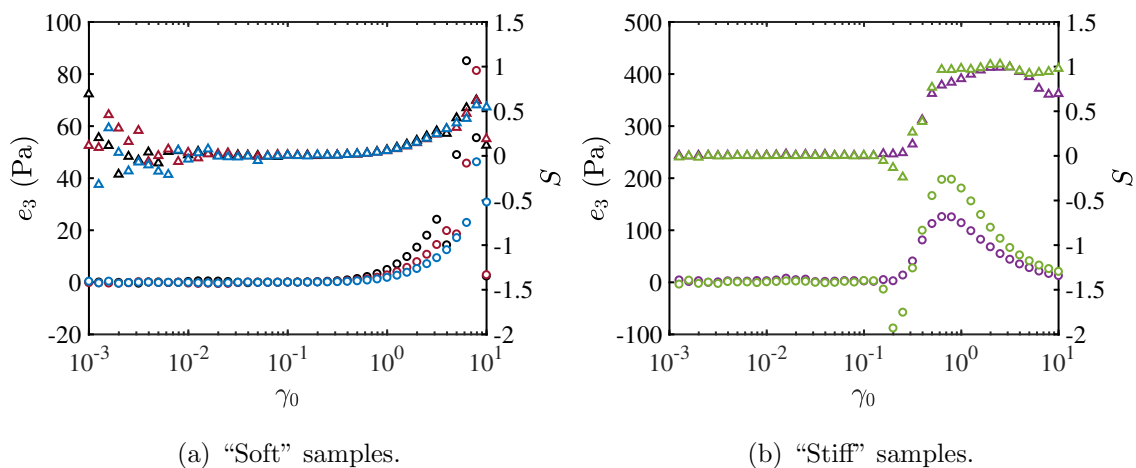


Figure 6.5.6: Third order elastic Chebyshev coefficient e_3 (circles) and strain-stiffening ratio S (triangles). Colors are the same as in Figure 6.5.1.

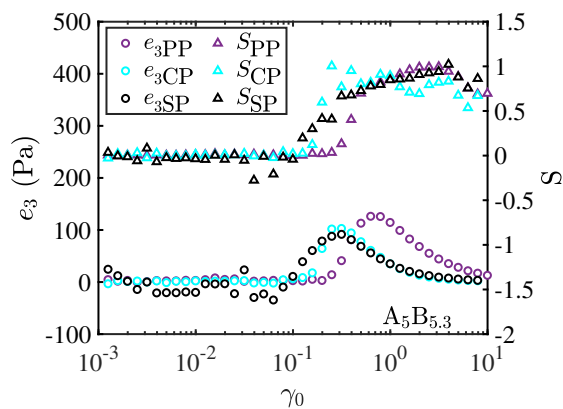


Figure 6.5.7: Third order elastic Chebyshev coefficient e_3 (circles) and strain-stiffening ratio S (triangles) for sample $A_5B_{5,3}$. Different rheometer plate geometries (indicated) are reported to investigate the existence or not of wall-slip.

stiffer networks. The shapes are different for the “soft” and “stiff” hydrogels, caused by different microstructures. The non-sinusoidal waveform shapes at large strain amplitudes are a consequence of higher harmonics. However, the predominant determining factor is the 3rd harmonic response, since higher-order contributions tend to decay rapidly, as later shown in Figure 6.5.11 by the relative harmonic intensity $I_{n/1}$ as a function of strain amplitude at $n = 3, 5, 7$ and 9 .

The narrow ellipses at low strains are indications of a predominantly elastic response. The almost rectangular shape at large strains for the stiff gels indicate yielding, followed by flow (the maximum stress), and then recovery. At extremely high strains, an “overshoot” is observed after yielding, where the loss modulus likewise decreases after reaching a maximum. The area enclosed within the Lissajous-Bowditch curves increases with increasing strain amplitude. The energy dissipation ratio ϕ_E as a function of strain amplitude for the “stiff” gels is shown in Figure 6.5.10. In the SAOS regime, ϕ_E is small, indicating a predominantly elastic response. A larger strain amplitude leads to a larger dissipation ratio. Eventually, a maximum ratio ≈ 0.85 – 0.90 is obtained, implying viscous behaviour (weak elasticity). For the “soft” hydrogels, $\phi_E = 0$ – 0.2 within the strain amplitude range $\gamma_0 = 0.001$ – 10 at $\omega \approx 10 \text{ rad s}^{-1}$, highlighting the significance of elasticity in this region.

The degree of nonlinearity can be quantified according to the ratio $I(n\omega)/I(\omega) \equiv I_{n/1}$, where $I(n\omega)$ is the magnitude at the n th harmonic and $I(\omega)$ is the intensity at the fundamental frequency ω . Figure 6.5.11 shows a log-log plot of $I_{n/1}$ versus strain amplitude in the range 0.1 – 10 for $n = 3, 5, 7$, and 9 . The relative intensities increase with strain amplitude with a plateau at high strain amplitudes that is more pronounced for the stiff gels.

[Lim et al. \(2013\)](#) reported such a plateau for polycaprolactone (PCL)/multiwall nanotube (MWNT) nanocomposites with MWNT concentrations above $0.5 \text{ wt}\%$ and attributed this to a change of microstructure, which was confirmed by measuring conductivity as a function of strain amplitude. They obtained conductivities that were independent of γ_0 until the critical strain amplitude (at maximum $I_{3/1}$) where the values decreased, concluding a break-up of the percolating structure from alignment of carbon nanotubes with the flow ([Lim et al., 2013](#)).

The relative intensities decrease exponentially from the highest, $I_{3/1}$, which is the first to appear above the noise level, to the higher order odd harmonics, $I_{5/1}, I_{7/1}, \dots$ etc. These higher order contributions are important when materials are subjected to extremely large

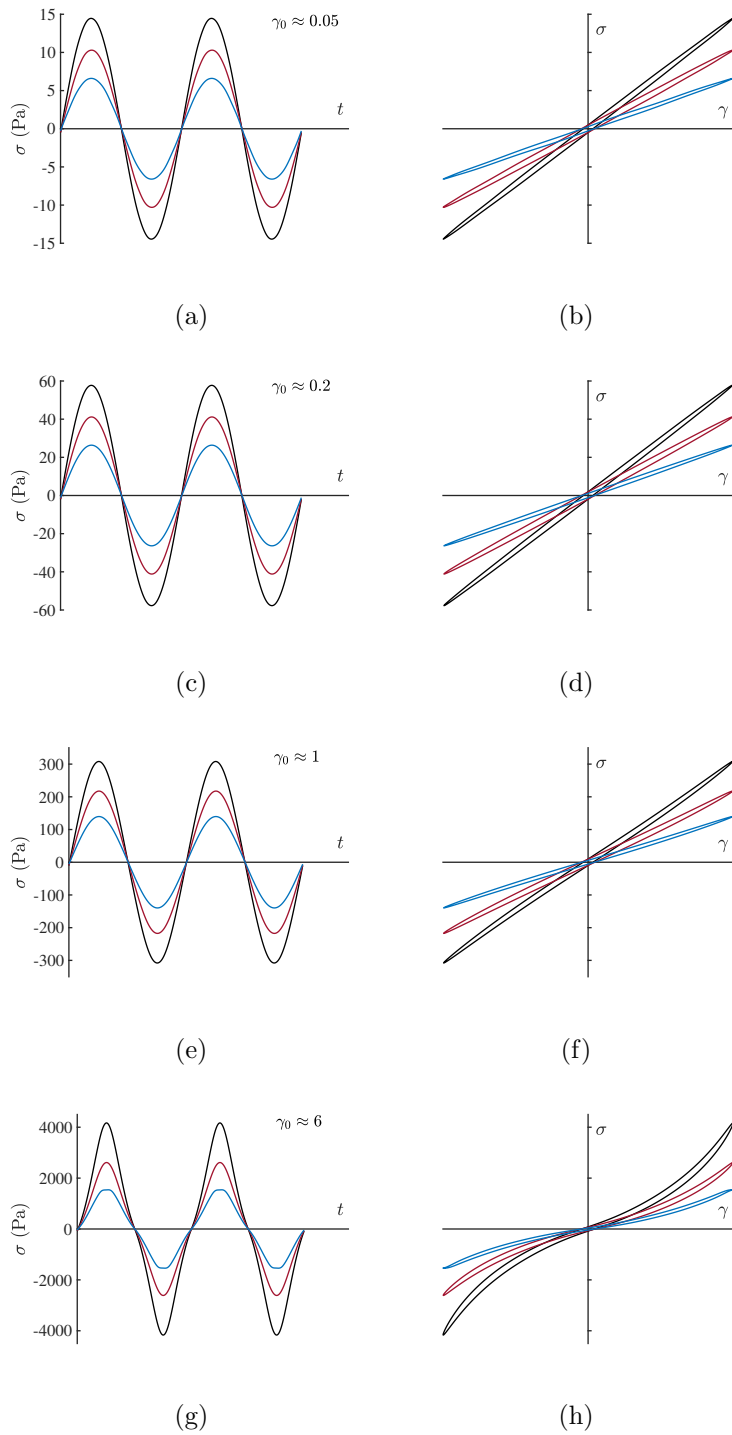


Figure 6.5.8: Stress waveforms (left) and Lissajous-Bowditch plots (right) for samples $A_3B_{2.6}$ (blue), $A_3B_{2.6}N_5$ (red), and $A_3B_{2.6}C_5$ (black) at specified strain amplitudes $\gamma_0 \approx 0.05, 0.2, 1$ and 6 with $\omega \approx 10 \text{ rad s}^{-1}$.

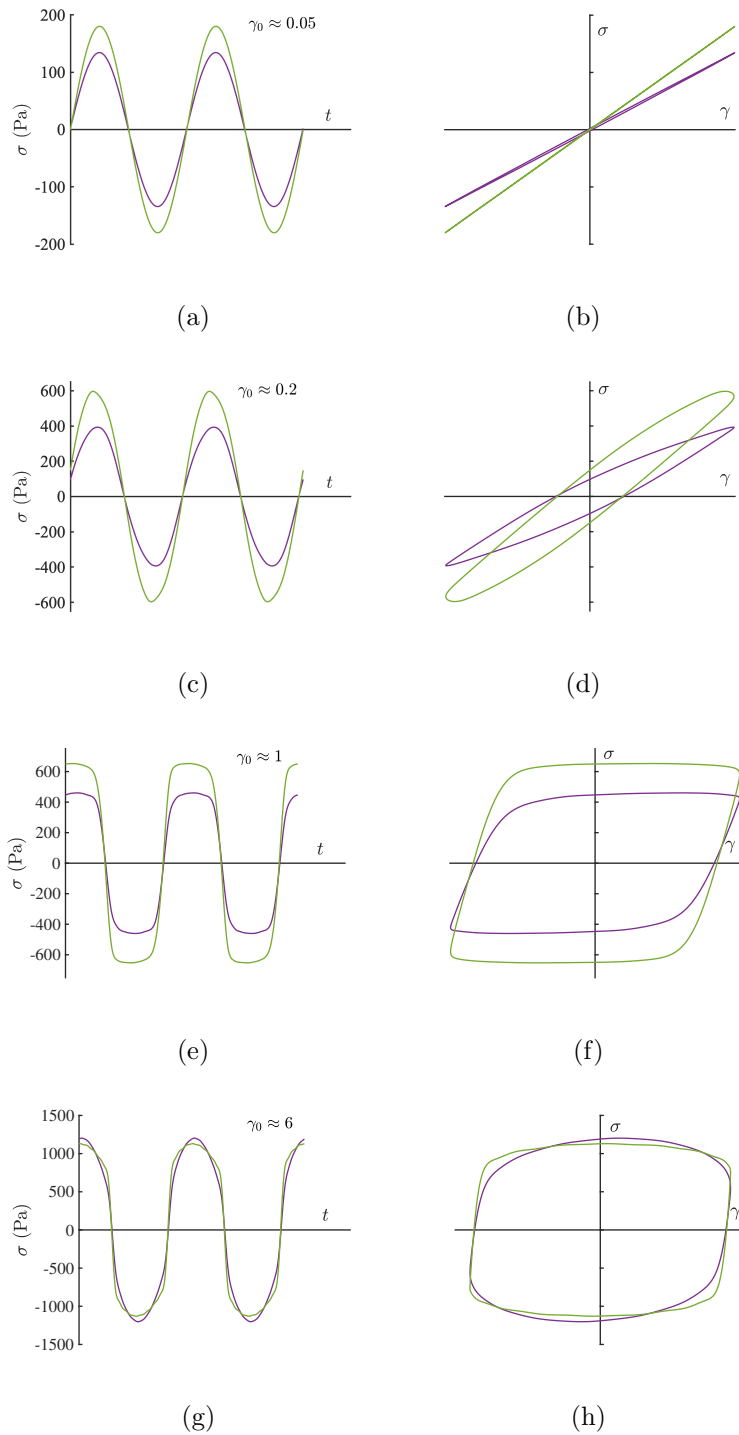


Figure 6.5.9: Stress waveforms (left) and Lissajous-Bowditch plots for samples $A_5B_{5.3}$, $A_5B_{5.3}N_2$ at specified strain amplitudes $\gamma_0 \approx 0.05, 0.2, 1$ and 6 with $\omega \approx 1 \text{ rad s}^{-1}$.

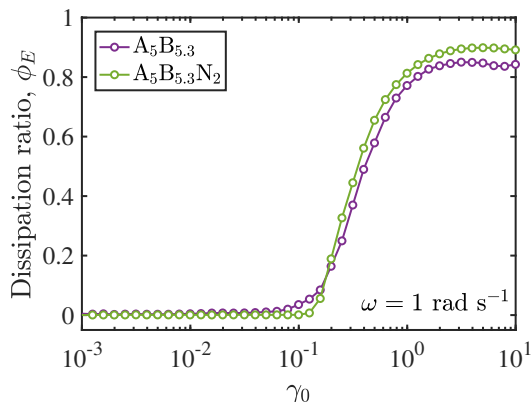


Figure 6.5.10: Dissipation ratio as a function of strain amplitude for “stiff” hydrogels $A_5B_{5.3}$ and $A_5B_{5.3}N_2$ at $\omega \approx 1 \text{ rad s}^{-1}$

deformation. They represent the extent of distortion of the stress signals. The higher harmonics decay faster for the soft gels compared to the stiff gels. Figure 6.5.11 clearly shows a distinction between the flow-aligned microstructure of the soft and stiff gels at medium to large strain amplitudes (0.1–10).

The third harmonic relative intensity $I_{3/1}$ is the most significant in quantifying the degree of nonlinearity. It is plotted as a function of strain amplitude (0.001–10) in Figure 6.5.12 for the soft and stiff gels. From fitting Eqn. (6.11) to the experimental LAOS data, the fitting parameters obtained are provided in Table 6.5.1. The measurements at larger strain amplitudes were not included in the fitting, since edge or slip effects may have developed (Neidhöfer et al., 2003). In the SAOS regime ($\gamma_0 < 0.1$), the relative intensity $I_{3/1}$ is dominated by noise, as it is only detectable at the onset of nonlinearity. There is little or no significant qualitative difference in $I_{3/1}$ between the PA hydrogels and the nanocomposite hydrogels, except at extremely large strain amplitudes ($\gamma_0 > 3$). Therefore, NPs do not affect the relative intensities up to a strain amplitude of 3, above which stress decay may occur, but the extent cannot be determined. The differences at larger strain amplitudes (> 3) may be an indication that silica significantly affects the nonlinear viscoelastic properties by inducing heterogeneous flow (Lee et al., 2016).

Apart from material nonlinearity contributing to the nonlinear response above the critical strain amplitude ($\gamma_{0,c} \approx 1/B$), Filipe et al. (2008) predicted an additional contribution, attributed to the instrument, from surface-flow instabilities. Bare NPs do not significantly

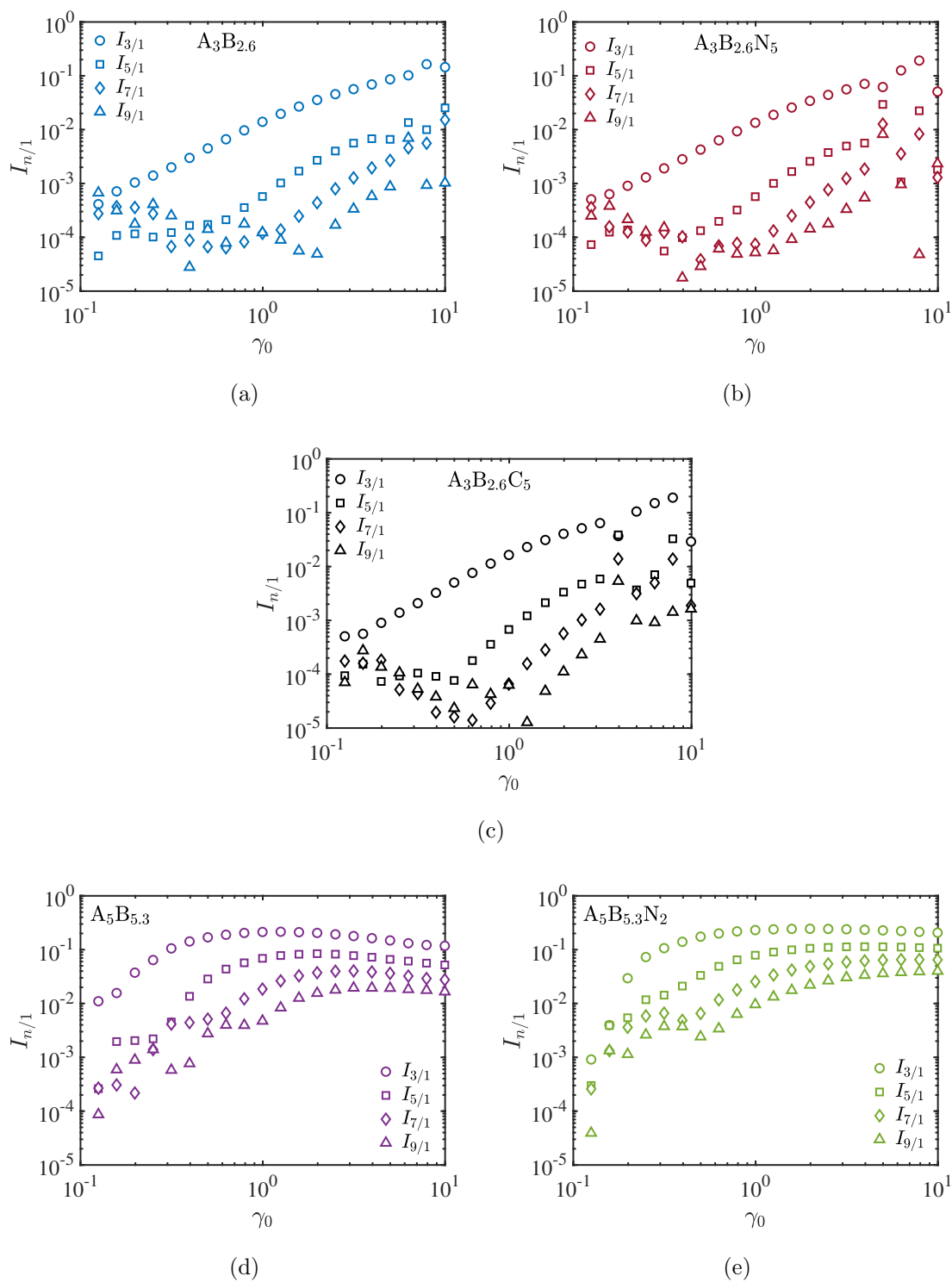


Figure 6.5.11: Relative harmonic intensity $I_{n/1}$ as a function of strain amplitude γ_0 measured at $\omega \approx 10 \text{ rad s}^{-1}$ (a, b, and c) and γ_0 measured at $\omega \approx 1 \text{ rad s}^{-1}$ (d and e).

Table 6.5.1: Parameters A , B and C from fitting Eqn. (6.11) to experimental $I_{3/1}$ data in the strain amplitude range specified at $\omega \approx 10 \text{ rad s}^{-1}$ for the soft gels and 1 rad s^{-1} for the stiff gels.

Sample	γ_0	A	B	C	R^2
A ₃ B _{2.6}	0.12–3.2	0.125 ± 0.003	0.286 ± 0.008	1.65 ± 0.03	0.9998
A ₃ B _{2.6} N ₅	0.12–3.2	0.125 ± 0.004	0.281 ± 0.008	1.67 ± 0.03	0.9999
A ₃ B _{2.6} C ₅	0.12–3.2	0.119 ± 0.004	0.347 ± 0.011	1.74 ± 0.06	0.9997
A ₅ B _{5.3}	0.12–2.5	0.209 ± 0.007	3.17 ± 0.16	3.43 ± 0.52	0.9941
A ₅ B _{5.3} N ₂	0.12–2.5	0.243 ± 0.008	2.80 ± 0.16	3.01 ± 0.44	0.9947

change the critical strain amplitude for both types of hydrogel, whereas $\gamma_{0,c}$ is reduced by PA-coated NPs in the soft hydrogel (sample A₃B_{2.6}C₅), as shown in Table 6.5.1. Coating the NPs with a similar polymer as the neat hydrogel tends to increase polymer chain branching, and may have contributed to the increase in topological constraints for the polymer chain.

Theoretical predictions for polymer melts show that the slope C equals 2 (Pearson and Rochefort, 1982, Hyun et al., 2007). Several experimental results have yielded C in the range 1.6–2.5 (Neidhöfer et al., 2003, Hyun et al., 2006, 2007, Vittorias et al., 2007). Hyun et al. (2006) attributed the sensitivity of $I_{3/1}$ with lower values of C (< 2) obtained for branch polypropylene (PP), to the number of branched chains compared to linear PP (with $C \approx 2$), more than the molecular weight or molecular weight distribution (MWD) of the linear chains.

The soft gels have scaling parameters C that are lower than the theoretical prediction $C = 2$. This prediction failed for the stiff hydrogels, as shown in Table 6.5.1. Parameter C as proposed by Neidhöfer et al. (2003) reflects contributions from the dynamic orientation of polymer chains under periodic shear flow. However, the hydrogel stiffnesses (A₅B_{5.3}, A₅B_{5.3}N₂) may prevent the macromolecules from adopting a preferred orientation when subjected to large strains. The experimentally obtained slopes are thus affected by the gel network. Parameter A reflects the maximum value of $I_{3/1}$ at high strain amplitudes. It has been estimated for polymer melts to have values in the range $A = 0.2$ – 0.3 (Hyun et al., 2011).

The nonlinear coefficient Q as a function of strain amplitude is shown in Figure 6.5.13. It is expected to approach a constant value Q_0 with a large width at small strain amplitude in

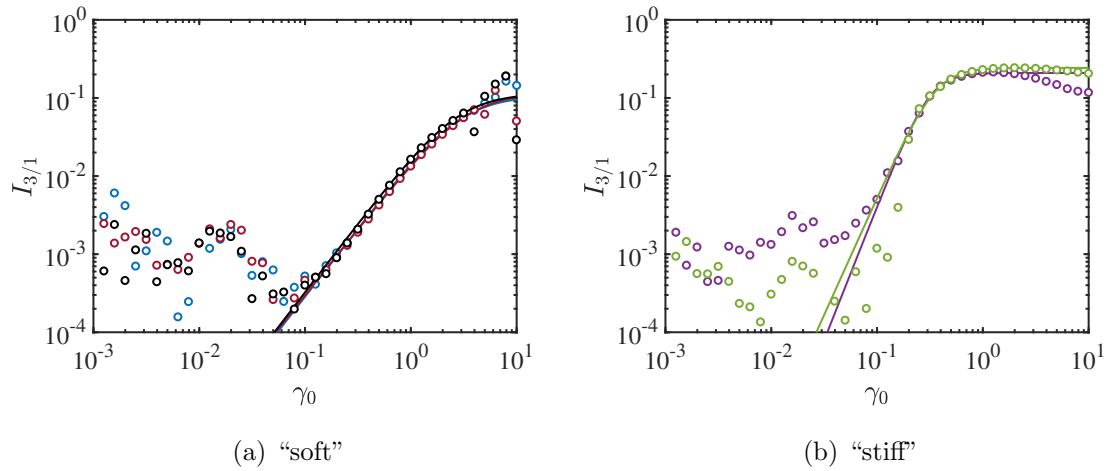


Figure 6.5.12: The relative third harmonic intensity $I_{3/1}$ as a function of strain amplitude γ_0 measured at $\omega \approx 10 \text{ rad s}^{-1}$ (a) for the soft gels and $\omega \approx 1 \text{ rad s}^{-1}$ (b) for the stiff gels. Lines are fits from Eqn. (6.11) to the experimental data in the strain range specified with fitting parameters in Table 6.5.1. Colors are the same as in Figure 6.5.11.

the LAOS regime. However, Q shows some scattering around Q_0 that may be attributed to the extremely low values of $I_{3/1}$ in the same strain amplitude range. The Q_0 value is therefore obtained from fitting Eqn. (6.15) to the experimental Q data, within the specified amplitude range in Table 6.5.2. Q as a function of γ_0 is qualitatively unaffected by the addition of NPs to the neat hydrogel (Figure 6.5.13) but deviates slightly when $\gamma_0 > 3$. The intrinsic nonlinearity represented by Q_0 for the “soft” hydrogels (0.018–0.022) is lower compared to the “stiff” hydrogels (0.98–1.2).

The degree of deviation from the linear/nonlinear viscoelastic properties of the nanocomposite hydrogels can be further quantified using the nonlinear viscoelastic ratio (NLR) from Eqn. (6.16) in Table 6.5.2. For the “soft” and “stiff” gels, $\text{NLR} < 1$ indicates that NPs have a weaker effect on the nonlinear properties as compared to the linear viscoelastic properties, by factors 0.59 for $\text{A}_3\text{B}_{2.6}\text{N}_5$, 0.44 for $\text{A}_3\text{B}_{2.6}\text{C}_5$, and 0.87 for $\text{A}_5\text{B}_{5.3}\text{N}_2$, compared to the neat hydrogels. This implies that there is less interaction between the NPs and the polymer chains. The first stress contribution in the nonlinear regime is enhanced by the strong gel network of the nanocomposite hydrogel among the higher harmonics (Hyun and Wilhelm, 2018). Kim and Hyun (2021) reported $\text{NLR} > 1$ for linear and branched polyethylene (PE)/silica polymer nanocomposites (PNCs), and implied better characterization of morphologies in the LAOS regime as compared to the SAOS regime. Kim et al. (2019) reported similar results

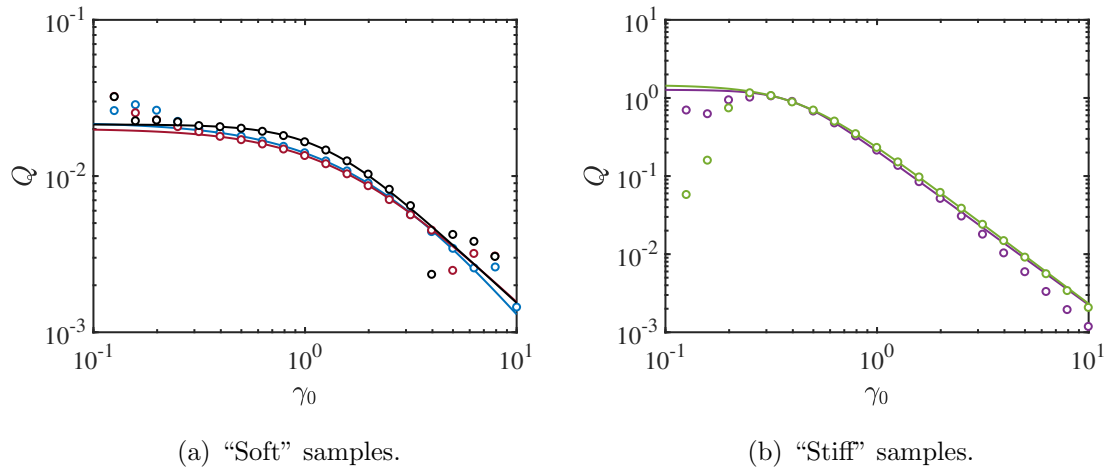


Figure 6.5.13: The nonlinear material coefficient Q as a function of strain amplitude γ_0 measured at $\omega \approx 10 \text{ rad s}^{-1}$ (a) for the “soft” gels and $\omega \approx 1 \text{ rad s}^{-1}$ (b) for the “stiff” gels. Lines are fits using Eqn. (6.15) to describe the experimental data in the strain range specified in Table 6.5.2. Fitting parameters are summarized in Table 6.5.2. Colors are the same as in Figure 6.5.11.

for polypropylene (PP)/silica PNCs. They showed the sensitivity of nonlinear parameters to the filler-matrix effect.

[Salehiyan et al. \(2014\)](#) investigated the addition of clay and fumed silica NPs on the dispersion morphologies of polypropylene (PP)/polystyrene (PS) blends using NLR to quantify NP dispersion. They reported $\text{NLR} < 1$ for the PP/PS/silica blends, which imply that silica does not improve the blend morphologies, attributing this to the presence of fumed silica with PS droplets, as identified from transmission electron microscopy (TEM). On the other hand, [Salehiyan et al. \(2014\)](#) obtained $\text{NLR} > 1$ for the PP/PS/clay blends, interpreted as clay NPs improving dispersion morphologies due to clay locating partially inside PS drops and mostly at the interface.

6.5.3 Hysteresis

Following strain sweep in the range $\gamma_0 \approx 0.001\text{--}10$ (forward cycle 1), a strain sweep in the range $\gamma_0 \approx 10\text{--}0.001$ (backward cycle) was carried out. Another sweep in the range $\gamma_0 \approx 0.001\text{--}10$ (forward cycle 2) ended the cycle. This was undertaken to identify hysteresis

Table 6.5.2: Fitting parameters from fitting Eqn. (6.15) to experimental Q data in the strain amplitude range specified at $\omega \approx 10 \text{ rad s}^{-1}$ for the soft gels and 1 rad s^{-1} for the stiff gels, complex modulus G^* in the linear regime, and NLR [Eqn. (6.16)] of the nanocomposite hydrogels.

Parameters	$A_3B_{2.6}$	$A_3B_{2.6}N_5$	$A_3B_{2.6}C_5$	$A_5B_{5.3}$	$A_5B_{5.3}N_2$
γ_0	0.31–6.30	0.31–6.30	0.31–6.30	0.31–6.30	0.31–6.30
Q_0	0.022 ± 0.001	0.020 ± 0.001	0.021 ± 0.002	1.27 ± 0.08	1.46 ± 0.06
C_1	0.493 ± 0.186	0.615 ± 0.164	0.820 ± 0.587	2.48 ± 0.08	2.38 ± 0.07
C_2	1.26 ± 0.21	1.40 ± 0.18	2.41 ± 0.16	3.75 ± 0.71	2.56 ± 0.24
C_3	-1.33 ± 0.50	-1.02 ± 0.31	-0.522 ± 0.011	-0.527 ± 0.125	-0.794 ± 0.102
R^2	0.999	0.999	0.988	0.999	1.00
G^* (kPa)	0.131	0.204	0.288	2.70	3.58
NLR	–	0.59 ± 0.03	0.44 ± 0.05	–	0.87 ± 0.06

in the nanocomposite hydrogel $A_5B_{5.3}N_2$. The data were processed using FT-rheology, and the nonlinear viscoelastic parameters are shown in Figure 6.5.14. No significant hysteresis was observed at small γ_0 . From the onset of nonlinearity, deviations can be seen in the nonlinear parameters, which may be attributed to slight hysteresis. The relative intensity $I_{3/1}$ and loss modulus G''_1 at low values of γ_0 are affected by instrument sensitivity or noise, and hydrogel stiffness.

6.6 Conclusions

Nonlinear rheological analysis was applied to distinguish the response of “soft” and “stiff” polyacrylamide hydrogels. Moreover, the effects of silica NP cross-linking on the flow-induced microstructure of these hydrogels at large strain amplitudes were investigated using FT-rheology and stress decomposition parameters. Such parameters yield valuable information on network structures that cannot be acquired from the linear response.

The inter-cycle nonlinear viscoelasticity of “soft” hydrogels exhibited type II behaviour, whereas “stiff” hydrogels exhibited type III behaviour at large deformation. These responses

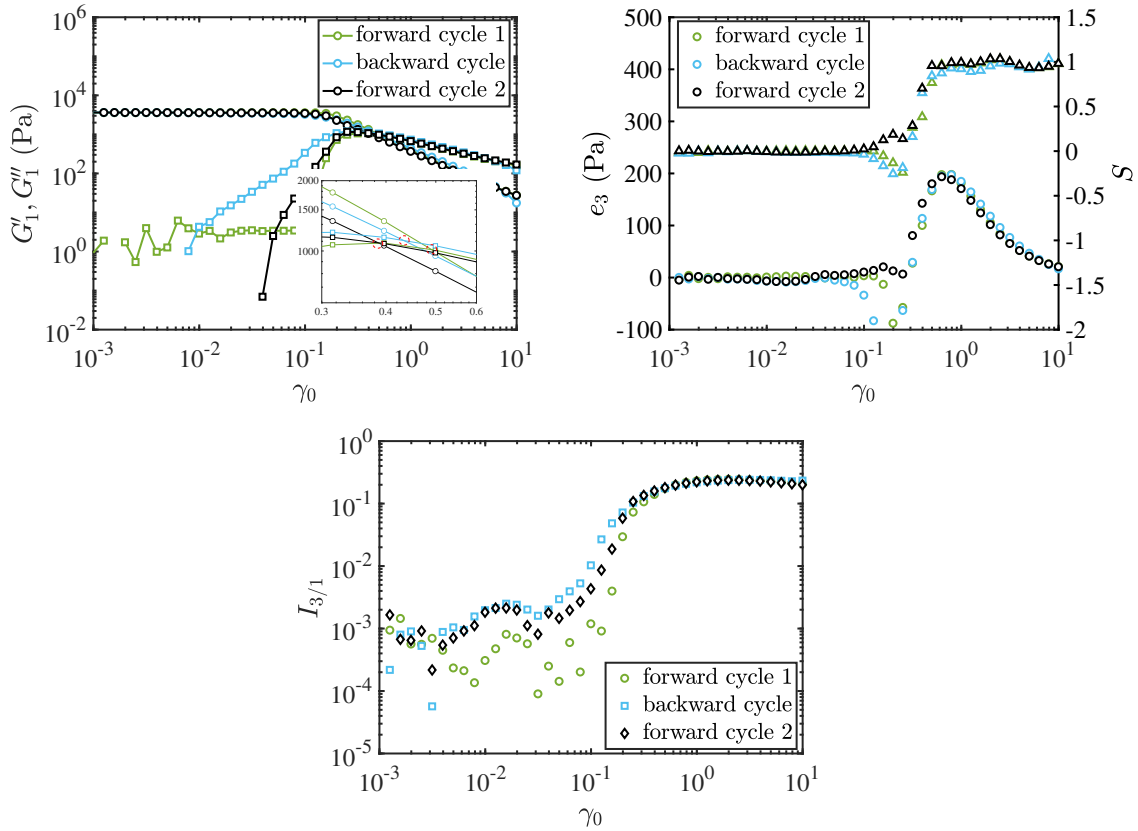


Figure 6.5.14: Nonlinear viscoelastic parameters as a function of strain amplitude at $\omega = 1 \text{ rad s}^{-1}$ for sample $A_5B_{5.3}N_2$. The data represent increasing (forward cycle 1), decreasing (backward cycle) and increasing (forward cycle 2) strain amplitude. The cross-over of the moduli for each cycle are identified by the red dashed circle in the inset.

were the same with or without silica NPs. The use of cone-plate and sandblasted plates as opposed to the flat-plate geometry did not change the weak strain overshoot behaviour of the “stiff” hydrogels. The onset of nonlinearity appeared at lower strain amplitude ($\gamma_0 \approx 0.1$) for “stiff” hydrogels ($\gamma_0 \approx 1$ for “soft” hydrogels). Loading the polymer with silica NPs (bare or polymer coated) increases the elastic and loss moduli, shear stress, and higher-order harmonic contributions at large strain amplitudes.

The intracycle parameters (e_3 and S) obtained through Chebyshev stress decomposition exhibited strain stiffening with increasing strain amplitude. Lissajous-Bowditch plots provided a visual description for understanding the microstructure at large deformation. The different shapes for the “soft” and “stiff” hydrogels at the same strain amplitude distinguished varying compositions and microstructures. Because the stress waveforms and Lissajous-Bowditch plots were not noticeably different, silica NPs in PA hydrogels had no substantial effect on the flow-induced microstructure resulting from large strain deformation. However, at larger strain amplitudes ($\gamma_0 > 3$), some deviations were observed, which may be attributed to heterogeneous deformation or slippage.

The insights gained from the LAOS analysis of silica cross-linked PA hydrogels provide guidance for practical applications involving large and rapid deformation with controllable microstructures and mechanical response.

Analysis of linearized rheological response

7.1 Preface

This chapter probes the nonlinear response of bis-acrylamide and silica nanoparticle cross-linked polyacrylamide hydrogels by superimposing a small oscillatory strain on a finite, steady mean strain that controls the degree to which the microstructure is perturbed from its as-prepared state. The tangent and steady-state storage modulus are then correlated with a model proposed by Professor Reghan J. Hill based on non-linear stretching of polymer chains—to furnish steady and local dynamic moduli.

Abstract

Neat and nanoparticle (NP)-loaded polyacrylamide (PA) hydrogels are subjected to small-amplitude oscillatory shear that is superposed on a finite-amplitude steady shear. Whereas the linear viscoelastic response, based on perturbing the microstructure from its as-prepared state, is well studied, this study seeks to understand what can be learned from small-amplitude dynamics about a state that may be far from equilibrium. The finite-amplitude steady shear transitions from the linear to the nonlinear regime and the resulting stress output at each imposed shear are transformed into local dynamic moduli using the discrete Fourier transform (DFT) analysis. The resulting tangent moduli capture the true material elasticity and dissipation in the nonlinear regime. Theoretical formulas that describe steady and local dynamic moduli are correlated with experimental data. The average number of statistical segments per sub-chain obtained from the fitting provides a relationship between strain stiffening and finite chain extensibility. The results show that NPs and chemical cross-links contributed to enhanced elasticity, strain stiffening, and nonlinear stretching of polymer chains between cross-linking junctions.

7.2 Introduction

Linear rheology is a powerful tool for understanding a material’s microstructure. Measurements in this regime are such that an oscillatory input causes a single frequency material response with amplitude proportional to that of the the forcing. However, for many materials, linear rheology breaks down when the microstructure deformed. The resulting nonlinear response is significant in many applications. For example, many biological gels exhibit strain stiffening at large deformations, and accurate determination of the viscoelasticity remains a challenge. For nonlinear rheology, the stress response to a sinusoidal strain is periodic but non-sinusoidal due to higher-order odd harmonics.

Nonlinear viscoelasticity has been interpreted using Fourier-transform (FT) [Wilhelm \(2002\)](#), [Neidhöfer et al. \(2003\)](#) and stress decomposition methods ([Cho et al., 2005](#)). FT-rheology used the relative harmonic intensities as a measure of nonlinearity to determine the onset of nonlinearity and accurately quantify the deviation from linearity. A drawback is the existence of higher order harmonics and their effective incorporation in the nonlinear moduli, since material deformation takes place over the entire range of applied shear stress (or strain) during a single large-amplitude oscillatory shear (LAOS) cycle ([Ewoldt et al., 2008](#), [Yao et al., 2008](#)). This limitation has been addressed with the stress decomposition method, which decomposes the nonlinear stress (or strain) into elastic and viscous components, furnishing generalized storage and loss moduli that are functions of frequency and strain amplitude ([Cho et al., 2005](#)). However, the stress decomposition method suffers from nonorthogonality of the resulting material parameters ([Ewoldt et al., 2008](#)). Both methods fail to address a low-signal limitation in the data processing. LAOS data contains both linear and nonlinear responses, the ratio of which is usually small, so isolating the nonlinear rheological response requires precise measurements that focus in the nonlinear regime.

Some researchers ([Vermant et al., 1998](#), [Gardel et al., 2004](#), [Yao et al., 2008](#)) have introduced a stress-controlled perturbative method that probes material properties by superposing a small amplitude oscillatory stress on a steady pre-stress to bring the material to a specified deformation. The small stress oscillation amplitude is usually chosen to be very small compared to the pre-stress. The properties of the specific state determines the material response signal, which enable the method to overcome the low-signal limitation of the FT-rheology and stress decomposition methods. However, irreversibility due to flow and material damage limits the interpretation of the superposed data, thereby complicating the perturbative

method (Vermant et al., 1998).

Irreversible damage to the microstructure at large deformation introduces time dependence in the rheological measurements (Yao et al., 2008). The use of the rotational inertia of a stress-controlled rheometer in performing stress perturbation instead of the rheometer’s motor was proposed by Yao et al. (2008) to limit the effects of time-dependent deformation and noisy loss modulus. The differential modulus protocol, commonly used in perturbative methods, is applicable for materials dominated by elasticity, but less robust in viscoelastic liquids, which readily flow or relax under imposed stress (or strain) (Ewoldt et al., 2008). The perturbative method is therefore not popular for interpreting nonlinear rheological response.

In this work, we apply an approach similar to the perturbative method to analyze the rheological response of PA hydrogels under finite deformation. A strain-controlled oscillation with small amplitude is superposed on a steady mean strain with finite/large amplitude. This furnishes dynamic moduli for the small-amplitude perturbations at a prescribed frequency and mean strain. Although the dynamic moduli under finite mean strain are measured at just a few frequencies, the insights from this study provide a basis for future work seeking full-range spectra. Note that the samples proved to be sufficiently elastic to limit the resolution of dissipation and time-dependent relaxation, furnishing noisy or negative loss moduli. The small energy dissipation ratios for these samples, $\phi_E = 0\text{--}0.2$, were reported in Chapter 6 within the strain-amplitude range $\gamma' = 0.001\text{--}10$ at $\omega \approx 10 \text{ rad s}^{-1}$. In the present study, the dynamic moduli are compared with those from steady-state and first-harmonic (from LAOS analysis) moduli. The experimental data are interpreted using a model based on a network of finitely extensible sub-chains, having as the only fitting parameter the average number of statistical segments per sub-chain.

7.3 Theory

7.3.1 Linearized dynamic response

We consider a time-dependent shear strain as comprising a steady mean and oscillatory disturbance of the form:

$$\gamma = \bar{\gamma} + \gamma' \cos(\omega t). \quad (7.1)$$

If the disturbance imparts a small dynamic perturbation to the microstructure, then the accompanying stress will be of the form:

$$\sigma = \bar{\sigma} + \sigma' \cos(\omega t + \delta). \quad (7.2)$$

In these formulas, $\bar{\sigma}$ and $\bar{\gamma}$ are the mean stress and strain, respectively; σ' and γ' are the stress and strain amplitudes, respectively; and δ measures the phase lag (> 0) of the response with respect to the forcing.

It is convenient to represent the time-dependent fluctuations above as the real part of a complex variable, generally

$$f(t) = \bar{f} + \Re[\hat{f}e^{i\omega t}], \quad (7.3)$$

so

$$\sigma = \bar{\sigma} + \Re[\hat{\sigma}e^{i\omega t}], \quad (7.4)$$

and

$$\gamma = \bar{\gamma} + \Re[\hat{\gamma}e^{i\omega t}], \quad (7.5)$$

where $e^{i\omega t} = \cos(\omega t) + i \sin(\omega t)$.

Defining a shear modulus

$$G = \frac{\sigma}{\gamma} = \frac{\bar{\sigma} + \Re[\hat{\sigma}e^{i\omega t}]}{\bar{\gamma} + \Re[\hat{\gamma}e^{i\omega t}]}, \quad (7.6)$$

we may linearize for small deviations relative to their respective mean, furnishing

$$G = \frac{\bar{\sigma}}{\bar{\gamma}} \left[1 + \Re\left[\frac{\hat{\sigma}e^{i\omega t}}{\bar{\sigma}}\right] - \Re\left[\frac{\hat{\gamma}e^{i\omega t}}{\bar{\gamma}}\right] \right] = \frac{\bar{\sigma}}{\bar{\gamma}} \left[1 + \Re\left[\frac{G^* \hat{\gamma}e^{i\omega t}}{\bar{\sigma}}\right] - \Re\left[\frac{\hat{\gamma}e^{i\omega t}}{\bar{\gamma}}\right] \right], \quad (7.7)$$

$$= \bar{G} + \frac{\gamma'}{\bar{\gamma}} [(G' - \bar{G}) \cos(\omega t) - G'' \sin(\omega t)] + O(\gamma'^2), \quad (7.8)$$

which may be compared to the measured time series

$$G = \bar{G} \left[1 + \frac{\sigma'}{\bar{\sigma}} \cos(\omega t + \delta) - \frac{\gamma'}{\bar{\gamma}} \cos(\omega t) \right], \quad (7.9)$$

where

$$\cos(\omega t + \delta) = \cos \delta \cos(\omega t) - \sin \delta \sin(\omega t),$$

giving

$$G = \bar{G} \left[1 + \left(\frac{\sigma'}{\bar{\sigma}} \cos \delta - \frac{\gamma'}{\bar{\gamma}} \right) \cos(\omega t) - \frac{\sigma'}{\bar{\sigma}} \sin \delta \sin(\omega t) \right].$$

7.3.2 Nonlinear extension

Finite chain extensibility has been attributed as the major reason for strain stiffening at large elongations, and these can be described by the non-Gaussian statistics of strongly deformed chains (Rubinstein and Colby, 2003). The force versus extension for such a chain is given by the inverse Langevin function, which may be approximated (Itskov et al., 2010, 2012)

$$\xi = 3x + \frac{9}{5}x^3 + \frac{297}{175}x^5 + \frac{1539}{875}x^7 + \dots, \quad (7.10)$$

where $\xi = fb/(k_B T)$ is the scaled force f , b is the segment length, and $k_B T$ is the thermal energy; and $x = r/(Nb)$ is the scaled extension r with N the number of chain segments.

Consider a nonlinear spring/polymer for which the equilibrium/steady shear stress

$$\bar{\sigma} = \bar{\sigma}(\bar{\gamma})$$

and the dynamic stress, under the foregoing oscillatory forcing/strain, is

$$\sigma = \bar{\sigma} + \Re[G^*(\omega)e^{i\omega t}]\gamma' = \bar{G}\bar{\gamma} + \gamma'[G' \cos(\omega t) - G'' \sin(\omega t)],$$

so

$$\frac{\sigma}{\gamma} = \bar{G} + \frac{\gamma'}{\bar{\gamma}}[(G' - \bar{G}) \cos(\omega t) - G'' \sin(\omega t)] + O(\gamma'^2),$$

as derived above.

Now, let us define

$$\bar{G} = \frac{\bar{\sigma}}{\bar{\gamma}} \text{ and } G^\dagger = \frac{\partial \bar{\sigma}}{\partial \bar{\gamma}}, \quad (7.11)$$

and set

$$\bar{\gamma} = r/r_0 - 1 = \sqrt{N}x - 1, \quad (7.12)$$

where $r_0 = b\sqrt{N}$ is the mean-squared end-to-end distance in the as-prepared state. Equation (7.10) may then be written

$$\xi = \xi_0 + \frac{3(5N+9)}{5N^{3/2}}\bar{\gamma} + \frac{27}{5N^{3/2}}\bar{\gamma}^2 + \frac{9}{5N^{3/2}}\bar{\gamma}^3 + \dots$$

or

$$\xi - \xi_0 = \frac{3(5N+9)}{5N^{3/2}} \left[\bar{\gamma} + \frac{5N^{3/2}}{3(5N+9)} \frac{27}{5N^{3/2}} \bar{\gamma}^2 + \frac{5N^{3/2}}{3(5N+9)} \frac{9}{5N^{3/2}} \bar{\gamma}^3 + \dots \right], \quad (7.13)$$

where $\xi_0 = 3(5N+3)/(5N^{3/2})$.

The force-extension for a single chain translates to free-energy per unit volume under shear, furnishing an equilibrium/steady-state elastic shear stress

$$\bar{\sigma} = G_0 \left[\bar{\gamma} + \frac{9}{(5N+9)} \bar{\gamma}^2 + \frac{3}{(5N+9)} \bar{\gamma}^3 + \dots \right], \quad (7.14)$$

where G_0 is the shear modulus (under infinitesimal shear strain). It then follows that

$$\bar{G} = G_0 \left[1 + \frac{9}{(5N+9)} \bar{\gamma} + \frac{3}{(5N+9)} \bar{\gamma}^2 + \dots \right], \quad (7.15)$$

$$G^\dagger = G_0 \left[1 + \frac{18}{(5N+9)} \bar{\gamma} + \frac{9}{(5N+9)} \bar{\gamma}^2 + \dots \right], \quad (7.16)$$

and

$$\frac{\gamma'}{\bar{\gamma}} (G^\dagger - \bar{G}) = \frac{9G_0\gamma'}{(5N+9)} \left[1 + \frac{2}{3} \bar{\gamma} + \dots \right]. \quad (7.17)$$

If we take $G' \approx G^\dagger$, then a quasi-steady response furnishes

$$G = \frac{\sigma}{\gamma} \approx \bar{G} + \frac{9G_0\gamma'}{(5N+9)} \left[1 + \frac{2}{3} \bar{\gamma} + \dots \right] \cos(\omega t) - \frac{\gamma'}{\bar{\gamma}} G'' \sin(\omega t) + O(\gamma'^2), \quad (7.18)$$

where

$$\bar{G} = G_0 \left[1 + \frac{9}{(5N+9)} \bar{\gamma} + \frac{3}{(5N+9)} \bar{\gamma}^2 + \dots \right]. \quad (7.19)$$

The foregoing physically motivated shear moduli are to be compared with those defined by the stress time series and strain amplitudes. Under steady shear strain $\bar{\gamma}$, we have

$$\frac{\bar{\sigma}}{\bar{\gamma}} = G'(\bar{\gamma}, \omega = 0) = \bar{G}(\bar{\gamma}), \quad (7.20)$$

whereas under combined steady and oscillatory shear strain (mean strain $\bar{\gamma}$, perturbation strain amplitude $\gamma' \ll 1$), we have

$$\frac{\sigma(t) - \bar{\sigma}}{\gamma'} = G'(\bar{\gamma}, \omega) \cos(\omega t) - G''(\bar{\gamma}, \omega) \sin(\omega t). \quad (7.21)$$

Note that subjecting a sample to oscillatory shear with finite-strain amplitude γ' defines

$$\frac{\sigma(t)}{\gamma'} = G'(\gamma', \omega) \cos(\omega t) - G''(\gamma', \omega) \sin(\omega t) \quad (7.22)$$

or (from first harmonic analysis)

$$\frac{\sigma(t)}{\gamma'} = G'_1(\gamma', \omega_1) \cos(\omega t) - G''_1(\gamma', \omega_1) \sin(\omega t). \quad (7.23)$$

7.4 Materials and methods

7.4.1 Materials

Acrylamide (AAm) solution (40 w/v%, Fisher Scientific, U.S.A.), *N,N'*-methylene (bis) acrylamide (2 w/v%, Fisher Scientific), ammonium persulfate (APS) powder ($\geq 98\%$, Fisher Scientific, U.S.A.) and *N,N,N',N'*-tetramethylethylenediamine (TEMED, 99%, GE Healthcare Life Science, Germany) were monomer, chemical cross-linker, initiator and catalyst, respectively. Silica NPs, available as Ludox[®] TM50 (50 w% colloidal suspension, Sigma-Aldrich Inc., U.S.A.) with diameter $d \approx 30$ nm, served as a physical cross-linker. All were used as provided by the manufacturers. Polyacrylamide (PA)-coated silica NP dispersions, prepared as described in a previous study (1.25 w/v% PA and 5 w/v% Ludox[®] TM50), were used as a physical cross-linker.

Hydrogels were prepared by mixing acrylamide solution, bis-acrylamide solution, and silica NPs in a centrifuge tube, diluted using reverse-osmosis (RO) water (Type 1, $\sigma \approx 5.6 \mu\text{S m}^{-1}$, $\Omega \approx 18 \text{ MOhm cm}$ at 25°C). NP volume fractions and chemical cross-linker concentrations are listed in Table 7.4.1. Samples are identified using nomenclature $A_x B_y N_\phi$ for bare silica NP loaded hydrogels, and $A_x B_y C_\phi$ for PA-coated silica NP loaded hydrogels, where x is the acrylamide concentration (w/v%), y is the ratio of bis-acrylamide cross-linker c_{bis} (w/v%) to acrylamide c_a (w/v%) concentrations, and ϕ is the bare NP (or PA-coated NP) volume fraction (v%). All the concentrations are based on the total volume of the pre-gel solution in a centrifuge tube. Dissolved oxygen was removed following addition of 50 μl of freshly prepared APS solution (0.44 mol l^{-1}) by bubbling N_2 gas through the solutions for ≈ 5 min. TEMED catalyst (50 μl) was added immediately before conducting rheological measurements.

7.4.2 Methods

The moduli defined in Eqns. (7.20)–(7.23) were measured using a strain-controlled ARES-G2 rheometer (TA Instruments, U.S.A.) with parallel plate geometry. The pre-gel mixture was pipetted directly onto the bottom plate, and the 25 mm diameter top plate was carefully lowered so that the gap between the plates was 0.5 mm. Gelation reactions were carried

Table 7.4.1: Compositions and steady-state linear viscoelastic properties of PA hydrogels and nanocomposite hydrogels at $\omega \approx 10 \text{ rad s}^{-1}$ with $\gamma_0 \approx 0.02$.

Sample	c_a (w/v%)	c_{bis}/c_a (w/w%)	ϕ (v%)	G'_∞ (Pa)	G''_∞ (Pa)
“Soft”					
A ₃ B _{2.6}	3	2.6	0	131	1.3
A ₃ B _{2.6} N ₅	3	2.6	5	204	1.6
A ₃ B _{2.6} C ₅	3	2.6	5	288	6.3
“Stiff”					
A ₅ B _{5.3}	5	5.3	0	2890	1.1

out between the parallel plates of the instrument. An “evaporation blocker” provided by the manufacturer, and silicone oil at the edges of the gels between the plates were used to prevent evaporation.

Arbitrary waveform

The arbitrary waveform test mode of the ARES-G2 rheometer allows the strain time series Eqn. (7.1) to be applied. All data were obtained at $T = 21^\circ\text{C}$ and a sampling rate of 1000 pts/s. The value of γ' was prescribed large enough to register a satisfactory signal to noise ratio but small enough to register a linear dynamic response.

The input strain and the system-generated stress are measured as a function of time, without subjecting the samples to strains that irreversibly damage the samples. The raw stress and strain time series were processed using the FT-rheology software package incorporated in TRIOS. A discrete Fourier transform (DFT) analysis converts the input strain $\gamma(t)$ and output stress $\sigma(t)$ from the time domain to the frequency domain. The transformation provides the complex modulus $G^*(\omega)$ (Franck, 2002):

$$G^*(\omega) = \frac{\tilde{\sigma}(\omega)}{\tilde{\gamma}(\omega)}, \quad (7.24)$$

where (\cdot) denotes the Fourier transform. The quantities $\tilde{\sigma}(\omega)$ and $\tilde{\gamma}(\omega)$ are complex. The rheological properties of the samples: elastic and loss moduli, G' and G'' , can subsequently

be determined as the real and imaginary part of the complex modulus (Macosko and Larson, 1994).

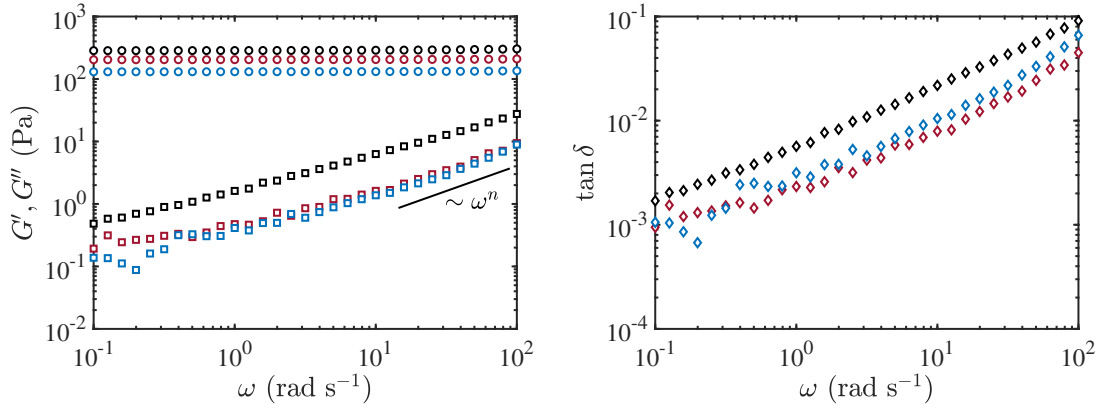
7.5 Results and discussion

The moduli and loss tangent spectra in the linear viscoelastic regime shown in Figure 7.5.1 with $\gamma_0 \approx 0.02$ and 21°C. These demonstrate the storage modulus for all samples to be frequency independent, and the loss moduli spectra of the “soft” samples to have power-law scaling with exponents $0.64 < n < 0.85$. All samples are viscoelastic solids with very weak dissipation. As highlighted elsewhere, pre-coating the silica NPs enhances the stiffness and dissipation due to entanglement coupling.

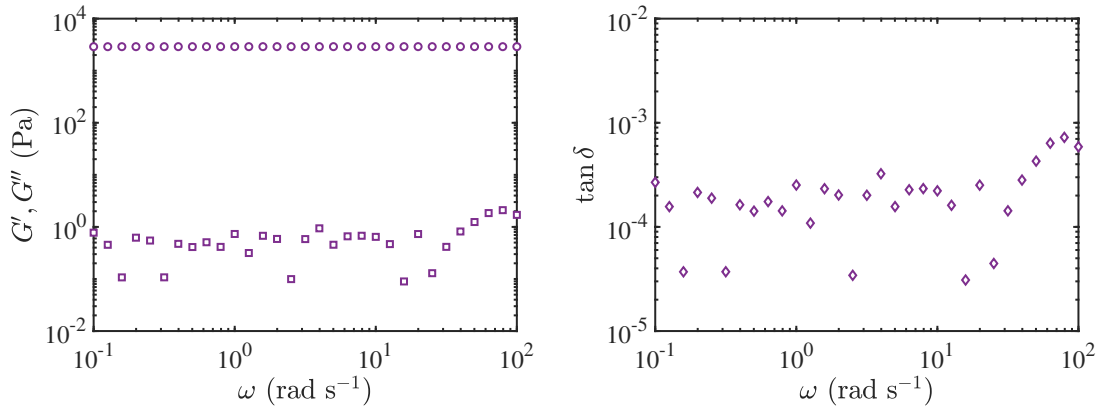
Representative time series of the the imposed strain Eqn. (7.1) and the resulting stress response Eqn. (7.2) are shown in Figure 7.5.2 for steady and mixed shear.

The moduli from such time series are shown in Figures 7.5.3 and 7.5.4 for the various samples. Note that the moduli are plotted versus either the steady-shear amplitude $\bar{\gamma}$ or oscillatory-shear amplitude γ' , as appropriate for the various moduli defined by Eqns. (7.20)–(7.23). When there is an oscillatory component, $\omega = 10 \text{ rad s}^{-1}$. For the “stiff” sample, $\omega = 1 \text{ rad s}^{-1}$ is reported for comparison. As expected from the linear responses above, the loss moduli are extremely small compared to the storage moduli. Moreover, whereas the storage moduli increase quadratically with strain, the loss moduli from the mixed infinitesimal oscillatory shear (blue squares) are practically independent of the strain amplitude, and loss moduli from the finite-amplitude oscillatory shear (red squares) increase with strain amplitude. If we interpret the loss moduli as a viscous stress—proportional to the strain rate $\gamma\omega$ —then the constancy of the mixed infinitesimal oscillatory shear modulus with respect to $\bar{\gamma}\omega$ identifies the effective viscosity as reflecting the strain rate $\gamma'\omega$, which is indeed a constant. On the other hand, under finite-amplitude oscillatory shear, the weak increase of G'' with respect to γ' , reflects a viscosity that is weakly shear thinning, consistent with the linear visco-elastic response furnishing $G'' \sim \omega^n$ with $n \approx 0.65\text{--}0.85$, so $\eta' \sim \omega^{n-1}$.

Now turning to the storage moduli, these all increase quadratically with respect to strain amplitude, as predicted by Eqns. (7.15) and (7.16). The coefficients in quadratic fitting formulas are provided in Tables 7.5.1 and 7.5.2, where the leading coefficient may be con-



(a) “Soft” samples.



(b) “Stiff” sample.

Figure 7.5.1: Storage (circles) and loss (squares) moduli spectra, loss tangent spectra with $\gamma_0 \approx 0.02$ (linear viscoelastic regime) and $T \approx 21^\circ\text{C}$ for samples $A_3B_{2.6}$ (blue), $A_3B_{2.6}N_5$ (red), $A_3B_{2.6}C_5$ (black), and $A_5B_{5.3}$ (purple).

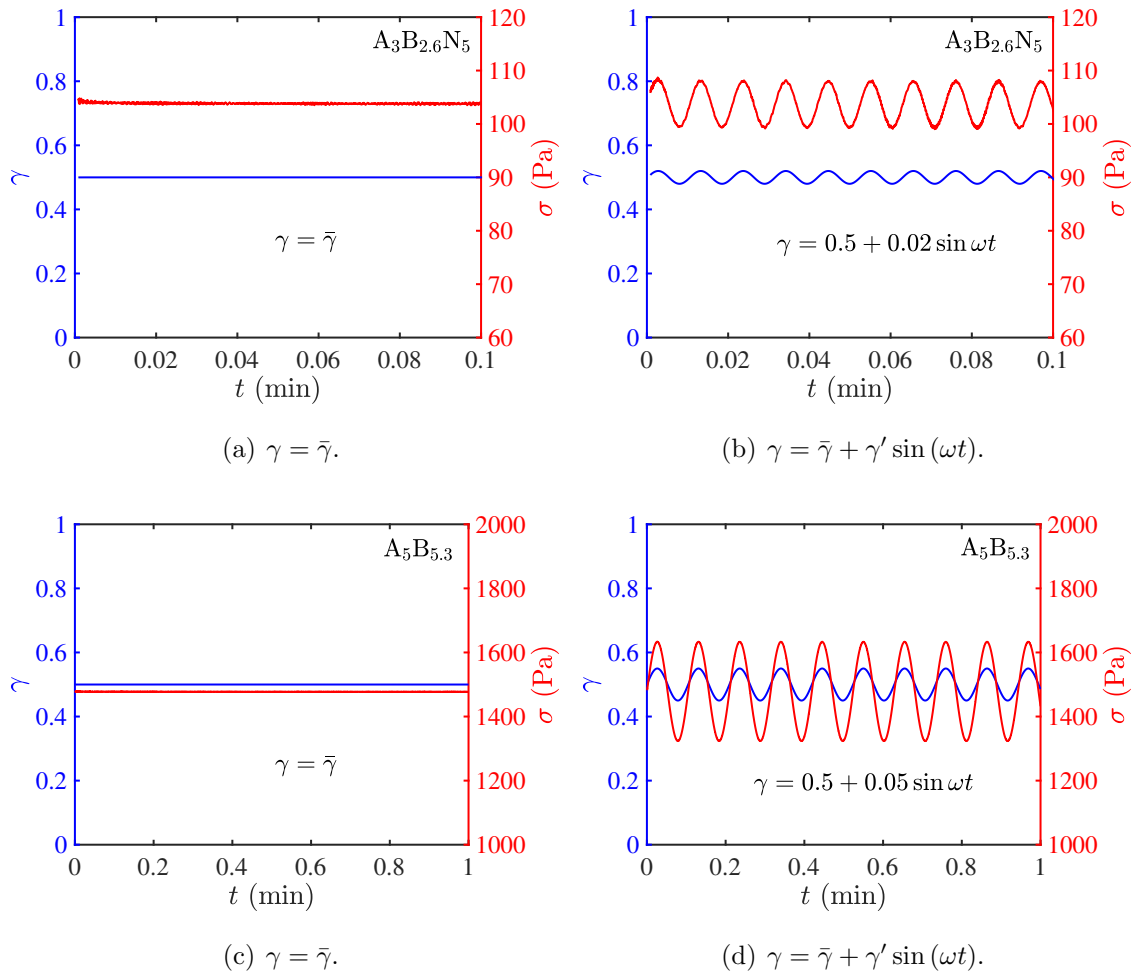


Figure 7.5.2: Stress and strain time series for steady shear $\gamma = \bar{\gamma}$ (left), and mixed shear $\gamma = \bar{\gamma} + \gamma' \sin(\omega t)$ (right). Nanocomposite sample $A_3B_{2.6}N_5$ (top) and hydrogel sample $A_5B_{5.3}$ (bottom) at $T \approx 21^\circ\text{C}$.

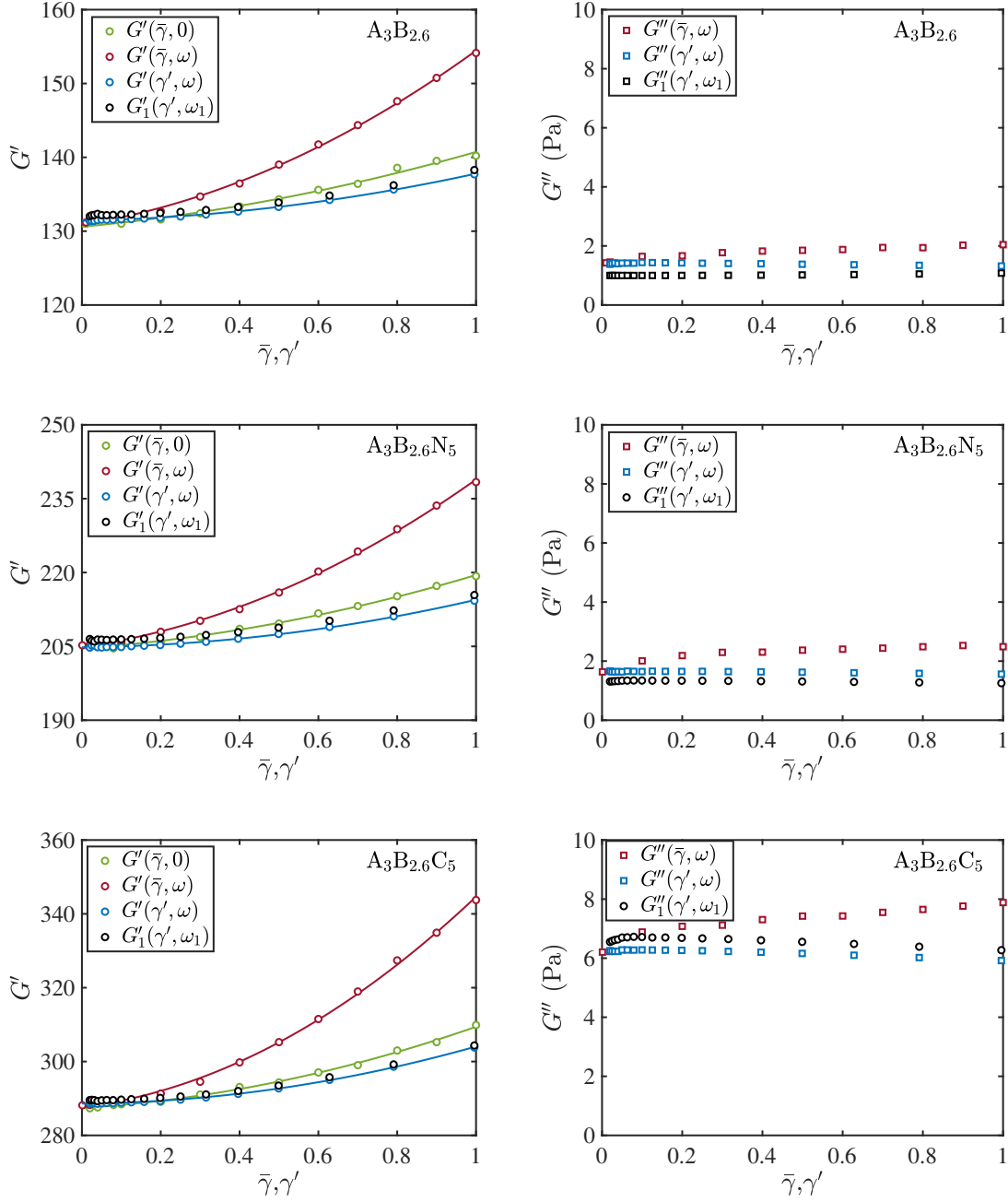
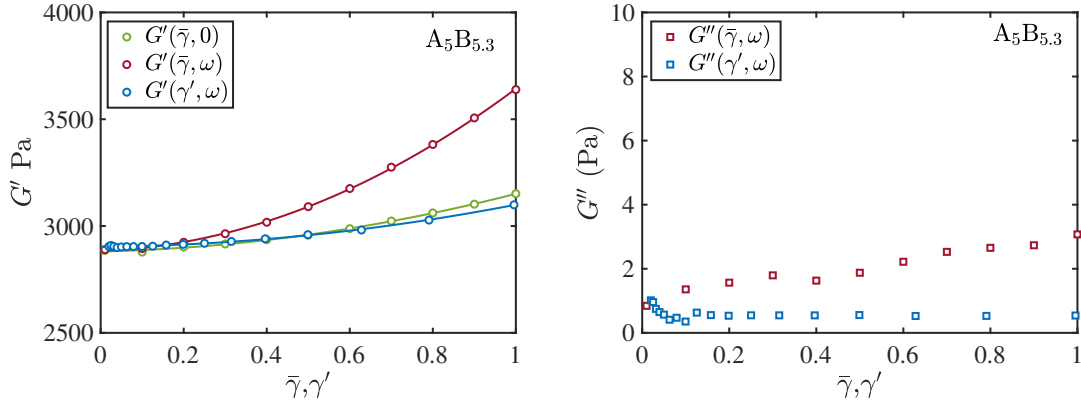
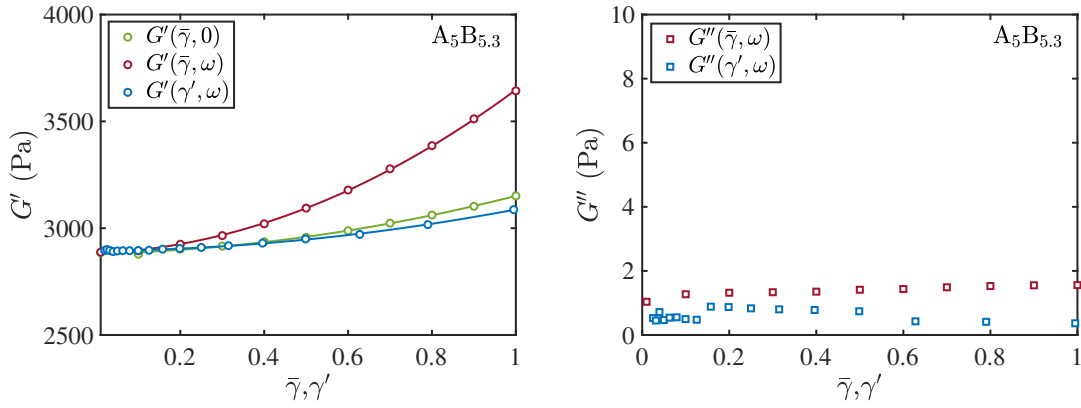


Figure 7.5.3: Storage (left) and loss (right) moduli versus strain at $\omega = 10 \text{ rad s}^{-1}$. Solid lines are quadratic fits. Moduli are defined by Eqn. (7.20) (steady shear, green), Eqn. (7.21) (mixed infinitesimal oscillatory shear with $\gamma' = 0.02$ (linear dynamic response) and varying $\bar{\gamma}$, red), Eqn. (7.22) (finite-amplitude oscillatory shear, blue), Eqn. (7.23) (finite-amplitude oscillatory shear, black).



(a) $\omega \approx 1 \text{ rad s}^{-1}$



(b) $\omega \approx 10 \text{ rad s}^{-1}$

Figure 7.5.4: Storage (left) and loss (right) moduli versus strain for sample $A_5B_{5.3}$ at $\omega = 1$ (top) and 10 rad s^{-1} (bottom). Solid lines are quadratic fits. Moduli are defined by Eqn. (7.20) (steady shear, green), Eqn. (7.21) (mixed infinitesimal oscillatory shear with $\gamma' = 0.02$ (linear dynamic response) and varying $\bar{\gamma}$, red), Eqn. (7.22) (finite-amplitude oscillatory shear, blue).

Table 7.5.1: Quadratic fitting parameters defined by $y = a + b\gamma + c\gamma^2$, for the curves shown in the left panel of Figure 7.5.3 at $\omega = 10 \text{ rad s}^{-1}$.

Sample	y (Pa)	a (Pa)	b (Pa)	c (Pa)	R^2
A ₃ B _{2.6}	$G'(\bar{\gamma}, 0)$	130.6	5.05	5.08	0.991
	$G'(\bar{\gamma}, \omega)$	130.9	8.57	15.0	0.999
	$G'(\gamma', \omega)$	131.4	1.15	5.23	0.999
A ₃ B _{2.6} N ₅	$G'(\bar{\gamma}, 0)$	204.6	5.95	8.97	0.997
	$G'(\bar{\gamma}, \omega)$	204.9	11.2	22.8	0.999
	$G'(\gamma', \omega)$	204.8	0.89	8.75	0.998
A ₃ B _{2.6} C ₅	$G'(\bar{\gamma}, 0)$	287.4	6.71	15.3	0.997
	$G'(\bar{\gamma}, \omega)$	287.6	13.3	43.7	0.999
	$G'(\gamma', \omega)$	288.6	0.95	14.5	0.999

sidered the shear modulus $G_0 \approx G'_\infty(\omega)$ at $\omega = 10 \text{ rad s}^{-1}$. Note that the steady shear modulus $G'(\bar{\gamma}, 0)$ is related to the dynamic modulus $G'(\bar{\gamma}, \omega)$ in the same way that \bar{G} is related to G^\dagger by Eqn. (7.11). This motivates fitting Eqns. (7.15) and (7.16) to the data, for which the number of sub-chain segments N is the only fitting parameter upon normalizing each strain-dependent modulus with its infinitesimal strain value $G'(0)$.

The normalized moduli are plotted in Figures 7.5.5 and 7.5.6. Panels on the left show quadratic fits (coefficients provided in Tables 7.5.3 and 7.5.4) to the data, and panels on the right show fits of the theoretical formulas Eqns. (7.15) and (7.16) with the fitted values of N listed in Tables 7.5.5 and 7.5.6. Note that the steady-state modulus $\bar{G}/G'(0)$ has been fitted to $G'(\bar{\gamma}, 0)/G'(0)$ and $G'(\gamma', \omega)/G'(0)$, whereas $G^\dagger/G'(0)$ has been fitted only to $G'(\bar{\gamma}, \omega)/G'(0)$.

The strain was limited to the range 0.01–1 to avoid artifacts from structural damage at larger strain. Yao et al. (2008) reported the possibility of irreversible flows and inability to separate relaxation effects from those of flow as factors that may affect differential measurements, e.g., leading to noisy or negative values of the loss modulus with each imposed strain (or stress). However, these effects are predominant for viscoelastic liquids, increased stiffness is required to overcome these limitations. The right panels of Figures 7.5.3 and

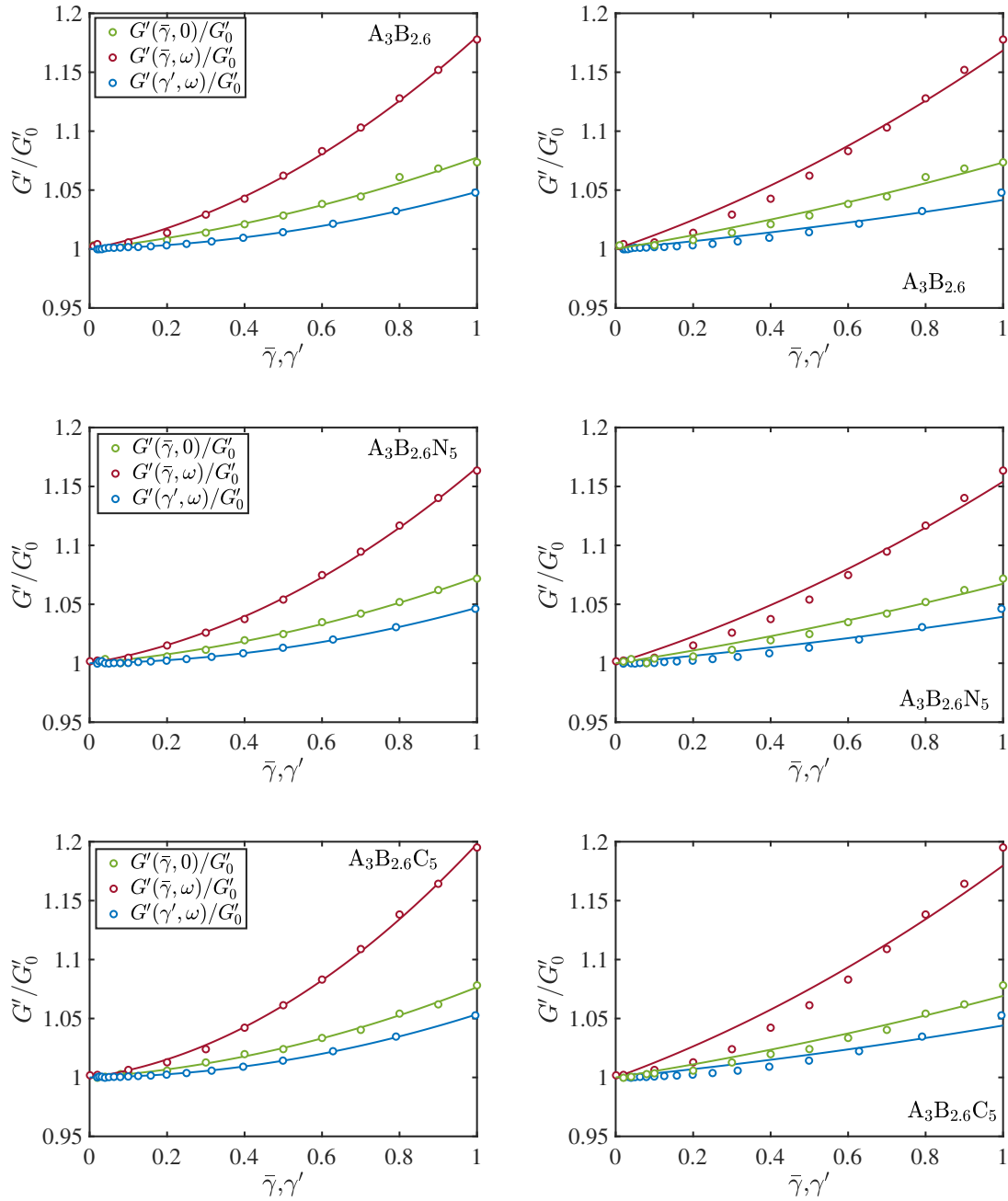


Figure 7.5.5: Normalized storage moduli from Figure (7.5.3) versus strain at $\omega = 10 \text{ rad s}^{-1}$. Solid lines in the left panels are quadratic fits with parameters specified in Table 7.5.3. Solid lines in the right panels are fits of the theoretical Eqn. (7.15) (blue and green) and Eqn. (7.16) (red) to ascertain the values of N (polymer segments between cross-links) provided in Table 7.5.5.

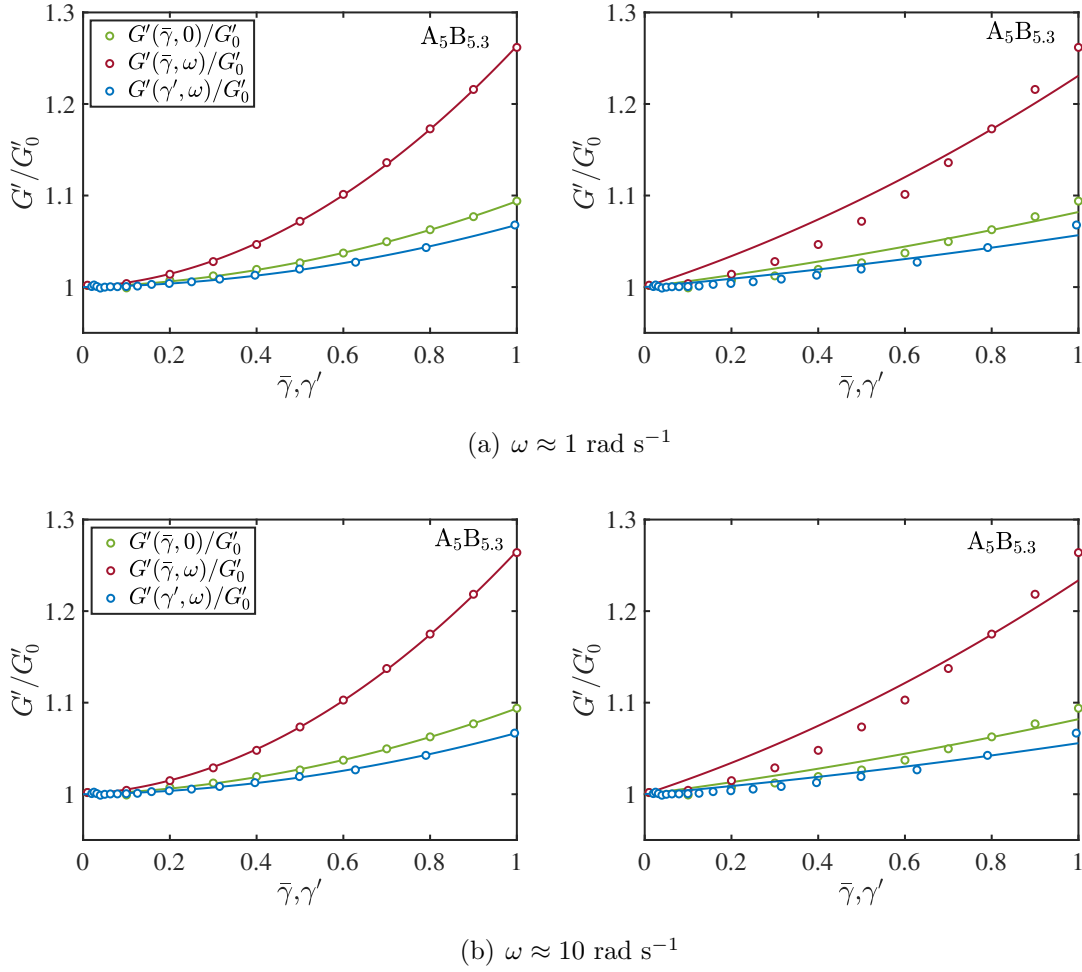


Figure 7.5.6: Normalized storage moduli from Figure (7.5.4) versus strain at $\omega = 1$ (top) and 10 rad s^{-1} (bottom). Solid lines in the left panels are quadratic fits with parameters specified in Table 7.5.4. Solid lines in the right panels are fits of the theoretical Eqn. (7.15) (blue and green) and Eqn. (7.16) (red) to ascertain the values of N (polymer segments between cross-links) provided in Table 7.5.6.

Table 7.5.2: Quadratic fitting parameters defined by $y = a + b\gamma + c\gamma^2$, for the curves shown in the left panel of Figure 7.5.4 at $\omega = 1$ and 10 rad s^{-1} .

Sample	ω (rad s ⁻¹)	y (Pa)	a (Pa)	b (Pa)	c (Pa)	R^2
A ₅ B _{5.3}	0	$G'(\bar{\gamma}', 0)$	2881	44.1	226.0	0.998
	1	$G'(\bar{\gamma}, \omega)$	2884	69.5	689.8	0.999
	1	$G'(\gamma', \omega)$	2903	20.5	175.5	0.998
A ₅ B _{5.3}	10	$G'(\bar{\gamma}, \omega)$	2882	80.0	685.3	0.999
	10	$G'(\gamma', \omega)$	2894	18.4	176.8	0.998

7.5.4 show loss moduli that are positive and much less noisy. In the nonlinear regime, the tangent loss moduli $G''(\bar{\gamma}, \omega)$ for all samples have higher magnitudes than the linear loss moduli $G''(\gamma', \omega)$. The true material dissipation in the nonlinear regime is expected to be higher than that predicted by $G''(\gamma', \omega)$ because of higher harmonics.

Each storage modulus was normalized with its limiting value at vanishing strain as shown in the left panels of Figures 7.5.5 and 7.5.6. Quadratic fit parameters are shown in Tables 7.5.3 and 7.5.4. LAOS analysis reported in Chapter 6 confirmed strain stiffening at large strain. Strain stiffening in the nonlinear regime has been attributed to finite chain extensibility (Rubinstein and Colby, 2003). Hence, the steady and local dynamic moduli captured by the theoretical formulas Eqns. (7.15) and (7.16) can be correlated with the experimental data.

According to Eqns. (7.15) and (7.16), the ratio of the quadratic and linear coefficients (e/d) in Tables 7.5.3 and 7.5.4 are 1/3 for the steady-state normalized modulus and 1/2 for the local dynamic normalized modulus, respectively. However, the values are somewhat higher, falling in the range 1–15 for the “soft” samples and 5–10 for the “stiff” sample. This might be attributed to elasticity limiting chain extensibility since materials with fewer entanglements or cross-links have larger N . The ratio e/d increases with the addition of NPs (or PA-coated NPs), which may reflect NPs restricting free rotation of the polymer segments, thereby enhancing chain stiffening. Without NPs, the ratio e/d likewise increases with increased cross-link density and monomer concentration.

The right panels in Figures 7.5.5 and 7.5.6 show fits of the steady and local dynamic

Table 7.5.3: Quadratic fitting parameters defined by $y_0 = 1 + d\gamma + e\gamma^2$, for lines shown in the left panel of Figure 7.5.5 at $\omega = 10 \text{ rad s}^{-1}$. These parameters are consistent with the values from the fitting coefficients in Table (7.5.1).

Sample	y_0	d	e	R^2	e/d
A ₃ B _{2.6}	$G'(\bar{\gamma}, 0)/G'(0)$	0.0387	0.0389	0.988	1.005
A ₃ B _{2.6} N ₅		0.0291	0.0438	0.996	1.505
A ₃ B _{2.6} C ₅		0.0233	0.0532	0.997	2.283
A ₃ B _{2.6}	$G'(\bar{\gamma}, \omega)/G'(0)$	0.0655	0.1147	0.998	1.751
A ₃ B _{2.6} N ₅		0.0549	0.1111	0.999	2.024
A ₃ B _{2.6} C ₅		0.0462	0.1520	0.999	3.290
A ₃ B _{2.6}	$G'(\gamma', \omega)/G'(0)$	0.0088	0.0398	0.999	4.523
A ₃ B _{2.6} N ₅		0.0044	0.0427	0.999	9.704
A ₃ B _{2.6} C ₅		0.0033	0.0503	0.999	15.24

Table 7.5.4: Quadratic fitting parameters defined by $y_0 = 1 + d\gamma + e\gamma^2$, for lines shown in Figure 7.5.6 at $\omega = 1$ and 10 rad s^{-1} . These parameters are consistent with the values from the fitting coefficients in Table (7.5.2) for hydrogel sample A₅B_{5.3}.

ω (rad s ⁻¹)	y_0	d	e	R^2	e/d
0	$G'(\bar{\gamma}, 0)/G'(0)$	0.0153	0.0785	0.998	5.129
1	$G'(\bar{\gamma}, \omega)/G'(0)$	0.0241	0.2392	0.999	9.934
10		0.0278	0.2378	0.999	8.563
1	$G'(\gamma', \omega)/G'(0)$	0.0071	0.0609	0.998	8.615
10		0.0064	0.0606	0.998	9.527

Table 7.5.5: Fitting parameter N in Eqns. (7.15) (blue and green lines) and (7.16) (red lines) shown in the right panels of Figure 7.5.5 at $\omega = 10 \text{ rad s}^{-1}$ in the strain range 0–1. $S = (X^T X)^{-1} s^2$, where s^2 is the mean squared error, X is the Jacobian of the fitted values with respect to N , and X^T is the transpose of X . The Student’s t is at the 95% confidence level ([The MathWorks, 2022](#)).

Sample	$G'/G'(0)$	$N \pm t\sqrt{S}$	R^2
A ₃ B _{2.6}	$G'(\bar{\gamma}, 0)/G'(0)$	30.89 ± 1.93	0.981
A ₃ B _{2.6} N ₅		33.80 ± 2.11	0.981
A ₃ B _{2.6} C ₅		32.89 ± 2.57	0.972
A ₃ B _{2.6}	$G'(\bar{\gamma}, \omega)/G'(0)$	30.25 ± 1.68	0.988
A ₃ B _{2.6} N ₅		33.24 ± 2.01	0.983
A ₃ B _{2.6} C ₅		28.23 ± 2.26	0.973
A ₃ B _{2.6}	$G'(\gamma', \omega)/G'(0)$	50.41 ± 4.77	0.971
A ₃ B _{2.6} N ₅		52.49 ± 5.90	0.960
A ₃ B _{2.6} C ₅		52.60 ± 6.79	0.923

moduli according to Eqns. (7.15) and (7.16) with the number polymer segments N as the sole fitting parameter, available in Tables 7.5.5 and 7.5.6. Equation (7.15) is not expected to be valid for correlating the linear normalized storage modulus $G'(\gamma', \omega)/G'(0)$ at large strain because it is derived for steady-state elastic shear stress. $G'(\gamma', \omega)/G'(0)$ is not an accurate representation of the storage modulus measured in the nonlinear regime, which explains the slightly higher values of N . The steady and local dynamic moduli both furnish $N \approx 30$ (“soft” samples) and 24 (“stiff” sample) for the steady-state and tangent modulus. This predicts an accurate characterization of the nonlinear storage modulus based on non-linear chain stretching. Strain stiffening in the nonlinear regime may therefore be directly linked to the non-linear stretching of polymer chains between cross-linking junctions.

7.6 Conclusions

The tangent modulus obtained by superposing a small oscillatory strain on a steady mean strain provides a convenient way of analyzing the nonlinear shear at large deformation. Pre-

Table 7.5.6: Fitting parameter N in Eqns. (7.15) (blue and green lines) and (7.16) (red lines) shown in the right panels of Figure 7.5.6 at $\omega = 1$ and 10 rad s^{-1} in the strain range 0–1 for hydrogel sample A₅B_{5.3}. $S = (X^T X)^{-1} s^2$, where s^2 is the mean squared error, X is the Jacobian of the fitted values with respect to N , and X^T is the transpose of X . The Student's t is at the 95% confidence level ([The MathWorks, 2022](#)).

ω (rad s ⁻¹)	$G'/G'(0)$	$N \pm t\sqrt{S}$	R^2
0	$G'(\bar{\gamma}, 0)/G'(0)$	27.48 ± 3.15	0.947
1	$G'(\bar{\gamma}, \omega)/G'(0)$	21.59 ± 2.52	0.949
10		21.32 ± 2.43	0.951
1	$G'(\gamma', \omega)/G'(0)$	40.64 ± 4.98	0.931
10		41.43 ± 5.16	0.929

cise control of the waveform, transient testing, and predominantly elastic behaviour of the samples were factors that contributed to the effectiveness of the rheological data and interpretation using this method. The nonlinear extension models for the steady and local dynamic moduli response were especially useful for correlating the experimental measurements. The strain stiffening behaviour at large deformation was captured by nonlinear extension of polymer chains between cross-linking junctions. Increased elasticity from chemical and nanoparticle cross-linking may have limited the extensibility of the chains by resisting the motion of the chains. Many entanglements or cross-links per chain corresponds to smaller number of chain segment N .

Conclusions and future work

8.1 Summary

The goal of this thesis was to characterize polymer-nanoparticles (NPs) interactions, compare the effects of polymer-coated NPs with bare NPs as physical cross-linkers in polymer solutions and hydrogels, and ascertain the effect of these interactions on NP dynamics and viscoelastic properties in the linear and nonlinear regime.

In chapter 3, the influence of PA on silica stability, structure, and mechanical properties was investigated. The adsorbed amounts were measured using thermogravimetric analysis, and the optimal parameters of the modified Langmuir isotherm revealed strong concentration dependence.

Electroacoustic spectroscopy was used to study the interactions between the NPs and the polymer network. Polymer coating reduces the mobility and increases the ζ -potential and the hydrodynamic diameter of the NPs at $\text{pH} = 9$. Rheological characterization of PA/NP suspensions furnished significant hydrodynamic interactions at higher NP volume fractions by correlating experimental data with the Krieger-Dougherty model. The loss modulus spectra reflected a steady shear viscosity that is increased by NPs.

The understanding of the relaxation time and temperature dependence of the viscoelastic properties of bare and PA-coated NP cross-linked PA solution was studied in chapter 4 in comparisons with the neat polymer solutions. This allows for effective tuning of the macroscopic properties of the material. Bare and PA-coated silica NP act as physical cross-linkers in the polymer matrix by increasing the viscosity, storage, and loss moduli of the resulting nanocomposites compared to the neat polymer. These NPs profoundly slow the relaxation of polymer solutions, with significant increases at high temperatures (34–56°C). The enhanced elastic modulus observed at these temperatures was not reversible. Cole-Cole plots

confirm the homogeneity of the mixtures at low temperatures. However, at high temperatures, the plots revealed the existence of a two-phase system with long relaxation times for the nanocomposites. Time-temperature superposition of dynamic spectra furnished negative apparent activation energy at higher temperatures, possibly attributed to polymer detachment from the NPs followed by chains swelling and blob network formation. Time-concentration superposition furnished a master plot with horizontal shift factors that showed little/no significance of PA-coating on the relaxation times of the bare/PA-coated nanocomposites.

Rheological properties in the linear viscoelastic regime of dual-cross-linked hydrogels with both silica NPs (bare or PA-coated) and chemical (bis-acrylamide) cross-linkers were investigated in chapter 5. These hydrogels were synthesized with unusually low chemical cross-linker ratios to highlight the effects of NP cross-linking. NPs acted as physical cross-linkers and furnishing enhanced mechanical properties. PA-coated NPs provided additional polymer-polymer and polymer-NPs attractive interactions, leading to increased storage and loss moduli, compared to bare silica NPs. Vertical and horizontal shift factors from time-concentration superposition with varying bis-cross-linker ratios yielded relaxation exponents for the dual-cross-linked hydrogels that were lower than bis-cross-linked hydrogels. These were attributed to additional physical entanglements with longer relaxation times. Time-temperature superposition extended the moduli spectra to lower frequencies and furnished apparent activation energies that increased with NPs volume fraction in the range 21–56°C.

Large amplitude oscillatory shear (LAOS) test protocols were used to study the effects of silica NP cross-linking on the flow-induced microstructure of polyacrylamide hydrogels in chapter 6. The nonlinear responses of “soft” and “stiff” hydrogels were compared. The use of bare or PA-coated silica NPs in cross-linking polyacrylamide hydrogels in the strain range 0.001–10, led to an increase in the moduli, shear stress, and higher-order harmonic contributions at large strain amplitude, but did not significantly affect the flow-induced microstructure resulting from large strain deformation. The onset of nonlinearity appears at lower strain amplitude for the “stiff” hydrogels. The “soft” hydrogels can only be stretched 100% before it becomes nonlinear, while the “stiff” hydrogels by 10%. NPs slightly reduce the onset of nonlinearity.

In chapter 7, the strain stiffening response at large deformation was further analyzed by specifying user-defined strain input that superimposes a mean strain on a small oscillatory strain. The tangent moduli obtained from the resulting stress and input strain were compared

with steady-state moduli. Both moduli were correlated with nonlinear extension models, which capture the material strain stiffening at large deformation.

8.2 Contributions to knowledge

Original contributions to knowledge include:

- Thermogravimetric analysis was used as a technique to measure the adsorbed amount of polyacrylamide (PA) onto colloidal silica. The results suggest the occurrence of adsorption that increases with polymer concentration and molecular weight in an aqueous solvent.
- Rheological properties of dual-crosslinked gels containing both chemical (bis) cross-linkers with low cross-linker ratio and physical (bare or PA-coated NPs) cross-linkers are reported, providing microstructural interpretations.
- Silica NPs have been used to enhance the mechanical properties of polyacrylamide solutions previously. However, the temperature dependence of these properties compared to neat polymer solutions was unknown. Using a comprehensive set of data from rheology, the effects of temperatures and NPs (bare or PA-coated) on the polymer solutions were investigated. The results suggest that chain mobility increases for all samples at low temperatures. Further temperature increases led to an increase in the number of bonds and longer relaxation times for the nanocomposites compared to the neat polymer.
- Time-temperature superposition of the NP-cross-linked PA solutions in the range 21–56°C showed validity only in the limited temperature range 21–44°C. This range reduces with an increase in NPs volume fraction and PA coating. Beyond this range, the apparent activation energy is negative and the relaxation time unexpectedly increases. This was supported by the van Gorp-Palmen plots which superpose at the valid temperature range.
- Modification of NPs by polymer adsorption enhanced the viscoelastic properties of PA solutions and PA hydrogels when used as a physical cross-linker, compared to bare NPs

with the same volume fraction. The PA-pre coating increases polymer chain branching and enhances entanglement/coupling between the silica and hydrogel network.

- Linear rheology has been used as an extremely powerful measure for understanding some characteristics of microstructure. However, in making predictions of engineering performance, nonlinear rheology determines to what extent the material can be stretched or deformed and the deformation-induced microstructural changes. Using large amplitude oscillatory shear test protocols, the effect of silica NP cross-linking in “soft” and “stiff” hydrogels at large deformation was investigated. The onset of nonlinearity and the stress-strain curves were not greatly affected by NPs compared to the neat gels, but have distinctly different values for the “soft” and “stiff” gels.
- Superposing a mean strain on a small oscillatory strain provides a convenient way of characterizing the nonlinear material response. Correlating the tangent modulus from the superposition and steady-state modulus with the nonlinear rheological extension model captures the strain stiffening response at large deformation.

8.3 Suggestions for future work

- Distinct temperature effects were found for the NP-cross-linked polyacrylamide solutions in this thesis, which were not present in the NP-cross-linked polyacrylamide hydrogels. Thus, it is necessary to understand how chemical (bis) cross-links may have influenced these features by studying the samples at a much wider temperature range,
- Effects of PA-coated silica NPs on the mechanical properties of PA solutions and hydrogels were investigated with only one NP size and volume fraction. Although these NPs enhanced the mechanical properties compared to bare silica NPs, there were little/no significant distinctions in their concentration and temperature-dependent properties. Considering the importance of particle size and volume fraction in cross-linking, the coating should be applied to varying NP sizes and the effects at varying volume fractions should be studied.
- The presence of wall-slips at large deformations was investigated using the cone-plate and the sand-blasted geometries. However, based on the large amplitude oscillatory

shear responses at strain amplitudes > 3 for the “stiff” gels, it is necessary to explore modifying the parallel plates using sand-paper or glass slides.

- In chapters 6 and 7, large amplitude oscillatory shear (LAOS) test protocols were applied at a single frequency, which limited the understanding of the microstructural changes in the hydrogels at large deformation. It is important to explore the frequency dependence of LAOS and other nonlinear parameters for a comprehensive nonlinear rheology analysis of the gels.

References

- A. Abbasi M., M. Kamkar, A. Sanati-Nezhad, S. H. Hejazi, and U. Sundararaj. Nonlinear viscoelastic characterization of charged cellulose nanocrystal network structure in the presence of salt in aqueous media. *Cellulose*, 27(10):5729–5743, 2020.
- S. Abdurrahmanoglu, V. Can, and O. Okay. Equilibrium swelling behavior and elastic properties of polymer–clay nanocomposite hydrogels. *J. Appl. Polym. Sci.*, 109(6):3714–3724, 2008.
- V. Adibnia and R. J. Hill. Universal aspects of hydrogel gelation kinetics, percolation and viscoelasticity from PA-hydrogel rheology. *J. Rheol.*, 60(4):541–548, 2016.
- V. Adibnia and R. J. Hill. Viscoelasticity of near-critical silica-polyacrylamide hydrogel nanocomposites. *Polymer*, 112:457–465, 2017.
- V. Adibnia, K. W. Cho, and R. J. Hill. Nanoparticle coupling to hydrogel networks: New insights from electroacoustic spectroscopy. *Macromolecules*, 50(10):4030–4038, 2017a.
- V. Adibnia, S. M. Taghavi, and R. J. Hill. Roles of chemical and physical crosslinking on the rheological properties of silica-doped polyacrylamide hydrogels. *Rheol. Acta*, 56:123–134, 01 2017b.
- V. Adibnia, G. Afuwape, and R. J. Hill. Electrokinetic sonic amplitude of polyelectrolyte solutions and networks. *Macromolecules*, 53(17):7460–7468, 2020.
- D. Adolf and J. E. Martin. Time-cure superposition during crosslinking. *Macromolecules*, 23:3700–3704, 1990.
- G. Afuwape and R. J. Hill. Hexadecane-nanoemulsion-doped polyacrylamide hydrogels. *ACS Appl. Polym. Mater.*, 3(4):1727–1738, 2021.

- Y. Akagi, J. P. Gong, U.-I. Chung, and T. Sakai. Transition between phantom and affine network model observed in polymer gels with controlled network structure. *Macromolecules*, 46(3):1035–1040, 2013.
- M. Alberto Masuelli. Mark-houwink parameters for aqueous-soluble polymers and biopolymers at various temperatures. *J. polym. biopolym. phys. chem.*, 2(2):37–43, 2014.
- E. Aliabadian, S. Sadeghi, M. Kamkar, Z. Chen, and U. Sundararaj. Rheology of fumed silica nanoparticles/partially hydrolyzed polyacrylamide aqueous solutions under small and large amplitude oscillatory shear deformations. *J. Rheol.*, 62(5):1197–1216, 2018.
- J. Alves Júnior and J. Baldo. The behavior of zeta potential of silica suspensions. *New J. Glass Ceram.*, 04:29–37, 2014.
- B. J. Anderson and C. F. Zukoski. Rheology and microstructure of entangled polymer nanocomposite melts. *Macromolecules*, 42(21):8370–8384, November 2009.
- F. A. Anderson. Amended final report on the safety assessment of polyacrylamide and acrylamide residues in cosmetics¹. *Int. J. Toxicol.*, 24:21–50, 03 2005.
- J. M. Andrews and C. J. Roberts. Non-native aggregation of alpha-chymotrypsinogen occurs through nucleation and growth with competing nucleus sizes and negative activation energies. *Biochem. (Mosc.)*, 46(25):7558–7571, 2007.
- D. Atkins, P. Kékicheff, and O. Spalla. Adhesion between colloidal silica as seen with direct force measurement. *J. Colloid Interf. Sci.*, 188(1):234–237, 1997.
- P. Atkins and J. de Paula. *Atkins' Physical Chemistry*. OUP Oxford, ninth edition, 2010.
- M. Bahram, N. Mohseni, and M. Moghtader. An introduction to hydrogels and some recent applications. In Sutapa Biswas Majee, editor, *Emerging Concepts in Analysis and Applications of Hydrogels*, chapter 2. IntechOpen, Rijeka, 2016.
- S. Barany. Polymer adsorption and electrokinetic potential of dispersed particles in weak and strong electric fields. *Adv. Colloid Interface Sci.*, 222:58–69, 2015.
- E. Barrett-Catton, M. L. Ross, and P. Asuri. Multifunctional hydrogel nanocomposites for biomedical applications. *Polymers*, 13, 2021.
- A. Basu, Q. Wen, X. Mao, T. C. Lubensky, Paul A. Janmey, and A. G. Yodh. Nonaffine displacements in flexible polymer networks. *Macromolecules*, 44(6):1671–1679, 2011.

- M. Baumgärtel and N. Willenbacher. The relaxation of concentrated polymer solutions. *Rheol. Acta*, 35:168–185, 03 1996.
- K. A. Beningo, C.-M. Lo, and Y.-L. Wang. Flexible polyacrylamide substrata for the analysis of mechanical interactions at cell-substratum adhesions. In *Methods in Cell Biology*, volume 69 of *Methods in Cell Biology*, pages 325–339. Academic Press, 2002.
- H. E. Bergna and W. O. Roberts. *Colloidal Silica: Fundamentals and Applications*. Surfactant science series. CRC Taylor & Francis, 2006.
- H. Bessaies-Bey, J. Fusier, S. Harrisson, M. Destarac, S. Jouenne, N. Passade-Boupat, F. Lequeux, J.-B. d’Espinose de Lacaillerie, and N. Sanson. Impact of polyacrylamide adsorption on flow through porous siliceous materials: State of the art, discussion and industrial concern. *J. Colloid Interf. Sci.*, 531:693–704, 2018.
- P. S. Bhosale, J. Chun, and J. C. Berg. Electroacoustics of particles dispersed in polymer gel. *Langmuir*, 27 12:7376–9, 2011.
- T. Boudou, J. Ohayon, C. Picart, R. I. Pettigrew, and P. Tracqui. Nonlinear elastic properties of polyacrylamide gels: implications for quantification of cellular forces. *Biorheology*, 46: 191–205, 2009.
- S. Brunauer, P. H. Emmett, and E. Teller. Adsorption of gases in multimolecular layers. *J. Am. Chem. Soc.*, 60(2):309–319, 1938.
- G. Büyükköroğlu, D. D. Dora, F. Özdemir, and C. Hizel. Chapter 15 - Techniques for protein analysis. In D. Barh and V. Azevedo, editors, *Omics Technologies and Bio-Engineering*, pages 317–351. Academic Press, 2018.
- R. Byron Bird and P. J. Carreau. A nonlinear viscoelastic model for polymer solutions and melts—I. *Chem Eng Sci*, 23(5):427–434, 1968.
- D. Calvet, J. Wong, and S. Giasson. Rheological monitoring of polyacrylamide gelation: Importance of cross-link density and temperature. *Macromolecules*, 37, 10 2004.
- M. L. Carasso, W. N. Rowlands, and R. W. O’Brien. The effect of neutral polymer and nonionic surfactant adsorption on the electroacoustic signals of colloidal silica. *J. Colloid Interf. Sci.*, 193(2):200–214, 1997.

- E. M. Carlisle. Silicon: A requirement in bone formation independent of vitamin d1. *Calcif. Tissue Int.*, 33(1):27–34, 1981.
- O. Chaudhuri, J. Cooper-White, P. Janmey, D. Mooney, and V. Shenoy. Effects of extracellular matrix viscoelasticity on cellular behaviour. *Nature*, 584:535 – 546, 2020.
- A. Chaurasia, Y. Suzhu, C. K. F. Henry, V. T. Mogal, and S. Saha. *Properties and Applications of Polymer Nanocomposite*, pages 43–98. Springer London, 2015.
- Y. Chen, H. Zou, M. Liang, and P. Liu. Rheological, thermal, and morphological properties of low-density polyethylene/ultra-high-molecular-weight polyethylene and linear low-density polyethylene/ultra-high-molecular-weight polyethylene blends. *J. Appl. Polym. Sci.*, 129(3):945–953, 2013.
- K. S. Cho, K. Hyun, K. H. Ahn, and S. J. Lee. A geometrical interpretation of large amplitude oscillatory shear response. *J. Rheol.*, 49(3):747–758, 2005.
- G. Y. H. Choong, D. S. A. De Focatiis, and D. G. Hassell. Viscoelastic melt rheology and time-temperature superposition of polycarbonate-multi-walled carbon nanotube nanocomposites. *Rheol. Acta*, 52(8):801–814, 2013.
- L. Christensen, V. Breiting, T. Bjarnsholt, S. Eickhardt, E. Høgdall, M. Janssen, N. Pallua, and S. A. J. Zaat. Bacterial Infection as a Likely Cause of Adverse Reactions to Polyacrylamide Hydrogel Fillers in Cosmetic Surgery. *Clin. Infect. Dis.*, 56(10):1438–1444, 02 2013.
- L. Christensen, L. Camitz, K. E. Illigen, M. Hansen, R. Sarvaa, and P. G. Conaghan. Synovial incorporation of polyacrylamide hydrogel after injection into normal and osteoarthritic animal joints. *Osteoarthr. Cartil.*, 24(11):1999–2002, 2016.
- K. S. Cole and Robert H. Cole. Dispersion and absorption in dielectrics I. Alternating current characteristics. *J. Chem. Phys.*, 9(4):341–351, 1941.
- W. P. Cox and E. H. Merz. Correlation of dynamic and steady flow viscosities. *J Polym Sci*, 28(118):619–622, 1958.
- V. Daga and N. Wagner. Linear viscoelastic master curves of neat and Laponite-filled poly(ethylene oxide)-water solutions. *Rheol. Acta*, 45:813–824, 08 2006.

- S. Dai, X. Zhou, S. Wang, J. Ding, and N. Yuan. A self-healing conductive and stretchable aligned carbon nanotube/hydrogel composite with a sandwich structure. *Nanoscale*, 10: 19360–19366, 2018.
- Z. Dastjerdi, E. D. Cranston, R. Berry, C. Fraschini, and M. A. Dubé. Polymer nanocomposites for emulsion-based coatings and adhesives. *Macromol. React. Eng.*, 13(2):1800050, 2019.
- J. C. Day and I. D. Robb. Thermodynamic parameters of polyacrylamides in water. *Polymer*, 22(11):1530–1533, 1981.
- C. G. de Kruif, E. M. F. van Iersel, A. Vrij, and W. B. Russel. Hard sphere colloidal dispersions: Viscosity as a function of shear rate and volume fraction. *J. Chem. Phys.*, 83(9):4717–4725, 1985. doi: 10.1063/1.448997.
- J. Dealy and D. Plazek. Time-temperature superposition-a users guide. *Rheol. Bull.*, 78: 16–31, 01 2009.
- A. V. Delgado, F. González-Caballero, R. J. Hunter, L. K. Koopal, and J. Lyklema. Measurement and interpretation of electrokinetic phenomena. *J. Colloid Interf. Sci.*, 309(2): 194–224, 2007.
- A. K. Denisin and B. Pruitt. Tuning the range of polyacrylamide gel stiffness for mechanobiology applications. *ACS Appl. Mater. Interfaces*, 8 34:21893–902, 2016.
- C. Derec, G. Ducouret, A. Ajdari, and F. Lequeux. Aging and nonlinear rheology in suspensions of polyethylene oxide-protected silica particles. *Phys. Rev. E*, 67:061403, 2003.
- F. Di Lorenzo and S. Seiffert. Nanostructural heterogeneity in polymer networks and gels. *Polym. Chem.*, 6:5515–5528, 2015.
- C. Du and R. J. Hill. Complementary-DNA-strand cross-linked polyacrylamide hydrogels. *Macromolecules*, 52(17):6683–6697, 2019a.
- C. Du and R. J. Hill. Linear viscoelasticity of weakly cross-linked hydrogels. *J. Rheol.*, 63(1):109–124, 2019b.
- A. S. Dukhin and P. J. Goetz. Chapter 2 - Fundamentals of interface and colloid science. In *Characterization of Liquids, Dispersions, Emulsions, and Porous Materials Using Ultrasound (Third Edition)*, pages 19–83. Elsevier, 2017.

- A. Ebadi, Jafar S. Soltan Mohammadzadeh, and A. Khudiev. What is the correct form of BET isotherm for modeling liquid phase adsorption? *Adsorption*, 15(1):65–73, 2009.
- I. Emri and M. Gergesova. *Time-dependent behavior of solid polymers*, pages 247–330. EOLSS, 01 2010.
- R. H. Ewoldt, A. E. Hosoi, and G. H. McKinley. New measures for characterizing nonlinear viscoelasticity in large amplitude oscillatory shear. *J. Rheol.*, 52(6):1427–1458, 2008.
- R. H. Ewoldt, Peter Winter, Jason Maxey, and Gareth H. McKinley. Large amplitude oscillatory shear of pseudoplastic and elastoviscoplastic materials. *Rheol Acta*, 49(2):191–212, 2010.
- L. Fambri, A. Dorigato, and A. Pegoretti. Role of surface-treated silica nanoparticles on the thermo-mechanical behavior of poly(lactide). *Appl. Sci. Switz.*, 10(19):1–20, 2020.
- G. Fan, M. Li, X. Chen, A. Palyanitsina, and A. Timoshin. Polymer-nanosilica-assisted to evaluate oil recovery performances in sandstone reservoirs. *Energy Reports*, 7:2588–2593, 2021.
- T.-H. Fan and R. Tuinier. Hydrodynamic interaction of two colloids in nonadsorbing polymer solutions. *Soft Matter*, 6:647–654, 2010.
- X. Fan, H. Xu, Q. Zhang, D. Xiao, Y. Song, and Q. Zheng. Insight into the weak strain overshoot of carbon black filled natural rubber. *Polymer*, 167:109–117, 2019.
- M. H. Fanood and M. H. George. Estimation of the limiting viscosity number and Huggins constant of polyacrylamides in water and 1 M aqueous sodium chloride. *Polymer*, 28(13):2241–2243, 1987.
- J. D. Ferry. *Viscoelastic Properties of Polymers*. Wiley, 1970.
- G. Fijałkowska, K. Szewczuk-Karpisz, and M. Wiśniewska. Polyacrylamide soil conditioners: The impact on nanostructured clay minerals’ aggregation and heavy metals’ circulation in the soil environment. In O. Fesenko and L. Yatsenko, editors, *Nanomaterials and Nanocomposites, Nanostructure Surfaces, and Their Applications*, pages 111–127, Cham, 2021. Springer International Publishing.
- S. Filipe, I. Vittorias, and M. Wilhelm. Experimental correlation between mechanical non-linearity in LAOS flow and capillary flow instabilities for linear and branched commercial polyethylenes. *Macromol. Mater. Eng.*, 293(1):57–65, 2008.

- A. B. Fossati, M. M. Alho, and S. E. Jacobo. Polymer-functionalized nanoparticles for improving oil displacement. *Adv. Nat. Sci.: Nanosci. Nanotechnol.*, 9(1):015007, 2018.
- A. Franck. APN 007 Measuring and evaluating oscillation data. 2002.
- M. Funaki and P. A. Janmey. Chapter 23 - technologies to engineer cell substrate mechanics in hydrogels. In A. Vishwakarma and J. M. Karp, editors, *Biology and Engineering of Stem Cell Niches*, pages 363–373. Academic Press, Boston, 2017.
- A. K. Gaharwar, N. A. Peppas, and A. Khademhosseini. Nanocomposite hydrogels for biomedical applications. *Biotechnol. Bioeng.*, 111(3):441–453, 2014.
- F. Gao. *Advances in Polymer Nanocomposites - Types and Applications*. Woodhead Publishing, 2012.
- X. Gao, R.E. Jensen, S.H. McKnight, and J.W. Gillespie. Effect of colloidal silica on the strength and energy absorption of glass fiber/epoxy interphases. *Compos. - A: Appl. Sci. Manuf.*, 42(11):1738–1747, 2011.
- M. L. Gardel, J. H. Shin, F. C. MacKintosh, L. Mahadevan, P. Matsudaira, and D. A. Weitz. Elastic behavior of cross-linked and bundled actin networks. *Science*, 304(5675):1301–1305, 2004.
- G. Gerlach and K.-F. Arndt, editors. *Hydrogel Sensors and Actuators: Engineering and Technology*, volume 6. Springer, Berlin, Heidelberg, 1 edition, January 2010.
- P. Giannouli and E. R. Morris. Cryogelation of xanthan. *Food Hydrocoll.*, 17(4):495–501, 2003.
- G. Glorani, R. Marin, P. Canton, M. Pinto, G. Conti, G. Fracasso, and P. Riello. Pegylated silica nanoparticles: cytotoxicity and macrophage uptake. *J. Nanopart. Res. Interdiscip. Forum Nanoscale Sci. Technol.*, 19(8):294, Aug 2017.
- T. B. Goudoulas and N. Germann. Concentration effect on the nonlinear measures of dense polyethylene oxide solutions under large amplitude oscillatory shear. *J. Rheol.*, 62(5):1299–1317, 2018.
- T. B. Goudoulas, S. Pan, and N. Germann. Nonlinearities and shear banding instability of polyacrylamide solutions under large amplitude oscillatory shear. *J. Rheol.*, 61(5):1061–1083, 2017.

- C. Green, G. Cardon, and G. Butters. Water release from cross-linked polyacrylamide. *Proc. Hydrology Days Conference*, 01 2004.
- S. Gu, Y. Shi, L. Wang., and Z. Liu, W. and Song. Study on the stability of modified colloidal silica with polymer in aqueous environment. *Colloid Polym. Sci.*, 292(1):267–273, 2014.
- Y. Guévellou, Ch. Noïk, J. Lecourtier, and D. Defives. Polyacrylamide adsorption onto dissolving minerals at basic pH. *Colloids Surf., A*, 100:173–185, 1995.
- J. Guo, Y. and Bae, Z. Fang, P. Li, F. Zhao, and G. Yu. Hydrogels and hydrogel-derived materials for energy and water sustainability. *Chem. Rev.*, 120(15):7642–7707, 2020.
- E. Guth. Theory of filler reinforcement. *J. Appl. Phys.*, 16(1):20–25, 1945.
- H. C. Hamaker. The london—van der waals attraction between spherical particles. *Physica*, 4(10):1058–1072, 1937.
- C. D. Han and H.-K. Chuang. Criteria for rheological compatibility of polymer blends. *J. Appl. Polym. Sci.*, 30(11):4431–4454, 1985.
- U. A. Handge and P. Pötschke. Deformation and orientation during shear and elongation of a polycarbonate/carbon nanotubes composite in the melt. *Rheol. Acta*, 46(6):889–898, 2007.
- K. Haraguchi, S. Masatoshi, N. Kotobuki, and K. Murata. Thermoresponsible cell adhesion/detachment on transparent nanocomposite films consisting of poly(2-methoxyethyl acrylate) and clay. *J. Biomater. Sci. Polym. Ed.*, 22(18):2389–2406, 2011a.
- K. Haraguchi, K. Uyama, and H. Tanimoto. Self-healing in nanocomposite hydrogels. *Macromol Rapid Commun*, 32(16):1253–1258, 2011b.
- S. Harding. Dilute solution viscometry of food biopolymers. In *Functional properties of food macromolecules*, 2011.
- J. Hári and B. Pukánszky. Nanocomposites: Preparation, structure, and properties. In M. Kutz, editor, *Applied Plastics Engineering Handbook*, Plastics Design Library, chapter 8, pages 109–142. William Andrew Publishing, Oxford, 2011.
- P. A. Hassan, G. Verma, and R. Ganguly. Soft materials - properties and applications. In S. Banerjee and A. K. Tyagi, editors, *Functional Materials*, pages 1–59. Elsevier, London, 2012.

- P. C. Hiemenz and R. Rajagopalan. *Principles of Colloid and Surface Chemistry, Revised and Expanded*. CRC Press, 2016.
- R. J. Hill, D. A. Saville, and W. B. Russel. Electrophoresis of spherical polymer-coated colloidal particles. *J. Colloid Interf. Sci.*, 258(1):56–74, 2003.
- D. Horinek. *DLVO Theory*, pages 343–346. Springer New York, New York, NY, 2014.
- M. Hoseini, A. Haghtalab, and M. H. N. Famili. Rheology and morphology study of immiscible linear low-density polyethylene/poly(lactic acid) blends filled with nanosilica particles. *J. Appl. Polym. Sci.*, 134(46):45526, 2017.
- Z. Hu, M. Haruna, H. Gao, E. Nourafkan, and D. Wen. Rheological properties of partially hydrolyzed polyacrylamide seeded by nanoparticles. *Ind. Eng. Chem. Res.*, 56(12):3456–3463, March 2017.
- M. L. Huggins. The viscosity of dilute solutions of long-chain molecules. IV. Dependence on concentration. *J. Am. Chem. Soc.*, 64(11):2716–2718, November 1942.
- R. J. Hunter. Chapter 2 - Charge and potential distribution at interfaces. In *Zeta Potential in Colloid Science*, pages 11–58. Academic Press, 1981.
- R. J. Hunter. Recent developments in the electroacoustic characterisation of colloidal suspensions and emulsions. *Colloids Surf., A*, 141(1):37–66, 1998.
- E. D. E. R. Hyde, A. Seyfaee, F. Neville, and R. Moreno-Atanasio. Colloidal silica particle synthesis and future industrial manufacturing pathways: A review. *Ind. Eng. Chem. Res.*, 55(33):8891–8913, 2016.
- K. Hyun and W. Kim. A new non-linear parameter q from FT-rheology under nonlinear dynamic oscillatory shear for polymer melts system. *Korea-Aust. Rheol. J.*, 23(4):227–235, 2011.
- K. Hyun and M. Wilhelm. Establishing a new mechanical nonlinear coefficient Q from FT-rheology: First investigation of entangled linear and comb polymer model systems. *Macromolecules*, 42, 12 2008.
- K. Hyun and M. Wilhelm. *Nonlinear Oscillatory Shear Mechanical Responses*. Springer International Publishing, Cham, 2018.

- K. Hyun, S. H. Kim, K. H. Ahn, and S. J. Lee. Large amplitude oscillatory shear as a way to classify the complex fluids. *J. Non-Newtonian Fluid Mech.*, 107(1):51–65, 2002.
- K. Hyun, K. H. Ahn, S. J. Lee, M. Sugimoto, and K. Koyama. Degree of branching of polypropylene measured from Fourier-transform rheology. *Rheol. Acta*, 46(1):123–129, 2006. cited By 45.
- K. Hyun, E. S. Baik, K. H. Ahn, S. J. Lee, M. Sugimoto, and K. Koyama. Fourier-transform rheology under medium amplitude oscillatory shear for linear and branched polymer melts. *J. Rheol.*, 51(6):1319–1342, 2007.
- K. Hyun, M. Wilhelm, C. O. Klein, K. S. Cho, J. G. Nam, K. H. Ahn, S. J. Lee, R. H. Ewoldt, and G. H. McKinley. A review of nonlinear oscillatory shear tests: Analysis and application of large amplitude oscillatory shear (LAOS). *Prog. Polym. Sci.*, 36(12):1697–1753, 2011.
- Y. Isono and T. Aoyama. Filler effects on temperature shift factors in viscoelastic properties of carbon black filled rubbers. *Nihon Reoroji Gakk*, 41:137–144, 01 2013.
- M. Itskov, A. E. Ehret, and R. Dargazany. A full-network rubber elasticity model based on analytical integration. *Math Mech Solids*, 15(6):655–671, 2010.
- M. Itskov, R. Dargazany, and K. Hörnes. Taylor expansion of the inverse function with application to the langevin function. *Math Mech Solids*, 17(7):693–701, 2012.
- H. S. Jeon, A. I. Nakatani, C. C. Han, and R. H. Colby. Melt rheology of lower critical solution temperature polybutadiene/polyisoprene blends. *Macromolecules*, 33(26):9732–9739, 2000.
- Y. Jia, J. Chen, W. Liu, and D. Yin. Construction of highly stretchable silica/polyacrylamide nanocomposite hydrogels through hydrogen bond strategy. *J. Polym. Res.*, 26(5):119, 2019.
- R. A. L. Jones and R. W. Richards. *Polymers at Surfaces and Interfaces*. Cambridge University Press, 1999.
- S. Jouenne and B. Levache. Universal viscosifying behavior of acrylamide-based polymers used in enhanced oil recovery. *J. Rheol.*, 64(5):1295–1313, 2020.
- I. M. Kalogeras. *Glass-Transition Phenomena in Polymer Blends*, pages 1–134. 07 2016.

- M. Kamkar, E. Aliabadian, A. Shayesteh Z., and U. Sundararaj. Application of nonlinear rheology to assess the effect of secondary nanofiller on network structure of hybrid polymer nanocomposites. *Phys. Fluids*, 30(2):023102, 2018.
- M. Kamkar, M. Janmaleki, E. Erfanian, A. Sanati-Nezhad, and U. Sundararaj. Viscoelastic behavior of covalently crosslinked hydrogels under large shear deformations: An approach to eliminate wall slip. *Phys. Fluids*, 33(4):041702, 2021.
- C. E. Kadow, P. C. Georges, P. A. Janmey, and K. A. Beningo. Polyacrylamide hydrogels for cell mechanics: Steps toward optimization and alternative uses. In *Cell Mechanics*, volume 83 of *Methods in Cell Biology*, pages 29–46. Academic Press, 2007.
- J.-H. Kim, H. Kim, Y. Choi, D. S. Lee, J. Kim, and G.-R. Yi. Colloidal mesoporous silica nanoparticles as strong adhesives for hydrogels and biological tissues. *ACS Appl. Mater. Interfaces*, 9(37):31469–31477, 2017.
- M. Kim and K. Hyun. Characterization of polyethylene/silica nanocomposites using different rheological analyses. *Korea-Aust. Rheol. J.*, 33(1):25–36, 2021.
- M. Kim, H. Y. Song, W. J. Choi, and K. Hyun. Evaluation of the degree of dispersion of polymer nanocomposites (PNCs) using nonlinear rheological properties by FT-rheology. *Macromolecules*, 52(22):8604–8616, 2019.
- S. Kim, J. Sung, K. Ahn, and S. Lee. Drying of the silica/PVA suspension: Effect of suspension microstructure. *Langmuir*, 25(11):6155–6161, 2009.
- C. O. Klein, H. W. Spiess, A. Calin, C. Balan, and M. Wilhelm. Separation of the nonlinear oscillatory response into a superposition of linear, strain hardening, strain softening, and wall slip response. *Macromolecules*, 40(12):4250–4259, 2007.
- W. Kozicki and P. Q. Kuang. An alternative method for evaluation of intrinsic viscosity. *Can. J. Chem. Eng.*, 74(3):429–432, 1996.
- I. M. Krieger and T. J. Dougherty. A Mechanism for Non-Newtonian Flow in Suspensions of Rigid Spheres. *Trans. Soc. Rheol.*, 3(1):137–152, 1959.
- W. M. Kulicke, R. Kniewske, and J. Klein. Preparation, characterization, solution properties and rheological behaviour of polyacrylamide. *Prog. Polym. Sci.*, 8(4):373–468, 1982.

- D. Kumar, T. Ganat, N. Lashari, M.A. Ayoub, S. Kalam, T.A. Chandio, and B.M. Negash. Experimental investigation of GO-HPAM and SiO₂-HPAM composite for cEOR: Rheology, interfacial tension reduction, and wettability alteration. *Colloids Surf., A*, 637, 2022.
- S. Kumar, Sarita, M. Nehra, N. Dilbaghi, K. Tankeshwar, and K.-H. Kim. Recent advances and remaining challenges for polymeric nanocomposites in healthcare applications. *Prog. Polym. Sci.*, 80:1–38, 2018.
- P. Lagarrigue, J. Soulié, D. Grossin, A. Dupret-Bories, C. Combes, and V. Darcos. Well-defined polyester-grafted silica nanoparticles for biomedical applications: Synthesis and quantitative characterization. *Polymer*, 211:123048, 2020.
- S. Lakkadwala, S. Nguyen, J. Nesamony, A. S. Narang, and S. H. S. Boddu. *Smart Polymers in Drug Delivery*, pages 169–199. Springer International Publishing, Cham, 2015.
- T. H. Larsen and E. M. Furst. Microrheology of the liquid-solid transition during gelation. *Phys. Rev. Lett.*, 100:146001, 2008.
- J. Laurens, J. Jolly, G. Ovarlez, H. Fay, T. Chaussée, and P. Sotta. Competitive adsorption between a polymer and solvents onto silica. *Langmuir*, 36, 06 2020.
- A. Lazaro, K. Sato, H. J. H. Brouwers, and J. W. Geus. Pore structure development of silica particles below the isoelectric point. *Micropor. Mesopor. Mat.*, 267:257–264, 2018.
- B. J. Lee and M. Schlautman. Effects of polymer molecular weight on adsorption and flocculation in aqueous kaolinite suspensions dosed with nonionic polyacrylamides. *Water*, 7:5896–5909, 10 2015.
- S. H. Lee, H. Y. Song, and K. Hyun. Effects of silica nanoparticles on copper nanowire dispersions in aqueous PVA solutions. *Korea-Aust. Rheol. J.*, 28(2):111–120, 2016.
- R. D. Lentz, R. E. Sojka, and J. A. Foerster. Estimating polyacrylamide concentration in irrigation water. *J. Environ. Qual.*, 25(5):1015–1024, 1996.
- K. Lewandowska, D. U. Staszewska, and M. Bohdanecký. The Huggins viscosity coefficient of aqueous solution of poly(vinyl alcohol). *Eur. Polym. J.*, 37(1):25–32, 2001.
- X. Li, Z. Xu, H. Yin, Y. Feng, and H. Quan. Comparative studies on enhanced oil recovery: Thermoviscosifying polymer versus polyacrylamide. *Energy Fuels*, 31, 02 2017.

- X. Li, Q. Sun, Q. Li, N. Kawazoe, and G. Chen. Functional hydrogels with tunable structures and properties for tissue engineering applications. *Front. Chem.*, 6, 2018.
- A. Liberman, N. Mendez, W. C. Trogler, and A. C. Kummel. Synthesis and surface functionalization of silica nanoparticles for nanomedicine. *Surf Sci Rep*, 69(2):132–158, 2014.
- H. T. Lim, K. H. Ahn, J. S. Hong, and K. Hyun. Nonlinear viscoelasticity of polymer nanocomposites under large amplitude oscillatory shear flow. *J. Rheol.*, 57(3):767–789, 2013.
- T.-W. Lin and S.-h. Hsu. Self-healing hydrogels and cryogels from biodegradable polyurethane nanoparticle crosslinked chitosan. *Adv. Sci.*, 7:1901388, 02 2020.
- L. M. Lira, K. A. Martins, and S. I. C. de Torresi. Structural parameters of polyacrylamide hydrogels obtained by the equilibrium swelling theory. *Eur. Polym. J.*, 45(4):1232–1238, 2009.
- S. Liu and M.-Y. Han. Silica-coated metal nanoparticles. *Chem. - Asian J*, 5:36–45, 2010.
- L. M. Liz-Marzán, M. A. Correa-Duarte, I. Pastoriza-Santos, P. Mulvaney, T. Ung, M. Giersig, and N. A. Kotov. Core-shell nanoparticles and assemblies thereof. In H. S. Nalwa, editor, *Handbook of Surfaces and Interfaces of Materials*, chapter 5, pages 189–237. Academic Press, Burlington, 2001.
- T. P. Lodge and P. C. Hiemenz. *Polymer Chemistry*. CRC Press, third edition, 2020.
- B. M. Moudgil M. Bjelopavlic, H. El-Shall. *Polymers in Particulate Systems: Properties and Applications*, volume 104, pages 105–133. Marcel Dekker, Publishers, 2001-11-01 2001.
- T. Ma, R. Yang, Z. Zheng, and Y. Song. Rheology of fumed silica/polydimethylsiloxane suspensions. *J. Rheol.*, 61(2):205–215, 2017.
- M. E. Mackay. *Rheological measurements on small samples*, pages 635–665. Springer Netherlands, Dordrecht, 1998.
- C. W. Macosko and R. G. Larson. *Rheology: Principles, Measurements, and Applications*. Advances in interfacial engineering series. VCH, 1994.
- A. Maghzi, A. Mohebbi, R. Kharrat, and M. H. Ghazanfari. Pore-scale monitoring of wettability alteration by silica nanoparticles during polymer flooding to heavy oil in a five-spot glass micromodel. *Transport Porous Med*, 87(3):653–664, 2011.

- Y.-W. Mai, Z. Yu, X. Xie, Q. Zhang, and J. Ma. Polymer nanocomposites and their applications. *Trans. Hong Kong Inst. Eng.*, 10:67–73, 12 2003.
- L. Mandelkern, F. A. Quinn, and P. J. Flory. Crystallization kinetics in high polymers. i. bulk polymers. *J. Appl. Phys.*, 25(7):830–839, 1954.
- E. Manias. Stiffer by design. *Nat. Mater.*, 6(1):9–11, 2007.
- J. E. Martin, D. Adolf, and J. P. Wilcoxon. Viscoelasticity of near-critical gels. *Phys. Rev. Lett.*, 61:2620–2623, 1988.
- N. K. Maurya and A. Mandal. Studies on behavior of suspension of silica nanoparticle in aqueous polyacrylamide solution for application in enhanced oil recovery. *Pet. Sci. Technol.*, 34(5):429–436, 2016.
- J. Mewis and N. J. Wagner. *Introduction to colloid science and rheology*, pages 1–35. Cambridge Series in Chemical Engineering. Cambridge University Press, 2011.
- M. Mohammadi, M. J. Ameri Shahrabi, and M. Sedighi. Comparative study of linearized and non-linearized modified Langmuir isotherm models on adsorption of asphaltene onto mineral surfaces. *Surf. Eng. Appl. Elect.*, 48(3):234–243, 2012.
- I. L. Mostinsky. Diffusion coefficient. *Thermopedia*, 2011.
- K. Nagase, M. Yamato, and T. Okano. *Temperature-responsive Polymers for Tissue Engineering*, chapter 12, pages 301–312. John Wiley, 2018.
- D. H. Napper. Steric stabilization. *J. Colloid Interf. Sci.*, 58(2):390–407, 1977.
- T. Neidhöfer, M. Wilhelm, and H. W. Spiess. Fourier-transform-rheology on linear polystyrene melts. *Appl Rheol*, 11:126–133, 06 2001.
- T. Neidhöfer, M. Wilhelm, and B. Debbaut. Fourier-transform rheology experiments and finite-element simulations on linear polystyrene solutions. *J. Rheol.*, 47(6):1351–1371, 2003.
- S. Nile, V. Baskar, D. Selvaraj, A. Nile, J. Xiao, and G. Kai. Nanotechnologies in food science: Applications, recent trends, and future perspectives. *Nano-Micro Lett.*, 12, 2020.
- L.-N. Niu, K. Jiao, H. Ryou, A. Diogenes, C. K. Y. Yiu, A. Mazzoni, J.-H. Chen, D. D. Arola, K. M. Hargreaves, D. H. Pashley, and F. R. Tay. Biomimetic silicification of demineralized hierarchical collagenous tissues. *Biomacromolecules*, 14:1661–8, 2013.

- S. C. P. Norris, J. Soto, A. M. Kasko, and S. Li. Photodegradable polyacrylamide gels for dynamic control of cell functions. *ACS Appl. Mater. Interfaces*, 13(5):5929–5944, 2021.
- Richard O’Brien. The effect of an absorbed polyelectrolyte layer on the dynamic mobility of a colloidal particle. *Part. Part. Syst. Charact.*, 19, 07 2002.
- R.W. O’Brien, D.W. Cannon, and W.N. Rowlands. Electroacoustic determination of particle size and zeta potential. *J. Colloid Interface Sci.*, 173(2):406–418, 1995.
- O. Okay and W. Oppermann. Polyacrylamide-clay nanocomposite hydrogels: Rheological and light scattering characterization. *Macromolecules*, 40(9):3378–3387, 2007.
- M. Oliveberg, Y. J. Tan, and A. R. Fersht. Negative activation enthalpies in the kinetics of protein folding. *Proc. Natl. Acad. Sci.*, 92(19):8926–8929, 1995.
- E. Y. X. Ong, M. Ramaswamy, R. Niu, N. Y. C. Lin, A. Shetty, R. N. Zia, G. H. McKinley, and I. Cohen. Stress decomposition in laos of dense colloidal suspensions. *J Rheol*, 64(2):343–351, 2020.
- Y. Osada, J. P. Gong, and Y. Tanaka. Polymer gels. *J. Macromol. Sci. Polymer Rev.*, 44(1):87–112, 2004.
- R. Pamies, J. Cifre, M. Martinez, and J. Torre. Determination of intrinsic viscosities of macromolecules and nanoparticles. comparison of single-point and dilution procedures. *Colloid Polym. Sci.*, 286:1223–1231, 09 2008.
- R. Parhi. Cross-linked hydrogel for pharmaceutical applications: A review. *Adv. Pharm. Bull.*, 7, 12 2017.
- A. Parola and L. Reatto. Depletion interaction between spheres of unequal size and demixing in binary mixtures of colloids. *Mol. Phys.*, 113, 04 2015.
- M. Parthasarathy and D. J. Klingenberg. Large amplitude oscillatory shear of er suspensions. *J. Non-Newtonian Fluid Mech.*, 81(1):83–104, 1999.
- D. Pearson and W. E. Rochefort. Behavior of concentrated polystyrene solutions in large amplitude oscillating shear fields. *J. Polym. Sci. B*, 20:83–98, 1982.
- B. Pelaz, P. del Pino, P. Maffre, R. Hartmann, M. Gallego, S. Rivera-Fernández, J. M. de la Fuente, G. U. Nienhaus, and W. J. Parak. Surface functionalization of nanoparticles with

- polyethylene glycol: Effects on protein adsorption and cellular uptake. *ACS Nano*, 9(7): 6996–7008, 2015.
- K. A. B. Pereira, K. L. N. P. Aguiar, P. F. Oliveira, B. M. Vicente, L. G. Pedroni, and C. R. E. Mansur. Synthesis of hydrogel nanocomposites based on partially hydrolyzed polyacrylamide, polyethyleneimine, and modified clay. *ACS omega*, 5:4759–4769, 2020.
- C. C. Perry. An overview of silica in biology: its chemistry and recent technological advances. *Prog. Mol. Subcell. Biol*, 47:295–313, 2009.
- L. Petit, L. Bouteiller, A. Brûlet, F. Lafuma, and D. Hourdet. Responsive hybrid self-assemblies in aqueous media. *Langmuir*, 23(1):147–158, 2007. PMID: 17190497.
- L. Petit, L. Carlsson, S. Rose, A. Marcellan, T. Narita, and D. Hourdet. Design and Viscoelastic Properties of PDMA/Silica Assemblies in Aqueous Media. *Macromol. Symp.*, 337(1):58–73, 2014.
- J. S. Piccin, T. R. S. Cadaval, L. A. A. de Pinto, and G. L. Dotto. *Adsorption Isotherms in Liquid Phase: Experimental, Modeling, and Interpretations*, pages 19–51. Springer International Publishing, Cham, 2017. ISBN 978-3-319-58136-1.
- D. Puglia and J. M. Kenny. Structure-property relationships of thermoset nanocomposites. In Q. Guo, editor, *Thermosets (Second Edition)*, chapter 7, pages 231–276. Elsevier, second edition edition, 2018.
- H. Qin, T. Zhang, N. Li, H.-P. Cong, and S.-H. Yu. Anisotropic and self-healing hydrogels with multi-responsive actuating capability. *Nat Commun*, 10(1):2202, 2019.
- S. Rafeian, H. Mirzadeh, H. Mahdavi, and M. E. Masoumi. A review on nanocomposite hydrogels and their biomedical applications. *Sci. Eng. Compos. Mater.*, 26(1):154–174, 2019.
- S. R. Raghavan and S. A. Khan. Shear-thickening response of fumed silica suspensions under steady and oscillatory shear. *J. Colloid Interf. Sci.*, 185 1:57–67, 1997.
- J. Ramier, C. Gauthier, L. Chazeau, L. Stelandre, and L. Guy. Payne effect in silica-filled styrene–butadiene rubber: Influence of surface treatment. *J. Polym. Sci. B Polym. Phys.*, 45(3):286–298, 2007.

- A. Rastogi, D. K. Tripathi, S. Yadav, D. K. Chauhan, M. Živčák, M. Ghorbanpour, N. I. El-Sheery, and M. Brestic. Application of silicon nanoparticles in agriculture. *3 Biotech*, 9(3):90, 2019.
- C. M. Roland. Dynamic mechanical behavior of filled rubber at small strains. *J. Rheol.*, 34(1):25–34, 1990.
- S. Rose, A. Marcellan, C. Hourdet, D. and Creton, and T. Narita. Dynamics of hybrid polyacrylamide hydrogels containing silica nanoparticles studied by dynamic light scattering. *Macromolecules*, 46(11):4567–4574, 2013.
- M. Rubinstein and R. H. Colby. *Polymer Physics*. OUP Oxford, 2003.
- J. R. Rumble. *CRC handbook of chemistry and physics: a ready-reference book of chemical and physical data*. CRC Press, 98 edition, 2017.
- W. B. Russel, D. A. Saville, and W. R. Schowalter. *Colloidal Dispersions*. Cambridge Monographs on Mechanics. Cambridge University Press, 1989.
- R. Salehiyan, Y. Yoo, W. Choi, and K. Hyun. Characterization of morphologies of compatibilized polypropylene/polystyrene blends with nanoparticles via nonlinear rheological properties from FT-rheology. *Macromolecules*, 47:4066–4076, 2014.
- B. Samiey and S. Abdollahi Jonaghani. A new approach for analysis of adsorption from liquid phase: A critical review. *J. Pollut. Eff. Cont.*, 3:1–9, 2015.
- Y. Sasaki and K. Akiyoshi. Nanogel engineering for new nanobiomaterials: from chaperoning engineering to biomedical applications. *Chem. Rec.*, 10(6):366–376, 2010.
- T. Savart and B. J. Dove, C. and Love. In situ dynamic rheological study of polyacrylamide during gelation coupled with mathematical models of viscosity advancement. *Macromol. Mater. Eng.*, 295(2):146–152, 2010.
- A. Schausberger and I. V. Ahrer. On the time-concentration superposition of the linear viscoelastic properties of plasticized polystyrene melts using the free volume concept. *Macromol Chem Phys*, 196(7):2161–2172, 1995.
- E. Senses, A. Isherwood, and P. Akcora. Reversible thermal stiffening in polymer nanocomposites. *ACS Appl. Mater. Interfaces*, 7(27):14682–14689, 2015.

- J. Sepulveda, C. Villegas, A. Torres, E. Vargas, F. Rodriguez, S. Baltazar, A. Prada, A. Rojas, J. Romero, S. Faba, and M. J. Galotto. Effect of functionalized silica nanoparticles on the mass transfer process in active PLA nanocomposite films obtained by supercritical impregnation for sustainable food packaging. *J Supercrit Fluid*, 161, 2020.
- Y. Shangguan, F. Chen, E. Jia, Y. Lin, J. Hu, and Q. Zheng. New insight into time-temperature correlation for polymer relaxations ranging from secondary relaxation to terminal flow: Application of a universal and developed WLF equation. *Polymers*, 9, Nov 2017.
- M. T. Shaw. *Normal Stresses—Ordinary Behavior for Polymeric Fluids*, chapter 6, pages 97–123. John Wiley, Ltd, 2011.
- D.-W. Shi, X.-L. Lai, Y.-P. Jiang, C. Yan, Z.-Y. Liu, W. Yang, and M.-B. Yang. Synthesis of inorganic silica grafted three-arm PLLA and their behaviors for PLA matrix. *Chin. J. Polym. Sci. (Engl. Ed.)*, 37(3):216–226, 2019.
- H. G. Sim, K. H. Ahn, and S. J. Lee. Large amplitude oscillatory shear behavior of complex fluids investigated by a network model: a guideline for classification. *J. Non-Newtonian Fluid Mech.*, 112(2):237–250, 2003.
- R. Singh, V. Mahto, and H. Vuthaluru. Development of a novel fly ash-polyacrylamide nanocomposite gel system for improved recovery of oil from heterogeneous reservoir. *J. Petrol Sci. Eng.*, 165:325–331, 2018.
- R. Singhal and I. Gupta. A study on the effect of butyl methacrylate content on swelling and controlled-release behavior of poly (acrylamide-co-butyl-methacrylate-co-acrylic acid) environment-responsive hydrogels. *Int. J. Polym. Mater. Polym. Biomater.*, 59(10):757–776, 2010.
- R. Singhal and K. Gupta. A review: Tailor-made hydrogel structures (classifications and synthesis parameters). *Polym.-Plast. Technol. Eng.*, 55(1):54–70, 2016.
- M. A. Skidmore and J. E. Turnbull. Separation and sequencing of heparin and heparan sulphate saccharides. In H. G. Garg, R. J. Linhardt, and C. A. Hales, editors, *Chemistry and Biology of Heparin and Heparan Sulfate*, chapter 6, pages 179–201. Elsevier Science, Amsterdam, 2005.

- P. Sobolčiak, A. Popelka, A. Tanvir, M. A. Al-Maadeed, S. Adham, and I. Krupa. Some theoretical aspects of tertiary treatment of water/oil emulsions by adsorption and coalescence mechanisms: A review. *Water*, 13(5), 2021.
- R. E. Sojka and R. Lentz. Reducing furrow irrigation erosion with polyacrylamide (PAM). *J. Prod. Agric.*, 10, 01 1997.
- R. E. Sojka, R. D. Lentz, and D. T. Westermann. Water and erosion management with multiple applications of polyacrylamide in furrow irrigation. *Soil Sci. Soc. Am. J.*, 62(6): 1672–1680, 1998.
- E. R. Sokol, M. M. Karram, and R. Dmochowski. Efficacy and safety of polyacrylamide hydrogel for the treatment of female stress incontinence: A randomized, prospective, multicenter north american study. *J. Urol.*, 192(3):843–849, 2014.
- R. Stringer. Electrophoresis — overview. In P. Worsfold, A. Townshend, and C. Poole, editors, *Encyclopedia of Analytical Science (Second Edition)*, pages 356–363. Elsevier, Oxford, 2005.
- M. A. C. Stuart and J. W. Mulder. Adsorbed polymers in aqueous media the relation between zeta potential, layer thickness and ionic strength. *Colloids Surf.*, 15:49–55, 1985.
- M. I. Sujana, S. D. Sarkar, S. Sultana, L. Bushra, R. Tareq, C. K. Roy, and M. S. Azam. Bi-functional silica nanoparticles for simultaneous enhancement of mechanical strength and swelling capacity of hydrogels. *RSC Adv*, 10:6213–6222, 2020.
- D. Sun, H. I. Hussain, Z. Yi, J. E. Rookes, L. Kong, and D. M. Cahill. Mesoporous silica nanoparticles enhance seedling growth and photosynthesis in wheat and lupin. *Chemosphere*, 152:81–91, 2016.
- W. Sun, Y. Yang, T. Wang, H. Huang, X. Liu, and Z. Tong. Effect of adsorbed poly(ethylene glycol) on the gelation evolution of Laponite suspensions: Aging time-polymer concentration superposition. *J. Colloid Interf. Sci.*, 376(1):76–82, 2012.
- T. Tadros. *Steric Stabilization*, pages 1048–1049. Springer Berlin Heidelberg, Berlin, Heidelberg, 2013.
- I. The MathWorks. *Curve Fitting Toolbox™ User’s Guide*. Natick, Massachusetts, United State, 2022.

- M. van Gorp and J. Palmen. Time-temperature superposition for polymeric blends. *Rheol. Bull.*, 67:5–8, 01 1998.
- M. Vera, C. Mella, and B. Urbano. Smart polymer nanocomposites: Recent advances and perspectives. *J. Chil. Chem. Soc.*, 65:4973–4981, 12 2020.
- J Vermant, L Walker, P Moldenaers, and J Mewis. Orthogonal versus parallel superposition measurements. *J. Non-Newton. Fluid Mech.*, 79(2):173–189, 1998.
- L. Vincent and A. J. Engler. Effect of substrate modulus on cell function and differentiation. In P. Ducheyne, editor, *Comprehensive Biomaterials II*, pages 88–101. Elsevier, Oxford, 2017.
- I. Vittorias, M. Parkinson, K. Klimke, B. Debbaut, and M. Wilhelm. Detection and quantification of industrial polyethylene branching topologies via Fourier-transform rheology, NMR and simulation using the pom-pom model. *Rheol. Acta*, 46(3):321–340, 2007.
- R. Vundavalli, S. Vundavalli, M. Nakka, and D. S. Rao. Biodegradable nano-hydrogels in agricultural farming - alternative source for water resources. *Procedia Mater. Sci.*, 10:548 – 554, 2015.
- S. Vyazovkin. Activation energies and temperature dependencies of the rates of crystallization and melting of polymers. *Polymers*, 12, 2020.
- S. Vyazovkin and N. Sbirrazzuoli. Isoconversional analysis of the nonisothermal crystallization of a polymer melt. *Macromol. Rapid Commun*, 23(13):766–770, 2002.
- H. J. Walls, S. B. Caines, A. M. Sanchez, and S. A. Khan. Yield stress and wall slip phenomena in colloidal silica gels. *J Rheol*, 47(4):847–868, 2003.
- M. Wang and R. J. Hill. Dynamic electric-field-induced response of charged spherical colloids in uncharged hydrogels. *J. Fluid Mech.*, 640:357–400, 2009.
- Q. Wang, J. L. Mynar, M. Yoshida, E. Lee, M. Lee, K. Okuro, K. Kinbara, and T. Aida. High-water-content mouldable hydrogels by mixing clay and a dendritic molecular binder. *Nature*, 463(7279):339–343, 2010.
- W. Wang and C. J. Roberts. Non-arrhenius protein aggregation. *The AAPS Journal*, 15: 840–851, 2013.

- Y. Wang, Y. Ding, X. Guo, and G. Yu. Conductive polymers for stretchable supercapacitors. *Nano Res*, 12(9):1978–1987, 2019.
- H. Wanyika, E. Gatebe, P. Kioni, Z. Tang, and Y. Gao. Mesoporous silica nanoparticles carrier for urea: potential applications in agrochemical delivery systems. *J. Nanosci. Nanotechnol*, 12:2221–8, 2012.
- Z. Wei, J. H. Yang, J. Zhou, F. Xu, M. Zrínyi, P. H. Dussault, Y. Osada, and Y. M. Chen. Self-healing gels based on constitutional dynamic chemistry and their potential applications. *Chem. Soc. Rev.*, 43:8114–8131, 2014.
- G. R. Wiese and T. W. Healy. Effect of particle size on colloid stability. *Trans. Faraday Soc.*, 66:490–499, 1970.
- M. Wilhelm. Fourier-Transform Rheology. *Macromol. Mater. Eng.*, 287(2):83–105, 2002.
- P. J. Willcox, D. W. Howie, K. Schmidt-Rohr, D. A. Hoagland, S. P. Gido, S. Pudjijanto, L. W. Kleiner, and S. Venkatraman. Microstructure of poly(vinyl alcohol) hydrogels produced by freeze/thaw cycling. *J. Polym Sci. Pol Phys*, 37(24):3438–3454, 1999.
- M. L. Williams, R. F. Landel, and J. D. Ferry. The temperature dependence of relaxation mechanisms in amorphous polymers and other glass-forming liquids. *J. Am. Chem. Soc.*, 77(14):3701–3707, 1955.
- J. P. Winer and P. A. Oake, S. and Janmey. Non-linear elasticity of extracellular matrices enables contractile cells to communicate local position and orientation. *PLoS One*, 4(7): 1–11, 07 2009.
- M. Wiśniewska. The temperature effect on the adsorption mechanism of polyacrylamide on the silica surface and its stability. *Appl. Surf. Sci.*, 258(7):3094–3101, 2012.
- F. Wu, X. Lan, D. Ji, Z. Liu, W. Yang, and M. Yang. Grafting polymerization of polylactic acid on the surface of nano-SiO₂ and properties of PLA/PLA-grafted-SiO₂ nanocomposites. *J. Appl. Polym. Sci.*, 129(5):3019–3027, 2013.
- J. Wu. Laponite®-doped poly(acrylic acid-co-acrylamide) hydrogels. 2022. Master’s thesis, McGill University.
- S. Wu and R. A. Shanks. Conformation of polyacrylamide in aqueous solution with interactive additives and cosolvents. *J. Appl. Polym. Sci.*, 89(11):3122–3129, 2003.

- B. Xiong, D. Loss, R. D. and Shields, T. Pawlik, R. Hochreiter, A. L. Zydney, and M. Kumar. Polyacrylamide degradation and its implications in environmental systems. *NPJ Clean Water*, 1(1):17, 2018.
- X. Xu, C. Gao, Q. Zheng, and X. Jiang. Linear/nonlinear rheological properties and percolation threshold of polydimethylsiloxane filled with calcium carbonate. *Nihon Reoroji Gakk*, 35(5):283–291, 2007.
- S. Yan, J. Yin, Y. Yang, Z. Dai, J. Ma, and X. Chen. Surface-grafted silica linked with l-lactic acid oligomer: A novel nanofiller to improve the performance of biodegradable poly(l-lactide). *Polymer*, 48(6):1688–1694, 2007.
- J. Yang, C.-R. Han, J.-F. Duan, F. Xu, and R.-C. Sun. In situ grafting silica nanoparticles reinforced nanocomposite hydrogels. *Nanoscale*, 5:10858–10863, 2013.
- T.-H. Yang. Recent applications of polyacrylamide as biomaterials. *Recent Pat. Mater. Sci.*, 1(1):29–40, 2008.
- N. Y. Yao, R. J. Larsen, and D. A. Weitz. Probing nonlinear rheology with inertio-elastic oscillations. *J. Rheol.*, 52(4):1013–1025, 2008.
- M. S. Yavuz, Y. Cheng, J. Chen, C. M. Cobley, Q. Zhang, M. Rycenga, J. Xie, C. Kim, K. H. Song, A. G. Schwartz, L. V. Wang, and Y. Xia. Gold nanocages covered by smart polymers for controlled release with near-infrared light. *Nat. Mater.*, 8(12):935–939, 2009.
- G. Yazar, O. Duvarci, M. Yildirim Erturk, and J. Kokini. LAOS (Large Amplitude Oscillatory Shear) applications for semisolid foods. *Food Eng. Ser*, pages 97–131, 11 2019.
- L. Ye, Y. Tang, and D. Qiu. Enhance the mechanical performance of polyacrylamide hydrogel by aluminium-modified colloidal silica. *Colloids Surf., A*, 447:103–110, 2014.
- W. Yu, P. Wang, and C. Zhou. General stress decomposition in nonlinear oscillatory shear flow. *J Rheol*, 53(1):215–238, 2009.
- F. Yziquel, P. J. Carreau, and P. A. Tanguy. Non-linear viscoelastic behavior of fumed silica suspensions. *Rheol. Acta*, 38(1):14–25, 1999.
- B Zhao and W.J Brittain. Polymer brushes: surface-immobilized macromolecules. *Prog Polym Sci*, 25(5):677–710, 2000.

Ł. Zych, A. M. Osyczka, A. Łacz, A. Różycka, W. Niemiec, A. Rapacz-Kmita, E. Dzierzkowska, and E. Stodolak-Zych. How surface properties of silica nanoparticles influence structural, microstructural and biological properties of polymer nanocomposites. *Materials*, 14(4), 2021.